Titre: Title:	Density effects on contaminant migration in saturated-unsaturated porous media
Auteur: Author:	Yin Fan
Date:	1995
Type:	Mémoire ou thèse / Dissertation or Thesis
Référence: Citation:	Fan, Y. (1995). Density effects on contaminant migration in saturated-unsaturated porous media [Ph.D. thesis, École Polytechnique de Montréal]. PolyPublie. https://publications.polymtl.ca/32306/

Document en libre accès dans PolyPublie
Open Access document in PolyPublie

URL de PolyPublie: PolyPublie URL:	https://publications.polymtl.ca/32306/
Directeurs de recherche: Advisors:	René Kahawita
Programme: Program:	Unspecified

UNIVERSITÉ DE MONTRÉAL

DENSITY EFFECTS ON CONTAMINANT MIGRATION

IN SATURATED-UNSATURATED POROUS MEDIA

YIN FAN

DÉPARTEMENT DE GENIE CIVIL

ÉCOLE POLYTECHNIQUE

THÈSE PRÉSENTÉE EN VUE DE L'OBTENTION

DU DIPLÔME DE PHILOSOPHIAE DOCTOR (Ph. D.)

(GÉNIE CIVIL)

MARS 1995

THE AUTHOR HAS GRANTED AN
IRREVOCABLE NON-EXCLUSIVE
LICENCE ALLOWING THE NATIONAL
LIBRARY OF CANADA TO
REPRODUCE, LOAN, DISTRIBUTE OR
SELL COPIES OF HIS/HER THESIS BY
ANY MEANS AND IN ANY FORM OR
FORMAT, MAKING THIS THESIS
AVAILABLE TO INTERESTED
PERSONS.

L'AUTEUR A ACCORDE UNE LICENCE
IRREVOCABLE ET NON EXCLUSIVE
PERMETTANT A LA BIBLIOTHEQUE
NATIONALE DU CANADA DE
REPRODUIRE, PRETER, DISTRIBUER
OU VENDRE DES COPIES DE SA
THESE DE QUELQUE MANIERE ET
SOUS QUELQUE FORME QUE CE SOIT
POUR METTRE DES EXEMPLAIRES DE
CETTE THESE A LA DISPOSITION DES
PERSONNE INTERESSEES.

THE AUTHOR RETAINS OWNERSHIP
OF THE COPYRIGHT IN HIS/HER
THESIS. NEITHER THE THESIS NOR
SUBSTANTIAL EXTRACTS FROM IT
MAY BE PRINTED OR OTHERWISE
REPRODUCED WITHOUT HIS/HER
PERMISSION.

L'AUTEUR CONSERVE LA PROPRIETE
DU DROIT D'AUTEUR QUI PROTEGE
SA THESE. NI LA THESE NI DES
EXTRAITS SUBSTANTIELS DE CELLE-
CI NE DOIVENT ETRE IMPRIMES OU
AUTREMENT REPRODUITS SANS SON
AUTORISATION.

ISBN   0-612-03692-8

Canada

UNIVERSITÉ DE MONTRÉAL

ÉCOLE POLYTECHNIQUE

Cette thèse institulée:

DENSITY EFFECTS ON CONTAMINANT MIGRATION

IN SATURATED-UNSATURATED POROUS MEDIA

présentée par: FAN, Yin

en vue de l'obtention du diplôme de: Philosophiae Doctor

a été dûment acceptée par le jury d'examen constitué de:

M. LECLERC Guy, Ph.D., président

M. KAHAWITA René, Ph.D., membre et directeur de recherche

M. CHAPUIS Robert, Ph.D., membre

M. UPPALURI Bindu, Ph.D., membre

Dedicated to my parents

ACKNOWLEDGEMENTS

First of all, I would like to express my greatest appreciation to Professor Rene Kahawita, my research surpervisor for his encouragement and wise guidance during the course of this research.

I owe a debt of gratitude to the Education Department of the Government of Quebec for the waiver of the foreign student tuition fees during my doctoral program at Ecole Polytechnique de Montreal.

In addition, thanks are due to Mr. Jean-Claude Tessier who furnished the triangular mesh generator that was used in this dissertation. I would also like to repeat my acknowledgement of the help I received from many members of the personnel as well as friends at the Ecole Polytechnique.

Finally, my sincere gratitude goes to my husband Zheng Zhang for his love and encouragement throughout my graduate study, and also for many helpful discussions.

RÉSUMÉ

Ce travail est consacré à une étude numérique concernant les écoulements de densité variable, ainsi qu'au transport de contaminants dans des milieux poreux saturés et non-saturés. Divers modèles numériques utilisant des techniques de différences finies, de volumes de contrôle et de volumes finis pour la formulation des équations gouvernant les champs d'écoulements ont été développées. La formulation aux volumes finis a été implantée sur un maillage triangulaire, ce qui a pour principal avantage de pouvoir directement être appliqué au traitement des domaines irréguliers. Dans cette formulation, le traitement numérique de l'équation de transport est réalisé en utilisant un schéma basé sur la méthode des caractéristiques pour le transport convectif, tandis que le terme diffusif est évalué sur un maillage triangulaire, en utilisant les volumes finis, avec interpolation linéaire pour la concentration.

Afin de partiellement valider le modèle, les résultats de trois différentes études récemment publiées dans la littérature ont été simulés. Deux de ces études sont des recherches expérimentales en laboratoire, tandis que la troisième est une étude basé sur les mesures prises autour d'un site d'enfouissement de déchets.

La première étude choisie pour la validation est de résultat d'une recherche en laboratoire récemment publiée par Schincariol & Schwartz (1990), concernant le comportement d'une solution saline dense, injectée horizontalement au milieu d'un

écoulement souterrain de densité moindre. Cette expérience a couvert les milieux poreux saturés homogènes et non-homogènes. Comme la géométrie du bassin utilisé était rectangulaire, les méthodes standards aux différences finies ont été utilisées afin de simuler numériquement le phénomène. Une bonne corrélation entre les résultats numériques et expérimentaux a été obtenue. En particulier, les expériences de laboratoire qui ont révélé la présence d'instabilités induites par la gravité, ayant la forme des ondes d'amplitude significatives le long de la bordure inférieure du panache a été fidèlement reproduit par le modèle numérique.

La seconde étude choisie pour valider le modèle est une série d'expériences de laboratoire effectuées par Oostrom et al. (1992). Dans chaque expérience, la trajectoire d'un dense panache de lixiviat appliqué en surface et marqué à l'aide de colorants a été suivie. Ce lixiviat a été synthétisé en utilisant des solutions aqueuses d'Iodure de Sodium et de Bromure de Sodium. L'montage expérimental consistait en un bassin rectangulaire contenant un milieu poreux homogène, dans lequel l'écoulement était induit par des réservoirs à niveaux constants. Comme dans le cas de la première expérience, celle-ci a révélé la formation d'instabilités gravitationnelles dans le panache. Cette série d'expériences a été numériquement simulée en utilisant une formulation de volume de contrôle sur un maillage rectangulaire. Les caractéristiques moyennes de l'écoulement ont été fidèlement reproduites par le modèle numérique. Par contre, les instabilités n'ont été correctement simulées qu'avec un domaine de calcul significativement allongé, éliminant effectivement l'influence des conditions frontières imposées à l'écoulement aux

sections situées en amont et en aval du point d'injection.

Afin d'avoir une connaissance plus approfondie du mécanisme d'instabilité, une analyse linéaire de stabilité a été effectuée. Les premiers résultats de cette analyse confirment qu'un panache dense est en fait instable, les deux paramètres gouvernant la stabilité étant un nombre de Rayleigh basée sur la concentration et une longueur caractéristique, cette dernière dépendant de la dispersivité transversale. Les courbes de stabilité critiques ont été calculées et présentées. Les estimés des deux paramètres des panaches observés lors des expériences confirment que leurs valeurs se situent en dehors des limites de stabilité, tel que prédit par l'analyse de stabilité.

Finalement, la propagation d'un panache de lixiviat au site d'enfouissement de déchets à Borden, Ontario a été simulée numériquement en utilisant une formulation en volumes finis sur un maillage triangulaire. Les mesures prises au site et autour ont été documentées par MacFarlane et al. (1983). Parce que les données prises in situ, ainsi que les propriétés du sol sont de faible résolution et entachées d'incertitude, seule une comparaison globale a pu être effectuée. Toutefois, il a été possible d'obtenir une modélisation satisfaisante des longueurs de propagation du panache. Les simulations numériques ont toutefois révélé que, même à cette échelle, des instabilités gravitationnelles se forment le long de la bordure inférieure du panache, avec des amplitudes verticales suffisamment importantes pour altérer le comportement dispersif du panache. Les estimations du nombre de Rayleigh de la concentration et de l'échelle

de longueur caractéristique ont révélé que le panache de lixiviat est instable et pourrait aboutir au type de comportement prédit par le modèle numérique.

Les analyses et les simulations numériques indiquent qu'un dense panache de lixiviat pénétrerait à une plus grande profondeur qu'un panache de même densité que le milieu récepteur. De plus, si le critère de stabilité est dépassé, des instabilités locales de grande amplitude peuvent apparaître, modifiant encore plus les caractéristiques dispersives du lixiviat.

Les modèles numériques développés ont démontré avoir d'excellentes caractéristiques de stabilité numérique. La formulation en volumes finis présentée est robuste et précise. En effet, due aux propriétés fondamentales de l'algorithme d'Euler-Lagrange pour l'équation de transport, on n'obtient pas de valeurs non-positives de la concentration ou des oscillations parasites dans la solution, tant qu'un certain critère de stabilité de base est satisfait. De plus, il est possible d'implanter aisément l'inclusion de termes sources d'adsorption et des réactions chimiques au modèle.

ABSTRACT

This work is devoted to a numerical investigation of variable density flow and contaminant transport in saturated-unsaturated porous media. Numerical models, using finite-difference techniques as well as control volume and finite volume formulations of the governing equations for the flowfield have been investigated. The finite volume formulation has been implemented on a triangular mesh, the chief advantage being its capacity to treat irregular computational domains. In this formulation, the numerical treatment of the transport equation is realised using a characteristics based scheme for the convective transport, while the diffusion term is evaluated on a triangular stencil using the finite volume formulation with linear interpolation for the concentration. The results of three separate studies published in the recent literature, two of which were experimental investigations under laboratory conditions, while the third consisted of field measurements taken around a waste landfill site have been simulated for partial validation purposes.

The first study chosen for validation is the recently reported laboratory investigation of Schincariol and Schwartz (1990) concerning the behaviour of a dense salt solution injected horizontally into the middle of a less dense ambient groundwater flow. Their experiments covered both homogeneous and non-homogenous saturated porous media. Due to the simple rectangular geometry of their flow tank, standard finite-difference methods were used to numerically simulate the process. Good agreement

between the numerical and experimental results were obtained. In particular, the experimentally observed appearance of gravitationally induced instabilities in the form of lobe shaped protuberances along the lower edge of the plume, was faithfully reproduced by the numerical model.

The second study chosen to validate the model were the laboratory experiments of Oostrom et al. (1992). In this experiment, the trajectory of a dense surface applied leachate plume was tracked using dye techniques. The heavy leachate plumes were synthesised using aqueous solutions of Sodium Iodide and Sodium Bromide. The experimental apparatus consisted of a rectangular flow tank packed with a homogeneous porous medium, the mean Darcy flow being generated by the use of constant head tanks. Again, these experiments also revealed the formation of gravitational instabilities in the plume. This series of experiments were numerically simulated using a control volume formulation on a rectangular mesh. Good agreement as far as the mean flow characteristics were obtained. However the instabilities were correctly simulated only when the computational domain was significantly increased lengthwise, effectively removing the influence of the imposed boundary conditions on the flow, to sections situated further upstream and downstream from the injection point.

To gain a more meaningful insight into the stability mechanism, a linear analysis of the stability characteristics was undertaken. The basic results confirm that a dense plume is in fact unstable, the two parameters governing the stability being a concentration

Rayleigh Number and a characteristic length scale which is dependant on the transverse dispersivity. Curves of critical stability have been traced out and presented. Estimates of the two relevant parameters for the unstable plumes observed in the experiments, confirm the fact that their values lie outside the stability limits predicted by the simple analysis.

Finally, as a case study, the spread of a leachate plume from a waste landfill site in Borden, Ontario was numerically simulated using the finite volume formulation on a triangular mesh. Field measurements taken at and around the site have been reported by MacFarlane et al.(1983). Due to the lack of resolution and uncertainty in the field data as well as in the soil properties, only global comparisons were possible. These did however provide satisfactory agreement as to the propagation lengths of the plume. The numerical simulations did however reveal that even at these scales, gravitational instabilities form along the lower edge of the plume with amplitudes of vertical extent sufficiently large to alter the dispersion behaviour of the plume. Estimates of concentration Rayleigh number and characteristic length scales revealed that the leachate plume is unstable and would lead to the type of behaviour predicted by the numerical model.

The analysis and numerical simulations indicate that a dense leachate plume would, as expected, penetrate to greater depths than one of neutral density. Furthermore, if the stability criteria are exceeded, local instabilities of large amplitude are possible, resulting in further important modifications to its dispersion characteristics.

The numerical models reported here have displayed excellent numerical stability characteristics. The finite volume formulation presented here is robust and accurate. Due to the basic properties of the Lagrangian-Eulerian algorithm for the transport equation, non-positive values of concentration or parasitic oscillations in the solution do not arise, provided that certain basic stability criteria are satisfied. Addition of source terms to model adsorption and chemical reactions may be easily implemented.

CONDENSÉ EN FRANÇAIS

L'eau souterraine constitue une composante importante des ressources hydriques disponibles, souvent exploitée pour des fins domestiques, industrielles et agricoles. Récemment, l'intérêt du public a été éveillé face à la contamination des nappes d'eau par des déchets industriels, par la lixiviation des dépotoirs et par des activités agricoles comme l'application des pesticides et des engrais. De plus, à l'occasion d'audiences publiques tenues aux États-unis, des inquiétudes concernant la sécurité des dépôts de déchets radioactifs souterrains ont été exprimées. Il existe donc un besoin d'outils de modélisation de la migration d'un panache de contaminant au travers les nappes d'eau.

Ce travail porte sur une étude numérique des écoulements de densité variable, ainsi que sur le transport de contaminants dans des milieux poreux saturés et non-saturés. Les équations gouvernant ce phénomène comprennent l'équation de Darcy, l'équation de continuité pour un fluide incompressible, l'équation de transport des polluants et une équation d'état qui relie la densité du fluide à sa concentration en polluant. La plupart des modèles existants qui traitent de ce sujet, considèrent que la densité du fluide contenu dans le panache est égale à celle du milieu ambiant. En fait, des études ont démontré qu'une densité de 0.2 % plus haute que celle de l'eau peut modifier considérablement le comportement du panache. Des sources de polluant, pré-sentes à la surface du sol, produisent des quantités de lixiviats considérables ayant des différences de densité qui varient typiquement entre 0.5 % et 4 % par rapport à l'eau pure. Ces différences de

densité ont pour résultat d'affecter le comportement du polluant pendant son transport dans l'eau souterraine, rendant la propagation considérablement différente de celle qui existerait si le panache était de densité "neutre".

La plupart des études touchant les écoulements de densité variable dans les milieux poreux sont consacrées au traitement du problème des intrusions salines près des aquifères littorales. Très peu de travaux ont abordé la compréhension des migrations de lixiviat à partir des dépotoirs de surface.

La majorité des modèles de transport et des logiciels de traitement des écoulements souterrains utilisent les techniques des différences finies et des éléments finis. Le modèle SUTRA développé par Voss (1984) est le plus fréquemment utilisé aux États-Unis. Il est disponible dans le domaine public. Un autre modèle, MOCDENSE, fut récemment développé aux États-Unis (Sanford et Konikow, 1985). Dans le présent travail, diverses techniques numériques comme celles des différences finies, des volumes de contrôle et des volumes finis ont été étudiées et analysées pour application.

La technique des différences finies a été mise en oeuvre sur un domaine rectangulaire de calcul avec les équations d'écoulement exprimées en terme de fonction de courant. La discrétisation dans le temps est une discrétisation avancée tandis que pour les termes convectifs apparaissant dans l'équation de transport, une technique de différentiation amont a été utilisée. Les équations algébriques pour la fonction de courant

ont été résolues par substitution en bloc SOR (Successive Over Relaxation). À chaque pas de temps, les valeurs de la fonction de courant dans les rangées et les colonnes dans la matrice de résolution sont obtenues ligne par ligne en faisant alterner la direction de "balayage" de la solution. En effet, c'est une simple modification de la technique d'élimination de Gauss.

Pour l'équation de transport, les variables de concentration sont résolues d'une façon implicite en direction x et ensuite implicite pour une matrice tridiagonale. Les valeurs de vitesses requises dans cette étape sont fournies par l'étape précédente de la résolution de fonction de courant. Les valeurs de concentration ainsi obtenues sont utilisées pour recalculer les valeurs de fonction de courant jusqu'à ce que la convergence soit atteinte. La solution est ensuite avancée dans le temps pour le prochain pas de résolution. Si la convergence n'est pas obtenue dans un certain nombre d'itérations entre les équations de fonction de courant et de concentration, le pas de temps est réduit de moitié et le processus est répété.

Un autre schéma numérique a été utilisé, celui de la formulation en "volume de contrôle" inspire par le travail de Patankar (1980). Cette méthode consiste en une intégration des équations gouvernantes autour d'un volume de contrôle qui, dans la version originale, était un maillage rectangulaire. Les flux traversant l'interface entre les volumes sont évalués sur une base physique. La technique de résolution des équations matricielles obtenue avec cette méthode est légèrement différente de la précédente. Pour

calculer le champs d'écoulement, on commence avec un champ de pression approximatif (par exemple une distribution hydrostatique). Ensuite, l'écoulement permanent est obtenu utilisant la technique point par point de Gauss-Seidel pour la résolution. Des valeurs initiales pour la concentration étant déjà imposées (par exemple zéro partout excepté dans la frontière d'entrée du panache où la concentration est égale à un). Ces valeurs sont utilisées pour calculer la densité à l'aide d'une équation d'état, puis le champ de pression est ensuite recalculé. Le champ d'écoulement (les vitesses de Darcy) est calculé en utilisant le champ de pression. Les valeurs de vitesse sont entrées dans l'équation de transport qui permet le calcul du champ de concentration. Une vérification de convergence est imposée pour les champs de pression et de concen-tration. Après la convergence, la solution est avancée dans le temps et le processus est répété. Les résultats obtenus avec cette formulation sont très satisfaisants d'après la validation en laboratoire.

Une extension du concept de volume de contrôle est la formulation en volumes finis. Dans cette dernière, les équations de base sont intégrées sur des volumes de géométrie arbitraire, ce qui a pour principal avantage de pouvoir être appliqué direc-tement au traitement des domaines irréguliers. Dans cette étude, la formulation en volumes finis a été implantée sur un maillage triangulaire qui peut aisément être généré par des préprocesseurs existants. Dans cette formulation, le traitement numérique de l'équation de transport a été réalisé en utilisant un schéma basé sur la méthode des caractéristiques pour le transport convectif, tandis que le terme de diffusion a été évalué

sur un maillage triangulaire en utilisant les volumes finis avec interpolation linéaire pour la concentration.

Afin de valider partiellement le modèle, les résultats de trois études différentes récemment publiées dans la littérature ont été simulés. Deux de ces études sont des recherches expérimentales en laboratoire, tandis que la troisième est constituée de mesures prises autour d'un site d'enfouissement de déchets.

La première étude choisie pour la validation est le résultat d'une recherche en laboratoire récemment publiée par Schincariol and Schwartz (1990), concernant le comportement d'une solution saline dense, injectée horizontalement au milieu d'un écoulement souterrain de densité moindre. Cette expérience concernait les milieux poreux saturés homogènes et non-homogènes. Leur appareil consistait en un réservoir étroit par rapport à sa hauteur et sa longueur. Le réservoir était rempli avec des billes de verre de diamètres variés. Des réservoirs à niveau constant étaient installés à l'entrée et à la sortie du réservoir pour ainsi permettre un bon réglage du débit. Les dimensions du réservoir d'étude était de 116.8 cm de long par 71 cm de haut et une largeur de 5 cm. Le réservoir était fermé en haut permettant ainsi des tests sur un milieu saturé. La solution dense de chlorure de sodium pouvait être introduite par une fente située au milieu. Comme la géométrie du bassin utilisé était rectangulaire, les méthodes standards aux différences finies ont été utilisées afin de simuler numéri-quement le phénomène. Une bonne corrélation entre les résultats numériques et expérimentaux a été obtenue.

En particulier, les expériences de laboratoire qui ont révélé la présence d'instabilités induites par la gravité, ayant la forme d'ondes d'amplitudes significatives le long de la bordure inférieure du panache ont été fidèlement reproduites par le modèle numérique.

La seconde étude choisie pour valider le modèle décrit une série d'expériences de laboratoire effectuées par Oostrom et al. (1992). Dans chaque expérience, la trajectoire d'un panache dense de lixiviat appliqué en surface et marqué à l'aide de colorants a été suivie. Ce lixiviat a été synthétisé en utilisant des solutions aqueuses d'Iodure de Sodium et de Bromure de Sodium. Le montage expérimental consistait en un bassin rectangulaire contenant un milieu poreux homogène, dans lequel l'écoulement était induit par des réservoirs à niveaux constants. Comme dans le cas de la première expérience, celle-ci a révélé la formation d'instabilités gravitationnelles dans le panache. Cette série d'expériences a été numériquement simulée en utilisant une formulation en volume de contrôle sur un maillage rectangulaire. Les caractéristiques moyennes de l'écoulement ont été fidèlement reproduites par le modèle numérique. Par contre, les instabilités n'ont été correctement simulée qu'avec un domaine de calcul significativement allongé, éliminant effectivement l'influence des conditions frontières imposées à l'écoulement aux sections situées en amont et en aval du point d'injection.

Afin d'obtenir une connaissance plus approfondie du mécanisme d'instabilité, une analyse linéaire de la stabilité a été effectuée. Dans cette technique, une perturbation 3-dimensionnelle dans l'espace et avec une amplification exponentielle dans le temps est

superposée sur les équations gouvernantes. Sa soustraction de l'équation de base résulte en une équation différentielle décrivant le comportement des perturbations. Après avoir imposé des conditions frontières sur les perturbations, il reste à déterminer le profil moyen de la concentration. Dans cette étude, des considérations physiques (vérifiées par la suite par calcul) nous ont amené à proposer une forme "Gaussienne" pour la variation de la concentration dans le plan vertical. Les équations différentielles pour les perturbations ont été résolues en faisant une expansion en série de fonction de valeurs propres qui satisfont les conditions frontières. Étant donné que les conditions frontières sont homogènes, le problème en est un de valeur propre.

Les premiers résultats de cette analyse confirment qu'un panache dense est en fait instable, les deux paramètres gouvernant la stabilité étant un nombre de Rayleigh basé sur la concentration et une longueur caractéristique, cette dernière dépendante de la dispersivité transversale. Les courbes de stabilité critique ont été calculées et présentées. Les estimés des deux paramètres des panaches observés lors des expériences confirment que leur valeur se situe en dehors des limites de stabilité, prédites par l'analyse de stabilité.

Finalement, la propagation d'un panache de lixiviat au site d'enfouissement de déchets à Borden, Ontario, a été simulée numériquement en utilisant une formulation en volumes finis sur un maillage triangulaire. Le site de Borden était un camp militaire durant la période de 1940 à 1976. Pendant ces 36 ans, il a été estimé que 80% des

déchets se consistaient en cendres, bois et autres débris de construction. Le reste des dépôts avait une composition de déchets surtout domestiques et industrielles. La composition du sol et sa conductivité sont apparemment très variables, contenant du sable et de l'argile. Les mesures prises au site et autour ont été documentées par MacFarlane et al. (1983). Parce que les données prises in situ, ainsi que les propriétés du sol sont de faible résolution et entachées d'incertitude, seule une comparaison globale a pu être effectuée. Toutefois, il a été possible d'obtenir une modélisation satisfaisante des longueurs de propagation du panache. Les simulations numériques ont toutefois révélé que, même à cette échelle, des instabilités gravitationnelles se forment le long de la bordure inférieure du panache, avec des amplitudes verticales suffisamment importantes pour altérer le comportement dispersif du panache. Les estimations du nombre de Rayleigh de la concentration et de l'échelle de longueur caractéristique ont révélé que le panache de lixiviat est instable et pourrait aboutir au type de comportement prédit par le modèle numérique.

Les analyses et les simulations numériques indiquent qu'un panache dense de lixiviat pénétrerait à une plus grande profondeur qu'un panache de même densité que le milieu récepteur. De plus, si le critère de stabilité est dépassé, des instabilités locales de grande amplitude peuvent apparaître, modifiant encore plus les caractéristiques dispersives du lixiviat.

Les modèles numériques développés ont démontré d'excellentes caractéristiques

de stabilité numérique. La formulation en volume finis présentée est robuste et précise. En effet, dû aux propriétés fondamentales de l'algorithme d'Euler-Lagrange pour l'équation de transport, on n'obtient pas de valeurs non-positives de la concentration ou des oscillations parasites dans la solution, tant qu'un certain critère de stabilité de base est satisfait. De plus, il est possible d'implanter aisément l'inclusion de terme-sources d'absorption et les réactions chimiques dans la modélisation.

TABLE OF CONTENTS

LIST OF FIGURES

LIST OF TABLES

LIST OF APPENDIXES

LIST OF SYMBOLS

C   concentration (ML^{-3} or M/M)

C_0 characteristic concentration (ML^{-3})

$\mathcal{C}$ dimensionless concentration, C/C_0

D_{ij} dispersion coefficient tensor (L^2T^{-1})

D_{xx}, D_{xz}, D_{zz} components of dispersion coefficient tensor (L^2T^{-1})

D_d^* molecular diffusion coefficient (L^2T^{-1})

D_h coefficient of hydrodynamic dispersion (L^2T^{-1})

$\mathcal{D}_{ij}$ dimensionless quantities

K_{sat} hydraulic conductivity in saturated porous media (LT^{-1})

K_{ij} hydraulic conductivity tensor (LT^{-1})

K_{xx}, K_{xz}, K_{zz} components of hydraulic conductivity tensor (LT^{-1})

K_0 characteristic hydraulic conductivity (LT^{-1})

$\mathcal{K}_{ij}$ dimensionless quantities, K_{ij}/K_0

L   characteristic length (L)

Q_0 Leakage rate (L^3T^{-1})

R_a Concentration Rayleigh number

S   saturation

S_p mass storage (T^2L^{-2})

S_g $S_g = \rho (S_p + c) g$

S_c $S_c = \phi S \varepsilon$

S_t	sources or sinks
T^*	tortuosity
a_L	longitudinal dispersivity (L)
a_T	transverse dispersivity (L)
c	water capacity $(M^{-1}LT^2)$
f_e	interpolation factor
g	gravitational acceleration (LT^{-2})
h	hydraulic head (L)
J_x	mass flux in x direction $(ML^{-2}T^{-1})$
J_z	mass flux in z direction $(ML^{-2}T^{-1})$
J_k	mass flux at interface k, k=e, w, n, s, $(ML^{-2}T^{-1})$
k_{ij}	permeability tensor (L^2)
k_r	Relative permeability (L^2)
k_{xx}, k_{xz}, k_{zz}	components of permeability tensor (L^2)
$\vec{n}$	outward unit vector normal to the surface
n_i	porosity
p	pressure $(ML^{-1}T^{-2})$
p^*	pressure head (L), $p^* = \dfrac{p}{\rho_0 g}$
$\tilde{p}$	dimensionless pressure, $\tilde{p} = \dfrac{p}{\rho_0 g (h_1 - h_2)}$
q_i	specific discharge in the i direction, i=x, z (LT^{-1})
q_0	characteristic specific discharge (LT^{-1})
q_L	leachate rate (LT^{-1})

t	time (T)
u	velocity in x direction (LT^{-1})
v	velocity in z direction (LT^{-1})
α	coefficient of soil compressibility $(L^3 M^{-1})$
β	coefficient of fluid compressibility $(LT^{-2} M^{-1})$
ψ	stream function (L)
$\bar{\psi}$	dimensionless stream function
ϕ	porosity of the porous medium
ρ	fluid density (ML^{-3})
ρ_i	density of fluid i, (ML^{-3})
ρ_0	reference freshwater density, (ML^{-3})
ρ_{max}	density corresponding to the maximum concentration (ML^{-3})
μ	Absolute viscosity $(ML^{-1}T^{-1})$
ε	relative density difference, $\varepsilon = (\rho_{max} - \rho_0)/\rho_0$
θ	Volumetric water content
θ_r	residual volumetric water content
θ_s	field-saturated volumetric water content
τ	dimensionless time
ω	relaxation factor

CHAPTER 1

INTRODUCTION

1.1   General

Groundwater constitutes an important component of many water resource systems, supplying water for domestic, industrial, and agricultural use. In recent years, public attention has been focused on groundwater contamination by hazardous industrial wastes, by leachate from landfills, from oil spills, from agricultural activities such as the use of fertilizers, pesticides and herbicides and by salt-water intrusion. There has also been considerable concern expressed on the security of radioactive wastes in repositories located in deep geological formations.

The major processes of contaminant transport through the subsurface region are advection, dispersion/diffusion, adsorption, decay and source or sinks which depend on the three-dimensional configuration of geologic deposits through which flow takes place, and the physical/chemical properties of the contaminant. Problems relating to the degradation of groundwater quality are difficult to overcome due to the heterogeneities inherent in subsurface systems, making zones of degraded groundwater extremely difficult to detect. The U.S. Environmental Protection Agency (1977) has reported that almost every known instance of aquifer contamination has been discovered only after a water-supply well has been affected. Frequently, by the time subsurface pollution is

conclusively identified, it is too late to apply remedial measures that would be of much benefit. Groundwater pollution often results in aquifers or parts of aquifers being damaged beyond repair.

In order to better manage the environment and protect valuable groundwater resources, identification of the areas and mechanisms by which pollutants can enter the groundwater flow system coupled with the development of reliable predictive tools modelling the transport of contaminants within the flow system are required. The development of mathematical models that will faithfully represent the physical processes involved, are invaluable tools for the evaluation of future industrial or waste disposal sites that may ultimately pose a threat to the surrounding areas. These models may also be used to design a campaign of field measurements surrounding a particular source when non-compliance with norms is suspected. Details of numerical models, as well as methods of measurement will be presented in the following sections.

1.2   Contaminant transport models

When both forced convection (i.e. transport driven by a hydraulic gradient) and free convection (i.e. buoyancy driven transport) act together to control solute concentration, mixed convective flow occurs. Depending on the relative magnitude of these two forces, some of these mixed systems may be characterized by the development of hydrodynamic instabilities causing perturbations in the hydraulic as well as in the

concentration field of the combined flow. These instabilities are of gravitational origin and are closely related to the analogous problem of the onset of convection in a fluid layer heated from below (the so-called Bénard problem).

The appearance of these instabilities coupled with the free convective flow can cause significant variations in the dispersion of the contaminant plume from that which would normally be expected for the neutrally buoyant case. The primary reason for these instabilities is that within the plume, there will be local regions in which a dense fluid overlies a light ambient resulting in a system that is gravitationally unstable. These local instabilities are not to be confused with the "mean" flow which of course, is influenced by the average density gradients causing descent of the plume.

Numerical models for the simulation of groundwater flow and contaminant transport in subsurface regions have been in development for more than three decades. To date, most contaminant transport studies in groundwater have been restricted to transport due to forced convection, i.e. buoyancy effects due to density variations have not been included (Bear, 1987, Yeh, 1990, 1992). One of the models distributed by the USGS (United States Geological Survey) is MOC, developed by Konikow and Bredehoeft (1977), simulating the flow of groundwater that has a constant and uniform fluid density. The work that has been done on mixed convective flows has focused on freshwater-seawater interaction in coastal aquifers.

1.3 Density gradient models

Surface based pollutant sources release considerable amounts of heavy leachate into the soil. Freeze and Cherry (1979) note that total dissolved solid concentrations for leachate from sanitary landfills typically range from 5,000 to 40,000 mg/L (i.e. approximately 0.5% to 4.0% density difference between the leachate and the groundwater). This density difference frequently results in considerable modification to the transport behaviour once the plume penetrates into the groundwater region.

Most of the numerical simulations concerning density effects deals with the fresh/salt water interface problem. One of the most intensively studied coastal aquifers in North America is the Biscayne aquifer of southeastern Florida (Kohout, 1960a, 1960b). Lee and Cheng (1974) and Segol and Pinder (1976) have simulated transient conditions in the Biscayne aquifer with finite-element numerical models.

One of the most popular models available in the public domain, which may be used for modelling variable density leachate movement is SUTRA (Saturated-Unsaturated Transport), developed by Voss (1984), and distributed by the U.S. Geological Survey. SUTRA has been applied to the analysis of an anisotropic coastal aquifer system (Souza and Voss, 1987) and to the simulation of a regional aquifer containing a narrow freshwater-saltwater transition zone (Voss and Souza, 1987). No attempts have been made to use the model to simulate the behaviour of dense leachate

plumes emanating from disposal facilities.

Another model issued by the USGS and able to incorporate variable density flow is MOCDENSE (Sanford and Konikow, 1985) which is an extension of the model MOC (Konikow and Bredehoeft, 1977). MOCDENSE has been used by Koch and Zhang (1992) to simulate dense plumes, emanating from a landfill, in an unconfined, saturated isotropic homogeneous aquifer.

1.4   Other methods

Another approach to the study of groundwater contamination is with laboratory experiments as well as field measurements. Laboratory experiments if carefully performed under controlled conditions, can provide valuable insight into the basic physical mechanisms underlying the dispersion processes. Some of the earliest works on density effects is that of Wooding (1963) and Bachmat and Elrick (1970), who experimentally studied the hydrodynamic instability of miscible fluids of varying density in a vertical porous column. Paschke and Hoopes (1984) investigated the behaviour of a buoyant plume in an analogous manner to that used in hydraulics for jets and plumes discharging into an ambient cross flow. List (1965) using a flow tank, injected dense solutions into a model of a confined homogeneous aquifer to study the stability of fluids of different densities during horizontal flow through an isotropic medium. His complementary stability analysis indicated that a system composed of a heavier fluid

overlying a lighter one will always be unstable. Schincariol and Schwartz (1990), using a flow container, experimentally studied the variable density flow and mixing in homogeneous and heterogeneous media. Oostrom et al. (1992) also studied the behaviour of dense surface injected leachate plumes in homogeneous porous media. These two series of laboratory experiments were accomplished under carefully controlled conditions. In both cases, it was observed that the negatively buoyant plumes became subject to gravitationally induced perturbations along their lower boundary. The experimentally observed instabilities were in the form of lobe shaped protuberances that manifested themselves as just mentioned, near the lower edge of the plume. (They may be interpreted as being the "salt-finger" type instability observed in statically unstable layers with a superposed mean flow component). As they developed spatially and temporally however, they penetrated deeper and deeper into the plume resulting in considerable modification to the overall dispersion.

In field measurements, samples may be analyzed by taking them from selected wells surrounding a suspected source. This method has been used in some of the investigations on leachate from landfills (Kimmel and Braids, 1980, MacFarlane et al. 1983). It is also possible to design a field experiment where a known tracer is injected into the soil or an aquifer and the migration of the tracer followed over a period of time.

This approach is especially useful when inhomogeneities and anisotropies in the surrounding soil characteristics need to be studied and quantified, for example for

purposes of model validation.

1.5   Comparison of methods

The advantages of field measurements are probably self-evident. They provide "in situ" parameter values. The disadvantages in practice, may lie in the expense involved; and from a scientific point of view, probably in the nonuniqueness in the interpretation of results. A given measurement may be attributed to different components. A laboratory experiment however, may avoid these difficulties, it may be designed to study only some specific phenomena at each time. It still requires however, considerable outlays of time and money in its preparation and execution; furthermore its flexibility is limited, especially when a sensitivity analysis needs to be realised. Numerical simulations are probably the most flexible methods and are also currently the most cost-effective, due to the enormous strides taken in developing more and more powerful computing hardware at diminishing cost. However, there are some computational limitations, such as whether the governing equations correctly describe the physical phenomena, whether the numerical algorithms correctly represent convergent solutions to the governing equations, the limits of computer capacity (although this envelope is being pushed upwards on an almost daily basis!), etc.

As mentioned earlier, surface based pollutant sources release considerable amounts of heavy leachate into the soil. Under certain conditions, these dense contaminant plumes

may become unstable with the appearance of gravitational instabilities which may result in the enhancement of the overall dispersion characteristics resulting in large regions of contamination. The recent experimental work of Schincariol and Schwartz (1990) and of Oostrom et al. (1992) has amply demonstrated that negatively buoyant plumes tend to manifest gravitational instabilities. It appears therefore, that the inclusion of density effects in modelling the behaviour of a contaminant plume, is crucial to an understanding of its transport and dispersion characteristics. A perusal of the relevant literature leads to the conclusion that there does not appear to exist any detailed numerical studies dealing with the sensitivity of the concentration distribution to the interaction of the density driven flow and heterogeneities in the hydraulic conductivity.

1.6   Scope and Objectives

Consequently, the thrust of the present work is to numerically study the behaviour of dense leachate plumes in saturated-unsaturated aquifers with a view to ultimately predicting the resultant contaminant concentration distribution. Crucial to this study will be an examination of the density effect on the transport and dispersion behaviour of a contaminant plume with particular attention being paid to ascertain whether experimentally observed gravitational instabilities that form along the lower edge of the plume are reproduced in the numerical model. Appropriate numerical simulation models for density dependant flow and transport in saturated-unsaturated porous media will be developed. One of the motivations of this research lies in the belief that a fundamental

comprehensive study of variable density flow and transport will eventually lead to the development of accurate simulation tools that would be useful for better management of the environment.

In Chapter 2, previous work that is relevant to the subject is reviewed. This comprises experiments, field studies as well as computational work. Chapter 3 describes the governing equations for variable density flow and transport in saturated-unsaturated porous media, while Chapter 4, describes the numerical methods retained for simulating the variable density flow and transport. Chapter 5 and Chapter 7 are devoted to a comparison of the numerical simulations with the experimental results provided by Schincariol and Schwartz (1990) as well as by Oostrom (1992), respectively. Chapter 6 theoretically examines the stability characteristics of a dense plume in a lighter ambient. Chapter 8 describes the application of the present work to a case study. Conclusions and recommendations for further research form the basis of Chapter 9.

CHAPTER 2

REVIEW OF PREVIOUS WORK

For a majority of aquifer contamination problems, such as leachate from landfill or spill of various materials, the assumption that the fluid density is independent of the concentration of the solute generally holds. Two notable exceptions are salt water intrusion into coastal aquifers (Henry, 1964; Pinder and Cooper, 1970), and the leaching of DAPL's (denser than water aqueous phase liquids) from waste disposal facilities into the ambient moving groundwater (Kimmel and Braids, 1980).

A large body of literature exists that treats the salt water intrusion phenomenon as a problem involving the flow of immiscible fluids (Mualem and Bear, 1974, Liu et al., 1981, Taigbenu et al., 1984, Essaid, 1990). Freshwater and saltwater are actually miscible fluids and therefore, a transition zone caused by hydrodynamic dispersion exists. Across this zone, the density of the mixed water varies from that of fresh water to that of salt water. In order to evaluate the behaviour of a saline intrusion, the equations describing density dependent fluid flow and mass transport have to be solved simultaneously (Pinder and Gray, 1977).

The literature available on the leaching of DAPLs from land disposal sites into ambient groundwater is somewhat limited. However, some of the basic principles of saltwater intrusion may be applied to the leaching of DAPLs. In the next section,

laboratory experiments and field evidence of density affected flow and transport are discussed, followed by an overview of numerical models for density coupled flow and transport.

2.1   Stability experiments in soil columns

Experiments in which water-saturated, long vertical columns, filled with a homogeneous isotropic porous material, were connected to an open reservoir containing an aqueous solution with a density greater than water were reported in a series of paper by Wooding (1959, 1962a, 1962b, 1963, 1969). In most of the experiments reported, there was no initial velocity component. Convection currents developed in the column at the unstable interface between the two fluids. The denser fluid was marked with a suitable dye and its motion could be seen to take the form of a long finger which descended into the column and displaced the lighter fluid. It appeared that there existed a finite discontinuity or jump in the average fluid properties at the leading edge of the finger (Wooding 1962a). Wooding (1959, 1962b) concluded that configurations of the isodensity surfaces vary in shape and rate in a manner much different from those predicted by ordinary molecular diffusion alone. Similar studies were performed by Bachmat (1969). He concluded that whenever a heavier liquid rests on top of another liquid miscible with the first in a porous medium, a redistribution of the liquid is spontaneously induced. Even when the initial boundary between both liquids is horizontal on average, the curvature of the actual microscopic boundaries, combined with molecular

diffusion, will induce a macroscopic rotation of the mixture. The mass flux, as a result, is much higher than that which would be predicted by local dispersion and diffusion (Bachmat, 1969).

Krupp and Elrick (1969) summarized the tendency to produce unstable flow (Fig.2.1) for the four different combinations of two aqueous phase liquids and two flow directions in a vertical column. They assumed that an increase in the concentration usually results in an increase in density and viscosity of the solution. In the top portion of Figure 2.1, a salt solution overlies lighter, less viscous water. When the flow is vertically downwards, the viscosity ratio indicates the tendency for stable displacement to be favoured. The density ratio indicates unstable flow, independent of the direction of flow. For the configuration shown in the lower portion of Fig. 2.1, only the viscosity ratio in combination with downward flow, suggests unstable displacement. Krupp and Elrick (1969) experimentally studied each of the four possibilities illustrated in Fig. 2.1 and concluded that the density difference between the liquids was a much more significant factor than the viscosity in causing unstable flow during the displacement.

According to Bachmat and Elrick (1970), the magnitude of the vertical flux of salt through any horizontal plane of the porous material may be expressed macroscopically in terms of its average over that plane. In general, this flux may be regarded as a sum of several contributions:

a.   ordinary molecular diffusion in a porous material;

b. mechanical dispersion due to fluctuations of the local vertical component of the velocity and of the local salt concentration relative to their macroscopic values at a point in the considered plane;

c. convective dispersion due to fluctuations of the macroscopic values of the velocity and concentration at a point in the plane relative to their averaged values in that plane, and

d. convection by the average velocity over a horizontal cross section of the porous material.

They also concluded that the vertical spread of the salt within the porous material occurs in the form of fingers, the number and configuration of which are not reproducible in practical experiments. The distribution of fingers is usually asymmetric relative to a plane passing through the centerline of the column.

2.2 Flow container experiments

Flow container experiments investigating effects of density differences between leachate or injected solutions and the ambient groundwater on flow and transport, were reported by List (1965), Paschke and Hoops (1984), Schincariol and Schwartz (1990) and Oostrom (1992).

List (1965) conducted a series of experiments in a flow container with inside

dimensions of 250 cm long, 35 cm deep and 15 cm wide to investigate the stability along a moving density interface. The confined aquifer model contained a homogeneous sand with K_{sat}=85 m/day. In the experiments, saline water with concentrations up to 14 g/L (1% density contrast) was introduced into the confined aquifer through a slit at the top of the flow container. The horizontal Darcy flux in these experiments ranged from 15 to 36 m/day. List (1965) found that all the contaminant plumes were stable. Realizing that the stability of the plumes was a result of the combination of a relatively high Darcy flow and low density contrast, he attempted an experiment with a 30 g/L saline input solution (2.1% density contrast) and a Darcy flux of 1.2 m/day to determine whether instabilities could be generated in the experimental apparatus. The resulting plume was indeed unstable and lobe shaped waves developed at the lower end of the plume.

List (1965) also included a theoretical analysis of the stability of the two-dimensional horizontal motion of two miscible fluids of different density in an infinite porous medium, with the fluid of higher density, ρ_2, overlaying the lighter fluid of density ρ_1, in a saturated, isotropic, homogeneous porous medium. The investigation was carried out by assuming sinusoidal perturbations to the velocity vector and the vertical density profiles. He obtained a neutral (or critical) stability curve relating the Rayleigh number, λ_T, to the wave number of the sinusoidal perturbations, for disturbances which neither grow nor decay with time, this was the definition of the critical limit. The Rayleigh number was expressed as

$$\lambda_T = \frac{lgk\nabla\rho}{\varepsilon D_T \mu}$$
(2.1)

Where l (L) is the mixing zone between the two fluids, k the intrinsic permeability, ε the porosity, g the gravitational constant, μ the viscosity, and D_T the lateral dispersion coefficient. Based on his analysis, the author found that the flow is always unstable when the Rayleigh number λ_T is positive, that is when $\Delta\rho = \rho_2 - \rho_1 > 0$. However, depending on the magnitude of λ_T and the wave number of the perturbation, the growth rate of unstable waves could be so low as to form a quasi-stable flow.

Paschke and Hoopes (1984) developed an analytical model for buoyant plume characteristics for steady flow in a homogeneous, isotropic aquifer by using mass and momentum conservation equations. Their analysis showed the buoyant plume to consist of a near-source region which is influenced by the characteristics of the plume source, and a far field region in which the plume is influenced primarily by the ambient flow. The model was developed from the equations of motion, using similarity distributions. Some of the assumptions made in this model are:

a.   the groundwater flow is uniform, steady, and horizontal;

b.   the aquifer is fully saturated, homogeneous, isotropic, and of infinite extent;

c.   the leachate, with the same viscosity as water, but a higher density, is miscible with the ambient groundwater.

Equations for the trajectory and the area of the plume, and the concentration at

the plume centerline were derived by the authors for the near source and the far field region. The location of the plume source was chosen as the origin. The vertical coordinate of the centerline trajectory, z_c was shown to be a function of the parameters l, δ, N, and the horizontal distance from the source, x_c. The parameter l is a characteristic length scale for the plume reflecting the relative importance of the vertical motion due to the source leakage rate to the ambient groundwater velocity and dispersive mixing, while δ is a measure of the importance of the source area on the plume behaviour. The parameter N is a combination of some numerical constants, reflecting velocity and density difference distributions across the plume. Paschke and Hoopes (1984) found that in the near source region z_c was proportional to $x_c^{1/2}$ and in the far field z_c was proportional to $x_c^{1/3}$, which is flatter than in the near source region. They also showed that the concentration at the centerline of the plume decreases as z_c^{-1} in the near source region and that plume dilution due to mixing causes the concentration to decrease in proportion to z_c^{-2} in the far field, which is faster than in the near source region.

Paschke and Hoopes (1984) conducted experiments in a flow container filled with a coarse sand to test their analytical model. The K_{sat} of the sand was approximately 0.70 cm/s. The dimensions of the porous medium were 184 × 60 × 30 cm. Forty-nine sampling ports were installed for extracting fluid samples from the sand tank. The ports were arranged in seven columns with seven ports in each column. The sand was fully saturated and the water was kept under a positive pressure head. Constant head tanks on either end of the flow container controlled the steady flow through the sand. The salt

water leachate ($NaNO_3$) was introduced into the porous medium from a third constant head tank through a small opening (0.79 cm diameter) in the sand cover. The leakage rate, $Q_0(L^3/T)$, the density difference between the leachate and the ambient groundwater, $\Delta\rho_0/\rho_a$ (M/L^3), and the pore water velocity, $U_a(L/T)$, were varied between the tests. Q_0 varied between 0.049 and 0.256 cm^3/s, $\Delta\rho_0/\rho_a$ between 0.03 and 0.20, and U_a between 0.031 and 0.058 cm/s. Each of the experiments was left undisturbed until the plume had reached steady state conditions. Sampling was begun after approximately 2 pore volumes of the medium had passed through the apparatus. According to Paschke and Hoopes (1984), the measured plume characteristics were in reasonable agreement with the model predictions. The predicted patterns of plume trajectory, concentration, and boundary were similar to the measured ones. Unstable plume behaviour was not reported by Paschke and Hoopes (1984). The relatively high flow rates in the flow container probably stabilized the buoyant plumes.

Schincariol and Schwartz (1990) experimentally studied the variable density groundwater flow in homogeneous, layered and lenticular saturated porous media. The dense NaCl solutions were introduced into the middle of the less dense ambient groundwater in a flow container. The flow container produced a uniform groundwater flow field at typical groundwater flow velocities for a variety of different spatial distributions of hydraulic conductivity. The flow container was 116.8 cm long, 71.0 cm wide, and 5 cm deep. The length and width dimensions provided a travel path for the tracer that was sufficiently long to permit the instabilities to develop. Influent and

effluent reservoirs were placed at each end of the tank to buffer the effect of the inflow/outflow. The solutions containing the salt were injected through an injection chamber into the saturated porous medium. The injected dense NaCl solution was marked with a coloured dye (Rhodamine WT liquid) to facilitate the photographic monitoring of flow and transport.

For the experiments in the homogeneous porous medium, the hydraulic conductivity K was 0.056 cm/s, the average specific discharge was between 0.000111 to 0.00217 cm/s, the salt concentration of the injected solution ranged from 1000 to 100,000 mg/L. Results show that the tendency for the plume to sink increased as its density increased. An important feature in many of the trials was the tendency for gravitational instabilities to alter the plume. Instabilities were manifested by lobeshaped protuberances that formed first along the bottom edge of the plume and later within the plume. Enhanced spreading of solute perpendicular to the ambient groundwater flow field resulted in dilute and concentrated zones within the plume. The threshold at which density became noticeable was about 1000 mg/L. In the layered medium, the hydraulic conductivity varied between 0.0019 to 0.3 cm/s; reductions in hydraulic conductivity of the order of half an order of magnitude or less could influence the flow of the dense plume. Interfaces between layers seemed to act as barriers. Dense water might accumulate along bedding interfaces, which when dipping could result in plume migration velocities larger than ambient groundwater velocities. The plumes developed in the case of the lenticular porous medium were much more complex than for the other cases. The

combination of convective dispersion and nonuniform flow due to heterogeneities resulted in relatively large dispersion.

Oostrom et al. (1992) experimentally investigated dense aqueous phase leachate plumes in homogeneous porous media. The behaviour of contaminant plumes with different densities was examined in three flow containers packed with homogeneous porous media simulating an unconfined aquifer. The dimensions for the flow container A were 80 × 40 × 5 cm, flow container B 205 × 100 × 7.8 cm, and flow container C 167 × 100 × 5.1 cm. The saturated hydraulic conductivities were 0.9236 cm/s, 0.0718 cm/s and 0.0417 cm/s, respectively. Each flow container had three chambers: an inlet head chamber, a chamber containing the porous medium, and an outlet chamber. During an experiment, the head h_1 in the inlet head chamber and the head h_2 in the outlet head chamber were kept constant by controlling their water levels. By manipulating the water level h_1 and h_2 in the two head chambers, different horizontal discharge rates Q_x and Darcy Fluxes q_x could be established. An unsaturated zone was allowed to exist near the top of the porous medium in each of the flow containers. The contaminant plumes consisted of NaI or NaBr solutions introduced into each flow container from a line source located at the surface of the porous medium and extending over the total width of the container. Results showed that for a given porous medium, dense plumes were either stable or unstable depending on the magnitude of the horizontal flow velocity, the contaminant leakage rate, and the density difference between the contaminant solution and the ambient groundwater. When a dense plume becomes unstable, lobe-shaped

gravitational instabilities develop which are unsteady and three dimensional. Their experimental results suggest that the behaviour of dense contaminant plumes overlying a less dense groundwater stream in a homogeneous porous medium depends on the magnitude of certain nondimensional parameters. They concluded that the gravitational instabilities begin to develop when the value of these nondimensional parameters exceed certain critical values.

Although not directly related to dense leachate plumes evolving from land disposal facilities, some of the results of the experimental sand-box work by Mulqueen and Kirkham (1972) is of interest to this study.

Mulqueen and Kirkham (1972) conducted a series of experiments to study the leaching of concentrated NaCl solutions, ranging from 3.8 to 15.2 g/l, into tile drains from a surface layer of salinized sand. Intense fingering developed in all experiments. This fingering caused a rapid and erratic redistribution of salt within the model and a large variation of the salt concentration in the drainage water. It was not possible to predict when or where a finger would start or how it would subsequently develop. According to Mulqueen and Kirkham (1972), the behaviour of the unstable fingering was controlled by the interaction between the density gradients and the hydraulic gradient.

2.3   Field evidence of density affected flow and transport

Report on changes in leachate plume trajectories or the development of unstable density currents as a result of density differences between contaminated plumes and the ambient groundwater have been scarce. Based on the behaviour of some leachate plumes from landfills and waste dumps, Van der Molen and Van Ommen (1988) concluded that such phenomena are probably more common than is usually supposed. As an example they mentioned that for a certain plume in the sandy coastal dunes of the Netherlands, the downward velocity was about 45 times higher than the vertical velocity from natural recharge. Studies of leachate from municipal sanitary landfills revealed that the load of dissolved solids can be substantial. Freeze and Cherry (1979) present representative ranges in leachate concentrations from sanitary landfills. When the total dissolved solids in the leachate range from 5000 to 40,000 mg/L, an initial density difference between the leachate and the ambient groundwater of 0.5 - 4.0 % can be expected.

Kimmel and Braids (1980) investigated the plume behaviour of leachate plumes under the Babylon and Islip landfills on Long Island, New York. They found the highest salt concentrations near the bottom of the aquifer beneath the landfills. Kimmel and Braids (1980) assumed that the leachate flowed out of the landfill as pulsations of high density fluid after periods of recharge, and move as pockets, or slugs, diagonally downward through the aquifer. The vertical velocity of these pockets was thought to be considerable, explaining their presence at the bottom beneath the landfill instead of

somewhere farther downstream. It was further assumed that these pockets retained their original density while moving vertically, otherwise there would be an insufficient density gradient to carry them downward, and pockets would not be found near the aquifer bottom. Relatively little mixing appeared to take place before the leachate pockets reached the bottom of the aquifer. The movement of leachate is depicted in Figure 2.2.

MacFarlane et al. (1983) studied the migration of contaminants in groundwater at the Borden landfill which is located within the confines of the Canadian Forces Base, Borden, Ontario. This landfill occupies approximately 5.4 ha, and received refuse during 1940 - 1976. The landfill has caused the development of a plume of contaminated groundwater that occupies approximately 39 ha and extends more than 700 meters north of the landfill. Their observations about the vertical downward movement of contaminant plumes are particularly interesting. They noted that during much of the years, flow in the aquifer was essentially horizontal from the area south of the landfill to the area north, but the zone of leachate contamination beneath the landfill has penetrated downward through the entire aquifer thickness to a maximum depth of about 20 meters below the water table. If horizontal flow was the only influence on the distribution of the zone of contamination beneath the landfill, the plume would only exist at shallow depths. They pointed out that one major cause for the downward movement appeared to be the transient downward-directed hydraulic gradient beneath the landfill, especially in the spring and summer, which produces strong downward flow every year. Another possible reason could be the greater density of the contaminated water relative to the natural

groundwater in the aquifer. MacFarlane et al. (1983) stated that, although a comprehensive analysis was not possible due to the lack of available modelling techniques, a preliminary assessment of the possible effect of density can be instructive. They divided the domain below the landfill into two regimes, an upper one consisting of higher average total dissolved solids (TDS) of 2000 mg/l and a temperature of 11^0C, and a lower one comprised of groundwater with TDS of 100 mg/l and a temperature of 7^0C. The upper and lower regime, therefore, had densities of $\rho=1.0012g/cm^3$ and $\rho=1.000g/cm^3$ respectively. The authors compared the density driving force, assumed to be $\Delta\rho/\rho_0 =0.001$, with the downward components of hydraulic gradient beneath the landfill, which were approximately 0.01 in the spring or summer and of the order of 0.001 or less during the remaining months of the year. This indicates that in the spring and early summer, the driving force due to density is small in comparison to the downward hydraulic gradient caused by mounding of the water table beneath the landfill. During the rest of the year however, the density force is of the same general magnitude or greater than the downward component of the hydraulic gradient and is not much smaller than the average horizontal component of the hydraulic gradient in the vicinity of the landfill.

A third effect that could contribute to downward movement of contaminated water is the lower fluid viscosity in the zone of elevated temperature beneath the landfill. Temperature has a much larger effect on viscosity (or resistance to flow) of water than it does on the density. Lower viscosity causes the hydraulic conductivity to be

corresponding higher. MacFarlane et al. (1983) estimated that in the Borden aquifer, this effect is small because a temperature difference of 4^0C causes a viscosity difference of 0.1 cP, which corresponds to a relative increase in hydraulic conductivity of only 10%. Kimmel and Braids (1980) also considered the viscosity effect to be small because the presence of an electrolyte (e.g., NaCl) in water causes the viscosity of water to be relatively invariable over a wide temperature range.

A similar vertical downward movement of the tracer cloud was observed by LeBlanc et al. (1984) during a tracer test in the Cape Cod aquifer. They also concluded that vertical components of flow associated with areal recharge and sinking of the denser tracer cloud into the native groundwater were the cause of the downward movement of tracer cloud.

2.4   Numerical simulation of variable density flow and transport

In groundwater flow systems, the density of the groundwater is usually nearly constant. It may vary slightly as a result of small variations in either temperature or pressure or as a result of the presence of trace quantities of dissolved contaminants. Sometimes however, the density can vary significantly; this can considerably modify the flow dynamics of the system. Frind (1982a) listed four examples of these situations:

1.   Seawater intrusion in coastal areas.

2   Transport in the groundwater of leachate percolating from landfills and industrial

waste disposal sites.

3.   Long-term salt dissolution from underground salt formations.

4.   Transport of salt due to agricultural irrigation.

Some of the earliest work on simulating variable density flow and transport was that of Henry (1964). He developed an analytical solution for the steady-state salt distribution in a confined coastal aquifer by means of a Fourier-Galerkin double-series expansion. He found that dispersion and gravitational forces interact to cause the establishment of a saltwater convection cell and that consequently the steady state condition is one of dynamic equilibrium. His solution was based on the assumption of a constant dispersive mechanism in the aquifer. It was further assumed that the propagation of pressure was very fast relative to salt transport and that the release of water from storage was negligible. Under these assumptions, the equation governing groundwater flow can be simplified to

$$\nabla (\rho q) = 0 \qquad\qquad (2.2)$$

The salt transport for this problem is expressed by the advection-dispersion equation. A schematic representation of initial and boundary condition for Henry's problem is presented in Fig 2.3.

A transient solution to the seawater intrusion problem was obtained in 1970 by Pinder and Cooper (1970), who used the method of characteristics. This transient solution was shown to approach Henry's steady-state solution from two different starting

conditions, one starting from an initial sharp interface at the seaward boundary, the other starting from a sharp interface calculated on the basis of static equilibrium. Steady state, however, was not attained because of high computing costs.

Lee and Cheng (1974) reformulated Henry's problem in terms of stream functions and developed a numerical solution for the steady-state salt distribution using a finite element method. They also assumed constant dispersion. Reasonable agreement with Henry's solution was found.

The first transient solution based on velocity dependent dispersion coefficients was developed in 1975 by Segol et al. (1975), using a Galerkin finite element method. A distinctive feature of this work is that they solve for the pressure and the two velocity components simultaneously at each node in the finite element grid, thus obtaining a continuous velocity field. This scheme, now known as the so-called 'three equation scheme' (Pinder and Gray , 1977), is considered a valuable benchmark against which other solutions should be compared (Frind, 1982a). The calculated velocities are subsequently substituted into the transport equation and concentration distributions obtained. The concentration distribution is used to update the fluid density values. This iterative procedure is repeated until an error criterion is met. Segol's transient solution also approaches Henry's steady-state solution, but steady state itself was not reached because of high computing cost.

One of the most popular models available publicly which may be used for modelling of variable density leachate movement is SUTRA (Saturated-Unsaturated Transport), developed by Voss (1984), and distributed by the U.S. Geological Survey. SUTRA is intended for two dimensional simulation of flow and transport in saturated and unsaturated porous media. Flow and transport input parameters may vary in value throughout the simulated region. The dependent variables in the model are the fluid pressure p and fluid solute mass fraction C (mass solute per mass of total fluid). Users of the program have to create rather complicated input files, including initial and boundary conditions and information on the chosen grid. Basic knowledge of the finite element method is required. When SUTRA is used for simulation of systems with unsaturated flow or when the simulation includes time dependent boundary conditions or sources, some Fortran programming is necessary. The SUTRA manual (Voss, 1984) contains comparisons with several published solutions of Henry's problem. SUTRA has been applied in the analysis of an anisotropic coastal aquifer system (Souza and Voss, 1987) and simulation of regional aquifer containing a narrow freshwater-saltwater transition zone (Voss and Souza, 1987). No attempts have been made to use the model to simulate the behaviour of dense leachate plumes emanating from disposal facilities.

Another model issued by the USGS and able to incorporate variable density flow is MOCDENSE (Sanford and Konikow, 1985) which is an extension of the model MOC (Konikow and Bredehoeft, 1977). The dependent variables in the model are the hydraulic pressure p and solute concentration C. The transient groundwater flow equation is solved

by an implicit finite difference method and the solute transport equation is solved by a two step process. Whereas advection is computed by a method of characteristics, the dispersion is calculated by an explicit finite difference method. The model MOCDENSE was used by Koch and Zhang (1992) to simulate dense plumes, emanating from a landfill, in an unconfined, saturated isotropic homogeneous aquifer with permeability $k_x=k_z=10^{-11}$ m^2, specific storativity 10^{-5} and porosity 0.2. A 5.4 m head difference was imposed on the 300 m high by 1400 m long aquifer. Specific information on the recharge rate and the contaminant leakage rate from the landfill were not included. One of the conclusions drawn was that hydrodynamic dispersion has a large impact on the density effects. A large dispersivity leads to increased spreading of the plume and to an overall reduction in the influence of density variations in the plume. For sufficiently small values of the dispersivity, convective instabilities and fingering phenomena occur at the horizontal plume boundaries, which lead to enhanced vertical mixing of the leachate. In such cases the inclusion of the density effect becomes extremely crucial for a proper evaluation of the fate of the contaminants.

The equations governing density-dependent transport are the Darcy equation, the continuity equation for the fluid, the continuity equation for the solute, and the constitutive equation relating fluid density to concentration. The fluid continuity equation in non-linear transport problems is often written in terms of pressure. It was noted (Frind, 1982a) that a disadvantage of this formulation is that numerically large static pressures may dominate the dynamic pressure changes that cause motion. The resulting scheme

may therefore operate at less than optimum numerical efficiency. A more efficient way is to use an "equivalent freshwater head" instead of pressure. Finite element models with equivalent freshwater hydraulic head as a dependent variable or, equivalent freshwater hydraulic head and contaminant concentration as the dependent variables were reported by Frind (1982a,b), Huyakorn et al. (1987), Senger and Fogg (1990a,b) and Galeati et al (1992). The equivalent fresh water head ψ (L) was defined by Frind (1982a) as

$$\psi = \frac{p}{\rho_0 g} + z \qquad (2.3)$$

where ρ_0 (ML^{-3}) is the density of the fresh water.

Frind (1982b) used his model to simulate dense leachate transport in an unconfined aquifer. The leachate moved from a disposal site on the surface into a saturated aquifer by means of natural recharge. Unsaturated flow was neglected. For density differences of up to 0.71% (10 g/l total dissolved solids in the leachate) between leachate and the ambient groundwater, Frind (1982a) showed that the dispersive mechanism dominated the density effects all the time and no instabilities were observed with its set of parameters. This may, however, very well be the results of the high dispersivity values used in its model: a_L=10 m, a_T=1 m.

Huyakorn et al. (1987), using the equivalent freshwater head formulation, presented a three-dimensional finite element model for the simulation of saltwater intrusion in single and multiple coastal aquifer systems with either a confined or phreatic

top aquifer. They improved the density-coupling of the transport and flow equations using a Picard sequential solution algorithm with special provisions to enhance fast convergence of the iterative solution. Spatial discretization of three-dimensional regions is performed using a vertical slicing approach designed to accommodate complex geometry with irregular boundaries, layering, and/or lateral discontinuity. Four examples were presented to demonstrate the model verification and utility. They concluded that the model formulation and solution algorithms were cost effective and able to handle a variety of flow conditions.

Senger and Fogg (1990a,b) used both stream function and equivalent freshwater heads to simulate steady state flow of variable density groundwater in a regional, cross-sectional flow model through the Pola Duro Basin, Texas, where fluid densities vary between 1.0 and 1.15g/cm^3. Their modelling showed that the regional groundwater flow pattern in the Palo Duro Basin was not significantly affected by variations in fluid densities, because the topographically driven flow component dominated buoyancy forces associated with dense brine. An exception was near the eastern boundary where high fluid densities caused stronger downward flow. However, the distribution of equivalent freshwater heads (EFH) was considerably different when assuming variable densities versus uniform densities. They concluded that flow velocities computed from an equivalent freshwater head (EFH) solution showed some irregular scatter compared with those computed from the stream function solution. The latter velocities were more accurate than those computed from the equivalent freshwater head (EFH) solution due

to the typically finer discretization in the vertical direction for regional, cross-sectional models.

Galeati et al. (1992) numerically solved the problem of density-dependent transport of salt in an unconfined coastal aquifer by means of an implicit Eulerian-Lagrangian finite element formulation. They noted that such a formulation lead to symmetric positive definite finite element matrices, unconditional stability, with reduced numerical dispersion. The final algorithm was suitable for parallel computation. The method had been used to study the effect of dewatering on seawater intrusion within a vertical cross section through an aquifer in southern Italy, related to the construction of a thermoelectric power plant. It should be pointed out that using the concept of equivalent freshwater head as a basis for analysing variable-density flow may lead to significant errors in predicted flow directions and velocity magnitudes. Since density is not a constant at each point in the aquifer, the equivalent freshwater head may not exist and cannot be extracted from field data. This contradiction may be found in Huyakorn et al.(1987).

2.5   Numerical methods used in simulating groundwater flow and transport

In modelling groundwater flow and transport, the flow and transport equations are coupled through the Darcy velocities and the constitutive relation between fluid density and concentration. As a result of the dependency of the density on concentration, the

flow and transport equations have to be solved simultaneously, using numerical methods.

The method used by modellers depends mainly on the properties of the equations. The flow equation is of a parabolic nature. In saturated-unsaturated porous media, it is a nonlinear parabolic equation. The transport equation, when advection is the dominant transport process, is of a hyperbolic nature. However, if a system is dominated by dispersive fluxes, the transport equation is of a parabolic nature. Numerical methods developed for parabolic partial differential equations are generally not suitable for hyperbolic equations, and vice versa. The principal numerical methods currently in use for the flow and transport equations are finite differences, finite elements, finite volumes, the method of characteristics and/or some hybrid combination of these methods.

The finite difference method is probably the oldest, most popular, and conceptually the simplest of the numerical procedures (Pinder, 1988). It consists of discretizing the problem area into rectangular cells which are identified with discrete points or nodes. Partial differential equations encountered in subsurface simulation are approximated using a truncated Taylor series expansion about each point. A set of approximating algebraic equations thereby replaces the original continuous partial differential equations. Because the finite difference approach is conceptually simple and the resulting set of algebraic equations is amenable to solution using a number of effective algorithms, this approach plays a very significant role in subsurface simulation.

The finite element method is based on the weighted residual principle. The solution of the problem is approximated by a summation of basic functions, the trial function. This trial function is then substituted into the partial differential equations. Generally, since the trial function do not exactly satisfy the partial differential equations a residual results which is not equal to zero. By selecting a set of appropriate weighing functions the residual may be forced to zero in an average sense. This last step generates the necessary algebraic equations that need to be solved for the coefficients of the trial function. The Galerkin method uses one of the basis functions as the weighing function. The choice of the nodal system and the order of the weighting and basis functions, greatly influence the accuracy of the simulations. It has been found that for the transport equation, when advection terms are important, the standard Galerkin formulation faces numerical oscillations because it leads to a set of algebraic equations similar to that obtained using central differences in a finite difference method (Huyakorn 1977, Hirsch, 1988). In the finite difference method, these difficulties are overcome by using backward (upwind) differences to approximate the advective terms, depending on the sign of the advection velocity. In finite elements, an upwind finite element approach has been developed by choosing weighting functions of asymmetric form which are dependent on the direction of flow velocity along each side of the element (Heinrich et al., 1977, Huyakorn, 1977, Christie et al. 1976, Roe, 1992).

Patankar (1980) introduced a control volume formulation for the advection-dispersion equation. The most attractive feature of the control volume formulation is that

the integral conservation of quantities such as mass is exactly satisfied over any group of control volumes and, of course, globally, over the whole calculation domain. The problem now becomes on how to approximate the flux between the control volume interfaces. Patankar (1980) constructed an interpolation formula or profile between the nodes inspired by the exact solution to the steady state problem.

Baliga and Patankar (1980, 1983, 1988) were the first to introduce the idea of control volume finite element methods for advection-dispersion problems. They discretized the domain using three-node triangular elements. Within each element, the transported scalar (in both the convection and diffusion terms) is interpolated using a flow-oriented function that considers the relative strengths of advection and dispersion in the mean flow direction, as well as transverse dispersion. This interpolation function is derived from a simplified version of the appropriate governing equations, written with respect to an elemental flow-oriented coordinate system. The aligning of one of the axes of the local element coordinate system with the mean flow direction in the element helps to reduce the false diffusion.

The method of characteristics is an intuitively attractive method for the solution of the advective-dispersive transport equation. The method utilizes the characteristic curves and characteristic equation to eliminate difficulties such as numerical dispersion and oscillations associated with a dominant convective term. Usually one begins by using the classic finite difference method to solve the flow equation. Fluid velocities are

obtained through numerical differentiation of this solution and subsequent substitution into Darcy's law. Mathematical particles identified with fluid concentrations are now moved along characteristic curves using this velocity field. A new concentration field is established by averaging the particle concentrations in each finite difference cell. The resulting field is modified using the change in concentration determined through a finite difference solution to the characteristic equation which accommodate dispersion. Pinder and Cooper (1970) calculated the transient position of the seawater front by solving the flow equation for fluid pressure, using a finite difference procedure, and the transport equation, using the method of characteristics.

The advection-dispersion equation is generally solved numerically with methods that treat the problem from one of the following three perspectives: the Eulerian, Lagrangian, or a combination of the two, the Eulerian-Lagrangian perspective. Reviews and discussions of these three groups of methods have been provided by Neuman (1981, 1984) and Yeh (1990, 1992).

In the Eulerian approach the equation is discretized by a finite difference or a finite element grid system fixed in space. Eularian methods perform well when the transport problem is dispersion dominated and the concentration distribution is relatively smooth. The upwind finite difference methods and upwind finite element methods were developed to eliminate oscillations for advection dominated transport problems, but introduce large numerical dispersion. Numerical dispersion has to be controlled by using

a finer grid system and a smaller time step, or by using higher-order approximations in space, time or both (Laumbach, 1975, Holly and Preissman, 1980). A drawback of Eulerian methods is that they often suffer from restrictions on grid size and time step duration.

In the Lagrangian approach, either a deforming grid or a fixed grid in a deforming coordinate system may be used. Yeh (1990) pointed out that the Lagrangian methods also may be used to circumvent the problem of oscillation, but they have severe drawbacks. First, for a long-term simulation, excessive deformation of the grid system will result, which unfortunately is prone to numerical instability. Second, when the region of interest is composed of multimedia, the deformed grid may cross the material boundaries, which may cause difficulties in the handling of equation parameters, especially if sorption and chemical reactions are important. Third, when multiple sources are encountered, concentration fronts may propagate in different directions and cross each other at various angles, which would result in mesh tangling so that the simulation is stymied.

In the combination Eulerian-Lagrangian approach a fixed grid is used but with two steps for the computations: the first step is to compute the Lagrangian concentration with particle-tracking methods, and the second step is to compute the final concentration with either finite difference, finite element, or some other numerical method. In this method one adopts a Lagrangian viewpoint when dealing with the advection terms and

a Eulerian viewpoint when dealing with other terms in the transport equation. In the Lagrangian step, either continuous forward particle tracking (Konikow and Bredehoeft, 1977), single step reverse particle tracking (Molz et al., 1986), or the combination of both (Neuman, 1984, Yeh, 1990, 1992) has been used. The main advantage of a combined of Eulerian-Lagrangian approach is that it can handle advection dominant problems, and overcome the problem of oscillations in the solution. The disadvantage of this approach is that in general the accuracy of the Lagrangian-Eulerian approach depends on the order of interpolation which is used to obtain the Lagrangian values. A first-order interpolation can always eliminate oscillation, but its ability to reduce numerical dispersion depends on the spatial variation of the solution and time step. Thus this approach is usually time consuming.

CHAPTER 3

DEVELOPMENT OF GOVERNING EQUATIONS

Growing concern about groundwater and soil contamination from a variety of sources has generated increased interest in the transport of contaminants in the subsurface region.

In the case of miscible solute contaminant transport, differences in fluid properties are ignored in most mathematical models which treat the contaminant as a passive tracer. However, it has been shown that many solute contaminant plumes which originate from waste disposal facilities are significantly denser than the ambient groundwater in natural aquifers. Due to density differences, these dense plumes tend to penetrate deeper into the underlying aquifers than neutral plumes; furthermore the appearance of gravitational instabilities lead to an enhanced mixing and dilution of the contaminants. Negatively buoyant plumes are likely to contaminate aquifers to greater depths than plumes with the same density as the ambient groundwater (neutral plumes). Although considerable progress has been made over the last few years, the present understanding of contaminant plume behaviour is incomplete, especially when variable density is involved. This is particularly due to the scarcity of well documented, detailed field and laboratory experiments. In the following section, we will discuss the governing equations of variable

density flow and contaminant transport in saturated-unsaturated porous media. As a preliminary step, however, we would like to explain the concept of the continuum approach to porous media and the representative elementary volume.

3.1 The continuum approach to porous media

3.1.1 Definition of porous medium

Examples of porous materials are numerous. Soil, porous or fissured rocks, ceramics, fibrous aggregates, filter paper, sand and a loaf of bread are just a few. Somewhat less obvious examples, but still part of this group, are large geologic formations of karstic limestone, where the open passages (such as solution channels or caverns) may be of substantial size and far apart. All of these materials have some characteristics in common that permit them to be grouped and classified as porous media. A porous medium may be defined as (Bear, 1972):

1. A portion of space occupied by heterogeneous or multiphase matter. At least one of the phases comprising this matter is not solid. They may be gaseous and/or liquid phases. The solid phase is called the solid matrix. That space within the porous medium that is not part of the solid matrix is referred to as void space (or pore space).

2. The solid space should be distributed throughout the porous medium within the domain occupied by a porous medium; solid must be present inside each

representative elementary volume (defined later). Another basic feature of a porous medium is that the various openings comprising the void space are relatively narrow.

3.   At least some of the pores comprising the void space should be interconnected.

The above definitions demonstrates the hopelessness of any attempt to describe in an exact microscopic manner the geometry of the internal solid surfaces that bound the flow domain inside a porous medium. Directing our attention to the fluid or fluids contained in the void space, and trying to describe phenomena associated with them, such as motion, mass transport, etc., the same difficulties are encountered. This obliges us to introduce the continuum approach as a tool for handling phenomena in porous media.

3.1.2   Molecular and microscopic levels

First, the concept of fluid requires some further elaboration. Actually, fluids are composed of a large number of molecules that move about, colliding with each other and with the solid wall of the container in which they are placed. By employing theories of classical mechanics, we could fully describe the motion of a given system of molecules: e.g., given their initial positions in space and their momenta, we could predict their future positions. However, despite the apparent simplicity of this approach, it is exceedingly difficult to solve the problem of the motion of even three molecules (assuming that we know all the forces, which is also doubtful). In addition, because the number of

molecules is so large, their initial positions and momenta cannot actually be determined.

Instead of treating the problems, say of fluid motion, at the molecular level, we may adopt a different approach, statistical in nature, to derive information regarding the motion of a system composed of many molecules, averaging phenomena in the fluid continuum filling the void space. We refer to the continuum level as the microscopic one. At this microscopic level, we overlook the actual or molecular structure of a fluid and regard it as a continuum.

Essential to the treatment of fluids as continua is the concept of a particle. A particle is an ensemble of many molecules contained in a small volume. Its size is much larger than the mean free path of a single molecule. It should, however, be sufficiently small as compared to the considered fluid domain that by averaging fluid and flow properties over the molecules included in it, meaningful values, i.e., values relevant to the description of bulk fluid properties, will be obtained. These values are then related to some centroid of the particle. Then at every point in the domain occupied by a fluid, we have a particle possessing definite dynamic and kinematic properties.

Associated with the question of particle size, or of the elementary volume that should be considered as a point within the fluid continuum, is the definition of the fluid density.

Density is the ratio between the mass Δm of an amount of matter and the volume ΔU occupied by it. Following Bear (1972), let us consider a point P in the fluid, and let Δm_i denote the fluid mass in a sufficiently large volume, ΔU_i, for which P is the centroid. The average density, ρ_i, of the fluid in ΔU is $\rho_i = \Delta m_i/\Delta U_i$. Obviously, if ΔU_i is too large, say of the order of magnitude of the entire field of flow, it is meaningless to assign the value ρ_i to the point P, i.e., to represent the ratio $\Delta m_i/\Delta U_i$ for the fluid in the vicinity of P. This is especially true when the fluid is inhomogeneous. To determine how small ΔU_i should be in order for ρ_i to represent the fluid in the neighbourhood of P, we gradually reduce ΔU_i around P, determining the ratio $\Delta m_i/\Delta U_i$ for a sequence of volumes ΔU_i: $\Delta U_1 > \Delta U_2 > \Delta U_3 \cdots$. The results of these computations are shown in Fig.3.1.

If we start from a sufficiently large ΔU_i, gradual changes may be observed in ρ_i if the fluid is inhomogeneous. Fluctuations around ρ_i diminish as ΔU_i becomes smaller. Then as ΔU_i converges on P, a range of practically no changes in ρ_i with changes in ΔU_i is observed. However, as ΔU_i is made smaller and the number of molecules in it becomes smaller too, a range is reached below a certain volume ΔU_0 where the number of molecules in ΔU_i is so small that any further reduction of ΔU_i appreciably affects the ratio $\Delta m_i/\Delta U_i$. This happens when the characteristic length dimension of ΔU_i becomes of the order of magnitude of the average distance λ between the molecules (mean free path of molecules). As $\Delta U_i \rightarrow 0$ very wild fluctuations in the ratio $\Delta m_i/\Delta U_i$ are observed, and it is meaningless to use ρ_i as a definition for the density of the fluid at P. Hence the

fluid's density at P is defined as:

$$\rho(P) = \lim_{\Delta U_j \to \Delta U_0} \rho_j = \lim_{\Delta U_j \to \Delta U_0} (\Delta m_j / \Delta U_j) \tag{3.1}$$

The characteristic volume ΔU_0 is called the physical point of the fluid at the mathematical point P. The volume ΔU_0 may now be identified with the volume of a particle at P. By the procedure just described, a material made of a collection of molecules in a vacuum is replaced by a continuum filling the entire space. We obtain a fictitious smooth medium (instead of the molecules), called fluid, for each point of which a continuous function of space ρ is defined. For any two close points P and P':

$$\rho(P) = \lim_{P' \to P} \rho(P') \tag{3.2}$$

We can now treat physical phenomena from the molecular level to the microscopic level. We have a fluid continuum enclosed by solid surfaces — the solid surfaces of the porous medium. At each point of this fluid continuum we may define the specific physical, dynamic and kinematic properties of the fluid particle. In principle the flow of a fluid in a porous medium may be treated at this level, at which we focus our attention at what happens at a point within the fluid, regarded as a continuum. For example, we may use the Navier-Stokes equations for the flow of viscous fluid to determine the velocity distribution of the fluid in the void space, satisfying specified boundary conditions, say, of vanishing velocity, on all fluid-solid interfaces. However, this approach is usually impractical due to our inability to describe the complex

configuration of this boundary. Moreover, even if we could solve for values of state variable, e.g. pressure, at the microscopic level, we could not verify these solutions by measurements at this level.

To circumvent these difficulties, another level of description is needed. This is a coarser level of averaging — the macroscopic level, This is again a continuum approach, but at a higher level.

The following paragraph deals with the macroscopic approach to the dynamics of fluid in porous media.

3.1.3   Porosity and representative elementary volume

In the section 3.1.2 we have seen that essential to the concept of a continuum is the particle, or the physical point, or the representative volume over which an average is performed. This is also true in the passage from the microscopic to the macroscopic level. Our task now is, therefore, to determine the size of the representative porous medium volume around a point P within it. From the discussion in the previous paragraph we know that this volume should be much smaller than the size of the entire flow domain, as otherwise the resulting average cannot represent what happens at P. On the other hand, it must be large enough (greater than the size of a single pore) that it includes a sufficient number of pores to permit a meaningful statistical average required

in the continuum concept.

We shall now define volumetric porosity and the representative elementary volume (REV) associated with it, following the same procedure as that described in paragraph 3.1.2 for the definition of density. Let P be a mathematical point inside the domain occupied by the porous medium. Consider a volume ΔU_i much larger than a single pore or grain, for which P is the centroid. For this volume we may determine the ratio:

$$n_i = n_i(\Delta U_i) = (\Delta U_v)_i / \Delta U_i \qquad (3.3)$$

Where $(\Delta U_v)_i$ is the volume of void space within ΔU_i. Repeating the same procedure, a sequence of values $n_i(\Delta U_i)$, $i=1,2,3,...$ may be obtained by gradually shrinking the size of ΔU_i around P as a centroid: ΔU_i: $\Delta U_1 > \Delta U_2 > \Delta U_3 \cdots$.

For large values of ΔU_i, the ratio n_i may undergo gradual changes as ΔU_i is reduced, especially when the domain considered is inhomogeneous. Below a certain value of ΔU_i, depending on the distance of P from boundaries of inhomogeneity, these changes or fluctuations tend to decay, leaving only small-amplitude fluctuations that are due to the random distribution of pore sizes in the neighbourhood of P. However, below a certain value ΔU_0 we suddenly observe large fluctuations in the ratio n_i. This happens as the dimensions of ΔU_i approach those of a single pore. Finally, as $\Delta U_i \rightarrow 0$, converging on the mathematical point P, n_i will become either one or zero, depending on whether

P is inside a pore or inside the solid matrix of the medium. Figure 3.2 shows the relationship between n_i and ΔU_i.

The medium's volumetric porosity $n(P)$ at point P is defined as the limit of the ratio n_i as $\Delta U_i \to \Delta U_0$:

$$n\ (P)\ =\ \lim_{\Delta U_i \to \Delta U_0}\ n_i\ (\Delta U_i (P))\ =\ \lim_{\Delta U_i \to \Delta U_0}\ \frac{(\Delta U_v)_i (P)}{\Delta U_i} \tag{3.4}$$

For values of $\Delta U_i < \Delta U_0$, we must consider the actual presence of pores and solid particles; in this range there is no single value that can represent the porosity at P. The volume ΔU_0 is therefore the representative elementary volume (REV) or the physical (or material) point of the porous medium at the mathematical point P. Obviously, the limit $\Delta U_i \to 0$ is meaningless. From the definition of the REV it follows that its dimensions are such that the effect of adding or subtracting one or several pores has no significant influence on the value of n.

We shall assume that both ΔU_0 and ΔU_v vary smoothly in the vicinity of P. Then

$$n\ (P)\ =\ \lim_{P' \to P}\ n\ (p') \tag{3.5}$$

which means that n is a continuous function of the position of P within the porous medium.

Thus, by introducing the concept of porosity and the definition of REV, we have replaced the actual medium by a fictitious continuum in which we may assign values of any property (whether of the medium or of the fluids filling the void space) to any mathematical point inside it. The continuum model of a porous medium eliminates the need for specifying the microscopic configuration of the individual phase and enables the solution of flow problems through porous media by available methods of mathematical analysis. The configuration of the void-solid boundary and the interphase boundaries within the averaging volume, as well as the effect of conditions that prevail on them, appear in the macroscopic description of the flow in the form of coefficients. The numerical values of these coefficients have to be determined experimentally for any given porous medium.

3.2   Density dependent fluid flow in saturated-unsaturated porous media

According to Bear (1987), subsurface water may be divided vertically into zones depending on the relative proportion of the pore space occupied by water: a zone of saturation, in which all pores are completely filled with water, and an overlying zone of aeration or an "unsaturated" zone, in which the pores contain both gases (mainly air and water vapour) and water.

Figure 3.3 shows a schematic distribution of subsurface water. Water (e.g., from precipitation and/or irrigation) infiltrates the ground surface, moves downward, primarily

under the influence of gravity, and accumulates, filling all the interconnected interstices of the rock formation above some impervious stratum. A zone of saturation is thus formed above this impervious bedrock. In the saturated zone (Fig.3.3) an upper boundary, the water table, or phreatic surface is defined as the surface on which the pressure is atmospheric. It is revealed by the water level in a well penetrating the aquifer, which the flow is essentially horizontal. Actually, saturation extends a certain distance above the water table, depending on the type of soil. Well, springs and streams are fed by water from the zone of saturation.

The zone of aeration extends from the water table to the ground surface. It usually consists of three subzones: the soil water zone, the intermediate zone and the capillary zone (capillary fringe).

The soil water zone is adjacent to the ground surface and extends downward through the root zone. The moisture distribution in this zone is affected by conditions at the ground surface: seasonal and diurnal fluctuations of precipitation, irrigation, air temperature and air humidity, and by the presence of a shallow water table. Water in this zone moves downward during infiltration (e.g., from precipitation, flooding of the ground surface or irrigation), and upward by evaporation and plant transpiration. Temporarily, during a short period of excessive infiltration, the soil in this zone may be almost completely saturated.

The intermediate zone extends from the lower edge of the soil water zone to the upper limit of the capillary zone. It does not exist when the water table is too high, in which case the capillary fringe may extend into the soil water zone, or even to the ground surface. Temporarily, water moves downward through this zone as gravitational water.

The capillary fringe extends upward from the water table. Its thickness depends on the soil properties and on the uniformity of pore sizes. The capillary rise ranges from practically nothing in coarse materials to as much as 2 - 3 m and more in fine materials (e.g. clay). Within the capillary zone there is usually a gradual decrease in moisture content with distance above the water table. Just above the water table, the pores are practically saturated. Moving higher, only the smaller connected pores contain water. At a still higher level, only the smallest connected pores are still filled with water. In the capillary fringe, the pressure is less than atmospheric and vertical as well as horizontal flow of water may take place.

When the saturated zone below the water table is much thicker than the capillary fringe, the flow in the unsaturated zone is often neglected. However, in most drainage problems, or groundwater contamination, from such cause as the migration of fertilizers and pesticides from agricultural and domestic usage, of solvents and toxic substances from industrial usage, and of countless other inorganic and organic chemicals into the topsoil and through the unsaturated zone, the flow in the unsaturated zone may be of

primary importance.

A general form of Darcy's law, which is commonly used to described saturated-unsaturated flow in porous media, may be used to express the pressure and density driven components for flow of a nonhomogeneous fluid (Bear, 1972):

$$v_i = -\frac{k_{ij}k_r}{\varepsilon\, S\mu}\left(\frac{\partial p}{\partial x_j} + \rho g\frac{\partial z}{\partial x_j}\right) \qquad (3.6)$$

where v_i is the pore fluid velocity in the i direction (L/T), k_{ij} is the permeability tensor (L^2), p is the pressure ($ML^{-1}T^{-2}$), g is the acceleration due to gravity (LT^{-2}), ρ is the fluid density (ML^{-3}), ϕ is the porosity of the porous medium, μ is the absolute viscosity ($ML^{-1}T^{-1}$), and S is the degree of fluid saturation in pores.

In order to discuss the relative importance of pressure and density driven flows, *Bear* (1972) rewrote Eq.(3.6) in the form

$$v_i = -\frac{k_{ij}\rho_0 g}{\varepsilon\,\mu}\frac{\partial}{\partial x_j}\left(\frac{p}{\rho_0 g} + z\right) - \frac{k_{ij}g(\rho_f - \rho_0)}{\varepsilon\,\mu}\frac{\partial z}{\partial x_j} \qquad (3.7)$$

where ρ_0 is some reference density, usually the density of the ambient groundwater. In Eq.(3.7) it is assumed that the porous medium is saturated ($k_r=1$ and S=1). According to Eq.(3.7), the motion may be interpreted as being caused by two driving forces: one resulting from piezometric head differences, where the head (($p/\rho_0 g$)+z) is referred to a fictitious homogeneous fluid of density ρ_0, and the other resulting from a buoyancy force, directed vertically upwards, acting on a fluid particle of density ρ_f embedded in a fluid

of density ρ_0. *Bear* [1972] went on to evaluate the orders of magnitude of the two terms on the right hand side of Eq.(3.7). The orders of magnitude of the two terms are $O(k\rho_0 g/(\phi\mu)(\Delta h/L)$ and $O(kg\ \Delta\rho/\phi\mu)$, respectively , where Δh and $\Delta\rho$ are the characteristic head and the density differences, L is a characteristic length. The ratio between the two orders of magnitude is $O\ (\Delta\rho/\rho_0)\ /(\Delta h/L)$. Bear pointed out that we may distinguish between two cases, according to the relative magnitude of $\Delta\rho/\rho_0$ with respect to $\Delta h/L$. When $\Delta h/L$ is so small that $(\Delta\rho/\rho_0)/(\Delta h/L) \gg 1$, the flow is determined mainly by the buoyancy force and the flow regime is one of free convection. When $(\Delta\rho/\rho_0)/(\Delta h/L) \ll 1$, the flow is governed mainly by the external head gradients and the flow regime is one of forced convection. Bear noted that actually the criterion should be based on a comparison between the vertical component of the hydraulic gradient and the vertically directed buoyancy gradient. A free convection flow regime may still exist when the horizontal components of the external driving force are large. Obviously, as he pointed out, the division into two different flow regimes is not a clear-cut one, and the definition of a flow regime as belonging to either of the two regimes is rather arbitrary, especially at intermediate values of $(\Delta\rho/\rho_0)/(\Delta h/L)$. Moreover, we have used the characteristic quotients $\Delta\rho/\rho_0$ and $\Delta h/L$ to characterize the entire flow domain. We could have based the discussion on local values of grad h and $\Delta\rho/\rho_0$, as the flow regime may be different in different portions of the flow domain depending on the local values of grad h.

3.2.1 Governing equation of groundwater flow with pressure as the variable

The basic fluid mass balance equation or continuity equation is (Bear, 1979)

$$\frac{\partial(\phi S \rho)}{\partial t} + \nabla \cdot (\rho \, \vec{q}) = S_t \tag{3.8}$$

where S_t represents the sources and sinks, q is the Darcy flux (LT^{-1}), has the form

$$q = \phi S \vec{v} = \theta \, \vec{v} \tag{3.9}$$

here $\theta = \phi S$ is the volumetric fluid content.

The first term of Eq.(3.8) can be expanded by making use of the equation of state for the density of a fluid under isothermal conditions, $\rho = \rho \,(p,C)$, which states that fluid density depends on the pressure, p, and the concentration of the dissolved solids, C, to yield

$$\frac{\partial(\phi S \rho)}{\partial t} = \frac{\partial(\phi S \rho)}{\partial p}\frac{\partial p}{\partial t} + \frac{\partial(\phi S \rho)}{\partial C}\frac{\partial C}{\partial t} \tag{3.10}$$

By developing the first term on the right-hand side of Eq.(3.10), we may obtain (Bear and Verruijt, 1987)

$$\frac{\partial(\phi S \rho)}{\partial t} = (S\phi\frac{\partial \rho}{\partial p} + S\rho\frac{\partial \phi}{\partial p} + \phi\rho\frac{\partial S}{\partial p})\frac{\partial p}{\partial t} + \phi S\frac{\partial \rho}{\partial C}\frac{\partial C}{\partial t} \tag{3.11}$$

The first two terms in the brackets on the right hand side represents changes due to the fluid and soil compressibility respectively, and can be replaced by a suitable

coefficient of storage, S_p (T^{2}L^{-2}) defined as (Bear and Verruijt, 1987)

$$S_p = \phi S \beta + S(1-\phi)\alpha(\chi + p\frac{\partial \chi}{\partial p}) \tag{3.12}$$

In this equation, β $(LT^{-2}M^{-1})$ is the coefficient of fluid compressibility, and α

(L^3M^{-1}) the coefficient of soil compressibility. χ is an empirical coefficient that represents

the fraction of the soil's cross-sectional area occupied by water. The coefficients β and

α are defined as,

$$\beta = \frac{1}{\rho}\frac{\partial \rho}{\partial p} \tag{3.13}$$

$$\alpha = \frac{1}{1-\phi}\frac{\partial \phi}{\partial p} \tag{3.14}$$

The third term of Eq.(3.11) represents the change in storage with fluid pressure

in the unsaturated zone given by the fluid retention curve. Assuming that the differential

water capacity, c $(M^{-1}LT^2)$, obtained by differentiation of the appropriate saturation-

capillary pressure relationship, is defined by

$$c = \phi\frac{\partial S}{\partial p} = \frac{d\theta}{dp} \tag{3.15}$$

Inserting the coefficient of fluid mass storage and the differential water capacity

in Eq.(3.11), results in

$$\frac{\partial(\phi S \rho)}{\partial t} = \rho(S_p + c)\frac{\partial p}{\partial t} + \phi S\frac{\partial \rho}{\partial C}\frac{\partial C}{\partial t} \tag{3.16}$$

Combining Eqs.(3.6), (3.8), and (3.16) gives the expanded density dependent fluid mass balance equation, with sources and sinks, for isothermal conditions, as follows

$$\rho\,(S_p+c)\frac{\partial p}{\partial t}+\phi S\frac{\partial \rho}{\partial C}\frac{\partial C}{\partial t}-\nabla\cdot[(\frac{k_{ij}k_r\rho}{\mu})\cdot(\nabla p+\rho g\nabla z)]=S_t \qquad (3.17)$$

3.2.2 Governing equation of groundwater flow with stream function as the variable

The general form of the governing equation for the variable density flow in saturated-unsaturated porous media was given in section 3.2.1. In this section, we will discuss a special case: the variable density flow in saturated porous media with some assumptions that allow derivation of the flow equation with the stream function as the variable.

The Continuity Equation may be rewritten in saturated porous media:

$$\frac{\partial(\phi\rho)}{\partial t}+\nabla\cdot(\rho q)=S_t \qquad (3.18)$$

Darcy's Law:

$$q_i=-\frac{k_{ij}}{\mu}(\frac{\partial p}{\partial x_j}+\rho g\frac{\partial z}{\partial x_j}) \qquad (3.19)$$

Assuming that the relation between density and concentration is given by

$$\rho = \rho_0 (1 + \varepsilon \tilde{C})$$ (3.20)

$$\varepsilon = \frac{\rho_{max} - \rho_0}{\rho_0}$$ (3.21)

where ρ_0 is a reference freshwater density, ρ_{max} is the density corresponding to the maximum concentration, C is a dimensionless concentration that varies between zero and unity. The dimensionless parameter ε has a value in the range of 0.025 - 0.030 for salt concentration in seawater.

Substituting Eq. (3.20) into Eq. (3.18), the flow equation then becomes

$$\rho S_p \frac{\partial p}{\partial t} + \phi \rho_0 \varepsilon \frac{\partial \tilde{C}}{\partial t} = \rho_0 (1 + \varepsilon \tilde{C}) \nabla \cdot q + \rho_0 \varepsilon \, q \cdot \nabla C$$ (3.22)

where S_p is the mass storage. Following Lee and Cheng (1974) we assume that the fluid and aquifer are incompressible, so $S_p = 0$, and also since ε is much less then unity, the terms containing ε may be neglected. This results in the zeroth order approximation of the continuity equation which has the form

$$\nabla \cdot q = 0 \quad or \quad \frac{\partial}{\partial x}(q_x) + \frac{\partial}{\partial z}(q_z) = 0$$ (3.23)

A stream function ψ may now be introduced (Senge and Fogg 1990; Lee and Cheng, 1974; Henry, 1964).

Assuming that the principal directions of hydraulic conductivity coincide with the

coordinate axes (K_{xz}=0), the flow equations may be written as

$$q_x = -K_{xx} \left(\frac{\partial(p/(\rho_0 g))}{\partial x} \right) \qquad (3.24)$$

$$q_z = -K_{zz} \left(\frac{\partial(p/(\rho_0 g))}{\partial z} + (1 + \varepsilon \tilde{C}) \right) \qquad (3.25)$$

For two-dimensional flow, the fluid flux defined in terms of a stream function may be expressed as:

$$q_x = \frac{\partial \psi}{\partial z} \qquad (3.26)$$

$$q_z = -\frac{\partial \psi}{\partial x} \qquad (3.27)$$

Eliminating the pressure terms in (3.24), (3.25) by cross differentiation, we arrive at the equation:

$$\frac{\partial}{\partial x} \left(\frac{1}{K_{zz}} \frac{\partial \psi}{\partial x} + \varepsilon \tilde{C} \right) + \frac{\partial}{\partial z} \left(\frac{1}{K_{xx}} \frac{\partial \psi}{\partial z} \right) = 0 \qquad (3.28)$$

Comparison of Eq. (3.28) and (3.23) shows that horizontal flux in the continiuty equation is expressed by the stream function gradient and a reletive density term ($\varepsilon \tilde{C} = \frac{\rho - \rho_0}{\rho_0}$). The lateral density gradient expresses the rotation of the fluid due to variable density (Senger and Fogg, 1990).

3.2.3 Mathematical models for the hydraulic properties in the unsaturated zone

The soil water retention and hydraulic conductivity functions are the crucial parameters for predicting saturated-unsaturated flow. Their theoretical description and measurement remains a continuous and sometimes frustrating challenge for hydrologists and soil scientists. While in situ field measurements undoubtedly are the most representative of actual flow conditions, current methods are likely to remain approximate in nature. This is due in part to simplifying assumptions inherent in most field methods, and in part to problems of obtaining undisturbed samples. Field methods usually require the use of a tensiometer for the measurement of water content using gravimetric, neutron, or gamma ray techniques. Most current methods are based on simplifying assumptions about the flow regime during redistribution of soil water after reaching saturated or near-saturated steady state flow (Nielsen et al 1986).

Direct field methods to determine the unsaturated hydraulic conductivity are time consuming, expensive, and usually subject to simplifying assumptions. An attractive alternative to direct measurement is the theoretical calculation of the hydraulic conductivity from more easily measured field or laboratory soil water retention data. Mualem (1976) derived a new model for predicting the hydraulic conductivity from knowledge of the soil-water retention curve. Mualem's derivation leads to a simple integral formula for the unsaturated hydraulic conductivity which enables one to derive closed-form analytical expressions. Van Genuchten (1980) derived such expressions using

the equation for the soil-water retention curve which is both continuous and has a continuous slope. The resulting conductivity models generally contain three independent parameters which may be obtained by matching the proposed soil-water retention curve to experimental data.

Van Genuchten's equation was given by (Van Genuchten, 1980, 1985)

$$\theta = \theta_r + \frac{\theta_s - \theta_r}{[1 + |\alpha h|^n]^m}$$ (3.29)

where θ_r and θ_s are the residual and field-saturated volumetric water contents, respectively, h is the pressure head, and α, n and m are empirical constants. In practice, θ_r and θ_s must also be considered empirical. He then noted that using the simplifying assumption that m = 1-1/n, Eq. (3.29) can be combined with the predictive conductivity model of Mualem (1976) to yield an expression for $K(S_e)$ of the form

$$K = K_s S_e^l [1 - (1 - S_e^{1/m})^m]^2$$ (3.30)

where

$$S_e = \frac{\theta - \theta_r}{\theta_s - \theta_r}$$ (3.31)

here l is an empirical parameter that was estimated by Mualem to be approximately 0.5 for most soils. Equation 3.31 works well for medium and coarse-textured soil, while predictions for fine-textured materials generally are less accurate (Van Genuchten, 1985).

3.3   Solute transport in saturated-unsaturated porous media

The major processes of contaminant transport through a groundwater system are advection, dispersion, diffusion, adsorption, various chemical and biological reactions, and decay phenomena all of which may be regarded as sources and/or sinks for the solute (Bear 1987).

3.3.1   Advection

Advection refers to the transport of a material by the mean motion of a fluid in a porous medium. This mechanism is often considered to be the major transport process. The advection flux J_a, expressing the flux carried by the water at its average velocity V, may be described as (Bear, 1987):

$$J_a = \theta\, VC \tag{3.32}$$

3.3.2   Molecular diffusion

Molecular diffusion is the result of the thermal kinetic energy of the molecules, which in the presence of a concentration gradient, results in a net flux of solute toward the low-concentration zone (Bear, 1972). At the microscopic level, the flux vector, $J^{(d)}$, due to molecular diffusion is expressed by Fick's law

$$J_d = -D_d \cdot \nabla C \tag{3.33}$$

where D_d is the coefficient of molecular diffusion in a fluid continuum (equals about 10^{-5} cm^2/sec in a dilute system). By averaging (3.33) over the REV, and introducing certain simplifying assumptions, Bear (1987) derived an expression for the macroscopic flux in the form

$$\bar{J}_d = -D_d T^* \cdot \nabla \bar{C} = -D_d^* \cdot \nabla \bar{C} \tag{3.34}$$

where $D_d^* = T^* D_d$ is the coefficient of molecular diffusion in a porous medium and T^* often referred to as the tortuosity, is a second-rank symmetric tensor that expresses the effect of the configuration of the water occupied portion of the REV. We use the averaging symbol $^-$ in Eq. (3.34) in order to emphasize the difference between this equation and (3.33).

3.3.3 Mechanical dispersion

The process of mechanical dispersion describes the volume-average deviations of concentration from those predicted by the mean motion alone. Bear (1972, 1987) pointed out that we must refer to what happens at the microscopic level to explain this phenomena. According to Gillham and Cherry (1982), there are three microscopic mechanisms that give rise to velocity variations in homogeneous media (Fig. 3.4):

1.   The velocity distribution associated with the flow of viscous fluid through a pore.

The velocity of the soil distribution is zero at the solid surface and reaches a maximum at the centre of a pore.

2.   Variations in velocity as a result of differences in the pore geometries.

3.   Fluctuations in the stream lines with respect to the mean flow direction.

The mechanical dispersive flux J_m, is a macroscopic flux that expresses the effect of the microscopic variations of the velocity in the vicinity of a considered point. It may be described in terms of a Fick's law, analogous to the molecular diffusive flux (Bear, 1987):

$$\overline{J}_m = -D_m \cdot \nabla \overline{C} \tag{3.35}$$

Where D_m is a second rank symmetric tensor called the coefficient of mechanical dispersion.

According to Bear (1987), by adding the dispersive flux, expressed by (3.35), and diffusive flux, expressed by (3.34), we obtain J_h,

$$J_h = -(D_m + D_d^*) \cdot \nabla C = -D_h \cdot \nabla C \tag{3.36}$$

where the coefficient D_h is called the coefficient of hydrodynamic dispersion.

The total flux, q_{total} of a pollutant, by advection, dispersion, and diffusion may now be written in the form

$$q_{total} = \theta \left(C \vec{V} - D_h \cdot \nabla C \right)$$ (3.37)

The mechanical dispersion coefficient is related to a dispersivity tensor which expresses the microscopic configuration of the solid-fluid interface. Following Scheidegger (1961) and Bear (1961), the dispersivity is a fourth rank tensor with 81 components. Based on certain assumptions on the porous medium and the principle directions of the dispersivity tensor, the number of nonzero components can be greatly reduced. In an isotropic porous medium, the components of the mechanical dispersion tensor are related to two widely used parameters: a_L (L), the longitudinal dispersivity, and a_T (L), the transversal dispersivity. According to Bear (1987), the longitudinal dispersivity a_L expresses the heterogeneity of the porous medium at the microscopic scale, i.e., due to the presence of pores and solids. In laboratory experiments with homogeneous sand columns it was found that a_L is of an order of magnitude of the average sand grain diameter. The transverse dispersivity is estimated as being 10 to 20 times smaller than a_L.

For an isotropic porous medium, the mechanical dispersion coefficient may be expressed as follows (Bear, 1972, 1987):

$$(D_m)_{ij} = a_T |V| \delta_{ij} + (a_L - a_t) \frac{V_i V_j}{|V|}$$ (3.38)

where δ_{ij} is the Kronecker delta with $\delta_{ij}=0$ for $i \neq j$ and $\delta_{ij}=1$ for $i=j$. So the hydrodynamic dispersion coefficient becomes

$$(D_h)_{ij} = a_T|V|\delta_{ij} + (a_L - a_T)\frac{V_i V_j}{|V|} + D_d \delta_{ij}$$ (3.39)

3.3.4 Governing equation for contaminant transport in saturated-unsaturated porous media

The macroscopic mass balance equation of pollutant can be written as

$$\frac{\partial(\theta C)}{\partial t} = -\nabla \cdot q_{total} - f + \theta \rho \Gamma + RC_R - PC$$ (3.40)

where q_{total} is the total mass flux ($ML^{-2}T^{-1}$), expressed by Eq.(3.37), f denotes the quantity of pollutant that leaves the water by ion exchange or adsorption through the water-solid interface as a result of chemical or electrical interactions between the pollutant and the solid surface, Γ the rate of which that mass of a polutant is added to the water by various decay phenomena. Pollutant may be added by injecting polluted water into a porous medium domain or removed from a porous medium domain by withdrawing (polluted) water. P and R denotes the rates of water withdrown or added, respectively. θ the volumetric water content and C the pollutant concentration in the aqueous phase (M/L^3).

Sources and sinks of the pollutant, expressed by the term $\theta\rho\Gamma$, results from various processes, e.g., chemical reactions among components within the liquid, radioactive decay and biodegradation, and growth due to bacterial activities.

In order to obtain an expression for f, we turn to the equation for the same pollutant component in the solid phase (Bear, 1987). Let F denote the mass of the pollutant on the solid per unit mass of solid. With ρ_s denoting the solid's density and θ_s denoting the solid's volumetric fraction and neglecting any advective, dispersive, or diffusive flux of pollutant present in the solid phase, the pollutant mass balance on the solid surface reduces to

$$\frac{\partial (\theta_s \rho_s F)}{\partial t} = f \tag{3.41}$$

By eliminating f from (3.40), and substituting (3.37) into (3.40), we obtain

$$\frac{\partial (\theta C)}{\partial t} + \frac{\partial (\theta_s \rho_s F)}{\partial t} = -\nabla \cdot \theta (C \vec{V} - D_h \cdot \nabla C) + \theta \rho \Gamma + R C_R - PC \tag{3.42}$$

Equation (3.42) is a single equation in the two state variables, C and F. We need an additional relationship between C and F. An adsorption isotherm is an expression that relates the quantity of an adsorbed component to its quantity in the fluid phase, at constant temperature. In general, the isotherms may be divided into two classes:

1. Equilibrium isotherms, that are based on the assumption that the quantities of the component on the solid and in the adjacent solution are continuously in equilibrium. Any change in the concentration of one of them produces an instantaneous change in the other.

2. Nonequilibrium isotherms, which assume that equilibrium is not achieved instantaneously, but rather that it is approached at a certain rate which, in general,

depends on both C and F.

The most common approach is a special form of the Freundlich isotherm,

$$F = K_d C \qquad (3.43)$$

where a simple linearity is assumed between F and C. The coefficient K_d ($L^3 M^{-1}$) is the slope of the linear exchange isotherm. Further details and forms of isotherm may be found in Bear (1987).

It should be mentioned that it has been observed that the dispersivity increases as the scale of the experiment increases. Field-observed dispersion coefficients are orders of magnitude higher than those found in laboratory scale tests. This scale dependency has been reported and discussed by many researchers. For more details the reader is referred to Pickens and Grisak (1981), Gelhar (1986), Sudicky (1986), Dagan (1986), Arya et al. (1988), Neuman (1990) and Oostrom (1991).

3.4   Initial and boundary conditions

3.4.1   Initial and boundary conditions for the flow equation

To completely define a unique problem, the governing equations must be constrained by appropriate initial and boundary conditions. It is assumed that an initial

distribution of pressure (or stream functions) may be described in the region of interest, R, as

$$p = p_i(x,y,z,0) \tag{3.44}$$

or

$$\psi = \psi_i(x,y,z,0) \tag{3.45}$$

where R is the region of interest and p_i or ψ_i is the prescribed initial condition, which may be defined or alternatively obtained by solving the governing equation for the steady state.

The specification of boundary conditions is the most difficult and intricate task in groundwater flow modelling. From the dynamic point of view, a boundary segment may be classified as flow-through or impervious. From the physical point of view, it may be considered as a soil-air interface, or soil-soil interface, or soil-water interface. From the mathematical point of view, it may be treated as a Dirichlet boundary on which the function values are prescribed, these conditions are normally applied using physical arguments, to the soil-water interfaces such as occur in streams, rivers, lakes, artificial impoundments, and coastal lines. Neumann boundary conditions on the other hand, are those in which the gradients of the function are known, these conditions do not occur or may not be specified very often in real-world problems. They may be applied to the bottom of the media where natural drainage takes place, or to a Cauchy boundary on

which the total flux is specified. These conditions are normally applied to surface water bodies with known infiltration rates through their bottom layers of sediment or liners into subsurface media. An even more mathematically difficult boundary is that on which the boundary conditions are not known a priori, but are themselves part of the solution to be sought. In other words, on the mathematically variable boundary, either Dirichlet or Cauchy conditions may prevail and vary with time. As to which condition prevails at a particular time may be determined only during the cyclic process of solving the governing equations. These conditions commonly occur at a soil-air interface.

Independent of the point of view from which they were derived, all boundary conditions must eventually be transformed into a mathematical statement for quantitative simulation. Thus, we will specify the boundary condition from the mathematical point of view in concert with dynamic and physical considerations. The boundary conditions imposed on any segment of the boundary are taken to be either Dirichlet, Neumann, Cauchy, or Variable. Thus, the boundary may be split into 4 parts, B_D, B_N, B_C, and B_V denoting Dirichlet, Neumann, Cauchy, and Variable boundaries, respectively. Here we only give the pressure boundary conditions imposed on the first three types of boundaries, stream function boundary conditions may be specified in a similar fashion.

Dirichlet conditions :

$$p = p_D(x_b, y_b, z_b, t) \qquad on \qquad B_D \qquad (3.46)$$

Neumann Conditions:

$$- \vec{n} \cdot K \cdot \nabla p = q_N \ (x_b, y_b, z_b, t) \qquad on \qquad B_N \qquad (3.47)$$

and   Cauchy conditions:

$$- \vec{n} \cdot K \cdot (\nabla P + \rho g \nabla z) = q_C(x_b, y_b, z_b, t) \qquad on \qquad B_C \qquad (3.48)$$

where (x_b, y_b, z_b) is the spatial coordinate on the boundary ; n is the outward unit vector

normal to the surface, p_D , q_N , and q_C are the prescribed Dirichlet function values,

Neumann flux, and Cauchy flux, respectively.

The conditions imposed on a boundary of the variable-type, which is normally a

soil-air or soil-water interface, treated separately for precipitation and nonprecipitation

periods, take the following mathematical form.

During precipitation periods, we impose

$$p = p_P(x_b, y_b, z_b, t) \qquad on \qquad B_V \qquad (3.49a)$$

or

$$- \vec{n} \cdot K \cdot \nabla (p + \rho g z) = q_P(x_b, y_b, z_b, t) \qquad on \qquad B_V \qquad (3.49b)$$

where p_p is the allowed pressure which depends on the allowed ponding depth and q_p is

the throughfall of infiltration. Either Eq. (3.49a) or (3.49b) is applied to the boundary B_v

when the exact boundary conditions cannot in general be predicted a priori. Such a case would arise at the ground surface where either Dirichlet (ponding) or Cauchy (infiltration) conditions could prevail. The change over from Dirichlet conditions specified by Eq. (3.49a) to Cauchy conditions specified by Eq. (3.49b) or vice versa is determined during the cyclic process of solving the governing Equation (3.17).

During a non-precipitation period , we impose

$$p = p_p(x_b, y_b, z_b, t) \qquad on \quad B_V \qquad (3.50a)$$

or

$$p = p_m(x_b, y_b, z_b, t) \qquad on \quad B_V \qquad (3.50b)$$

or

$$-\vec{n} \cdot K \cdot (\nabla p + \rho g \nabla z) = q_e(x_b, y_b, z_b, t) \qquad on \quad B_V \qquad (3.50c)$$

where p_m is the minimum allowed pressure at the air-soil interface and q_e is the maximum allowed evaporation rate, which is the potential evaporation. Again, only one of equations (3.50a) through (3.50c) is used at any point on the variable boundary at any instant of time.

Equations (3.44) through (3.50c) with governing equation (3.17) constitute a

general mathematical statement of the physics of flow in saturated-unsaturated subsurface media. Analytical solutions for this general system do not exist. Numerical algorithms have therefore to be devised to solve the problem.

3.4.2 Initial and boundary conditions for the transport equation

Initial conditions include information on the concentration distribution at t = 0 at all points within the considered region, R.

$$C = C(x,y,z,0) \qquad \in R \qquad (3.51)$$

Due to physical inputs imposed in the domain's environment, the concentration C = C(x,y,z,t), may be specified as a known function, say $g_1(x,y,z,t)$, at all points of a given boundary (or boundary segment), B_D, independent of what happens within R; we can write the boundary condition in the form

$$C = g_1(x,y,z,t) \qquad on \ B_D \qquad (3.52)$$

When the physical phenomena occurring in the environment impose a known flux, say g_2 (x,y,z,t), at all points of a boundary segment, B_C, independent of what happens within the domain considered, the condition

$$\vec{n} \cdot (\theta C \vec{V} - \theta D \cdot \nabla C) = g_2(x,y,z,t) \qquad on \ B_C \qquad (3.53)$$

where n is the outward unit vector normal to the surface, may be used . Since both C and

∇C are involved in (3.53), this is a Cauchy boundary condition.

Another type of boundary condition is the Von Neumann boundary conditions. It has the form

$$\vec{n}\cdot(-\theta D\cdot\nabla C) = g_3(x,y,z,t) \qquad on \quad B_N \qquad (3.54)$$

where $g_3(x,y,z,t)$ is a known function. An impervious boundary, or a seepage face, frequently results in this type of boundary condition.

Equations (3.51) through (3.54) with the governing equations constitute a general mathematical statement of contaminant transport in saturated-unsaturated subsurface media. Due to the complexity of the problem, numerical methods need to be devised in order to solve the problem.

CHAPTER 4

NUMERICAL CONSIDERATIONS

Surface contaminant plumes emanating from water disposal facilities are often denser than the ambient groundwater. Under certain conditions these dense plumes may become unstable, resulting in larger than expected dispersion and contamination of large regions of an aquifer. For a given aquifer, the stability of dense plumes is governed by the groundwater flow velocity, the contaminant leachate rate, the coefficients of dispersion and the density difference between the contaminant solution and the ambient groundwater. The thrust of the present work is to numerically study the behaviour of dense leachate plumes in saturated-unsaturated aquifers and ultimately predict the resultant contaminant concentration distribution. Of particular interest is to ascertain whether experimentally observed gravitational instabilities that form along the lower edge of the plume can be reproduced in the numerical model.

First, using the stream function approach, a standard finite difference method is employed to simulate the laboratory experiments of Schincariol and Schwartz (1990) on an intruding negatively buoyant plume. Secondly, a finite volume formulation on a rectangular mesh will be discussed and implemented to numerically reproduce the laboratory results of Oostrom (1992) on a dense plume caused by leaching at the surface. Finally, an attempt has been made to model leachate concentration from a landfill in Borden, Ontario. Subsurface concentration distributions obtained from core samples have

been measured and reported by MacFarlane et al. (1983). Of particular interest in this simulation was to ascertain if the gravitational instabilities observed in the previously mentioned laboratory experiments would be reproduced numerically at such large scales.

The numerical simulation for this case study was accomplished by a finite volume implementation of the governing flow equations on a triangular mesh. A hybrid technique using a finite volume formulation in conjunction with a characteristics based method was used for the transport equation. The results of these simulations (which will be discussed in Chapter 5, 7 and 8) indicate that good agreement between the experimental results of Schincariol and Schwartz and of Oostrom are obtained. For the Borden landfill, the plume simulation demonstrated gravitational instability. The field measurements however were not sufficiently detailed to reveal this effect. Nevertheless, it may be expected that the influence of these instabilities on the overall dispersion characteristics of the plume is likely to be important.

4.1 Simulation of the experimental results of Schincariol and Schwartz

Since the numerical results are to be compared with the experimental data of Schincariol and Schwartz, a brief description of their experimental setup is given here. For further details, the reader is referred to the original paper.

4.1.1   Experimental apparatus (Schincariol and Schwartz)

A flow tank is filled with a porous medium consisting of various sizes of industrial glass beads (Fig. 4.1). Influent and effluent reservoirs are placed at each end of the tank to buffer the effect of the inflow/outflow. A dense Sodium Chloride (NaCl) solution is introduced into the middle of the lighter groundwater through a centrally disposed slot. The flow tank produces a uniform groundwater flow field at typical groundwater flow velocities for a variety of different spatial distributions of hydraulic conductivity. The tank itself is 116.8 cm long, 71.0 cm wide, and 5 cm deep. The length and width dimensions provide a travel path for the tracer that is of sufficient length to permit the development of the local instabilities .

The specific objectives of this study are to obtain the concentration distribution using numerical techniques in order to compare with the experimentally observed data. In the following section, the governing system of equations for the flow regime together with the appropriate boundary conditions are briefly presented. This is followed by details of the numerical methods employed to solve the governing equations.

4.1.2   Governing equations

The general form of the governing equations for the variable density flow and transport problems in saturated-unsaturated porous media were given in Chapter 3. Since

the experiment was conducted in isotropic, saturated porous media, we will choose the two-dimensional flow equation which uses the stream function as the dependent variable and the transport equation in which adsorption is not considered and in which sources and sinks are assumed absent. For the convenience of the discussion, we rewrite these governing equations in the following form

The flow equation in the two-dimensional vertical plane:

$$\frac{\partial}{\partial x}(\frac{1}{K_{zz}}\frac{\partial \psi}{\partial x}) + \frac{\partial}{\partial z}(\frac{1}{K_{xx}}\frac{\partial \psi}{\partial z}) = \varepsilon \frac{\partial \tilde{C}}{\partial x} \qquad (4.1)$$

The transport equation for the solute (Bear,1972):

$$\phi \frac{\partial C}{\partial t} + \frac{\partial}{\partial x_i}(Cq_i - D_{ij} \cdot \frac{\partial C}{\partial x_j}) = 0 \qquad (4.2)$$

The relation between density and concentration:

$$\rho = \rho_0(1 + \varepsilon \tilde{C}) \qquad (4.3)$$

$$\varepsilon = \frac{\rho_{max} - \rho_0}{\rho_0} \qquad (4.4)$$

The volume flux is expressed as:

$$q_x = \frac{\partial \psi}{\partial z} \qquad (4.5)$$

$$q_z = -\frac{\partial \psi}{\partial x} \qquad (4.6)$$

where i and j are space coordinates, q_i the specific discharge in the i direction (LT^{-1}), k_{ij} is the permeability tensor (L^2), μ is the fluid viscosity ($ML^{-1}T^{-1}$), ρ the fluid density

(ML^{-3}), p the fluid pressure ($ML^{-1}T^{-2}$), g gravitational acceleration (LT^{-2}), ϕ the effective porosity of the medium, C solute concentration (ML^{-3}), D_{ij} the dispersion tensor (L^2T^{-1}). ρ_0 is a reference freshwater density, ρ_{max} the density corresponding to the maximum concentration and C a dimensionless concentration that varies between zero and unity,

For an isotropic porous medium in two dimensions, D_{ij} may be written as

$$D_{ij} = \begin{bmatrix} D_{xx} & D_{xz} \\ D_{zx} & D_{zz} \end{bmatrix} \qquad (4.7)$$

$$D_{xx} = a_L \frac{q_x^2}{\sqrt{q_x^2 + q_z^2}} + a_T \frac{q_x^2}{\sqrt{q_x^2 + q_z^2}} + D_d^* \qquad (4.8)$$

$$D_{zz} = a_T \frac{q_x^2}{\sqrt{q_x^2 + q_z^2}} + a_L \frac{q_z^2}{\sqrt{q_x^2 + q_z^2}} + D_d^* \qquad (4.9)$$

$$D_{xz} = \phi D_{zx} = (a_L - a_T) \frac{q_x q_z}{\sqrt{q_x^2 + q_z^2}} \qquad (4.10)$$

where a_L, a_T are respectively the longitudinal and transverse dispersivities. D_d^* is the molecular diffusion coefficient.

4.1.3 Dimensionless equations

Introducing the characteristic quantities for length, conductivity, specific discharge and concentration, Equations (4.1) and (4.2) may also be cast in the following

dimensionless form:

$$\frac{\partial}{\partial \tilde{x}}(\frac{1}{\tilde{K}_{zz}} \frac{\partial \Psi}{\partial \tilde{x}}) + \frac{\partial}{\partial \tilde{z}}(\frac{1}{\tilde{K}_{xx}} \frac{\partial \Psi}{\partial \tilde{z}}) = \frac{\varepsilon K_0}{q_0} \frac{\partial \tilde{C}}{\partial \tilde{x}} \tag{4.11}$$

$$\frac{\partial \tilde{C}}{\partial \tau} = \frac{\partial}{\partial \tilde{x}}(\tilde{D}_{xx} \frac{\partial \tilde{C}}{\partial \tilde{x}} + \tilde{D}_{xz} \frac{\partial \tilde{C}}{\partial \tilde{z}}) + \frac{\partial}{\partial \tilde{z}}(\tilde{D}_{zx} \frac{\partial \tilde{C}}{\partial \tilde{x}} + \tilde{D}_{zz} \frac{\partial \tilde{C}}{\partial \tilde{z}})$$
$$- \tilde{q}_x \frac{\partial \tilde{C}}{\partial \tilde{x}} - \tilde{q}_z \frac{\partial \tilde{C}}{\partial \tilde{z}} \tag{4.12}$$

where

$$\tilde{x} = \frac{x}{L}, \qquad \tilde{z} = \frac{z}{L} \tag{4.13}$$

$$\tilde{K}_{xx} = \frac{K_{xx}}{K_0}, \qquad \tilde{K}_{zz} = \frac{K_{zz}}{K_0} \tag{4.14}$$

$$\tilde{\Psi} = \frac{\Psi}{q_0 L}, \qquad \tilde{C} = \frac{C}{C_0}, \qquad \tau = \frac{q_0 t}{\phi L} \tag{4.15}$$

$$\tilde{D}_{xx} = \tilde{a}_L \frac{\tilde{q}_x^2}{\sqrt{\tilde{q}_x^2 + \tilde{q}_z^2}} + \tilde{a}_T \frac{\tilde{q}_z^2}{\sqrt{\tilde{q}_x^2 + \tilde{q}_z^2}} + \tilde{D}_d^* \tag{4.16}$$

$$\tilde{D}_{zz} = \tilde{a}_T \frac{\tilde{q}_x^2}{\sqrt{\tilde{q}_x^2 + \tilde{q}_z^2}} + \tilde{a}_L \frac{\tilde{q}_z^2}{\sqrt{\tilde{q}_x^2 + \tilde{q}_z^2}} + \tilde{D}_d^* \tag{4.17}$$

$$\tilde{D}_{xz} = \tilde{D}_{zx} = (\tilde{a}_L - \tilde{a}_T) \frac{\tilde{q}_x \tilde{q}_z}{\sqrt{\tilde{q}_x^2 + \tilde{q}_z^2}} \tag{4.18}$$

$$\tilde{q}_x = \frac{q_x}{q_0} = \frac{\partial \tilde{\Psi}}{\partial \tilde{z}} \tag{4.19}$$

$$\tilde{q}_z = \frac{q_z}{q_0} = -\frac{\partial \psi}{\partial \tilde{x}} \tag{4.20}$$

$$\tilde{a}_L = \frac{a_L}{L}, \qquad \tilde{a}_T = \frac{a_T}{L}, \qquad \tilde{D}_d^* = \frac{D_d^*}{Lq_0} \tag{4.21}$$

where, L, K_0, q_0 and C_0 are the characteristic quantities.

4.1.4   Initial and boundary conditions

Initially, the flow is horizontal, so the initial condition for the stream function is a linear distribution from top to bottom (Fig. 5.1). The initial condition for the concentration is everywhere zero. The boundary conditions to be imposed for the stream function equations may be obtained from information on the fluxes or flow patterns at the boundaries. For impervious boundaries, a Dirichlet boundary condition is appropriate.

The boundary condition for the concentration is imposed in a similar fashion. The Dirichlet boundary condition is used for an inflow boundary. Von Neumann boundary conditions $\partial C/\partial z = 0$ are imposed on the impervious boundaries (top and bottom of the container). For the outflow boundary, the "uniform" condition $\partial C/\partial x = 0$ may be used.

4.1.5 Numerical scheme

The governing Equations (4.11),(4.12) with the boundary conditions may be solved numerically. A first order forward difference approximation is used for the time derivatives. The diffusion terms are treated using second-order central difference approximations. In the convection dominated flow, special attention has to be paid to the convective terms. It is well known that using the second-order central difference approximations to discretize the convective terms in the transport equation can produce wiggles in the solutions at high Peclet number. This may be avoided using upwind schemes. Upwind schemes such as the first-order upwind scheme, the second-order upwind scheme, the third-order upwind scheme, and the QUICK scheme (Quadratic Upstream Interpolation for Convective Kinematics) (Leonard, 1979) may be used.

Using higher order upwind schemes, a slight disadvantage appears, in that the discretized equations are no longer represented by a tri-diagonal matrix but take a penta-diagonal form.

A general finite difference expression for an arbitrary scalar function in upwind form may be written as follows:

$$U\frac{\partial f}{\partial x}\Big|_x = A^u f_{i-2} + B^u f_{i-1} + C^u f_i + D^u f_{i+1} + E^u f_{i+2} \tag{4.22}$$

Where A^u, B^u, C^u, D^u, and E^u are functions of u whose expression for different upwind

schemes are listed in Table 4.1 (details are given in Appendix A).

Table 4.1 The coefficients for the different schemes

Scheme	A^u	B^u	C^u	D^u	E^u
Central difference	0	$-\dfrac{u}{2\Delta x}$	0	$\dfrac{u}{2\Delta x}$	0
1-order upwind	0	$-\dfrac{|u|+u}{2\Delta x}$	$\dfrac{|u|}{\Delta x}$	$-\dfrac{|u|-u}{2\Delta x}$	0
2-order upwind	$\dfrac{|u|+u}{4\Delta x}$	$-\dfrac{|u|+u}{\Delta x}$	$\dfrac{3|u|}{2\Delta x}$	$-\dfrac{|u|-u}{\Delta x}$	$\dfrac{|u|-u}{4\Delta x}$
3-order upwind	$\dfrac{|u|+u}{12\Delta x}$	$-\dfrac{|u|+2u}{3\Delta x}$	$\dfrac{|u|}{2\Delta x}$	$-\dfrac{|u|-2u}{3\Delta x}$	$\dfrac{|u|-u}{12\Delta x}$
QUICK	$\dfrac{|u|+u}{16\Delta x}$	$-\dfrac{2|u|+5u}{8\Delta x}$	$\dfrac{3|u|}{8\Delta x}$	$-\dfrac{2|u|-5u}{8\Delta x}$	$\dfrac{|u|-u}{16\Delta x}$

Numerical experimentation reveals that the first-order upwind scheme can eliminate the wiggles and, as shown in Table 4.1, the discretized equations are in tri-diagonal form. It does suffer from the disadvantage however, of introducing numerical artificial diffusion. By choosing a fine mesh, the truncation errors and artificial diffusion can be greatly reduced. Consequently in this study, the convection terms in the transport equation have been treated using the first-order upwind scheme. For the stream function

equation, the central difference technique can be readily employed as no convection term is present. The resulting algebraic equations are solved by a line-by-line iterative method.

4.1.6 Discretized equations

For numerical computations, the governing differential equations (4.11),(4.12) are cast in discretized form. All the convection terms in the transport equation have been discretized with the first-order upwind scheme, while the dispersion terms have been discretized using central differences. For the time derivatives, the first order forward (finite) difference scheme has been adopted. The final discretization procedure is developed as follows.

4.1.6.1   Discretized flow equation

For the flow equation, the discretized representation with the stream function formulation is

$$
\frac{1}{K_{zz_{i+\frac{1}{2},j}}} \frac{\psi_{i+1,j}-\psi_{i,j}}{\Delta x^2} - \frac{1}{K_{zz_{i-\frac{1}{2},j}}} \frac{\psi_{i,j}-\psi_{i-1,j}}{\Delta x^2}
$$
$$
+ \frac{1}{K_{xx_{i,j+\frac{1}{2}}}} \frac{\psi_{i,j+1}-\psi_{i,j}}{\Delta z^2} - \frac{1}{K_{xx_{i,j-\frac{1}{2}}}} \frac{\psi_{i,j}-\psi_{i,j-1}}{\Delta z^2}
$$
$$
= R_a \frac{C_{i+1,j}-C_{i-1,j}}{2\Delta x} \tag{4.23}
$$

where $R_a = K_0 \varepsilon / q_0$. Written in compact form

$$a \ \psi_{i+1,j} - (a+b) \ \psi_{i,j} + b \ \psi_{i-1,j}$$
$$+ e \ \psi_{i,j+1} - (e+f) \ \psi_{i,j} + f \ \psi_{i,j-1} = d \qquad (4.24)$$

where

$$a = \frac{1}{K_{zz_{i+\frac{1}{2},j}}} \frac{1}{\Delta x^2} \qquad (4.25)$$

$$b = \frac{1}{K_{zz_{i-\frac{1}{2},j}}} \frac{1}{\Delta x^2} \qquad (4.26)$$

$$e = \frac{1}{K_{xx_{i,j+\frac{1}{2}}}} \frac{1}{\Delta z^2} \qquad (4.27)$$

$$f = \frac{1}{K_{xx_{i,j-\frac{1}{2}}}} \frac{1}{\Delta z^2} \qquad (4.28)$$

$$d = R_a \frac{C_{i+1,j} - C_{i-1,j}}{2\Delta x} \qquad (4.29)$$

4.1.6.2   Solution of the algebraic equations

The set of algebraic equations are solved using a line-by-line iterative method.
Then the solution of the discretized equations for each line may be obtained with the

standard Gauss-elimination procedure for a one-dimensional system, e.g. the TDMA (Tri-Diagonal Matrix Algorithm). Patankar (1980) pointed out that the convergence of the line-by-line method is fast, because the boundary-condition information from each end of the line is transmitted at once to the interior of the domain, no matter how many grid points lie along the line. By alternating the directions in which the TDMA sweep is employed, the influence of all boundaries is rapidly transmitted to the interior.

A Block SOR (Successive Over Relaxation) method (Camarero, 1986) has been used to solve the algebraic equation (4.24). All the nodes in a given column or row are solved implicitly in simultaneous fashion. The algorithm is now described for sweeps executed in either of the two coordinate directions.

SOR implicit by row

The configuration for a typical row relaxation is shown in Fig. 4.2. For example the system described by Eq. (4.24) is written for the unknown points along the row, the neighbouring

$$a \ \psi^-_{i+1,j} - (a+b) \ \psi^-_{i,j} + b \ \psi^-_{i-1,j}$$
$$+ e \ \psi^-_{i,j+1} - (e+f) \ \psi^-_{i,j} + f \ \psi^+_{i,j-1} = d$$

(4.30)

where ψ is the old value, ψ^+ is the corrected value, and ψ^- is the provisional value. An old value is corrected by the provisional value and a relaxation factor, ω, as follows

$$\psi^{+} = \psi + \omega(\psi^{-} - \psi) \tag{4.31}$$

Thus one obtains for the provisional values

$$\psi^{-}_{i,j} = \psi_{i,j} + CF_{i,j}/\omega \tag{4.32}$$

where the correction is defined as

$$CF_{i,j} = \psi^{+}_{i,j} - \psi_{i,j} \tag{4.33}$$

Substituting Eq. (4.32) into Eq. (4.30) one obtains

$$\frac{b}{\omega}CF_{i-1,j} - \frac{a+b+e+f}{\omega}CF_{i,j} + \frac{a}{\omega}CF_{i+1,j} = -RF_{i,j} - fCF_{i,j-1} \tag{4.34}$$

where the residual $RF_{i,j}$ is defined by

$$
\begin{aligned}
Rf_{i,j} = {}& a\psi_{i+1,j} - (a+b)\psi_{i,j} - b\psi_{i-1,j} \\
& + e\psi_{i,j+1} - (e+f)\psi_{i,j} + f\psi_{i,j-1} - d
\end{aligned}
\tag{4.35}
$$

SOR Implicit by column

The configuration for a typical column relaxation is shown in Fig. 4.3. The difference equation is written for every node along a given column yielding:

$$a \ \psi_{i+1,j} - (a+b) \ \psi^-_{i,j} + b \ \psi^+_{i-1,j}$$
$$+ e \ \psi^-_{i,j+1} - (e+f) \ \psi^-_{i,j} + f \ \psi^-_{i,j-1} = d \qquad (4.36)$$

From which as shown previously, the correction equations are obtained

$$\frac{f}{\omega} CF_{i,j-1} - \frac{a+b+e+f}{\omega} CF_{i,j} + \frac{e}{\omega} \ CF_{i,j+1} = - RF_{i,j} - bCF_{i-1,} \qquad (4.37)$$

where the residual $RF_{i,j}$ is defined by

$$Rf_{i,} = a\psi_{i+1,} - (a+b) \psi_{i,} - b\psi_{i-1,}$$
$$+ e\psi_{i,+1} - (e+f) \psi_{i,} + f\psi_{i,-1} - d \qquad (4.38)$$

Eqs.(4.34) (4.37) in conjunction with the boundary conditions may be solved by the standard Gauss-elimination method, for example, using the TDMA (Tri-Diagonal Matrix Algorithm).

4.1.6.3   Discretized transport equation

For the transport equation, the discretized representation is

$$\frac{C_{i,j}^{n+1} - C_{i,j}^{n}}{\Delta \tau} = \frac{D_{xx_{i+\frac{1}{2},j}}}{\Delta x^2} C_{i+1,j}^{n+1} + \frac{D_{xx_{i-\frac{1}{2},j}}}{\Delta x^2} C_{i-1,j}^{n+1}$$

$$+ \frac{D_{zz_{i,j+\frac{1}{2}}}}{\Delta z^2} C_{i,j+1}^{n+1} + \frac{D_{zz_{i,j-\frac{1}{2}}}}{\Delta z^2} C_{i,j-1}^{n+1}$$

$$- \left(\frac{D_{xx_{i+\frac{1}{2},j}} + D_{xx_{i-\frac{1}{2},j}}}{\Delta x^2} + \frac{D_{zz_{i,j+\frac{1}{2}}} + D_{zz_{i,j-\frac{1}{2}}}}{\Delta z^2} \right) C_{i,j}^{n+1}$$

$$+ \frac{D_{xz_{i+1,j}} + D_{xz_{i,j+1}}}{4\Delta x \Delta z} C_{i+1,j+1}^{n+1} - \frac{D_{xz_{i+1,j}} + D_{xz_{i,j-1}}}{4\Delta x \Delta z} C_{i+1,j-1}^{n+1} \qquad (4.39)$$

$$- \frac{D_{xz_{i-1,j}} + D_{xz_{i,j+1}}}{4\Delta x \Delta z} C_{i-1,j+1}^{n+1} + \frac{D_{xz_{i-1,j}} + D_{xz_{i,j-1}}}{4\Delta x \Delta z} C_{i-1,j-1}^{n+1}$$

$$+ \frac{|q_x| + q_x}{2\Delta x} C_{i-1,j}^{n+1} - \frac{|q_x|}{\Delta x} C_{i,j}^{n+1} + \frac{|q_x| - q_x}{2\Delta x} C_{i+1,j}^{n+1}$$

$$+ \frac{|q_z| + q_z}{2\Delta z} C_{i,j-1}^{n+1} - \frac{|q_z|}{\Delta z} C_{i,j}^{n+1} + \frac{|q_z| - q_z}{2\Delta z} C_{i,j+1}^{n+1}$$

To use the line-by-line iteration technique, it is better to cast the discretized equation separately in the i and then the j direction, respectively. Here n+1 has been removed for convenience.

For the i direction

$$a_i C_{i-1,j} + b_i C_{i,j} + e_i C_{i+1,j} = f_i \qquad (4.40)$$

where

$$a_i = - \left(\frac{D_{xx_{i-\frac{1}{2},j}}}{\Delta x^2} + \frac{|q_x| + q_x}{2\Delta x} \right) \qquad (4.41)$$

$$b_i = \frac{1}{\Delta\tau} + \frac{|q_x|}{\Delta x} + \frac{|q_z|}{\Delta z}$$

$$+ \frac{D_{xx_{i+\frac{1}{2},j}} + D_{xx_{i-\frac{1}{2},j}}}{\Delta x^2} + \frac{D_{zz_{i,j+\frac{1}{2}}} + D_{zz_{i,j-\frac{1}{2}}}}{\Delta z^2} \qquad (4.42)$$

$$e_i = -\left(\frac{D_{xx_{i+\frac{1}{2},j}}}{\Delta x^2} + \frac{|q_x| - q_x}{2\Delta x}\right) \qquad (4.43)$$

$$f_i = \frac{C_{i,j}^n}{\Delta\tau} + \frac{D_{zz_{i,j+\frac{1}{2}}}}{\Delta z^2} C_{i,j+1} + \frac{D_{zz_{i,j-\frac{1}{2}}}}{\Delta z^2} C_{i,j-1}$$

$$+ \frac{D_{xz_{i+1,j}} + D_{xz_{i,j+1}}}{4\Delta x\Delta z} C_{i+1,j+1} - \frac{D_{xz_{i+1,j}} + D_{xz_{i,j-1}}}{4\Delta x\Delta z} C_{i+1,j-1}$$

$$- \frac{D_{xz_{i-1,j}} + D_{xz_{i,j+1}}}{4\Delta x\Delta z} C_{i-1,j+1} + \frac{D_{xz_{i-1,j}} + D_{xz_{i,j-1}}}{4\Delta x\Delta z} C_{i-1,j-1} \qquad (4.44)$$

$$+ \frac{|q_z| + q_z}{2\Delta z} C_{i,j-1} + \frac{|q_z| - q_z}{2\Delta z} C_{i,j+1}$$

Similarly, for the j direction

$$a_j C_{i,j-1} + b_j C_{i,j} + e_j C_{i,j+1} = f_j \qquad (4.45)$$

where

$$a_j = -\left(\frac{D_{zz_{i,j-\frac{1}{2}}}}{\Delta z^2} + \frac{|q_z| + q_z}{2\Delta z}\right) \qquad (4.46)$$

$$b_j = \frac{1}{\Delta \tau} + \frac{|q_x|}{\Delta x} + \frac{|q_z|}{\Delta z}$$

$$+ \frac{D_{xx_{i+\frac{1}{2},j}} + D_{xx_{i-\frac{1}{2},j}}}{\Delta x^2} + \frac{D_{zz_{i,j+\frac{1}{2}}} + D_{zz_{i,j-\frac{1}{2}}}}{\Delta z^2}$$

(4.47)

$$e_j = -\left(\frac{D_{zz_{i,j+\frac{1}{2}}}}{\Delta z^2} + \frac{|q_z| - q_z}{2\Delta z} \right)$$

(4.48)

$$f_j = \frac{C_{i,j}^n}{\Delta \tau} + \frac{D_{xx_{i+\frac{1}{2},j}}}{\Delta x^2} C_{i+1,j} + \frac{D_{xx_{i-\frac{1}{2},j}}}{\Delta x^2} C_{i-1,j}$$

$$+ \frac{D_{xz_{i+1,j}} + D_{xz_{i,j+1}}}{4\Delta x \Delta z} C_{i+1,j+1} - \frac{D_{xz_{i+1,j}} + D_{xz_{i,j-1}}}{4\Delta x \Delta z} C_{i+1,j-1}$$

$$- \frac{D_{xz_{i-1,j}} + D_{xz_{i,j+1}}}{4\Delta x \Delta z} C_{i-1,j+1} + \frac{D_{xz_{i-1,j}} + D_{xz_{i,j-1}}}{4\Delta x \Delta z} C_{i-1,j-1}$$

(4.49)

$$+ \frac{|q_x| + q_x}{2\Delta x} C_{i-1,j} + \frac{|q_x| - q_x}{2\Delta x} C_{i+1,j}$$

4.1.6.4 The solution of the algebraic equations

Again, use is made of a line-by-line iterative procedure to solve the algebraic equations. We choose a grid line (say, in the y direction), assume that the C's along the neighbouring lines are known from their "latest" value, and solve the C's along the chosen line using the TDMA. This procedure is followed for all the lines in one direction and then repeated for the lines in the other direction.

4.1.7 Numerical procedure

The numerical solution of the fully coupled governing equations was obtained using the finite difference methods mentioned above. The solution procedure may be summarized by the following sequence and described by the flow chart in Fig. 4.2 :

1. Set initial values of all the variables C and ψ. The initial concentration field is set such that it is equal to zero everywhere except in the middle of the left boundary where there are 4 points set equal to 1; For the stream function field, the linear distribution is set from the top to the bottom boundaries.

2. Compute the Darcy velocity from the stream function field using Eqs.(4.19) and (4.20).

3. These values are then substituted into the transport equation (4.12) in which the advection term has been discretized by a first order upwind scheme. The resulting set of algebraic equations is solved using a line-by-line iteration method. The computation is performed by alternately sweeping in the i and j directions.

4. These concentration values are then input into the flow equation (4.11). The resulting set of algebraic equations is solved using the line-by-line iteration method. The computation is performed by alternately sweeping in the i and j directions.

5. A convergence check is now performed to determine if successive changes in stream function and concentration value are within prescribed tolerances. If the convergence criterion is not met, stages 2 and 3 are repeated using updated values

of concentration and stream function. Subsequent iterations are executed until the prescribed convergence criterion is satisfied or the maximum allowable number of nonlinear iterations is exceeded. If convergence of the nonlinear iterations is obtained, the computation proceeds to the next time level. If the solution fails to converge within the maximum number of iterations, the time step value is halved, and step 1 through 4 are repeated.

The criterion for convergence used was that the maximum relative change in the stream function and concentration satisfy the following inequality:

$$\left| \frac{(\psi_{ij}^{m+1} - \psi_{ij}^{m})}{\psi_{ij}^{m}} \right|_{max} \leq 0.0001 \tag{4.50}$$

$$\left| \frac{\tilde{c}_{ij}^{m+1} - \tilde{c}_{ij}^{m}}{\tilde{c}_{ij}^{m}} \right|_{max} \leq 0.0001 \tag{4.51}$$

Where m is the number of iterations. All computations were performed on a 386 based IBM PS/2 personal computer running at a clock speed of 20 mHZ.

4.2 Finite Volume method with a rectangular mesh

Since the numerical results described in this section are to be compared with the experimental data of Oostrom, a brief description of his experimental setup is given here.

For a detailed description, the reader is referred to the original papers (Oostrom, 1991, 1992).

4.2.1 Experimental apparatus of Oostrom(1992)

Three different flow containers packed with homogeneous porous media simulated an unconfined aquifer. Each flow container has three chambers (Fig. 4.5). During an experiment, the head h_1 and h_2 in the two head chambers were kept constant. An unsaturated zone was allowed to exist near the top of the porous medium in each of the flow containers. The contaminant plumes consisted of NaI and NaBr solutions introduced into each flow container from a line source located on top of the porous medium. By manipulating the water level h_1 and h_2 in the two head chambers, different horizontal discharge rates Q_x and Darcy flux q_x could be established.

Again, the specific objectives of the study described in this section were to obtain the concentration distributions using numerical techniques in order to compare with the experimentally observed data. In the following section, the governing system of equations for the flow regime together with the appropriate boundary conditions are briefly presented. This followed by details of the numerical methods used to solve the relevant governing equations.

4.2.2 Governing equations

The general form of the governing equations for the variable density flow and transport in saturated-unsaturated porous media were presented in Chapter 3. For convenience of the present discussion, we rewrite these governing equations in the following form (excluding sources and sinks):

The Flow Equation

$$\rho \, (S_p + c)\frac{\partial p}{\partial t} + \phi \, S \frac{\partial \rho}{\partial C}\frac{\partial C}{\partial t}$$
$$- \frac{\partial}{\partial x}(\rho \, \frac{k_{ij}}{\mu}\frac{\partial p}{\partial x}) - \frac{\partial}{\partial z}(\rho \, \frac{k_{ij}}{\mu}(\frac{\partial p}{\partial z} + \rho \, g)) = 0 \tag{4.52}$$

Transport Equation

$$\frac{\partial \, \theta \rho \, C}{\partial t} + \frac{\partial}{\partial x_i}(\rho \, q_i C - D_{ij} \cdot \frac{\partial C}{\partial x_j}) = 0 \tag{4.53}$$

the relation between density and concentration is given by

$$\rho = \rho_0(1 + \varepsilon \tilde{C}) \tag{4.54}$$

$$\varepsilon = \frac{\rho_{max} - \rho_0}{\rho_0} \tag{4.55}$$

Introducing $p^* = \dfrac{p}{\rho_0 g}$ and $K_{ij} = \dfrac{k_{ij}\rho_0 g}{\mu}$, Eq.(4.52) becomes

$$S_g \ \rho_0 \frac{\partial p^*}{\partial t} + S_c \ \rho_0 \frac{\partial C}{\partial t}$$

$$-\frac{\partial}{\partial x}(\rho \, K_{ij} \ \frac{\partial p^*}{\partial x}) - \frac{\partial}{\partial z}(\rho \, K_{ij} \ (\frac{\partial p^*}{\partial z} + \frac{\rho}{\rho_0})) = 0 \tag{4.56}$$

where

$$S_g = \rho \, (S_p + c) \, g, \qquad S_c = \phi S \varepsilon \tag{4.57}$$

i and j are space coordinates, q_i the specific discharge in the i direction (LT^{-1}), k_{ij} is the permeability tensor (L^2), μ is the fluid viscosity $(ML^{-1}T^{-1})$, ρ the fluid density (ML^{-3}), p the fluid pressure $(ML^{-1}T^{-2})$, g gravitational acceleration (LT^{-2}), θ the water content (dimensionless), S the saturation (dimensionless), S_p the mass storage (T^2L^{-2}), defined by Eq.(3.12), c the water capacity $(M^{-1}LT^2)$, defined by Eq. (3.15). C solute concentration (M/M), and D_{ij} the dispersion tensor $(ML^{-1}T^{-1})$. ρ_0 a reference freshwater density, ρ_{max} the density corresponding to the maximum concentration, C a dimensionless concentration that varies between zero and unity, For an isotropic porous medium in two dimensions, D_{ij} may be written as

$$D_{ij} = \begin{bmatrix} D_{xx} & D_{xz} \\ D_{zx} & D_{zz} \end{bmatrix} \tag{4.58}$$

$$D_{xx} = \rho(a_L \frac{q_x^2}{\sqrt{q_x^2 + q_z^2}} + a_T \frac{q_x^2}{\sqrt{q_x^2 + q_z^2}} + D_d^*) \tag{4.59}$$

$$D_{zz} = \rho(a_T\frac{q_x^2}{\sqrt{q_x^2+q_z^2}} + a_L\frac{q_z^2}{\sqrt{q_x^2+q_z^2}} + D_d^*) \tag{4.60}$$

$$D_{xz} = D_{zx} = \rho\,((a_L - a_T)\frac{q_x q_z}{\sqrt{q_x^2+q_z^2}}) \tag{4.61}$$

$$q_x = -K_{xx}\frac{\partial p^*}{\partial x} - K_{xz}\,(\frac{\partial p^*}{\partial z} + \frac{\rho}{\rho_0}) \tag{4.62}$$

$$q_z = -K_{xz}\frac{\partial p^*}{\partial x} - K_{zz}\,(\frac{\partial p^*}{\partial z} + \frac{\rho}{\rho_0}) \tag{4.63}$$

where a_L, a_T are respectively longitudinal and transverse dispersivities. D_d^* is the molecular diffusion coefficient.

4.2.3 Dimensionless equations

Introducing the characteristic quantities for pressure, length, conductivity, specific discharge and concentration, Equations (4.52) and (4.53) may also be cast in the following dimensionless form:

$$S_g\,(h_1-h_2)\frac{\partial \tilde{p}}{\partial \tau} + S_c\frac{\partial \tilde{C}}{\partial \tau} - \frac{\partial}{\partial \tilde{x}}\,(\frac{K_{ij}}{K_0}(1+\varepsilon\tilde{C})\frac{\partial \tilde{p}}{\partial \tilde{x}})$$
$$-\frac{\partial}{\partial \tilde{z}}\,(\frac{K_{ij}}{K_0}(1+\varepsilon\tilde{C})\frac{\partial \tilde{p}}{\partial \tilde{z}} + \frac{K_{ij}}{q_0}(1+\varepsilon\tilde{C})^2) = 0 \tag{4.64}$$

$$\frac{\partial \tilde{\rho} \theta \tilde{C}}{\partial \tau} = \frac{\partial}{\partial \tilde{x}} (\tilde{D}_{xx} \frac{\tilde{\partial}}{\partial \tilde{x}} + \tilde{D}_{xz} \frac{\partial \tilde{C}}{\partial \tilde{z}}) + \frac{\partial}{\partial \tilde{z}} (\tilde{D}_{zx} \frac{\partial \tilde{C}}{\partial \tilde{x}} + \tilde{D}_{zz} \frac{\partial \tilde{C}}{\partial \tilde{z}})$$

$$- \frac{\partial \tilde{\rho} \tilde{q}_x \tilde{C}}{\partial \tilde{x}} - \frac{\partial \tilde{\rho} \tilde{q}_z \tilde{C}}{\partial \tilde{z}}$$

(4.65)

where

$$\tilde{x} = \frac{x}{L}, \qquad \tilde{z} = \frac{z}{L}$$

(4.66)

$$\tilde{p} = \frac{p}{\rho_0 g (h_1 - h_2)}, \qquad \tilde{C} = \frac{C}{C_0}, \qquad \tau = \frac{q_0 t}{L},$$

$$K_0 = \frac{k \rho_0 g}{\mu}, \qquad q_0 = K_0 \frac{h_1 - h_2}{L}, \qquad \tilde{\rho} = \frac{\rho}{\rho_0}$$

(4.67)

$$\tilde{D}_{xx} = \tilde{\rho} (\tilde{a}_L \frac{\tilde{q}_x^2}{\sqrt{\tilde{q}_x^2 + \tilde{q}_z^2}} + \tilde{a}_T \frac{\tilde{q}_z^2}{\sqrt{\tilde{q}_x^2 + \tilde{q}_z^2}} + \tilde{D}_d^*)$$

(4.68)

$$\tilde{D}_{zz} = \tilde{\rho} (\tilde{a}_T \frac{\tilde{q}_x^2}{\sqrt{\tilde{q}_x^2 + \tilde{q}_z^2}} + \tilde{a}_L \frac{\tilde{q}_z^2}{\sqrt{\tilde{q}_x^2 + \tilde{q}_z^2}} + \tilde{D}_d^*)$$

(4.69)

$$\tilde{D}_{xz} = \tilde{D}_{zx} = \tilde{\rho} ((\tilde{a}_L - \tilde{a}_T) \frac{\tilde{q}_x \tilde{q}_z}{\sqrt{\tilde{q}_x^2 + \tilde{q}_z^2}})$$

(4.70)

$$\tilde{a}_L = \frac{a_L}{L}, \qquad \tilde{a}_T = \frac{a_T}{L}, \qquad \tilde{D}_d^* = \frac{D_d^*}{L q_0}$$

(4.71)

$$\tilde{q}_x = \frac{q_x}{q_0} = -\frac{K_{xx}}{K_0}\frac{\partial \tilde{p}}{\partial \tilde{x}} - \frac{K_{xz}}{K_0}\frac{\partial \tilde{p}}{\partial z} - \frac{K_{xz}(1+\varepsilon \tilde{C})}{q_0} \qquad (4.72)$$

$$\tilde{q}_z = \frac{q_z}{q_0} = -\frac{K_{xz}}{K_0}\frac{\partial \tilde{p}}{\partial x} - \frac{K_{zz}}{K_0}\frac{\partial \tilde{p}}{\partial \tilde{z}} - \frac{K_{zz}(1+\varepsilon \tilde{C})}{q_0} \qquad (4.73)$$

where, L, K_0, q_0 and C_0 are the characteristic quantities.

4.2.4   Initial and boundary conditions

The initial condition for the pressure may be obtained by solving the steady state flow equation. The initial condition for the concentration is that it is everywhere zero except at the location of the source at the top boundary, where it is equal to unity. The boundary conditions for the flow equation may be imposed as (Reference to Fig. 7.1): the bottom being impervious, the flux through this boundary is zero. Since there is no flux through the left and right boundaries above the water table, zero flux conditions are imposed there. At the top boundary, a zero flux is imposed everywhere except at the source location. A Dirichlet boundary conditions are imposed at the left and right boundaries below the water table, where a static pressure distribution is assumed.

The boundary conditions for the concentration is imposed in a similar fashion. The Dirichlet boundary condition is used for the left and top boundary. Since the bottom boundary is impervious, a Von Neumann boundary condition with $\partial C/\partial z = 0$ is imposed

there. For the right hand side, the condition $\partial C/\partial x = 0$ may be used.

4.2.5   Discretized equations

4.2.5.1   Control volume formulation of the flow equation

The control volume formulation used here closely follows that of Patankar (1980). The calculation domain is divided into a number of non-overlapping control volumes. The differential equation is integrated over each control volume. The result is the discretization equation containing the values for a group of grid points. The variables p and C are the mean values over the control volume, and may be considered as being defined at the centre of each control volume. The discretization equation obtained in this manner expresses the conservation principle.

The flow equation (4.56) can be rewritten as

$$S_g \rho_0 \frac{\partial p}{\partial t} + S_c \rho_0 \frac{\partial C}{\partial t} + \frac{\partial F_x}{\partial x} + \frac{\partial F_z}{\partial z} = 0 \qquad (4.74)$$

where we have removed the * for convenience, F_x and F_z are the mass fluxes defined by

$$F_x = -\rho K_{xx} \frac{\partial p}{\partial x} - \rho K_{xz} \left(\frac{\partial p}{\partial z} + \frac{\rho}{\rho_0} \right) \qquad (4.75)$$

$$F_z = -\rho K_{xz} \frac{\partial p}{\partial x} - \rho K_{zz} \left(\frac{\partial p}{\partial z} + \frac{\rho}{\rho_0} \right) \qquad (4.76)$$

The integration of Eq.(4.74) over the control volume shown in Fig. 4.6 would result in

$$(S_g \ (p - p^o) + S_c \ (C - C^o)) \ \frac{\rho_0 \Delta x \ \Delta z}{\Delta t}$$

$$+ \ F_e \ - F_w \ + \ F_n \ - \ F_s \ = 0 \tag{4.77}$$

where the quantities F_e, F_w, F_n and F_s are the integrated total fluxes over the control volume faces (e, w, n and s denote east, west, north and south); that is F_e stand for $\int F_x dy$ over the interface e, and so on.

Equation (4.77) may be rewritten as

$$\frac{S_g \ (p_P - p_P^o) + S_c \ (C_P - C_P^o)}{\Delta t} \rho_0 \Delta x \Delta z$$

$$= \rho_e K^e_{xx} \frac{p_E - p_P}{\delta x_e} \Delta z + \rho_e K^e_{xz} (\frac{p_1 - p_2}{\Delta z} + \frac{\rho_e}{\rho_0}) \Delta z$$

$$- \rho_w K^w_{xx} \frac{p_P - p_W}{\delta x_w} \Delta z - \rho_w K^w_{xz} (\frac{p_3 - p_4}{\Delta z} + \frac{\rho_w}{\rho_0}) \Delta z \tag{4.78}$$

$$+ \rho_n K^n_{zz} (\frac{p_N - p_P}{\delta z_n} + \frac{\rho_n}{\rho_0}) \Delta x + \rho_n K^n_{xz} \frac{p_1 - p_3}{\Delta x} \Delta x$$

$$- \rho_s K^s_{zz} (\frac{p_P - p_S}{\delta z_s} + \frac{\rho_s}{\rho_o}) \Delta x - \rho_s K^s_{xz} \frac{p_2 - p_4}{\Delta x} \Delta x$$

where p_1, p_2, p_3, p_4 may be obtained by interpolation from the neighbouring nodes. For example

$$p_1 = \frac{1}{4}(p_E + p_P + p_N + p_{NE})$$

$$p_2 = \frac{1}{4}(p_E + p_P + p_S + p_{SE})$$

(4.79)

$$p_3 = \frac{1}{4}(p_W + p_P + p_N + p_{NW})$$

$$p_4 = \frac{1}{4}(p_W + p_P + p_S + p_{SW})$$

The discretization equation can now be written as

$$a_p p_p = a_E p_E + a_W p_W + a_N p_N + a_S p_S + b$$

(4.79)

where

$$a_E = \rho_e \, K^e_{i,j} \, \frac{\Delta z}{\delta x_e}$$

(4.80)

$$a_W = \rho_w \, K^w_{i,j} \, \frac{\Delta z}{\delta x_w}$$

(4.81)

$$a_N = \rho_n \, K^n_{i,j} \, \frac{\Delta x}{\delta z_n}$$

(4.82)

$$a_S = \rho_s \, K^s_{i,j} \, \frac{\Delta x}{\delta z_s}$$

(4.83)

$$a_P^0 = \frac{S_g \, \rho_0 \, \Delta x \, \Delta z}{\Delta t}$$

(4.84)

$$b = a_P^0 p_P^0 - \frac{S_c \rho_0 (C_P - C_P^0)}{\Delta t} \Delta x \Delta z$$

$$+ (\frac{\rho_n K_{zz}^n}{\rho_0} + K_{xz}^n \frac{p_1 - p_3}{\Delta x}) \Delta x \rho_n - (\frac{\rho_s K_{zz}^s}{\rho_0} + K_{xz}^s \frac{p_2 - p_4}{\Delta x}) \Delta x \rho_s \qquad (4.85)$$

$$+ \rho_e K_{xz}^e (\frac{p_1 - p_2}{\Delta z} + \frac{\rho_e}{\rho_0}) \Delta z - \rho_w K_{xz}^w (\frac{p_3 - p_4}{\Delta z} + \frac{\rho_w}{\rho_0}) \Delta z$$

$$a_P = a_E + a_W + a_N + a_S + a_P^o \qquad (4.86)$$

Here p^o and C^o refer to the known values at time t, while all other values (p_P, p_E, p_W, p_N, p_S, and so on) are the unknown values at time $t+\Delta t$. The hydraulic conductivity at the interface, say e, may be calculated by the harmonic mean of K_{ij}^P and K_{ij}^E. The formulation is

$$\frac{1}{K_{ij}^e} = \frac{f_e}{K_{ij}^P} + \frac{1 - f_e}{K_{ij}^E} \qquad (4.87)$$

where the interpolation factor is a ratio defined in terms of the distances shown in

Fig.4.7.

The reason for using the harmonic mean instead of the arithmetic mean is that

$$f_e = \frac{\delta e^+}{\delta e} \qquad (4.88)$$

our main objective is to obtain a good representation for the flux q_e at the interface via

$$q_e = \frac{K^e(p_P - p_E)}{(\delta x)_e} \qquad (4.89)$$

which has, in fact, been used in deriving the discretization equation (4.78). The desired expression for K^e is the one that leads to a "correct" q_e.

Consider that the control volume surrounding the grid points is filled with a porous medium of uniform conductivity K^P, and the one around E with a porous medium of conductivity K^E. For the composite slab between points P and E, a steady one-dimensional analysis (without sources) leads to

$$q_e = \frac{p_P - p_E}{(\delta x)_{e^-}/K^P + (\delta x)_{e^+}/K^E} \qquad (4.90)$$

Combination of Eqs. (4.88)-(4.90) yields Eq. (4.87). It has been found that the harmonic mean (4.87) performs much better than the arithmetic mean formula (Patankar, 1980) for the reason cited above. Similar formulations may be obtained for the interfaces w, n and s.

4.2.5.2 Control volume formulation for the transport equation

For the transport equation, the discretized representation is similar to Eq. (4.78). Eq. (4.53) may be rewritten as

$$\frac{\partial \theta \rho C}{\partial t} + \frac{\partial J_x}{\partial x} + \frac{\partial J_z}{\partial z} = 0 \tag{4.91}$$

where J_x and J_z are the convection and diffusion fluxes defined by

$$J_x = \rho q_x C - D_{xx}\frac{\partial C}{\partial x} - D_{xz}\frac{\partial C}{\partial z} \tag{4.92}$$

$$J_z = \rho q_z C - D_{xz}\frac{\partial C}{\partial x} - D_{zz}\frac{\partial C}{\partial z} \tag{4.93}$$

The integration of Eq.(4.91) over the control volume shown in Fig. 4.6 would give

$$\frac{(\theta_P \rho_P C_P - \theta^o{}_P \rho^o{}_P C^o{}_P)\Delta x \, \Delta z}{\Delta t}$$
$$+ J_e - J_w + J_n - J_s + S_t = 0 \tag{4.94}$$

here

$$J_e = (\rho_e \, q_{x_e} \, C - D_{XX}^e \frac{\partial C}{\partial x}) \, \Delta z$$

$$J_w = (\rho_w \, q_{x_w} \, C - D_{XX}^W \frac{\partial C}{\partial x}) \, \Delta z$$

$$J_n = (\rho_n \, q_{z_n} \, C - D_{ZZ}^n \frac{\partial C}{\partial z}) \, \Delta x$$

$$J_s = (\rho_s \, q_{z_s} \, C - D_{ZZ}^S \frac{\partial C}{\partial z}) \, \Delta x \tag{4.95}$$

$$S_t = -D_{XZ}^e \frac{\partial C}{\partial z} \Delta x + D_{XZ}^W \frac{\partial C}{\partial z} \Delta x$$

$$+ D_{XZ}^n \frac{\partial C}{\partial x} \Delta z + D_{XZ}^s \frac{\partial C}{\partial x} \Delta z$$

We note that the integrated flow equation (4.77) is

$$(\rho_P\theta_P - \rho^o{}_P\theta^o{}_P)\frac{\Delta x \,\Delta z}{\Delta t} + F_e - F_w + F_n - F_s = 0 \tag{4.96}$$

where

$$F_e = \rho_e q_{x_e}\Delta z, \qquad F_w = \rho_w q_{x_w}\Delta z$$
$$F_n = \rho_n q_{z_n}\Delta x, \qquad F_s = \rho_s q_{z_s}\Delta x \tag{4.97}$$

If we now multiply Eq. (4.96) by C_P, and subtract it from Eq. (4.94), we obtain

$$(C_P - C^o{}_P)\frac{\theta^o{}_P\rho^o{}_P\,\Delta x\Delta z}{\Delta t} + S_t$$
$$+ (J_e - F_e C_P) - (J_w - F_w C_P) + (J_n - F_n C_P) - (J_s - F_s C_P) = 0 \tag{4.98}$$

The specific discharge q_x, q_z may be obtained from Eqs.(4.62) and (4.63) at the control volume interfaces. The assumption of uniformity over a control volume face enables the use of one-dimensional formulations. Terms such as J_e-$F_e C_P$ and J_w-$F_w C_P$ may be expressed in the following manner (Patankar, 1980)

$$J_e - F_e C_P = a_E(C_P - C_E)$$
$$J_w - F_w C_P = a_w(C_w - C_P) \tag{4.99}$$

where

$$a_E = D_e A(|P_e|) + [-F_e, 0]$$
$$a_W = D_w A(|P_w|) + [F_w, 0] \tag{4.100}$$

Here [g, h] is defined to denote the greater of g and h, D will be given below. With similar expressions for J_n-$F_n C_P$ and J_s-$F_s C_P$, we are now in a position to write the discretization equation.

The discretization may now be written as

$$a_p C_P = a_E C_E + a_W C_W + a_N C_N + a_S C_S + b \tag{4.101}$$

where

$$
\begin{aligned}
a_E &= D_e\, A(|P_e|) + [-F_e, 0] \\
a_W &= D_W\, A(|P_W|) + [F_W, 0] \\
a_N &= D_N\, A(|P_N|) + [-F_N, 0] \\
a_S &= D_S\, A(|P_S|) + [F_S, 0]
\end{aligned}
\tag{4.102}
$$

$$a_P{}^o = \rho_P{}^o\, \theta_P{}^o\, \frac{\Delta x \Delta z}{\Delta t} \tag{4.103}$$

$$b = a_P{}^o\, C_P{}^o + S_t \tag{4.104}$$

$$a_P = a_E + a_W + a_N + a_S + a_P{}^o \tag{4.105}$$

Here the 'F' have been defined in Eq. (4.97), and the 'D' are defined as

$$D_e = \frac{D_{XX}^e}{\delta x_e}\Delta z, \quad D_w = \frac{D_{XX}^W}{\delta x_w}\Delta z, \quad D_n = \frac{D_{ZZ}^n}{\delta z_n}\Delta x, \quad D_s = \frac{D_{ZZ}^S}{\delta z_s}\Delta x \tag{4.106}$$

The Peclet Number is to be taken as the ratio of F to D, Thus $P_e = F_e / D_e$, and so on.

The different schemes obtained depending on the interpolating function A(|P|), are shown in Table 4.2.

Table 4.2 The function A(|P|) for different schemes

Scheme	Formulae for A(|P|)
Central different	1-0.5 |P|
Upwind	1
Hybrid	[0, 1-0.5 |P|]
Power law	[0, (1-0.1 |P|)^5]
Exponential (exact)	|P| /(exp (|P|)-1)

The Power law scheme due to its (computationally) faster evaluation while being a good approximation to the exponential (exact) scheme has been retained in these simulations.

Term S_t in Equation (4.95) may be obtained by using similar interpolation functions used for deriving p_1, p_2, p_3 and p_4, also the same formulae for calculating the interface conductivity may be used to obtain the coefficients of dispersion at the interfaces.

4.2.5.3   Solution of the algebraic equation

The Gauss-Seidel point-by-point method is employed here to solve the algebraic

equation instead of the line-by-line iterative method, because in the unsaturated zone the

flux boundary condition may not necessarily be imposed along a line. This method

calculates the values of the variable by visiting each grid point in a certain order. In the

beginning, the guessed values were used to compute the steady state solution. Then this

solution becomes the initial values for the transient problem. If the discretization equation

is written as

$$a_P p_P = \sum a_{nb} p_{nb} + b \tag{4.107}$$

where the subscript nb denotes a neighbour point, then p_P at the visited point is calculated

from

$$p_P = \frac{\sum a_{nb} p_{nb}^* + b}{a_P} \tag{4.108}$$

where p_{nb}^* stands for the neighbour-point value present in computer storage. For

neighbours that have already been visited during the current iteration, p_{nb}^* is the freshly

calculated value; for yet-to-be-visited neighbours, p_{nb}^* is the value from the previous

iteration. In any case, p_{nb}^* is the latest available value for the neighbour-point pressure.

When all grid points have been visited in this manner, one iteration of the Gauss-Seidel

method is complete.

4.2.6   Numerical procedure

The numerical solution of the fully coupled governing equations was obtained using the finite volume methods mentioned above. The solution procedure may be summarized by the following sequence and described by the flow chart in Fig. 4.8:

1.   Start with guessed pressure values (may be the hydrostatic pressure distribution).

2.   Calculate the steady state flow solution using the Gauss-Seidel point-by-point method.

3.   Set initial values of the variable C. The initial concentration field is set such that it is equal to zero everywhere except at the source location where the concentration is equal to 1. The solution of the steady state flow equation with zero flux boundary condition will be the initial values for the pressure.

4.   These concentration values are inputs of Eq. (4.54) to calculate the density, and then inputs of the Flow Equation (4.79). The resulting set of algebraic equations is solved using the point-by-point iteration method.

5.   Compute the Darcy velocities from the pressure field using Eqs.(4.62) and (4.63).

6.   These values are then substituted into the Transport Equation (4.91). The resulting set of algebraic equations is solved using the point-by-point iteration method.

7.   A convergence check is now performed to determine if successive changes in pressure and concentration values are within prescribed tolerances. If the convergence criterions are not met, stages 4 and 5 are repeated using updated

values of concentration and pressure. Subsequent iterations are executed until the prescribed convergences criterions are satisfied or the maximum allowable number of nonlinear iterations is exceeded. If convergence of the nonlinear iterations is obtained, the computation proceeds to the next time level. If the solution fails to converge within the maximum number of iterations, the time step value is halved, and step 3 through 6 are repeated.

The criterions for convergence used were that the maximum relative change in the pressure and concentration satisfy the following inequality:

$$\left| \frac{(p_{ij}^{m+1} - p_{ij}^{m})}{p_{ij}^{m}} \right|_{max} \leq 0.0001 \tag{4.109}$$

$$\left| \frac{C_{ij}^{m+1} - C_{ij}^{m}}{C_{ij}^{m}} \right|_{max} \leq 0.0001 \tag{4.110}$$

Where m is the number of iterations.

4.3 A combined Finite Volume and Lagrangian-Eulerian method (Characteristics method) on a Triangular Stencil

The finite volume method was used to obtain numerical solutions to the equations for groundwater flow. The modified characteristic method in conjunction with a finite volume formulation was used to simulate contaminant transport. The finite

volume method ensures global mass conservation while the characteristics method allows the discrete extremum principle for the unsteady problem to be obtained, which plays an important role in preventing parasitic oscillations and negative values of concentration.

4.3.1. Governing equations

The governing equations for contaminant transport in saturated-unsaturated porous media in the absence of sources and sinks were given in section 4.2.2. For convenience we rewrite them as follows where * has been removed.

the Flow Equation

$$
S_g \, \rho_0 \frac{\partial p}{\partial t} + S_c \, \rho_0 \frac{\partial C}{\partial t}
$$
$$
- \frac{\partial}{\partial x}(\rho \, K_{ij} \, \frac{\partial p}{\partial x}) - \frac{\partial}{\partial z}(\rho \, K_{ij} \, (\frac{\partial p}{\partial z} + \frac{\rho}{\rho_0})) = 0
$$

(4.111)

Transport Equation

$$
\frac{\partial \, \theta C}{\partial t} + \frac{\partial}{\partial x_i}(C q_i - D_{ij} \cdot \frac{\partial C}{\partial x_j}) = 0
$$

(4.112)

with the relation between density and concentration being given by

$$
\rho = \rho_0(1 + \varepsilon \tilde{C})
$$

(4.113)

$$
\varepsilon = \frac{\rho_{max} - \rho_0}{\rho_0}
$$

(4.114)

Introducing q_x and q_z, D_{ij} the coefficient of hydrodynamic dispersion may be written as:

$$D_{ij} = \begin{bmatrix} D_{xx} & D_{xz} \\ D_{zx} & D_{zz} \end{bmatrix} \tag{4.115}$$

$$D_{xx} = a_L \frac{q_x^2}{\sqrt{q_x^2 + q_z^2}} + a_T \frac{q_x^2}{\sqrt{q_x^2 + q_z^2}} + D_d^* \tag{4.116}$$

$$D_{zz} = a_T \frac{q_x^2}{\sqrt{q_x^2 + q_z^2}} + a_L \frac{q_z^2}{\sqrt{q_x^2 + q_z^2}} + D_d^* \tag{4.117}$$

$$D_{xz} = D_{zx} = (a_L - a_T) \frac{q_x q_z}{\sqrt{q_x^2 + q_z^2}} \tag{4.118}$$

$$q_x = -K_{xx} \frac{\partial p}{\partial x} - K_{xz} \left(\frac{\partial p}{\partial z} + \frac{\rho}{\rho_0} \right) \tag{4.119}$$

$$q_z = - K_{xz} \frac{\partial p}{\partial x} - K_{zz} \left(\frac{\partial p}{\partial z} + \frac{\rho}{\rho_0} \right) \tag{4.120}$$

where a_L, a_T are respectively longitudinal and transverse dispersivity. D_d^* is the molecular diffusion coefficient.

4.3.2. Domain discretization

The domain of interest is first divided into three-node triangular elements (Baliga and Patankar, 1988). The centroid of the elements are then joined to the midpoints of the

corresponding sides, which creates polygonal control volumes around each node in the calculation domain. A simple domain discretization is shown in Figure 4.9, the solid lines denote the domain and element boundaries, the dashed lines represent the control volume faces, and the shaded areas show the control volumes associated with one internal node and two boundary nodes. In this discretization scheme, curved boundaries are approximated by piecewise-straight lines.

4.3.3. Control volume conservation flow equation

Consider a typical node i in the calculation domain: it could be an internal node, like the one shown in Figure 4.10a, or a boundary node, similar to the ones shown in Figures 4.10b and 4.10c. An integral formulation corresponding to Eq.(4.111) may be arrived at by applying the conservation principle for p to a control volume Ω, that is fixed in space. The resulting integral conservation equation, when applied to the polygonal control volume, surrounding node i in Figure 4.8, can be written as follows:

$$\int_\Omega S_g \, \rho_0 \, \frac{\partial p}{\partial t} \, d\Omega + \int_\Omega S_c \, \rho_0 \, \frac{\partial C}{\partial t} \, d\Omega + \int_a^o J \cdot \vec{n} \, ds + \int_o^c J \cdot \vec{n} \, ds$$

+ [similar contributions from other elements associated with node i]

+ [boundary contributions, if applicable] = 0   (4.121)

where $\vec{n}$ is a unit outward vector normal to the differential area elements ds. o, a, c, represent the centroid of the element, the midpoints of two corresponding sides, respectively, and J is the mass flux through ds

$$J_i = \rho\, q_i = -\rho\, K_{ij}\left(\frac{\partial p}{\partial x_j} + \frac{\rho}{\rho_0}\frac{\partial x_j}{\partial x_j}\right) \tag{4.122}$$

The form of Eq. (4.121) emphasizes that it can be assembled by using an element by element procedure. It should also be noted that the two-dimensional domain being considered in this description are assumed to have unit depth normal to the plane of interest, thus volume and area integrals reduce to area and line integrals, respectively.

4.3.3.1. Interpolation function for p

In each three node triangular elements, the pressure is interpolated linearly:

$$p = Ax + Bz + E \tag{4.123}$$

In each element, the constant A, B and E in this interpolation function can be uniquely determined in terms of the x, z coordinates of the three nodes and the corresponding values of p. Thus with reference to the element 123 shown in Figure 4.11

$$A = [(z_2 - z_1)p_1 + (z_3 - z_1)p_2 + (z_1 - z_2)p_3]/\text{det} \tag{4.124}$$

$$B = [(x_3 - x_2)p_1 + (x_1 - x_3)p_2 + (x_2 - x_1)p_3]/\text{det} \tag{4.125}$$

$$E = [(x_2 z_3 - x_3 z_2)p_1 + (x_3 z_1 + x_1 z_3)p_2 + (x_1 z_2 - x_2 z_1)p_3]/\text{det} \tag{4.126}$$

where

$$\text{det} = (x_1 z_2 + x_2 z_3 + x_3 z_1 - z_1 x_2 - z_2 x_3 - z_3 x_1) \tag{4.127}$$

4.3.3.2 Interpolation function for K_{ij}

In each three node triangular element, the centroidal value of K_{ij} is stored and assumed to prevail over the corresponding element.

$$K_{ij} = \frac{(K_{ij_1} + K_{ij_2} + K_{ij_3})}{3}$$

(4.128)

4.3.3.3 The formulation for the specific discharges

The specific discharges may be obtained from Eqs. (4.119) and (4.120) for each element. The specific discharge for the entire control volume will be the average over this volume.

$$q_x = \int_\Omega q_x d\Omega = \sum_i q_x^{e_i} = \sum_i (-K_{xx} \frac{\partial p}{\partial x} - K_{xz} (\frac{\partial p}{\partial z} + \frac{\rho}{\rho_0}))^{e_i}$$

(4.129)

$$q_z = \int_\Omega q_z d\Omega = \sum_i q_z^{e_i} = \sum_i (-K_{xz} \frac{\partial p}{\partial x} - K_{zz} (\frac{\partial p}{\partial z} + \frac{\rho}{\rho_0}))^{e_i}$$

(4.130)

4.3.3.4. Discretization equations

The discretization equations are obtained by first deriving algebraic approximations to the element contributions in the control volume conservation equations, such as equation (4.121) and then assembling them appropriately. Algebraic

approximations to the boundary contributions, if applicable, are then derived and added to the element contributions.

The following derivations are keyed to node 1 of the element 123 in Figure 4.11. In each element, the mass flux J can be expressed in terms of its components in the x and z directions:

$$J = J_x i + J_z j \tag{4.131}$$

The interpolation function (4.123) is used to approximate J_x and J_y:

$$J_x = -\rho \left(K_{xx} A + K_{xz} (B + \frac{\rho}{\rho_o}) \right) \tag{4.132}$$

$$J_z = -\rho \left(K_{xz} A + K_{zz} (B + \frac{\rho}{\rho_0}) \right) \tag{4.133}$$

The integrals in (4.121) are evaluated approximately by using Simpson's Rule:

$$
\int_a^o J \cdot \vec{n} \, ds = -\frac{(y_a - y_o)}{6} [(J_x)_o + 4(J_x)_r + (J_x)_a] \\
+ \frac{(x_a - x_o)}{6} [(J_z)_o + 4(J_z)_r + (J_z)_a]
\tag{4.134}
$$

$$
\int_o^c J \cdot \vec{n} \, ds = \frac{(y_c - y_o)}{6} [(J_x)_o + 4(J_x)_t + (J_x)_c] \\
- \frac{(x_c - x_o)}{6} [(J_z)_o + 4(J_z)_t + (J_z)_c]
\tag{4.135}
$$

The integral involving the term $\frac{\partial p}{\partial t}$ and $\frac{\partial C}{\partial t}$ is approximated as follows

$$\int_\Omega S_g \rho_0 \frac{\partial p}{\partial t} d\Omega + \int_\Omega S_c \rho_0 \frac{\partial C}{\partial t} d\Omega$$

$$= [\int_{1aoc} S_g \rho_0 d\Omega] \frac{\partial p}{\partial t} + [\int_{1aoc} S_c \rho_0 d\Omega] \frac{\partial C}{\partial t}$$

+ [Similar contributions from other elements associated with node 1] (4.136)

For each element associated with node 1, the Gausian integral rule is used to calculate the integration in Eq. (4.136).

Adding up Eqs. (4.132) - (4.136), the total contribution of element 123 to the conservation equation for node 1 is obtained. This total element contribution can be compactly expressed as follows

$$\int_a^o J \cdot \vec{n} \, ds + \int_o^c J \cdot \vec{n} \, ds + \int_{1aoc} S_g \rho_0 \frac{\partial p}{\partial t} d\Omega$$

$$+ \int_{1aoc} S_c \rho_0 \frac{\partial C}{\partial t} d\Omega = D_1 \ p_1 + D_2 \ p_2 + D_3 \ p_3 + D_4 \tag{4.137}$$

detailed expressions for the constants D_1, D_2, D_3 and D_4 in Eq. (4.137) are given in Appendix B.

4.3.3.5. Discretization equation for internal nodes

Expressions similar to Eq.(4.137) may be derived for the contributions of all elements associated with the internal node i shown in Figure 4.10a, Such expressions,

when substituted into Equation (4.121) yield the complete discretization equation for node i. A general representation of this equation may be cast in the following form

$$c_i \, p_i \; = \; \sum_n c_n \, p_n \, + \, d_i \tag{4.138}$$

where the summation is taken over all the neighbours of node i. Equations similar to Eq.(4.137) may be derived for all internal nodes in the calculation domain.

4.3.3.6   Discretization equation for boundary nodes

For nodes that lie on the boundaries of the calculation domain, the assembly of element contributions is not enough to complete Eq. (4.121). The control volume surfaces associated with boundary nodes have segments that lie along the domain boundaries. The conservation equations for such control volumes become complete only after the fluxes crossing the boundary segments are appropriately added to the corresponding, assembled, element contributions. Information regarding such boundary fluxes can be obtained from the prescribed boundary conditions pertaining to the problem of interest.

4.3.4   Modified characteristics method in conjunction with a finite volume method for the transport equation

Applying Lagrangian or material derivation of C with respect to t to transport equation (4.112), one may rewrite the equation in the following form:

$$\frac{D\,(\theta C)}{Dt} = \nabla \cdot (\theta\,D_{ij} \cdot \nabla C) - \nabla \cdot q_i C \qquad (4.139)$$

Using finite difference to approximate the time derivatives, results in

$$\frac{(\theta C^{n+1}) - (\theta C^{(1)})}{\Delta t} = \nabla \cdot (\theta\,D_{ij} \cdot \nabla C) - \nabla \cdot q_i C \qquad (4.140)$$

Here $C^{(1)}$ is the Lagrangian (convection) concentration which satisfies the following equation:

$$\frac{\partial C^{(1)}}{\partial t} + V \cdot \nabla C^{(1)} = 0 \qquad n\Delta t < t \le (n+1)\Delta t \qquad (4.141)$$

Here $V = q\,/\,\theta$, is the pore velocity.

4.3.4.1   Characteristic method for convective transport

Eq.(4.141) implies that the convection concentration $C^{(1)}$ remains constant along the characteristic curve defined by

$$\frac{\partial x}{\partial t} = u \quad , \qquad \frac{\partial z}{\partial t} = v \qquad (4.142)$$

If $V(u, v)$ is assumed to be constant along the characteristics for $n\Delta t < t \le (n+1)\Delta t$, and $P_i\,(x_i, z_i)$ is a node of the triangle element at $t = (n+1)\,\Delta t$, the foot $P_i'(x_i', z_i')$ of the characteristic curve AB (Figure 4.12) passing through $P_i\,(x_i, z_i)$ is defined by

$$x_i^/ = x_i - u^n(x_i^/, z_i^/)\Delta t$$

$$z_i^/ = z_i - v^n(x_i^/, y_i^/)\Delta t \tag{4.143}$$

and in the element e_i with three nodes (x_α', z_α'), $\alpha = 1,2,3$.

Linear interpolation of $C^{(1)}$ on the grid at time $t = (n+1)\Delta t$ gives:

$$C_i^{(1)} = C(P_i^/, n\Delta t) = \sum_{\alpha=1}^{3} L_\alpha C_\alpha \tag{4.144}$$

where

$$L_1 = \frac{(a_{22}x_i - a_{12}z_i) - f}{d} \tag{4.145}$$

$$L_2 = \frac{(a_{11}z_i - a_{21}x_i) - g}{d} \tag{4.146}$$

$$L_3 = 1 - L_1 - L_2 \tag{4.147}$$

$$a_{11} = x_1^/ - x_3^/ + [u_1(n\Delta t) - u_3(n\Delta t)]\Delta t \tag{4.148}$$

$$a_{12} = x_2^/ - x_3^/ + [u_2(n\Delta t) - u_3(n\Delta t)]\Delta t \tag{4.149}$$

$$a_{21} = z_1^/ - z_3^/ + [v_1(n\Delta t) - v_3(n\Delta t)]\Delta t \tag{4.150}$$

$$a_{22} = z_2^/ - z_3^/ + [v_2(n\Delta t) - v_3(n\Delta t)]\Delta t \tag{4.151}$$

$$b_1 = x_3^/ + u_3(n\Delta t)\Delta t \tag{4.152}$$

$$b_2 = z_3' + v_3(n\Delta t)\Delta t \tag{4.153}$$

$$f = a_{22}\,b_1 - a_{12}\,b_2 \tag{4.154}$$

$$g = a_{11}\,b_2 - a_{21}\,b_1 \tag{4.155}$$

$$d = a_{11}\,a_{22} - a_{12}\,a_{21} \tag{4.156}$$

From the above equations, we have

$$\min C_j^n \leq C_i^{(1)} \leq \max C_j^n \tag{4.157}$$

4.3.4.2   Control volume formulation for transport due to dispersion

Eq.(4.141) is integrated over the control volume Ω in the same fashion as used for the flow equation. The resulting integral equation, surrounding node i in Figure 4.10a, can be written as follows:

$$\int_\Omega \frac{D\,(\theta C)}{Dt}\,d\Omega + \int_a^o J\cdot\bar{n}\,ds + \int_o^c J\cdot\bar{n}\,ds + \int_\Omega \nabla\cdot q C d\Omega$$

+   [similar contributions from other elements associated with node i]

+   [boundary contributions, if applicable] = 0 $\tag{4.158}$

where J is the dispersion flux of C.

$$J = -D_{ij}\cdot\nabla C \tag{4.159}$$

4.3.4.2.1 Interpolation functions for D_{ij}

In each three node triangular element, the centroidal value of D_{ij} is stored and assumed to prevail over the corresponding element.

$$
\begin{aligned}
D_{xx} &= \frac{D_{xx_1} + D_{xx_2} + D_{xx_3}}{3}, \\
D_{xz} &= \frac{D_{xz_1} + D_{xz_2} + D_{xz_3}}{3}, \\
D_{zz} &= \frac{D_{zz_1} + D_{zz_2} + D_{zz_3}}{3}
\end{aligned}
\tag{4.160}
$$

4.3.4.2.2   Interpolation function for C

In each three node triangular element, the concentration is interpolated linearly:

$$ C = Ax + Bz + E \tag{4.161} $$

where the constants A, B and E are

$$ A = [(z_2 - z_1)\, C_1 + (z_3 - z_1)\, C_2 + (z_1 - z_2)\, C_3]/\text{det} \tag{4.162} $$

$$ B = [(x_3 - x_2)\, C_1 + (x_1 - x_3)\, C_2 + (x_2 - x_1)\, C_3]/\text{det} \tag{4.163} $$

$$ E = [(x_2 z_3 - x_3 z_2)\, C_1 + (x_3 z_1 + x_1 z_3)\, C_2 + (x_1 z_2 - x_2 z_1)\, C_3]/\text{det} \tag{4.164} $$

with det given by Eq. (4.127)

4.3.4.2.3   Discretization equation

In each element, the flux J can be expressed in terms of its components in the x and z directions:

$$J = J_x i + J_z j = -(D_{xx}\frac{\partial C}{\partial x} + D_{xz}\frac{\partial C}{\partial z})i - (D_{xz}\frac{\partial C}{\partial x} + D_{zz}\frac{\partial C}{\partial z})j \tag{4.165}$$

where i and j are unit vectors in the x and z directions, respectively.

The interpolation given in Eq. (4.161) is used to approximate J_x and J_z:

$$J_x = -A\,D_{xx} - B\,D_{xz}\,, \qquad J_z = -A\,D_{xz} - B\,D_{zz} \tag{4.166}$$

where A and B are given by Eqs. (4.162) and (4.163), respectively.

Using Eq.(4.166), and with reference to element 123 in Fig. 4.9, the integral in Eq.(4.158) that represents the dispersion transport of C can now be approximated as follows (Baliga, 1980, 1988):

$$\int_a^o J \cdot n \ ds = (A\,D_{xx} + B\,D_{xz})(y_a - y_o) \\ - (A\,D_{xz} + B\,D_{zz})(x_a - x_o) \tag{4.167}$$

$$\int_o^c J \cdot n \ ds = -(A\,D_{xx} + B\,D_{xz})(y_c - y_o) \\ + (A\,D_{xz} + B\,D_{zz})(x_c - x_o) \tag{4.168}$$

The other integral in the equation are approximated as follows:

$$\int_{1aoc} \nabla \cdot q C dv = \frac{A_e}{3} \nabla \cdot q C_1 \qquad (4.169)$$

$$\int_{1aoc} \frac{D(\theta C)}{\partial t} dv = \frac{A_e}{3} \frac{(\theta C_1)^{n+1} - (\theta C_1)^{(1)}}{\Delta t} \qquad (4.170)$$

where A_e is the area of the element 123:

$$A_e = \frac{|det|}{2} \qquad (4.171)$$

with det given by Eq.(4.127).

Substituting Eqs.(4.162) and (4.163) into Eqs.(4.167), and (4.168), and then adding up Eqs. (4.167) -(4.170), the total contribution of element 123 to the conservation equation for the control volume surrounding node 1 is obtained. This total contribution can be expressed compactly in the following form:

$$\int_{\Omega} \frac{D(\theta C)}{Dt} d\Omega + \int_a^o J \cdot \vec{n} ds + \int_o^c J \cdot \vec{n} ds + \int_{\Omega} \nabla \cdot q C d\Omega$$
$$= E_1 C_1 + E_2 C_2 + E_3 C_3 + E_4 \qquad (4.172)$$

Detailed expressions for the constants E_1, E_2, E_3, and E_4 in Eq. (4.172) are given in Appendix C.

Expressions similar to Eq. (4.172) may be derived for the contributions of all elements associated with the internal node i shown in Fig. 4.10. Such expressions, when substituted into Eq.(4.158), yield the complete discretization equation for node i. As

discussed in Section 4.3.3.6, the surfaces of control volumes associated with boundary nodes have segments that lie along domain boundaries. The conservation equation for such control volumes become complete only after the contributions of specified fluxes of C crossing the boundary segments, given in the form of boundary conditions for the problem of interest, are appropriately incorporated into the corresponding assembled element contributions.

The discretization equations for the flow equation and for the dispersion transport equation are solved by the Gauss-Seidel point-by-point iterative method which has been discussed in Section 4.2.2 .

4.3.5 Numerical considerations

The numerical solution of the fully coupled governing equations was accomplished using the finite volume methods combined with the modified characteristic method discussed above. The solution procedure may be summarized by the following sequence and described by the flow chart in Figure 4.13:

1.   Start with guessed pressure values (may be the hydrostatic distribution).

2.   Calculate the steady state flow solution using the Gauss-Seidel point-by-point method.

3.   Set initial values of the variable C. The solution of the steady state flow equation

with zero flux boundary conditions will be the initial pressure for the transient problem.

4. These concentration values are then inputs of the flow equation (4.139). The resulting set of algebraic equations is solved using the Gauss-Seidel point-by-point iteration method.

5. Compute the Darcy velocities from the total head field using Eqs.(4.130) and (4.131).

6. These values are then used to compute the convection contributed part of the concentration, followed by the calculation of the dispersion contribution using the Gauss-Seidel point-by-point iteration method.

7. A convergence check is now performed to determine if successive changes in pressure and concentration values are within prescribed tolerances. If the convergence criterions are not met, stages 4 and 5 are repeated using updated values of concentration and stream functions. Subsequent iterations are executed until the prescribed convergence criterions are satisfied or the maximum allowable number of nonlinear iterations is exceeded. If convergence of the nonlinear iterations is obtained, the computation proceeds to the next time level. If the solution fails to converge within the maximum number of iterations, the time step value is halved, and steps 3 through 6 are repeated.

The criterions for convergence used were that the maximum relative change in the stream function and concentration satisfy the following inequality:

$$\left| \frac{(p_{ij}^{m+1} - p_{ij}^{m})}{p_{ij}^{m}} \right|_{max} \leq 0.0001 \qquad\qquad (4.173)$$

$$\left| \frac{C_{ij}^{m+1} - C_{ij}^{m}}{C_{ij}^{m}} \right|_{max} \leq 0.0001 \qquad\qquad (4.174)$$

Where m is the number of iterations.

The finite volume model was tested by simulating the laboratory experiments of Oostrom (1992) and the Borden landfill site. The results of these comparisons will be presented in Chapter 8. It is useful to indicate here, that if all the angles of the triangles are acute, a discrete extremum principle for the unsteady problem, (which plays an important role in preventing parasitic oscillations and negative values of concentration in the numerical simulation) may be obtained.

CHAPTER 5

COMPARISON BETWEEN THE NUMERICAL SIMULATIONS

AND THE EXPERIMENTAL RESULTS OF SCHINCARIOL AND SCHWARTZ

The numerical model for simulating the experimental results of Schincariol and Schwartz has been detailed in Chapter 4. This chapter is devoted to presenting the details of the boundary conditions and parameters used in the simulation.

A flow tank is filled with saturated porous media. A dense Sodium Chloride (NaCl) solution is introduced through a slot in the middle of the tank. Figure 5.1 represents the computational domain and the associated boundary conditions. For the impervious boundaries AB and CD, an appropriate Dirichlet boundary condition is imposed:

$$\tilde{\psi} = \psi_1 \quad on \quad AB$$
$$\tilde{\psi} = \psi_2 \quad on \quad CD$$

(5.1)

For sides AD and BC, the flow is supposed uniform, the boundary condition may then be expressed as:

$$\tilde{\psi} = \psi_1 + (\psi_2 - \psi_1)\,\tilde{z} \quad on \quad AD$$
$$\frac{\partial \tilde{\psi}}{\partial \tilde{x}} = 0 \quad on \quad BC$$

(5.2)

The boundary condition for the concentration is imposed in a similar fashion. The Dirichlet boundary condition is used for side AD. AB and DC being impervious, Von Neumann boundary conditions $\partial C/\partial z = 0$ are imposed there. For the side BC, the condition $\partial C/\partial x = 0$ may be used.

5.1   Results for homogeneous media

According to the experiments of Schincariol and Schwartz (1990), conducted with the homogenous medium, the relevant parameters were estimated as follows:

$$K_0 = K_x = K_z = 5.6 \times 10^{-2} \text{ cm/s}$$

$$q_0 = (1.16 / 5) \times 10^{-4} \text{ cm/s}$$

$$L = 70 \text{ cm}$$

$$\phi = 0.38$$

$$\alpha_L = 0.310 \text{ cm}$$

$$\alpha_T = 0.0217 \text{ cm}$$

$$\rho_0 = 0.9983 \text{ g/cm}^3$$

The flow field and plume dispersion were simulated for a 2000 mg/L , a 5000 mg/L and a 10,000 mg/L NaCl source in a homogeneous medium.

As expected, for the homogeneous medium, the tendency for the plume to sink increases as its density increases. As observed by Schincariol and Schwartz (1990) in the

laboratory, gravitational instabilities are manifested by lobe shaped protuberances that form first along the bottom edge of the plume and later penetrate into the plume. Figures 5.2, 5.3 and 5.4 are the numerical simulations, which indicate the development of the instability over time for a 2000 mg/L, 5000 mg/L, and 10,000 mg/L NaCl source, respectively. Figure 5.5 is a comparison between the experimental results and the numerical ones for a 5000 mg/L source in the homogenous medium (Fan and Kahawita, 1994). The numerical simulation appears to match the experimental observations fairly well, the time at which the instabilities begin to develop being almost the same as the experiments would suggest. The amplitude behaviour of the instabilities are smaller than those noted in the experiments. This may have been caused by local variations in the experimental conditions but is more likely due to errors in the estimation of the relevant parameters used in the simulation.

The denser plumes with initial concentration of 25,000 and 100,000 mg/L exhibited a different behaviour from that just described. Figures 5.6 and 5.7 are the numerical simulations, which show the development of the plume over time for the 25,000 mg/L and 100,000 mg/L NaCl source, respectively. These solutions were so dense that they quickly sank to the bottom of the chamber. This behavior is consistent with what was observed in the experiments.

5.2   Results for heterogeneous media

In this part of the study, the simulation was restricted to the flow field occurring in the layered medium. In the laboratory experiments, each layer was composed of a porous medium having a distinct conductivity and mean particle diameter. This required different hydraulic conductivities and longitudinal dispersivities to be specified for different layers in the numerical simulation. The transverse dispersivity was chosen to be 10 times less than the longitudinal dispersivity. The different values for conductivity and longitudinal dispersivity used in the simulation are summarized here:

$$K_1 = 3.0 \times 10^{-1} \text{ cm/s}, \qquad \alpha_L = 0.065 \text{ cm}$$

$$K_2 = 5.6 \times 10^{-2} \text{ cm/s}, \qquad \alpha_L = 0.0310 \text{ cm}$$

$$K_3 = 2.2 \times 10^{-2} \text{ cm/s}, \qquad \alpha_L = 0.0210 \text{ cm}$$

$$K_4 = 1.2 \times 10^{-2} \text{ cm/s}, \qquad \alpha_L = 0.0150 \text{ cm}$$

$$K_5 = 1.9 \times 10^{-3} \text{ cm/sec}, \qquad \alpha_L = 0.0085 \text{ cm}$$

Other parameters used were:

$$L = 70 \text{ cm}$$

$$\phi = 0.38$$

The specific discharge q_0 to be used, was estimated according to the average linear velocity in each layer. This resulted in a value for

$$q_0 = 1.6325 \times 10^{-4} \text{ cm/s}$$

which appears to be slightly larger than the average specific discharge used in the laboratory experiment, where the value was 1.38×10^{-4} cm/s.

Figure 5.8 and 5.9 indicate the development of the instability over time for a 5000 mg/L and 10,000 mg/L NaCl source. Figure 5.10 and 5.11 represent a comparison between the experimental results and numerical simulations (Fan and Kahawita, 1994). The results obtained from both the experiments and the numerical simulation showed that the interface between layers acted as a sort of barrier for the denser flow.

The overall comparison between the laboratory experiments of Schincariol and Schwartz (1990), and the present numerical simulations appear to be satisfactory. Again, the times at which the instabilities along the lower edge of the plume manifest themselves are comparable. The discrepancies in the amplitude of the instabilities as well as in the characteristic length scales of the plume may be attributed to the uncertainties in the estimation of the relevant parameters and also in the lack of precision in the experimental data. It bears repeating here, that the resolution of the concentration values in the laboratory experiments was comparatively poor so that direct comparison was difficult. However, a rather consistent behaviour in the numerical simulations when compared to experiment is the slightly lower rate of growth of the top surface of the plume indicating that some adjustments to the transverse dispersivities may be needed.

In order to provide some insight into the conditions that govern the stability of a dense plume injected into the middle of a horizontal flow, a simplified linear stability analysis of the flow was undertaken in which the disturbances were assumed to be three dimensional. This stability analysis will be presented in Chapter 6.

CHAPTER 6

STABILITY ANALYSIS

6.1   Theoretical development

Consider a dense layer of fluid in a homogeneous porous medium that is bounded above and below by a lighter fluid environment. The stability of this layer is to be investigated with respect to three dimensional disturbances that are assumed to be small. The governing linearized equations for the perturbations C', h', u', v', w' which are respectively the concentration, pressure and the three components of velocities may be written as:

$$\frac{\partial C'}{\partial t} + w' \frac{\partial C_0}{\partial z} = D\left(\frac{\partial^2 C'}{\partial x^2} + \frac{\partial^2 C'}{\partial y^2} + \frac{\partial^2 C'}{\partial z^2}\right) \tag{6.1}$$

$$\frac{\partial u'}{\partial x} + \frac{\partial v'}{\partial y} + \frac{\partial w'}{\partial z} = 0 \tag{6.2}$$

$$u' = -K \frac{\partial (p'/\rho_0 g)}{\partial x} \tag{6.3}$$

$$v' = -K \frac{\partial (p'/\rho_0 g)}{\partial y} \tag{6.4}$$

$$w' = -K\left(\frac{\partial (p'/\rho_0 g)}{\partial z} + 1 + \varepsilon C'\right) \tag{6.5}$$

where $C_0 = C_0$ (z) is the base concentration distribution, which is a function of z only. D is the coefficient of molecular diffusion. $\varepsilon = (\rho_{max} - \rho_{min})/ \rho_{min}$, where ρ_{max}, ρ_{min} are the densities corresponding to the maximum and minimum concentrations, respectively.

In keeping of the standard hydrodynamic stability theory, an arbitrary disturbance may be decomposed into periodic components in the longitudinal and lateral directions. It is therefore assumed that the perturbations C', p', u', v', w' have the form:

$$u' = u_p(z)\exp(i(k_x x + k_y y) + qt) \tag{6.6}$$

$$v' = v_p(z)\exp(i(k_x x + k_y y) + qt) \tag{6.7}$$

$$w' = w_p(z)\exp(i(k_x x + k_y y) + qt) \tag{6.8}$$

$$p' = p_p(z)\exp(i(k_x x + k_y y) + qt) \tag{6.9}$$

$$C' = C_p(z)\exp(i(k_x x + k_y y) + qt) \tag{6.10}$$

where k_x and k_y are the wavenumbers in the longitudinal and lateral directions respectively and q is a time amplification factor.

Since only neutral disturbances are of interest here, i.e. disturbances that are neither amplified nor attenuated with time (critical stability), we substitute the above perturbations into Eq.(6.1)-(6.5) with q=0. First, substitute Eqs. (6.8),(6.10) into Eq.(6.1), results

$$w_p \frac{dC_0}{dz} = D(\frac{d^2C_p}{dz^2} - C_p(k_x^2 + k_y^2)) \tag{6.11}$$

Then eliminating $p_p(z)$ from Eqs. (6.3), (6.4) and (6.5) by cross differentiation, we obtain

$$\frac{\partial u'}{\partial y} - \frac{\partial v'}{\partial x} = 0 \tag{6.12}$$

$$\frac{\partial v'}{\partial z} - \frac{\partial w'}{\partial y} = K\varepsilon \frac{\partial C'}{\partial y} \tag{6.13}$$

Substituting Eqs. (6.6), (6.7), (6.8), (6.10) into Eqs. (6.2), (6.12) and (6.13), results in:

$$u_p ik_x + v_p ik_y + \frac{dw_p}{dz} = 0 \tag{6.14}$$

$$u_p ik_y - v_p ik_x = 0 \tag{6.15}$$

$$\frac{dv_p}{dz} - w_p ik_y = K\varepsilon C_p ik_y \tag{6.16}$$

Eliminating $u_p(z)$ and $v_p(z)$ from Eqs (6.14), (6.15) and (6.16), results in

$$\frac{d^2w_p}{dz^2} - (k_x^2 + k_y^2) w_p = K\varepsilon (k_x^2 + k_y^2) C_p \tag{6.17}$$

Equations (6.11) and (6.17) together constitute the following system of differential equations:

$$(\frac{d^2}{dz^2} - \alpha^2) w_p = K\alpha^2 \varepsilon C_p \tag{6.18}$$

$$(\frac{d^2}{dz^2} - \alpha^2) C_p = \frac{dC_0}{dz} \frac{W_p}{D} \tag{6.19}$$

where $a^2 = k_x^2 + k_y^2$, $d = d/dz'$.

Eliminating C_p, results in:

$$(\frac{d^4 w_p}{dz^4} - \alpha^2 \frac{d^2 w_p}{dz^2}) - \alpha^2 (\frac{d^2 w_p}{dz^2} - \alpha^2 w_p) = \frac{dC_0}{dz} \frac{w_p}{D} K\varepsilon\alpha^2 \qquad (6.20)$$

Defining dimensionless quantities $\Phi = L\alpha$, $w = w_p (L/D)$, $R = (K\varepsilon L)/D$, $C_0 = C_0/(C_{max} - C_{min})$, $z' = z/L$, the final dimensionless form of the differential equation for the perturbation w, viz.,

$$(\frac{d^2}{dz'^2} - \phi^2)^2 w = \phi^2 R_a \frac{dC_0}{dz'} w \qquad (6.21)$$

Here $R_a = (K\varepsilon L)/D$ may be interpreted as a concentration Rayleigh number.

The boundary conditions assumed for Eq. (6.21) are of the fixed type both above and below the liquid layer. All perturbations are then specified to vanish at these boundaries. This results in the following conditions for w:

$$w = \frac{\partial w}{\partial z'} = 0 \qquad (6.22)$$

Equation (6.21) together with (6.22) is a homogeneous system with homogeneous boundary conditions and therefore constitutes an eigenvalue problem. Equation (6.21) was solved approximately by expanding the eigenfunction in a Fourier series as indicated in Equation (6.23) with the requirement that it satisfies the boundary conditions (Eq.(6.22)) at z'=1 and z'=-1.

$$w = \frac{a_0}{2} + \sum_{n=1}^{\infty} (a_n \cos n\pi z' + b_n \sin n\pi z') \tag{6.23}$$

On the basis of what could be expected as being physically a realistic behaviour, the concentration profile C_0 was assumed to follow a Gaussian distribution:

$$C_0 = e^{-\frac{z^2}{(2c^2)}} \tag{6.24}$$

where $c = \sigma/L$, σ being the standard deviation of the Gaussian distribution. c may be interpreted as being a sort of concentration length scale.

Substituting these expressions into the differential equation with the relevant boundary conditions, we obtain

$$\frac{a_0}{2}\phi^4 + \sum_{n=1}^{\infty} ((n\pi)^2 + \phi^2)^2 (a_n \cos n\pi z' + b_n \sin n\pi z')$$

$$= \phi^2 R_a \frac{dC_0}{dz'} (\frac{a_0}{2} + \sum_{n=1}^{\infty} (a_n \cos n\pi z' + b_n \sin n\pi z')) \tag{6.25}$$

When Eq. (6.25) is multiplied by cos $m\pi z'$, sin $m\pi z'$, respectively, then integrated from z'=-1 to z'=1, the system of equations for evaluating the Fourier coefficients are obtained. For numerical computations, the infinite series expansion in Eq.(6.25) has to be truncated to a finite number, say N. Thus, we have the following equations:

Multiplying by cos mπz' and then integrating z' from -1 to 1:

for m=0,

$$a_0 = \frac{\phi^2 R_a}{2\lambda_0^2} \int_{-1}^{1} \frac{dC_0}{dz'} \, dz' \, a_0$$

$$+ \frac{\phi^2 R_a}{\lambda_0^2} (\int_{-1}^{1} \frac{dC_0}{dz'} \cos\pi z' dz' \, a_1$$

$$+ \int_{-1}^{1} \frac{dC_0}{dz'} \cos 2\pi z' dz' \, a_2 + \cdots \qquad (6.26)$$

$$+ \int_{-1}^{1} \frac{dC_0}{dz'} \sin\pi z' dz' \, b_1$$

$$+ \int_{-1}^{1} \frac{dC_0}{dz'} \sin 2\pi z' dz' \, b_2 + \cdots)$$

for m=1,

$$a_0 = \frac{\phi^2 R_a}{2\lambda_1^2} \int_{-1}^{1} \frac{dC_0}{dz'} \cos\pi z' dz' \, a_0$$

$$+ \frac{\phi^2 R_a}{\lambda_1^2} (\int_{-1}^{1} \frac{dC_0}{dz'} \cos\pi z' \cos\pi z' dz' \, a_1$$

$$+ \int_{-1}^{1} \frac{dC_0}{dz'} \cos\pi z' \cos 2\pi z' dz' \, a_2 + \cdots \qquad (6.27)$$

$$+ \int_{-1}^{1} \frac{dC_0}{dz'} \cos\pi z' \sin\pi z' dz' \, b_1$$

$$+ \int_{-1}^{1} \frac{dC_0}{dz'} \cos\pi z' \sin 2\pi z' dz' \, b_2 + \cdots)$$

Generally, for m=N

$$a_0 = \frac{\phi^2 R_a}{2\lambda_N^2} \int_{-1}^{1} \frac{dC_0}{dz'} \cos N\pi z' dz' \ a_0$$

$$+ \frac{\phi^2 R_a}{\lambda_N^2} (\int_{-1}^{1} \frac{dC_0}{dz'} \cos N\pi z' \cos \pi z' dz' \ a_1$$

$$+ \int_{-1}^{1} \frac{dC_0}{dz'} \cos N\pi z' \cos 2\pi z' dz' \ a_2 + \cdots \qquad (6.28)$$

$$+ \int_{-1}^{1} \frac{dC_0}{dz'} \cos N\pi z' \sin \pi z' dz' \ b_1$$

$$+ \int_{-1}^{1} \frac{dC_0}{dz'} \cos N\pi z' \sin 2\pi z' dz' \ b_2 + \cdots)$$

Multiply by sin mπz', then integrate z' from -1 to 1:

for m=1,

$$b_1 = \frac{\phi^2 R_a}{2\lambda_1^2} \int_{-1}^{1} \frac{dC_0}{dz'} \sin \pi z' dz' \ a_0$$

$$+ \frac{\phi^2 R_a}{\lambda_1^2} (\int_{-1}^{1} \frac{dC_0}{dz'} \sin \pi z' \cos \pi z' dz' \ a_1$$

$$+ \int_{-1}^{1} \frac{dC_0}{dz'} \sin \pi z' \cos 2\pi z' dz' \ a_2 + \cdots \qquad (6.29)$$

$$+ \int_{-1}^{1} \frac{dC_0}{dz'} \sin \pi z' \sin \pi z' dz' \ b_1$$

$$+ \int_{-1}^{1} \frac{dC_0}{dz'} \sin \pi z' \sin 2\pi z' dz' \ b_2 + \cdots)$$

for m=N,

$$b_N = \frac{\phi^2 R_a}{2\lambda_N^2} \int\limits_{-1}^{1} \frac{dC_0}{dz'} \sin N\pi z' dz' \; a_0$$

$$+ \frac{\phi^2 R_a}{\lambda_N^2} (\int\limits_{-1}^{1} \frac{dC_0}{dz'} \sin N\pi z' \cos \pi z' dz' \; a_1$$

$$+ \int\limits_{-1}^{1} \frac{dC_0}{dz'} \sin N\pi z' \cos 2\pi z' dz' \; a_2 + \cdots \tag{6.30}$$

$$+ \int\limits_{-1}^{1} \frac{dC_0}{dz'} \sin N\pi z' \sin \pi z' dz' \; b_1$$

$$+ \int\limits_{-1}^{1} \frac{dC_0}{dz'} \sin N\pi z' \sin 2\pi z' dz' \; b_2 + \cdots)$$

here

$$\lambda_n = (n\pi)^2 + \phi^2, \qquad 0 \le n \le N \tag{6.31}$$

The boundary condition (6.22) gives:

$$\frac{a_0}{2} - a_1 + a_2 - a_3 + \cdots + (-1)^N a_N = 0 \tag{6.32}$$

and

$$-\pi b_1 + 2\pi b_2 + 3\pi b_3 + \cdots + (-1)^N \pi \; b_N = 0 \tag{6.33}$$

Eqs. (6.26)-(6.33) may be written in matrix notation as:

$$[A] = \phi^2 R_a [S][A] \tag{6.34}$$

The equation of neutral stability is then:

$$| \delta_{nm} - \phi^2 R_a S_{nm} | = 0 \qquad 0 \le n \le 2N+1 \tag{6.35}$$

where

$$[S] = \begin{bmatrix} S_1 & S_2 \\ S_3 & S_4 \end{bmatrix} \tag{6.36}$$

$$[S_1] = \begin{bmatrix} X_{00} & X_{01} & X_{02} & \cdots & X_{0N} \\ X_{10} & X_{11} & X_{12} & \cdots & X_{1N} \\ & & \cdot & & \\ & & \cdot & & \\ & & \cdot & & \\ X_{N-1,0} & X_{N-1,1} & X_{N-1,3} & \cdots & X_{N-1,N} \end{bmatrix} \tag{6.37}$$

$$[S_2] = \begin{bmatrix} Y_{01} & Y_{02} & Y_{03} & \cdots & Y_{0N} \\ Y_{11} & Y_{12} & Y_{13} & \cdots & Y_{1N} \\ & & \cdot & & \\ & & \cdot & & \\ & & \cdot & & \\ Y_{N-1,1} & Y_{N-1,2} & Y_{N-1,3} & \cdots & Y_{N-1,N} \end{bmatrix} \tag{6.38}$$

$$[S_3] = \begin{bmatrix} Y_{10}^* & Y_{11}^* & Y_{12}^* & \cdots & Y_{1N}^* \\ Y_{20}^* & Y_{21}^* & Y_{22}^* & \cdots & Y_{2N}^* \\ & & \cdot & & \\ & & \cdot & & \\ & & \cdot & & \\ Y_{N-1,0}^* & Y_{N-1,1}^* & Y_{N-1,2}^* & \cdots & Y_{N-1,N}^* \\ \frac{1}{2} & -1 & 1 & \cdots & (-1)^n \\ 0 & 0 & 0 & \cdots & 0 \end{bmatrix} \tag{6.39}$$

$$[S_4] = \begin{bmatrix} Z_{11} & Z_{12} & Z_{13} & \cdots & Z_{1N} \\ Z_{21} & Z_{22} & Z_{3} & \cdots & Z_{2N} \\ & & \cdot & & \\ & & \cdot & & \\ & & \cdot & & \\ Z_{N-1,1} & Z_{N-1,2} & Z_{N-1,3} & \cdots & Z_{N-1,N} \\ 0 & 0 & 0 & \cdots & 0 \\ -\pi & 2\pi & -3\pi & \cdots & (-1)^n n\pi \end{bmatrix}$$

(6.40)

$$X_{nm} = \frac{1}{\lambda_n^2} \int_{-1}^{1} \frac{dC_0}{dz'} \cos n\pi z' \cos m\pi z' \, dz',$$

(6.41)

$$0 \le n \le N-1, \quad 1 \le m \le N$$

$$Y_{nm} = \frac{1}{\lambda_n^2} \int_{-1}^{1} \frac{dC_0}{dz'} \cos n\pi z' \sin m\pi z' \, dz',$$

(6.42)

$$0 \le n \le N-1, \quad 1 \le m \le N$$

$$Y_{nm}^* = \frac{1}{\lambda_n^2} \int_{-1}^{1} \frac{dC_0}{dz'} \sin n\pi z' \cos m\pi z' \, dz,$$

(6.43)

$$1 \le n \le N-1, \quad 1 \le m \le N$$

$$Z_{nm} = \frac{1}{\lambda_n^2} \int_{-1}^{1} \frac{dC_0}{dz'} \sin n\pi z' \sin m\pi z' \, dz',$$

(6.44)

$$1 \le n \le N-1, 1 \le m \le N$$

$$X_{n0} = \frac{1}{2\lambda_n^2} \int_{-1}^{1} \frac{dC_0}{dz'} \cos n\pi z' \, dz', \qquad 0 \le n \le N-1$$

(6.45)

$$Y_{n0}^{*} = \frac{1}{2\lambda_{n}^{*}} \int_{-1}^{1} \frac{dC_0}{dz'} \sin n\pi z' \ dz', \qquad 1 \leq n \leq N-1 \tag{6.46}$$

The infinite series expansion in Eq.(6.23) was truncated to between sixty and one hundred terms (N was between 60 to 100) depending on the concentration length scale c. Various checks on the precision of the computations were performed chiefly by increasing the number of terms in the series. This revealed that the calculations were of sufficient accuracy.

6.2   Results and discussion

A complete neutral stability curve is obtained by varying Φ and finding the corresponding eigenvalue R_a (the concentration Rayleigh Number) for a given value of the concentration length scale c. Treating c as a parameter allows different neutral stability curves to be traced. Figure 6.1 indicates the neutral stability curves obtained by plotting R_a vs. Φ for c = 0.1, 0.3, and 0.5. Figure 6.2 continues the neutral stability curves for c = 0.1, 0.05, 0.03 and 0.02.

It is interesting to note that as c is reduced from 0.5 to 0.1, the neutral stability curves in Fig.6.1 indicate that the flow becomes less stable. Figure 6.2 demonstrates however that a further reduction in c for example from 0.1 to 0.02, leads to the opposite effect. This behaviour has been clarified in the plot of minimum R_a vs. c presented in

Fig.6.3.

The results of the stability analysis indicate that contrary to what might normally be expected, the shape of the mean profile plays an important role in governing the stability of the plume. This "shape" effect has also been noted in studies of pure Bénard convection by Sparrow et al. (1964). The concentration Rayleigh number R_a still reflects on the basic stability of the plume. The role of the parameter c however, is to modify this behaviour as a function of the plume width. A very small value of c implies a narrow dense plume that would simply tend to descend rapidly due to its negative buoyancy, without any manifestation of gravitational instabilities. Furthermore, if the plume descends vertically, the further complication of the gravity vector now being parallel to the plume axis means that the only possibility of any instability developing is along the plume front. This is not generally observed, due probably to the local modification to the flow field in the form of relatively strong vertical currents. Very large values of c would imply a plume that is so wide that even locally, vertical density gradients are small resulting again in a stable plume. It is now possible to assume the following behaviour.

As the plume is discharged, its density is high but its width is narrow, causing it to descend at a rapid rate. During this period its width grows by entrainment of the ambient until at some point, a critical combination of the parameter c and the concentration Rayleigh number is reached. Gravitational instability is initiated which

becomes visible at some further distance downstream. Figures 6.4 and 6.5 present some typical instantaneous concentration profiles computed at different downstream cross-sections for the experiment of Schincariol and Schwartz. The profile at the cross-section near the point of entry of the plume may be approximated as a Gaussian distribution with c = 0.02. From the experiments of Schincariol and Schwartz (1990), it is possible to estimate the concentration Rayleigh number R_a for each NaCl source with L = 70 cm, K = 0.056 cm/sec and D = 3 $\times$ 10^{-5}. The results are presented in Table 6.1. From the results of the stability analysis, for c=0.02, the minimum R_a is about 121. Reference to Table 6.1 indicates that only for the source concentration of 1000 mg/L, is R_a less than 121. Thus gravitational instability will not occur for this value of the source concentration while for the other concentrations the stability limit will be exceeded. These predictions correspond fairly well with the experimental observations of Schincariol and Schwartz (1990).

Table 6.1 Concentration Rayleigh Number for Each NaCl Source

NaCl Concentration (mg/l)	$(\rho_{max} - \rho_0)/\rho_0$	R_a
1000	0.00070	91
2000	0.00140	182
5000	0.00361	471
10000	0.00701	915

It appears therefore, that the transverse dispersivity plays a dual role in governing

the stability of the plume. On one hand, for plumes with relatively high initial concentrations, it would increase the spread rate of the plume, driving it to the critical stability point, while on the other hand, plumes with low initial concentrations will be rapidly diluted to the point that the mean vertical density gradients will be too low to amplify small perturbations. The plume will therefore behave stably. In order to investigate the validity of this hypothesis, numerical experiments were conducted in which for a given initial concentration, the plume was allowed to develop in the streamwise direction with different values of the transverse dispersivity. The results indicated that if the transverse dispersivity was set too low, the plume remained narrow and stable. (Presumably at some distance downstream, the spread will be sufficient to cause gravitational instabilities to appear). If the transverse dispersivity value was too high, the plume spread rapidly and again remained stable. It was only at some intermediate values between these two extremes, that the characteristic lobe shaped protuberances appeared. These results tend to broadly confirm the hypothesis described earlier.

CHAPTER 7

COMPARISON OF THE NUMERICAL SIMULATIONS

WITH THE EXPERIMENTS RESULTS OF OOSTROM

In this chapter, the migration of a dense contaminant leachate plume in an unconfined aquifer will be examined. Some numerical simulations will be compared with the experimental results of Oostrom. Chapter 8 will be devoted to the simulation of the contaminant transport in the Borden, Ontario landfill as a full scale case study.

The numerical model used to simulate the experiments of Oostrom (1991, 1992) was presented and discussed in Chapter 4. In this chapter, we will discuss the boundary conditions and the parameters used in the simulation.

A flow tank is filled with a porous medium. Contaminant solutions in the aqueous phase are introduced from a source situated at the top of the unconfined aquifer. The solution penetrates downward through the unsaturated zone into the saturated zone. This experiment is meant to simulate the leaching of contaminants from a landfill site. The head h_1 in the inlet head chamber and the head h_2 in the outlet head chamber were kept constant. Figure 7.1 represents the computational domain and the boundary conditions. ABCH is the saturated zone, HCDEFG is the unsaturated zone. In the numerical simulation, the variables are pressure p^*, $p^*=p/\rho_0 g$ and concentration C. For p^*, the Dirichlet boundary condition is imposed on sides HA and BC and the remaining

boundaries use a flux boundary condition. For concentration C, a Dirichlet boundary condition is imposed on sides DE, EF, FG, GH and HA; Von Neumann boundary conditions are imposed elsewhere.

In the unsaturated zone, the characteristics of the porous medium were calculated with Eqs. 3.29 and 3.30. According to the water retention curves, the empirical constants α, n and m were 0.0471 cm^{-1}, 6.271 and m=1-1/n (Oostrom, 1991). The other parameters were estimated (Experiments Nos: 4 and 5 in flow container C, (1991)) as follows:

$$K_0 = K_x = K_z = 3.738 - 4.17 \times 10^{-2} \text{ cm/s}$$

$$\phi = 0.35$$

$$a_L = 0.02 \text{ cm}$$

$$a_T = 0.002 \text{ cm}$$

$$\rho_0 = 1.0000 \text{ g/cm}^3$$

$$S_g = 0.0001$$

$$q_L = 0.0167 \text{ cm/s}$$

Initial conditions for p* were obtained by computing the steady state solution with zero density differences, $q_L=0$ and h_1, h_2 constant. Initial conditions for the concentration were zero values everywhere.

The results of the numerical simulation will be presented in three groups. In each group, the behaviour of a neutrally buoyant plume, as well as that of dense plumes (with density differences of 0.0072, 0.014 and 0.028) have been studied.. The first group in

the simulation (Figures 7.2 - 7.5) used a computational domain identical to that of the physical domain, 170 cm long (in the x direction) and 100 cm high (in the z direction), with h_1, h_2 equal to 80 and 78cm, respectively. Figure 7.2 indicates the concentration contours of the neutral plume at time 10, 20, 30, 40 and 50 hours. The predicted plume barely penetrates the water table, most of it being transported within the capillary fringe; this is in agreement with the observed experimental results (Oostrom, 1991). Figures 7.3, 7.4 and 7.5 detail the predicted instability development for density differences of 0.072, 0.014 and 0.028, respectively. From Figure 7.3, 7.4 and 7.5, the increasing tendency for the plume to sink as its density increases may be noted. Figure 7.6 is the plume outlines curves from experimental result for the dense plume (density difference: 0.014, corresponding to the numerical simulation in Figure 7.4). The plume boundaries are drawn from the front and back of the flow container. Comparing Fig. 7.4 and 7.6, it may be seen that after 30 hours, the numerical simulation appears to match the mean plume trajectory of the experimental observations fairly well. At the initial stages (10 and 20 hours) however, the numerical solution does not indicate that the contaminant travels much faster in the z direction than in the (longitudinal) x direction as registered in the experimented results. Furthermore, the numerical simulation does not reproduce the gravitational instabilities which form along the bottom edge of the plume.

By analysing the numerical results, it appeared that the computational domain was not sufficiently long to remove the influence of the downstream Dirichlet boundary conditions which cause horizontal flow. Thus a second series of simulations were

performed using a longer computational domain, i.e. 300 cm by 100 cm, with h_1, h_2 equal

to 80 and 77. The results are presented in Figures 7.7 to 7.9. Comparing Fig. 7.8 and

Fig. 7.4, reveals that the predicted plume front has been modified, with the plume itself

having a greater tendency to sink. For a density difference of 0.028, instabilities may be

observed along the bottom edge of the predicted plume (Fig. 7.9).

Encouraged by these results, a third group of simulation was conducted using a

even longer domain, i.e. 500cm by 100cm with h_1, h_2 equal to 82 and 77. The results are

presented from Figs. 7.10 to 7.12. Comparing Fig 7.11 to the experimental results in

Fig.7.6, it may be observed that the numerical simulation now reproduced the

gravitational instabilities but with a smaller amplitude. This may have been caused by

local variations in the experimental conditions as well as errors in the estimation of the

relevant parameters used in the simulation, especially the parameters in the unsaturated

zone. With the parameters used in the simulation, it appears that in the unsaturated zone,

the horizontal velocity is too large compared with the experimental results, this cause the

plume to spread too quickly resulting in a local reduction of the density difference. Fig.

9.12 is the instability development for a contaminant source with a density difference of

0.028, The gravitational instabilities which form along the bottom edge of the plume are

evident.

The overall comparison between the laboratory experiments of Oostrom (1991)

and the present numerical simulations appear to be satisfactory. The discrepancies in the

amplitude of the instabilities may be attributed to the uncertainties in the estimation of the relevant parameters, especially in the unsaturated zone. The lack of experimental precision and errors in the experimental data could also be a factor.

CHAPTER 8

SIMULATION OF THE CONTAMINANT TRANSPORT

IN THE BORDEN (ONTARIO) LANDFILL

8.1   Brief introduction to the Borden Landfill

As described by MacFarlane et al. (1983), landfill operations at the Borden site spanned a period of 36 years, from 1940 to 1976. Gartner Lee and Associates Ltd. (1977) established that about 80% of the refuse deposited during the life of the landfill operation consisted of ash, wood and construction debris. The remaining refuse is composed of mainly domestic and commercial wastes.

According to MacFarlane (1980), the unconfined aquifer is locally very heterogeneous due to complex distributions of beds and lenses of fine to medium and coarse-grained sand. Some of the beds have a considerable silt content. The unconfined aquifer lies on an extensive deposit of clayey and sandy silt. The aquifer is thickest at the southwestern part of the area and thinnest at about 9.5 m near the northern end (Fig.8.1). The silt-clayey layer beneath the aquifer was identified as a relatively impervious layer that separated the unconfined aquifer from the deeper aquifers used for water supply.

The range of hydraulic conductivity was from 0.05×10^{-3} cm/s for silt fine-grained sand to 0.01 cm/s for fine, medium-grained sand. The average porosity was 0.38. Mean total precipitation averages 82.8 cm $yr.^{-1}$, of which 58.67 cm is in the form of rain, and 24.05 cm is snow.

The water table is farthest below ground surface in the landfill area and in the area northeast of the landfill. The maximum water-table depth is about 7-9 m. The refuse in the landfill is entirely above the water table except from late March to June, when the water table is at its highest because of recharge from snowmelt and spring rain. The contour map of water-table elevation used in the simulation is shown in Figure 8.2, thus, groundwater flow in the study area is northward with h_1 equal to 222 m and h_2 equal to 220 m.

8.2   Numerical simulation

The numerical model used in the simulation has been presented in Chapter 4. The calculation domain and triangular mesh are indicated in Figure 8.3. Due to the lack of information about the properties of the aquifer, we assumed that the unconfined aquifer is homogeneous and the characteristics of the unsaturated porous medium were calculated with Eqs. 3.29 and 3.30 with α, n and m being 0.0471 cm^{-1}, 6.271 and m=1-1/n. The infiltration rate was 25 % of the total precipatation as referenced by Ahmed (1992). The other parameter values used in the simulation were:

$$K_X = K_Z = 0.01 \text{ cm/s} = 8.64 \text{ m/day}$$

$$q_L = 25\% \times 82.8 \text{ cm/year} = 0.00058 \text{ m/day}$$

$$\phi = 0.38$$

$$a_L = 0.001 \text{ m}$$

$$a_T = 0.0001 \text{ m}$$

$$\rho_0 = 1.0000 \text{ g/L}$$

$$h_1 = 222.0 \text{ m}$$

$$h_2 = 220.0 \text{ m}$$

$$S_g = 0.00001$$

The initial condition for p was obtained from a steady state solution with q_L equal to zero. Zero values everywhere were the initial conditions used for C except inside the landfill, where C was set equal to 1. Boundary conditions for p and C were imposed in a similar fashion to that for p^*, C in Chapter 7. At the ground surface, the flux q_L was only imposed at the landfill location.

Figure 8.4 traces the development of the neutrally buoyant contaminant plume at times of 10, 20, 30 and 40 years. Figures 8.5 to 8.8 are the trajectories of the dense contaminant plumes at times 10, 20, 30 and 40 years, the density differences being 0.0014, 0.0025, 0.0036 and 0.0055, respectively. Comparing Figure 8.4 to 8.5, it may be seen that a density difference of 0.0014 is not enough to cause gravitational instability. However, from Figure 8.6, 8.7, and 8.8, the increasing tendency to sink as well as for

the plumes to became gravitationally unstable may be noted. The denser plumes have a tendency to contaminate larger regions by virtue of their increased vertical extent. More importantly, the gravitational instabilities serve to enhance this spreading which would not normally be anticipated on the basis of density differences alone.

Figure 8.9 is the field measurement for chloride and sulfate in 1979/1980, which is about 40 years after landfill operation. From Fig. 8.8 it may be seen that the calculated contaminant plume with a density difference of 0.0055 is compatible with the field measurements. The discrepancies in the amplitude immediately beneath are probably the influence of the initial conditions used in the numerical simulation. Other factors, such as the hydraulic conductivity, water table map, or infiltration rate used in the simulation may also cause these differences.

Figure 8.10 is the numerical simulation with the same parameters of Fig. 8.8 except that the infiltration rate (q_L) has been imposed on the entire ground surface. A comparison between Figs. 8.8 and 8.10, indicates that the infiltration imposed on the ground surface results in faster descent of the plume.

In Chapter 6, we concluded that the transverse dispersivity plays an important role in governing the stability of dense plumes. With high transverse dispersivity, the initial concentration will rapidly be smoothed out to the point that locally, the vertical density gradients will be too low to amplify any disturbance. In order to verify this conclusion,

some additional calculations to check the influence of the transverse dispersivity were performed. Figs. 8.11 and 8.12 are the numerical simulation results using the same parameters of Fig. 8.8 except that the transverse dispersivity has been set to 0.1 m and 0.5 m, respectively. From these two figures, it may be seen that for a_T=0.1m, the gravitational instability has formed along the lower edge of the plume; for a_T=0.5 however, no instability is apparent. Estimates of the concentration Rayleigh number with L=37m, K=8.64 m/day, ε=0.0055 and D=$a_T\bar{V}$ ($\bar{V}$ is the average velocity, the maximum value being about 0.06 m/day) were made and the results presented in Table 8.1. The profiles of cross section near the landfill may be approximated as half Gaussian distributions with c=0.03. From the stability analysis, for c=0.03, the minimum R_a is about 94. Reference to Table 8.1 indicates that for a_T less than 0.1 m, R_a falls within the unstable region; for a_T greater than 0.5 m, R_a is outside the unstable range.

Table 8.1   Concentration Rayleigh Number for different transverse dispersivities (density difference= 0.0055)

a_T (m)	R_a
0.0001	293040
0.01	2930.4
0.1	293.04
0.25	117.216
0.5	58.608
1	29.304

A further clarification is of pertinence here: although for these simulations, the concentration profile is not strictly Gaussian, its influence on the results of the instability analysis appear in an integral evaluation which is less sensitive to the details of its shape.

CHAPTER 9

CONCLUSIONS AND RECOMMENDATIONS

The work presented here has concentrated on studying variable density effects on negatively buoyant leachate and intrusion plumes in saturated-unsaturated porous media using numerical techniques. Various numerical formulations of the relevant governing equations for the hydrodynamic field and the transport of a variable density contaminant have been tested. The ultimate aim is to incorporate these formulations into reliable, robust simulation models for the migration of dense or neutrally buoyant plumes in homogeneous or heterogenous porous media.

Three different numerical approximations to the governing equations have been investigated:

- the standard finite difference approximation

- a control volume formulation

- a finite volume formulation closely related to the control volume formulation

- a hybrid Euler-Lagrange algorithm for the transport equation implemented on a triangular mesh

The finite difference and control volume formulations have been implemented on a cartesian mesh and validated using published data obtained from laboratory

experiments. These methods have been found to be computationally efficient, providing satisfactory solutions with minimal demand on computing resources. For example, it was possible to simulate the laboratory experiments using a 386 based Personal Computer. An important disadvantage with these methods arises however, when the physical domain to be modelled does not lend itself to a cartesian discretization. For such cases, either finite element or finite volume formulations on non-orthogonal computational elements are more appropriate. The body of literature available on finite element and, to a lesser extent, on finite volume techniques suggests that for the same results, finite volume techniques are computationally more robust as well as being more efficient.

A numerical model using a finite volume formulation has been implemented on a triangular mesh, the chief advantage as just mentioned, being the applicability to the treatment of irregular computational domains. The numerical treatment of the transport equation in the model is realised using a characteristics based scheme for the convective transport, while the diffusion term is evaluated on a triangular stencil using the finite volume formulation with linear interpolation for the concentration. Attempts to validate the model with field measurements taken around the Borden, Ontario waste landfill site have been partially successful.

The numerical efforts described here have been complemented with a stability analysis based on the plume mean flow characteristics. This part of the study was inspired by the experimental observations in the two laboratory experiments referred to

earlier, which indicated that negatively buoyant plumes tend to exhibit gravitationally induced instabilities along their lower edge. The simple analysis described in the present work provides a satisfactory insight into the mechanism for the development of the instability.

Two characteristic parameters: a concentration length scale and a concentration Rayleigh number are found to govern the stability of the plume. Estimates of these two parameters in the laboratory experiments as well as in the Borden landfill site indicate that these plumes will be inherently unstable. The laboratory experiments visually confirm the appearance of the instability. Complete validation for the Borden site is unfortunately not possible due to the lack of sufficiently detailed field data. The numerical model does however indicate that the dense leachate plume would be unstable. Perhaps the most important ramification of an unstable plume is the exaggerated increase in the vertical dispersion due to the appearance of the lobe shaped protuberances characteristic of this type of instability.

Future work should be devoted to numerically incorporating the effects of adsorption and chemical reactions on the leachate plume. The numerical aspects of this task will not necessarily be trivial. Further research into computationally more efficient algorithms is also very desirable since any evaluation of a "real-case" disposal site will require simulation of the contaminant migration over a typical period of the order of a hundred years.

REFERENCES

AHMED, S, KHANBILVARDI, R. M., FILLOS, J . and GIEASON, P. J., 1992, Two-dimensional leachate estimation through landfills, Journal of Hydraulic Engineering, Vol. 118, No. 2, pp. 306-322.

ARYA, A., HEWETT, T. A., LARSON, R. G. and GUPTA, V. G., 1988, Dispersion and reservoir heterogeneity, SPE Reservoir Engineering. Vol.3, pp. 139-148.

BACHMAT, Y., and ELRICK, D. E., 1970, Hydrodynamic instability of miscible fluids in a vertical porous column, Water Resources Research., 6(1), 156-171.

BACHMAT, Y., 1969, Hydrodynamic dispersion in a saturated homogeneous porous medium at low Peclet numbers and nonhomogeneous solution, Water Resources Research., 5, 139-143.

BALIGA, B. R. and PATANKAR, S. V., 1980, A new finite element formulation for convection diffusion problems, Numerical Heat Transfer, Vol. 3, pp. 393-409.

BALIGA, B. R. and PATANKAR, S. V., 1983, A control volume finite element method for two-dimensional fluid flow and heat transfer, Numerical Heat Transfer, Vol. 6, pp. 245-261.

BALIGA, B. R. and PATANKAR, S. V., 1988, Elliptic Systems: Finite Element Method II, in Minkowycz, W.J., Sparrow, E.M., Schneider, G.E., and Pletcher, R.H. (eds), Handbook of Numerical Heat Transfer, Chap. 11, pp. 421-461, Wiley, New York.

BEAR, J., 1961, On the tensor form of dispersion, Journal of Geophysical Resources, 66 (4), 1185-1197.

BEAR, J., 1972, Dynamics of Fluid in Porous Media, Elsevier, New York.

BEAR, J., and VERRUIJT, A., 1987, Modelling Groundwater Flow and Pollution, Reidel, Dordrechi.

CAMARERO, R., OZELL, B., REGGIO, M. and GARON, A., 1986, Grid Generation System for Turbomachinery Applications, Project CASTOR, EPM/RT-86/32, Ecole Polytechnique de Montreal, Montreal, Canada.

CHRISTIE, I, GRIFFITHS, D. F. and MITCHELL, A. R., 1976, Finite element methods for second order differential equations with significant first derivatives, International Journal for Numerical Methods in Engineering, Vol. 10, pp. 1389-1396.

DAGAN, G., 1986, Statistical theory of groundwater flow and transport: Pore to laboratory, laboratory to formation, Formation to regional scale, Water Resources

Research, Vol. 22, pp. 120S-135S.

ESSAID, H. I., 1990, A multilayered sharp interface model of coupled freshwater and seawater in coastal systems: Model development and application, Water Resources Research, Vol. 26, No.7, pp. 1431-1454.

FAN, Y. and KAHAWITA, R., 1994, A numerical study of variable density flow and mixing in porous media, Water Resources Research, Vol. 30, No.10, pp. 2707-2716.

FAN, Y. and KAHAWITA, R., 1994, Numerical study of the effects of a variable density contaminant in an unconfined aquifer, Computer techniques in environmental studies V, Vol. 1: Pollution modelling, pp. 165-172, Computational Mechanics Publications.

FREEZE ,R. A. and CHERRY. J.A. 1979, Groundwater, Prentice-Hall, Englewood Cliffs, N.J..

FRIND, E. O., 1982a, Seawater intrusion in continuous coastal aquifer-aquitard system, Advances in Water Resources, 5, pp. 89-97.

FRIND, E. O., 1982b, Simulating of long-term transient density-dependent transport in groundwater, Advances in Water Resources, 5, pp. 73-88.

GALEATI, G., GAMBOLATI, G. and NEUMAN, S. P., January 1992, Coupled and Partially Coupled Eulerian-Lagrangian Model of Freshwater-Seawater Mixing, Water Resources Research, Vol.28, No.1, pp.149-165.

GARTNER LEE ASSOCIATES LTD., 1977, Leachate migration study, CFB Borden. Final Report Prepared for Environment Canada, Toronto, Ont., Gartner Lee Associates, Toroton, Ont., May 1977, pp. 24 and appendices.

GELHAR, L. W., 1986, Stochastic subsurface hydrology from theory to application, Water Resource Research, Vol. 22, pp.135S-145S.

GELHAM, R. W. and CHERRY, J.A., 1982, Contaminant migration in saturated unconsolidated geologic deposits, In: Recent Trend in Hydrogeology. Special paper 189, pp. 31-62. T.N. Narasimhan (Ed.). Geological Society of America, Bouldr, Co.

HEINRICH, J. C., HUYAKORN, P. S., and ZIENKIEWICZ, O.C., 1977, An 'upwind' finite element scheme for the two-dimensional convective transport equation, International Journal for Numerical Methods in Engineering, Vol. 11, pp. 131-143.

HEINRICH, J. C. and ZIENKIEWICZ, O. C., 1977, Quardratic finite element scheme for two-dimensional convective transport problem, International Journal for Numerical Methods in Engineering, Vol. 11, pp. 1831-1844.

HENRY, H. R., 1964, Effects of dispersion on salt water encroachment in coastal aquifers, In: Sea Water in Coastal Aquifers, U.S. Geological Survey Water-Supply Paper 1613-c, pp. c71-c84.

HIRSCH, C., 1988, Numerical Computation of Internal and External Flows, Volume 1: Fundamentals of Numerical Discretization, John Wiley & Sons Ltd.

HOLLY, F. M., Jr., and A. PREISSMAN, 1977, Accurate calculation of transport in two-dimensions, Journal of the Hydraulics Division, American Society Civil Engineering, 103, pp. 1259-1277.

HUYAKORN, P. S., 1977, Solution of steady-state, convective transport equation using an upwind finite element scheme, Applied Mathematics Modelling, Vol. 1, pp. 187-195, March, 1977.

HUYAKORN, P. S., ANDERSON, P. F., MERCER,J. W. and WHITE H. O. Jr., 1987, Saltwater intrusion in aquifers: Development and testing of a three-dimensional finite element model, Water Resources Research, 23, pp. 293-312.

KIMMEL, G. E. and BRAIDS, O. C., 1980, Leachate Plumes in Ground Water from Babylon and Islip Landfills, Long Island, New York, Geological Survey Professional Paper 1085, U.S. Government Printing Office, Washington, D.C..

KOCH, M. and ZHANG, G., 1992, Numerical simulation of the effects of variable density in a contaminant plume, Ground Water, Vol. 30, No. 5, pp. 731-742.

KOHOUT, F. A., 1960a, Cyclic flow of salt water in the Biscayne aquifer of southeastern Florida, Journal of Geophysical Resources, 65, pp. 2133-2141.

KOHOUT, F. A., 1960b, Flow pattern of fresh water and salt water in the Biscayne aquifer of the Miami area, Florida, International Association Science Hydrology Publications, 52, pp. 440-448.

KONIKOW, L. F. and BREDEHOEFT, J. D., 1977, Computer model for two-dimensional solute transport and dispersion in groundwater. U.S. Geological Survey Water Resource Investigation Report, 77-19.

KRUPP, H. K. and ELRICK, D. E., 1969, Density effects in miscible displacement experiments. Soil Science, 107, pp. 372-380.

LAUMBACH, D. D., 1975, A high-accuracy, finite-difference technique for treating the convection-diffusion equation, Journal of Society Petrolem Engineering, 15, pp. 517-531.

LEBLANC, D.R., 1984, Sewage plume in a sand and gravel aquifer, Cape Cod,

Massachusetts, U.S. Geological Survey Water-Supply Paper 2218, U.S. Government Printing Office, Washington, D.C., 1984.

LEE, C. H and CHENG, T-S. R., 1974, On seawater encroachment in coastal aquifers, Water Resources Research, 10, pp.1039-1043, 1974.

LEONARD, B. P., 1979, A Stable and Accurate Convective Modelling Procedure Base on Quadratic Upstream Interpolation, Computer methods in Applied Mechanics and Engineering, Vol. 19, pp..59-98.

LIST, E. J., 1965, The stability and mixing of a density-stratified horizontal flow in a saturated porous medium, Rep. KH-r-11, California Institute of Technology, Pasadena.

LIU, P. L.-F., CHENG, A. H.-D., LIGGETT, J. A. and LEE, J. H., 1981, Boundary integral equation solutions of moving interface between two fluid in porous media, Water Resources Research, Vol. 17, pp. 1445-1452.

MACFARLANE, D. S., CHERRY, J. A., GILLHAM, R. W. and SUDICKY, E. A., 1983, Migration of contaminants in groundwater at a landfill: A case study. 1. Groundwater flow and plume delineation, Journal of Hydrology, 63, pp. 1-29.

MOLZ, F. J., MELVILLE, J. G., GüVEN, O., CROCKER, R. C., and MATTESON, K.

T., PERFORMANCE, 1986, Analysis and simulation of a two-well tracer test at the Mobile site, Water Resources Research, Vol. 22, pp. 1031-1037.

MUALEM,Y., 1976, A new model for predicting the hydraulic conductivity of unsaturated porous media, Water Resources Research, Vol. 12, pp. 513-522.

MUALEM, Y. and BEAR, J., 1974, The Shape of the Interface in Steady Flow in a Stratified Aquifer, Water Resources Research, Vol. 10, pp. 1207-1215.

MULQUEEN, J., and KIRKHAM, D. 1972, Leaching of a surface layer of sodium chloride into tile drains in a sand-tank model, Soil Science Society of America Journal, Vol. 36, pp. 3-9.

NEUMAN, P. S., 1981, A Eularian-Lagrangian numerical scheme for the dispersion-convection equation using conjugate space-time grids. Journal of Computational Physics, Vol. 41, pp. 270-294.

NEUMAN, P. S., 1984, Adaptive Eularian-Lagrangian finite element method for advection-dispersion. International Journal of Numerical Methods Engineering, 20: pp. 321-337.

NEUMAN, P. S., 1990, Universal scaling of hydraulic conductivities and dispersivities

in geological media, Water Resources Research, Vol.26, pp. 1749-1758.

NIELSEN, D. R., VAN GENUCHTEN, M. Th. and BIGGAR, J. W., 1986, Water flow and solute transport in the unsaturated zone, Water Resources Research, Vol. 22, No. 9, pp. 89s-108s, August.

OOSTROM, M., 1991, Behaviour of dense leachate plumes in unconfined aquifer models, Ph.D. dissertation, Department of Agronomy and Soils, Auburn University, Auburn, Alabama.

OOSTROM, M., HAYWORTH, J. S., DANE, J. H. and GUVER, O., 1992, Behavior of dense aqueous phase leachate plumes in homogeneous porous media, Water Resources Research, 28(8), 2123-2143.

PASCHKE, N.W., and HOOPES, J.A., 1984, Buoyant contaminant plumes in groundwater, Water Resources Research, 20 (9), 1183-1192.

PATANKAR, S.V., 1980, Numerical Heat Transfer and Fluid Flow, Hemisphere Publishing Co.

PICKENS, J. F. and GRISAK, W. C., 1981, Scale-dependent dispersion in a stratified granular aquifer, Water Resources Research, Vol.17, pp.1191-1211.

PICKENS, J F. and LENNOX, W. C., April 1976, Numerical Simulation of Waste Movement in Steady Groundwater Flow Systems. <u>Water Resources Research</u>, Vol. 12, No.2, pp. 171-180.

PINDER, G. F. and COOPER, H. H., 1970, A Numerical Technique for Calculating the Transient Position of the Seawater Front, <u>Water Resources Research</u>, Vol. 6, pp. 875-882.

PINDER, G.F. and GRAY, W.G., 1977, <u>Finite Element Simulation in Surface and Subsurface Hydrology</u>, Academic Press, New York.

PINDER, G.F., 1988, An overview of groundwater modelling, E. Custodio et al. (eds), <u>Groundwater Flow and Water Quality Modelling</u>, pp. 119-134.

ROE, P. L. and SIDILKOVER, D. 1992, Optimum positive linear schemes for advection in two and three dimensions, <u>SIAM Journal of Numerical Analysis</u>, Vol. 29, No. 6, pp. 1542-1568, December.

SANFORD, W. E. and KONIKOW L. F., 1985, A two-constituent solution-transport model for groundwater having variable density. <u>U.S. Geology Survey Water Resource Investigation Report, 85-4279.</u>

SCHINCARIOL, R. A. and SCHWARTZ, F. W., October 1990, An Experimental

Investigation of Variable Density Flow and Mixing in Homogeneous and Heterogeneous Media, Water Resources Research, Vol. 26, No. 10, pp. 2317-2329.

SCHEIDEGGER, A. E.,1961, General theory of dispersion in porous media, Journal of Geophysical Resources, 66, 3273-3278.

SEGOL, G. and PINDER, G. F., 1975, A Galerkin finite element technique for calculating the transient position of the saltwater front, Water Resources Research, 12, p. 65-77.

SENGER R. K. and FOGG, G. E., September 1990a, Stream Functions and Equivalent Freshwater Heads for Modelling Regional Flow of Variable-Density Groundwater, 1. Review of Theory and Verification, Water Resources Research, Vol. 26, No. 9, pp. 2089-2096.

SENGER R. K. and FOGG, G. E., September 1990b, Stream Functions and Equivalent Freshwater Heads for Modelling Regional Flow of Variable-Density Groundwater, 2. Application and Implications for Modelling Strategy, Water Resources Research, Vol. 26, No. 9, pp. 2097-2106.

SOUZA, W. R. and VOSS. C. I., 1987, Analysis of an anisotropic coastal aquifer system using variable density flow and solute transport simulation, Journal of Hydrology, 92, pp.

17-41.

SPARROW, E. M., GOLDSTEIN, R. J. and JOHNSON, V. K., 1964, Thermal Instability in a Horizontal Fluid Layer: Effect of Boundary Conditions and Nonlinear Temperature Profile, Journal of Fluid Mechanics, Vol. 18, Part 4., pp. 513.

SUDICKY, E. A., 1986, A natural gradient experiment of solute transport in a sand aquifer, 1. Spatial variability of hydraulic conductivity, and its role in the dispersion process, Water Resources Research, Vol. 22, pp. 2068-2082.

TAIGBUNE, A. E., LIGGETT, J. A. and CHENG, A. H.-D., 1984, Boundary integal solution to seawater intrusion into coastal aquifers, Water Resources Research, Vol. 20, pp. 1150-1158.

U.S. ENVIRONMENTAL PROTECTION AGENCY, 1977, The report to Congress: waste disposal practices and their effects on ground water, USEPA Office of Water Supply, Office of Solid waste Management Programs.

VAN DER MOLL, W.H. and VAN OMMEN, H. C., 1988, Transport of solutes in soils and aquifers, Journal of Hydrology, 100, pp. 433-451.

VAN GENUCHTEN, M. Th. 1980, A close-form equation for prediction the hydraulic

conductivity of unsaturated soils. Soil Science Society of America Journal, 44, pp. 892-898

VAN GENUCHTEN, M. Th. and NIELSEN, D. R., 1985, On describing and predicting the hydraulic properties of unsaturated soils, Annales Geophysicae, 3, 5, pp. 515-628.

VOSS C., 1984, A finite-element simulation model for saturated-unsaturated, fluid density dependent groundwater flow with energy transport or chemically reactive single-species solution transport. U.S. Geological Survey Water Resources Investigation Report, 84-4369.

VOSS C. and SOUZA, W. R., October 1987, Variable Density Flow and Solute Transport Simulation of Regional Aquifers Containing a Narrow Freshwater-Saltwater Transition Zone, Water Resources Research, Vol. 23, No. 10, pp. 1851-1866.

WOODING, R. A., 1959, The Stability of a Viscous Liquid in a Vertical Tube Containing Porous Material, Proceedings of Royal Society of London Series, A 252, pp. 120-134.

WOODING, R. A., 1962a, Free Convection of Fluid in a Vertical Tube filled with Porous Material, Journal of Fluid Mechanics, Vol. 13, pp. 129-14.

WOODING, R.A., 1962b, The Stability of an Interface Between Miscible Fluids in a Porous Medium, Journal of Applied Mathematics and Physics, Vol. 13, pp. 255-266.

WOODING, R.A., 1963, Convection in a saturated porous medium at large Rayleigh number or Peclet number, Journal of Fluid Mechanics, Vol. 15, pp. 527-544.

WOODING, R.A., 1969, Growth of Fingers at an unstable Diffusing Interface in a Porous Medium or Hele-Shaw Cell, Journal of Fluid Mechanics, Vol. 39, pp. 477-496.

YEH, G. T., June 1990, A Lagrangian-Eulerian Method With Zoomable Hidden Fine-Mesh Approach to Solving Advection-Dispersion Equations, Water Resources Research, Vol. 26, No. 6, pp. 1133-1144.

YEH, G. T. and CHANG, J. R., November 1992, An Exit Peak Capturing and Oscillation-free Scheme to Solve Advection-Dispersion Transport Equations, Water Resources Research, Vol. 28, No. 11, pp. 2937-2951.

APPENDIX A

UPWIND SCHEMES

Upwind schemes for approximating the convection terms.

(1)   First-order upwind:

$$u\frac{\partial f}{\partial x}\Big|_i = u\,\frac{f_i - f_{i-1}}{\Delta x} \qquad\qquad \text{for } u \geq 0$$

$$= u\,\frac{f_{i+1} - f_i}{\Delta x} \qquad\qquad \text{for } u < 0 \qquad\qquad (A.1)$$

$$= -\frac{|u| + u}{2\Delta x}\,f_{i-1} + 2\,|u|\,f_i - \frac{|u| - u}{2\Delta x}\,f_{i+1}$$

(2)   Second-order upwind:

$$u\frac{\partial f}{\partial x}\Big|_i = u\,\frac{3f_i - 4f_{i-1} + f_{i-2}}{2\Delta x} \qquad\qquad \text{for } u \geq 0$$

$$= u\,\frac{-f_{i+2} + 4f_{i+1} - 3f_i}{2\Delta x} \qquad\qquad \text{for } u < 0$$

$$\qquad\qquad\qquad\qquad\qquad\qquad\qquad\qquad (A.2)$$

$$= \frac{|u| + u}{4\Delta x}\,f_{i-2} - \frac{|u| + u}{\Delta x}\,f_{i-1} + \frac{3\,|u|}{2\Delta x}\,f_i$$

$$- \frac{|u| - u}{\Delta x}\,f_{i+1} + \frac{|u| - u}{4\Delta x}\,f_{i+2}$$

(3)   Third-order upwind:

$$u\frac{\partial f}{\partial x}\Big|_i = u\,\frac{2f_{i+1} + 3f_i - 6f_{i-1} + f_{i-2}}{6\Delta x} \qquad \text{for } u \geq 0$$

$$= u\,\frac{-f_{i+2} + 6f_{i+1} - 3f_i - 2f_{i-1}}{2\Delta x} \qquad \text{for } u < 0$$

$$= \frac{|u| + u}{12\Delta x}f_{i-2} - \frac{|u| + 2u}{3\Delta x}f_{i-1} + \frac{|u|}{2\Delta x}f_i$$

$$-\frac{|u| - 2u}{3\Delta x}f_{i+1} + \frac{|u| - u}{12\Delta x}f_{i+2}$$

(A.3)

(4)   QUICK:

$$u\frac{\partial f}{\partial x}\Big|_i = u\,\frac{3f_{i+1} + 3f_i - 7f_{i-1} + f_{i-2}}{8\Delta x} \qquad \text{for } u \geq 0$$

$$= u\,\frac{-f_{i+2} + 7f_{i+1} - 3f_i - 3f_{i-1}}{2\Delta x} \qquad \text{for } u < 0$$

$$= \frac{|u| + u}{16\Delta x}f_{i-2} - \frac{2|u| + 5u}{8\Delta x}f_{i-1} + \frac{3|u|}{8\Delta x}f_i$$

$$-\frac{2|u| - 5u}{8\Delta x}f_{i+1} + \frac{|u| - u}{16\Delta x}f_{i+2}$$

(A.4)

To summarize the schemes described above, a general form can be written as follows

$$u\frac{\partial f}{\partial x}\Big|_i = A^u f_{i-2} + B^u f_{i-1} + C^u f_i + D^u f_{i+1} + E^u f_{i+2}$$

(A.5)

APPENDIX B

Constants D_1, D_2, D_3 and D_4 in Eq. (4.138)

In the three-node triangular element 123 shown in Fig. 4.9, the dependent variable p is interpolated using the function given in Eq.(4.123):

$$p = Ax + Bz + E \tag{B.1}$$

The constants A, B and E in Eq. (B.1) can be uniquely determined in terms of the (x,z) coordinates of the three nodes and the corresponding values of p:

$$A = \frac{(z_2 - z_3)p_1 + (z_3 - z_1)p_2 + (z_1 - z_2)p_3}{det} \tag{B.2}$$

$$B = \frac{(x_3 - x_2)p_1 + (x_1 - x_3)p_2 + (x_2 - x_1)p_3}{det} \tag{B.3}$$

$$E = \frac{(x_2 z_3 - x_3 z_2)p_1 + (x_3 z_1 - x_1 z_3)p_2 + (x_1 z_2 - x_2 z_1)p_3}{det} \tag{B.4}$$

$$det = x_1 z_2 + x_2 z_3 + x_3 z_1 - x_2 z_1 - x_3 z_2 - x_1 z_3 \tag{B.5}$$

The mass flux may be written as

$$J_x = K_{xx}\frac{\partial p}{\partial x} + K_{xz}\frac{\partial p}{\partial z} + K_{xz}\rho g \tag{B.6}$$

$$J_z = K_{zx}\frac{\partial p}{\partial x} + K_{zz}\frac{\partial p}{\partial z} + K_{zz}\rho g \tag{B.7}$$

here

$$K_{xx} = \frac{k_{xx}k_r\rho}{\mu}, \quad K_{zz} = \frac{k_{zz}k_r\rho}{\mu}, \quad K_{xz} = K_{zx} = \frac{k_{zx}k_r\rho}{\mu} \tag{B.8}$$

Substituting Eq.(B.1)-(B.5) into Eq.(B.6) and (B.7), and used symbol f_1, f_2, f_3, g_1, g_2 and g_3 as follows:

$$f_1 = \frac{K_{xx}(z_2 - z_3) + K_{xz}(x_3 - x_2)}{\det}$$

$$f_2 = \frac{K_{xx}(z_3 - z_1) + K_{xz}(x_1 - x_3)}{\det} \tag{B.9}$$

$$f_3 = \frac{K_{xx}(z_1 - z_2) + K_{xz}(x_2 - x_1)}{\det}$$

$$g_1 = \frac{K_{zx}(z_2 - z_3) + K_{zz}(x_3 - x_2)}{\det}$$

$$g_2 = \frac{K_{zx}(z_3 - z_1) + K_{zz}(x_1 - x_3)}{\det} \tag{B.10}$$

$$g_3 = \frac{K_{zx}(z_1 - z_2) + K_{zz}(x_2 - x_1)}{\det}$$

Eq.(B.6),(B.7) may be written as

$$J_x = f_1 \, p_1 + f_2 \, p_2 + f_3 \, p_3 + k_{xz}\rho \, g \qquad (B.11)$$

$$J_z = g_1 \, p_1 + g_2 \, p_2 + g_3 \, p_3 + k_{zz}\rho \, g \qquad (B.12)$$

Finally, D_1, D_2, D_3 and D_4 may be obtained

$$D_1 = -(((z_c - z_o)f_1^c - (x_c - x_o)g_1^c) - ((z_a - z_o)f_1^a - (x_a - x_o)g_1^a))$$
$$+ \frac{(S_p\rho + \rho c)^*g\rho_0}{t} \frac{A}{3} \qquad (B.13)$$

$$D_2 = -(((z_c - z_o)f_2^c - (x_c - x_o)g_2^c) - ((z_a - z_o)f_2^a - (x_a - x_o)g_2^a)) \qquad (B.14)$$

$$D_3 = -(((z_c - z_o)f_3^c + (x_c - x_o)g_3^c) - ((z_a - z_o)f_3^a - (x_a - x_o)g_3^a)) \qquad (B.15)$$

$$D_4 = -(-(z_a - z_o)(K_{xz}\rho_a^2 + 4K_{xz}\rho_r^2 + K_{xz}\rho_o^2)$$
$$+ (x_a - x_o)(K_{zz}\rho_a^2 + 4K_{zz}\rho_r^2 + K_{zz}\rho_o^2)$$
$$+ (z_c - z_o)(K_{xz}\rho_o^2 + 4K_{xz}\rho_t^2 + K_{xz}\rho_c^2)$$
$$- (x_c - x_o)(K_{zz}\rho_o^2 + 4K_{zz}\rho_t^2 + K_{zz}\rho_c^2))/(6*\rho_0)$$
$$- \frac{p^n}{\Delta t}(\rho(S_p + c))^*g\rho_0\frac{A}{3}$$
$$+ \frac{C^{n+1} - C^n}{\Delta t}(\phi S\rho_0\varepsilon)^*\frac{A}{3} \qquad (B.16)$$

here A is the area of the triangular 123, $(S_p\rho + c\rho)^*$ and $(\phi S\rho_0\varepsilon)^*$ are the average value over the triangular 123 and

$$f_i^a = \frac{1}{6} \left[(f_i)_a + 4(f_i)_r + (f_i)_o \right] \qquad i=1,3$$

$$g_i^a = \frac{1}{6} \left[(g_i)_a + 4(g_i)_r + (g_i)_o \right] \qquad i=1,3$$

$$f_i^c = \frac{1}{6} \left[(f_i)_o + 4(f_i)_t + (f_i)_c \right] \qquad i=1,3$$

$$g_i^c = \frac{1}{6} \left[(g_i)_o + 4(g_i)_t + (g_i)_c \right] \qquad i=1,3$$

$$(B.17)$$

APPENDIX C

Constants E_1, E_2, E_3 and E_4 in Eq. (4.172)

In the three-node triangular element 123 shown in Fig. 4.9, the dispersion concentration C is interpolated using the function given in Eq.(4.161):

$$C = Ax + Bz + E \tag{C.1}$$

The constants A, B and E in Eq. (B.1) can be uniquely determined in terms of the (x,z) coordinates of the three nodes and the corresponding values of C:

$$A = \frac{(z_2 - z_3)\,C_1 + (z_3 - z_1)\,C_2 + (z_1 - z_2)\,C_3}{det} \tag{C.2}$$

$$B = \frac{(x_3 - x_2)\,C_1 + (x_1 - x_3)\,C_2 + (x_2 - x_1)\,C_3}{det} \tag{C.3}$$

$$E = \frac{(x_2 z_3 - x_3 z_2)\,C_1 + (x_3 z_1 - x_1 z_3)\,C_2 + (x_1 z_2 - x_2 z_1)\,C_3}{det} \tag{C.4}$$

$$det = x_1 z_2 + x_2 z_3 + x_3 z_1 - x_2 z_1 - x_3 z_2 - x_1 z_3 \tag{B.5}$$

The diffusion flux may be written as

$$J_x = D_{xx}\frac{\partial C}{\partial x} + D_{xz}\frac{\partial C}{\partial z} \tag{C.6}$$

$$J_z = D_{zx}\frac{\partial C}{\partial x} + D_{zz}\frac{\partial C}{\partial z}$$

(C.7)

Substituting Eq.(C.1)-(C.5) into Eq.(C.6) and (C.7), and used symbol f_1, f_2, f_3, g_1, g_2 and g_3 as follows:

$$f_1 = \frac{D_{xx}(z_2 - z_3) + D_{xz}(x_3 - x_2)}{\det}$$

$$f_2 = \frac{D_{xx}(z_3 - z_1) + D_{xz}(x_1 - x_3)}{\det}$$

(C.8)

$$f_3 = \frac{D_{xx}(z_1 - z_2) + D_{xz}(x_2 - x_1)}{\det}$$

$$g_1 = \frac{D_{zx}(z_2 - z_3) + D_{zz}(x_3 - x_2)}{\det}$$

$$g_2 = \frac{D_{zx}(z_3 - z_1) + D_{zz}(x_1 - x_3)}{\det}$$

(C.9)

$$g_3 = \frac{D_{zx}(z_1 - z_2) + D_{zz}(x_2 - x_1)}{\det}$$

Thus Eq.(C.6),(C.7) may be written as

$$J_x = f_1 C_1 + f_2 C_2 + f_3 C_3$$

(C.10)

$$J_z = g_1 \, C_1 + g_2 \, C_2 + g_3 \, C_3 \tag{C.11}$$

Finally, E_1, E_2, E_3 and E_4 may be obtained

$$E_1 = -((z_c - z_a) \, f_1 - (x_c - x_a) \, g_1) + \frac{\theta^{n+1}}{\Delta t} \frac{A}{3} \tag{C.12}$$

$$E_2 = -((z_c - z_a) \, f_2 + (x_c - x_a) \, g_2) \tag{C.13}$$

$$E_3 = -((z_c - z_a) \, f_3 + (x_c - x_a) \, g_3) \tag{C.14}$$

$$E_4 = -\frac{(\theta \, C)^{(1)}}{\Delta t} \frac{A}{3} + \nabla \cdot q C_1 \frac{A}{3} \tag{C.15}$$

here A is the area of the triangular 123.

	Flow Direction	Tendency to cause unstable by	
		Viscosity	Density
Salt + H_2O	Down	No	Yes
H_2O	Up	Yes	Yes
H_2O	Down	Yes	No
Salt + H_2O	Up	No	No

Figure 2.1 The four possible configuration of liquid configuration and flow direction

in a vertical column and the resulting tendency to produce unstable flow

(Krupp and Elrick, 1969)

PRECIPITATION
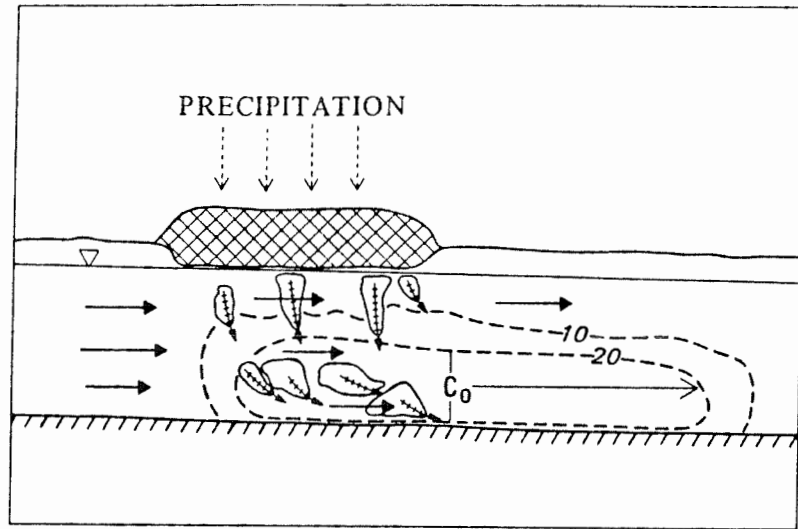
EXPLANATION
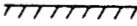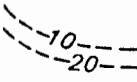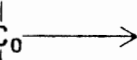
⊤⊤⊤⊤⊤⊤⊤ HYDROLOGIC BOUNDARY

LINE OF EQUAL DILUTION–Number
is dilution factor (see text section
"Flow of Leachate")

$C_0 \longrightarrow$ REGION OF APPROXIMATELY UNI-
FORM CONCENTRATION–C_0 is ini-
tial concentration of leachate-enriched
ground water at downgradient side
of landfill

$\longrightarrow$ DIRECTION OF GROUND-WATER
FLOW

LEACHATE POCKET–Direction of flow
and idealized shape of high-density
leachate pocket

▽ WATER TABLE

XXXXXXX LANDFILL DEPOSITS

Figure 2.2 Leachate movement and dispersion in groundwater
beneath a landfill (Kimmel and Braids, 1980)
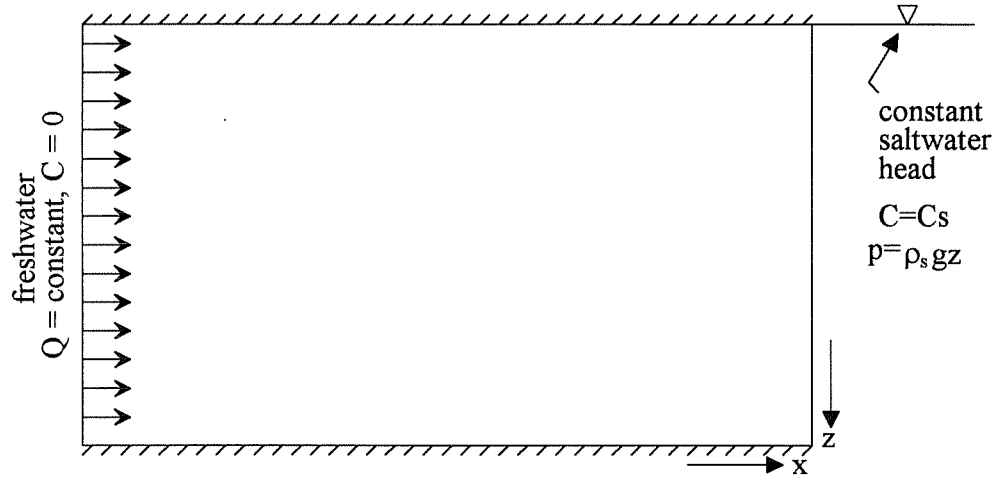
Figure 2.3   Boundary conditions for Henry's problem (Henry, 1964)
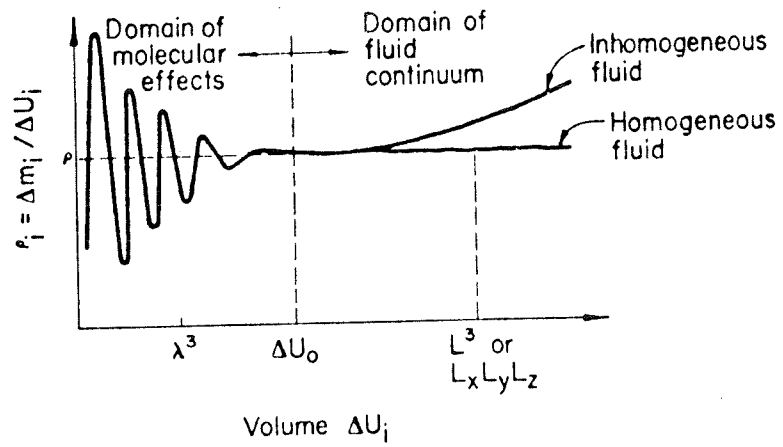
Figure 3.1 Definition of fluid density (Bear, 1972)
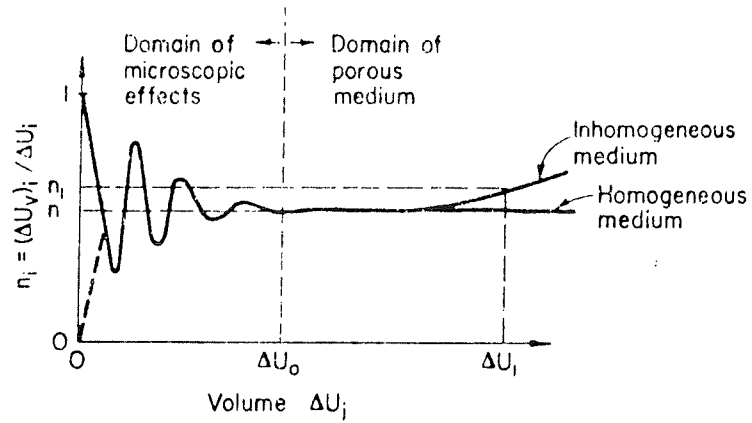
Figure 3.2 Definition of porosity and representative elementary volume (REV)
(Bear, 1972)
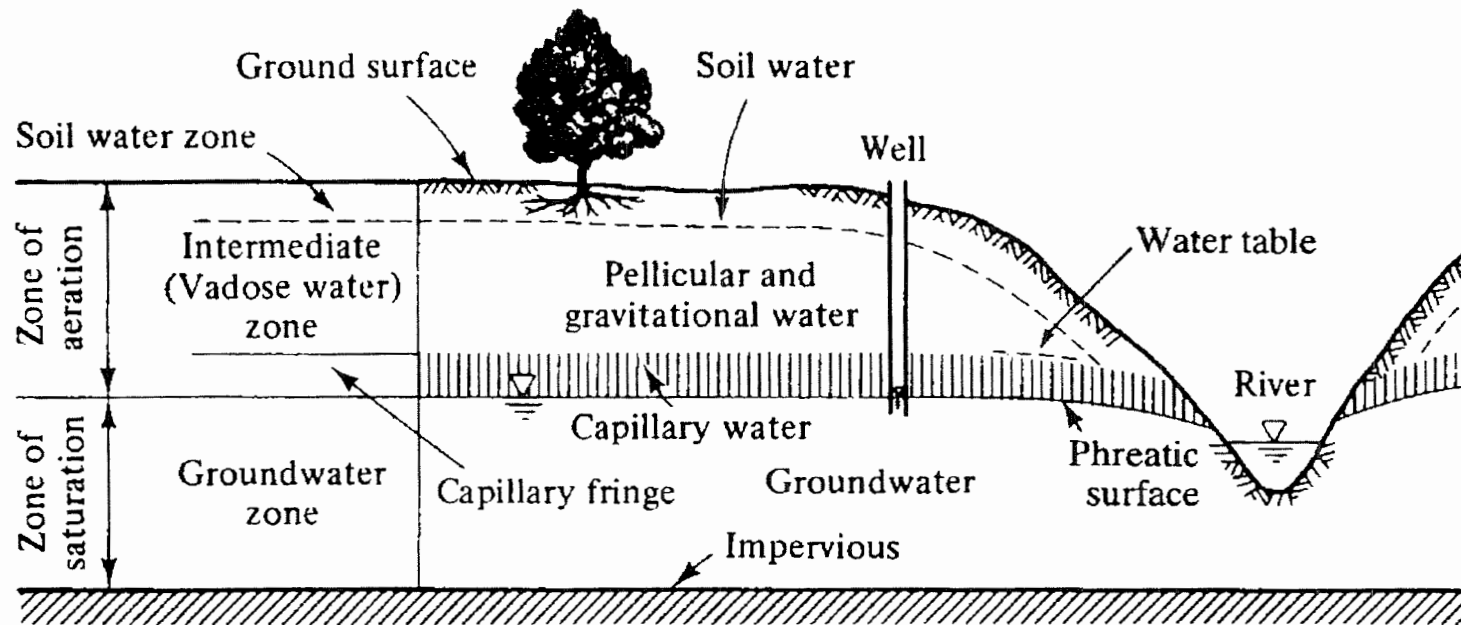
Figure 3.3   Distribution of subsurface water
(Bear, 1972)

(1)   (2)   (3)
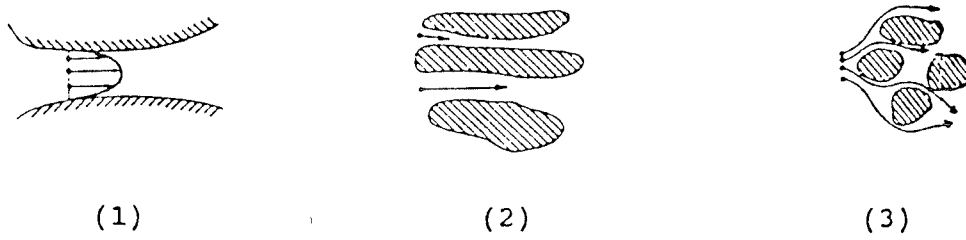
Figure 3.4 Components of mechanical dispersion

(Gillham and Cherry, 1982)
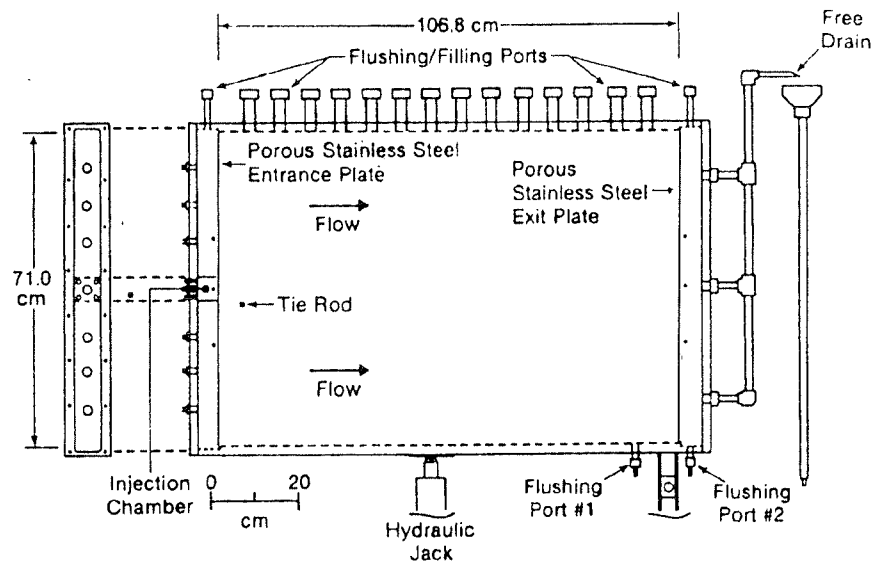
Figure 4.1 Flow container used in the experiment of Schincariol and Schwartz (1990)
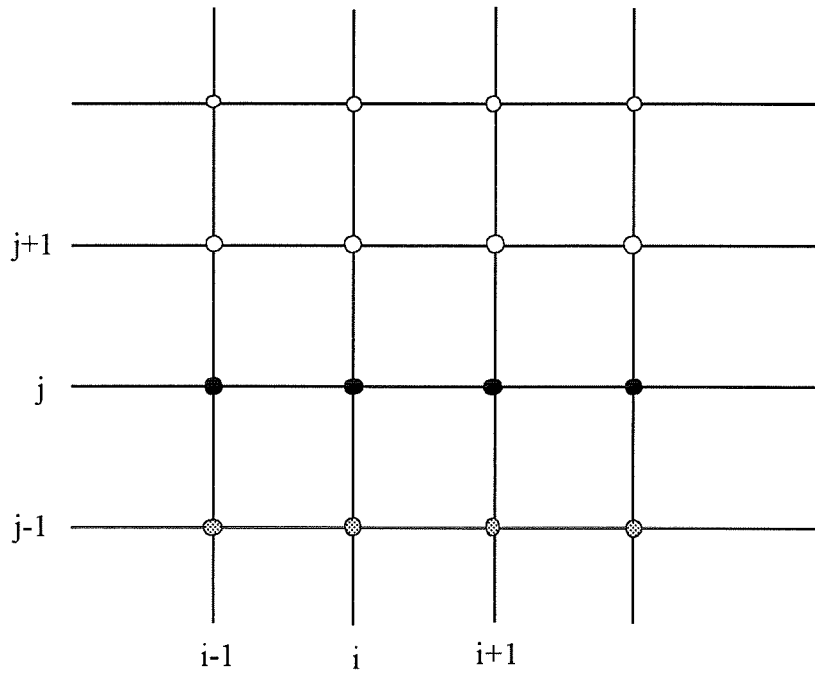
Figure 4.2   The configuration for relaxation along a row
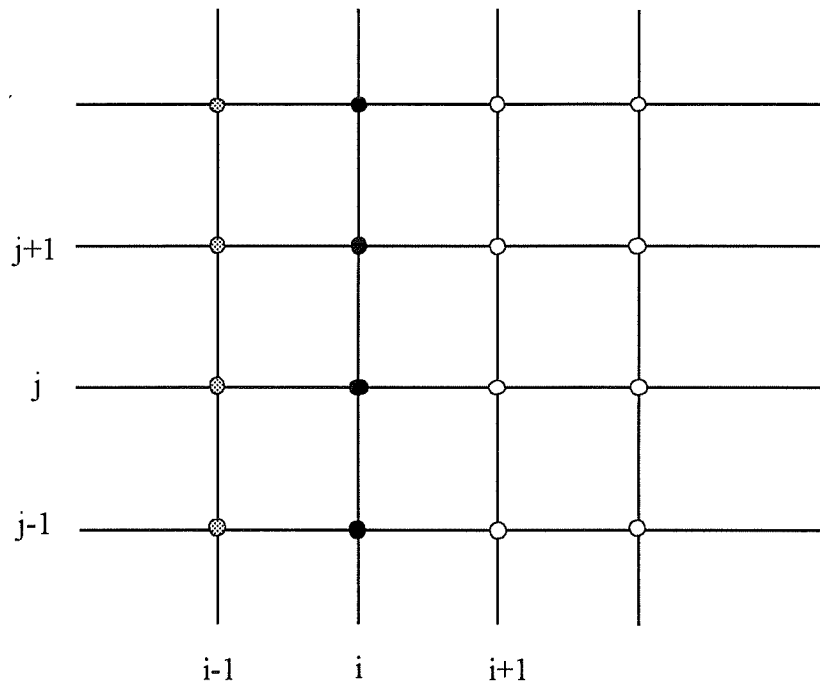
Figure 4.3   The configuration for relaxation along a column
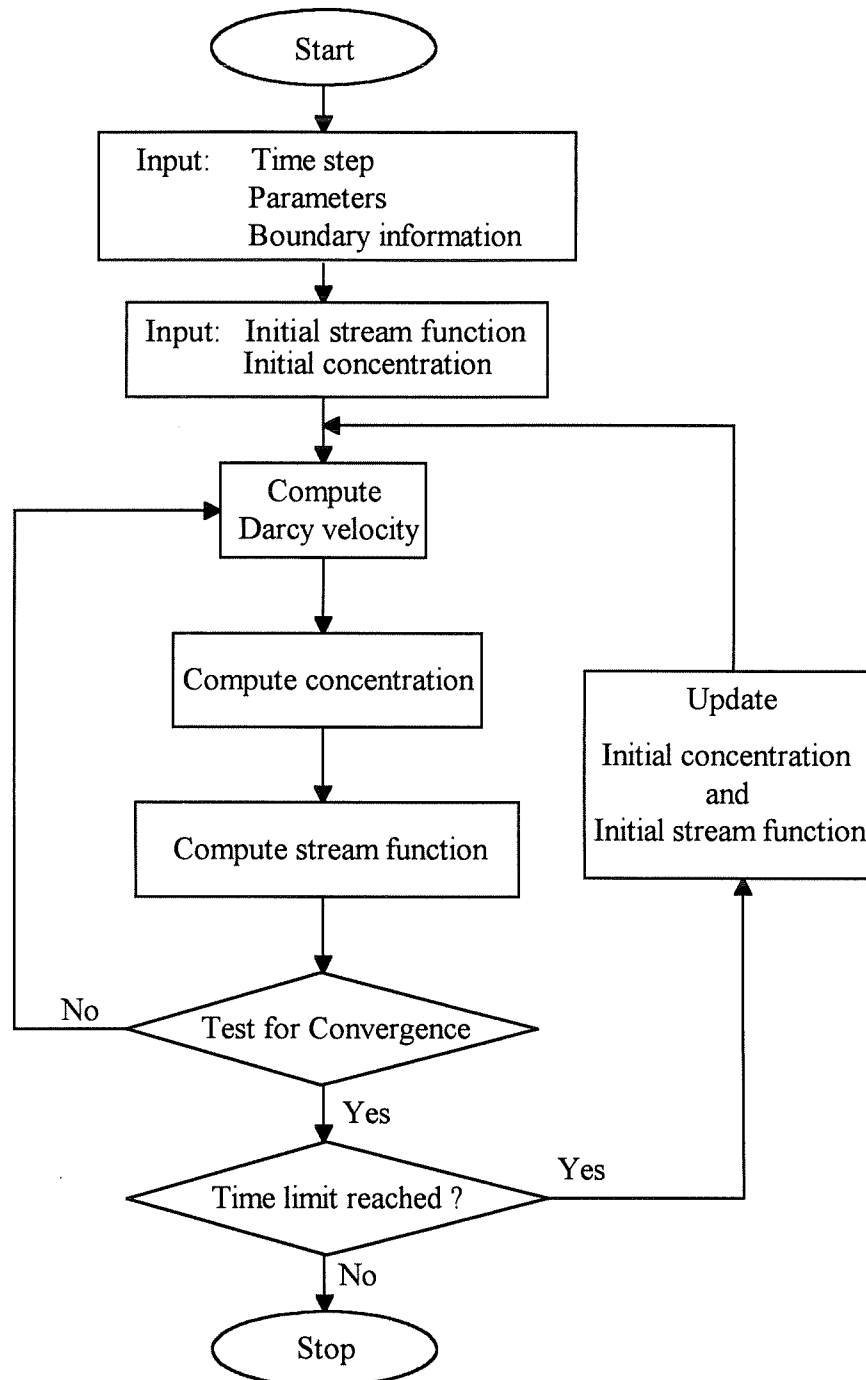
Figure 4.4 Flow chart of computation procedure
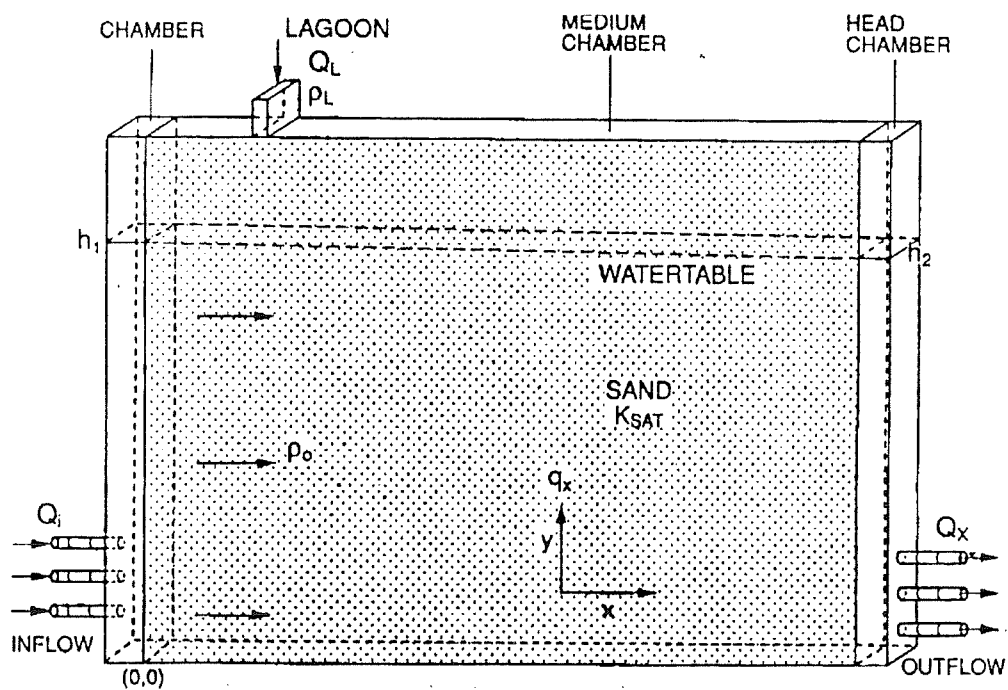
Figure 4.5 Flow container used in the experiment of Oostrom (1992)
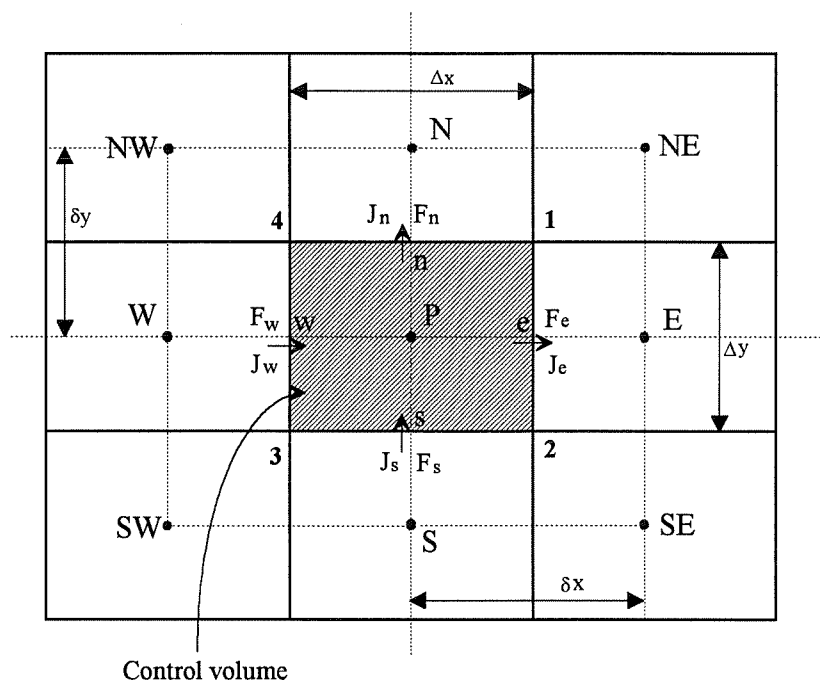
Figure 4.6 Control volume for a quadrilateral mesh
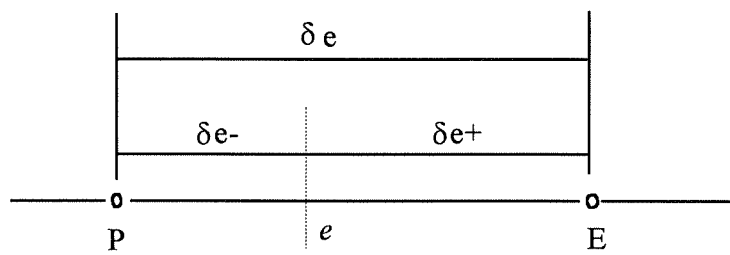
Figure 4.7   Distances associated with the interface *e*
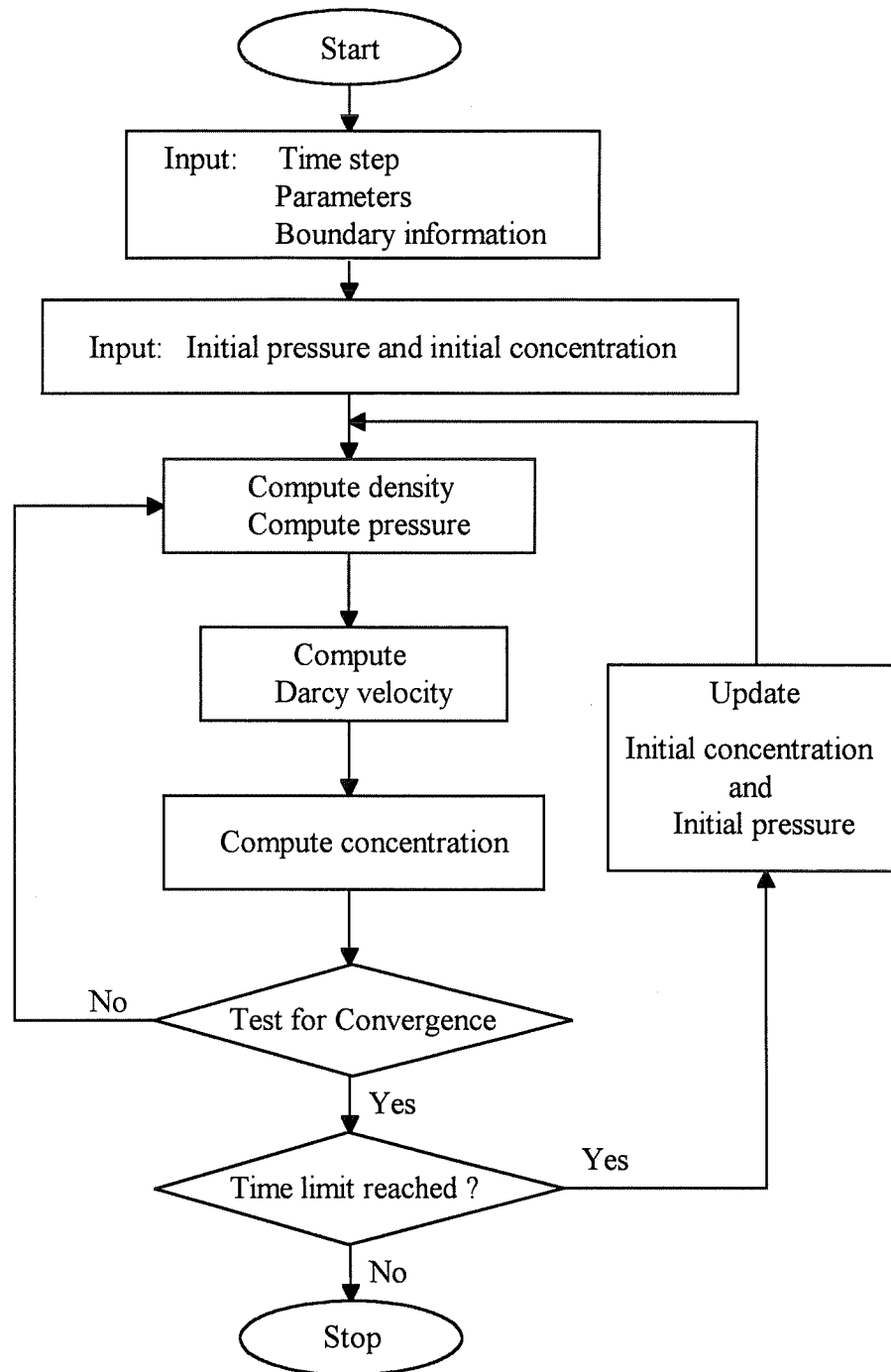
Figure 4.8   Flow chart of computation procedure
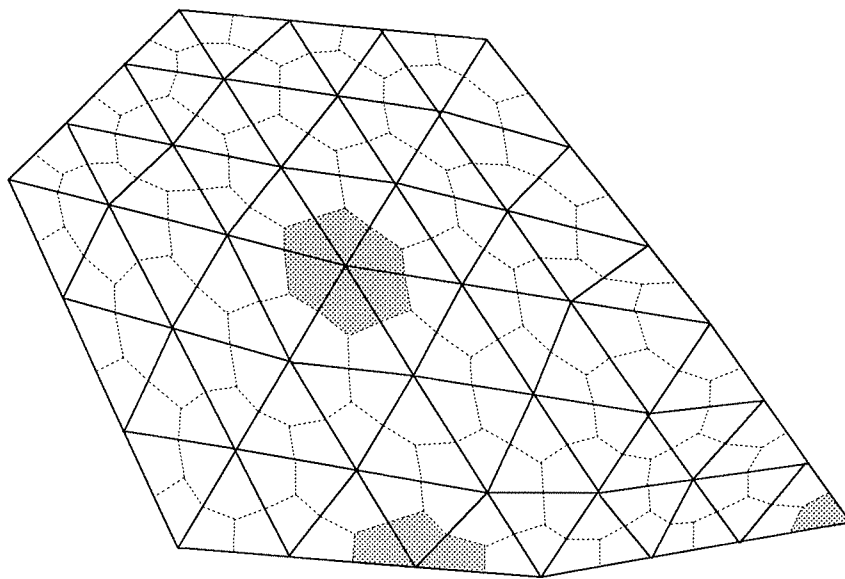
Figure 4.9   An irregular shaped calculation domain and its discretization into three-node triangular elements and polygonal control volumes
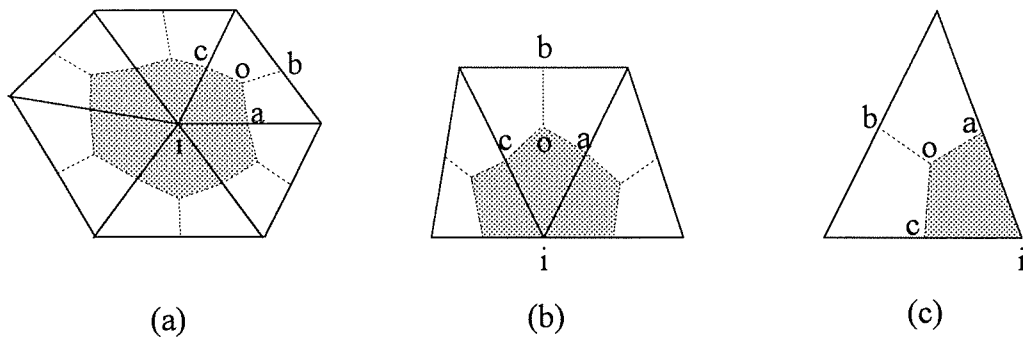
Figure 4.10   Details of the discretization in Fig. 4.9 and related nomenclature
(a) an internal node;
(b) a boundary node with three associated elements;
(c) a boundary node with one associated element.
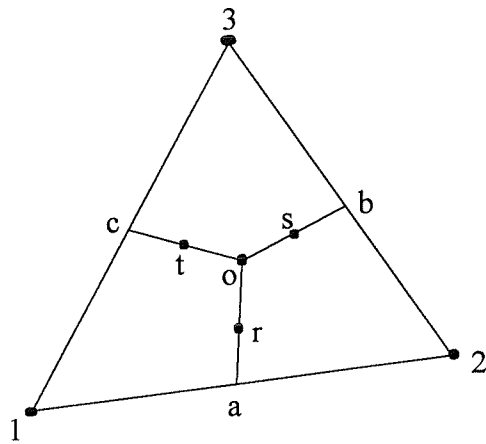
Figure 4.11   A typical three-node triangular element and the related nomenclature
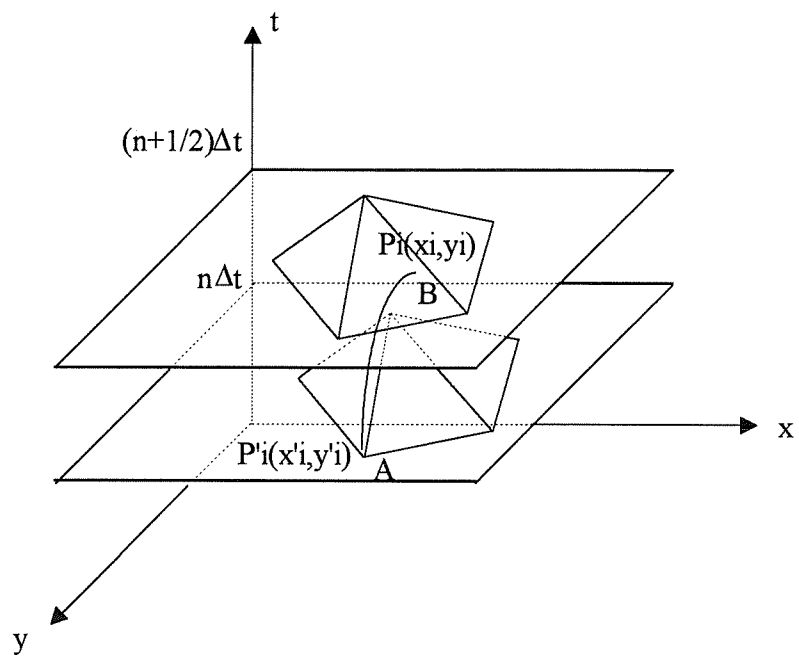
Figure 4.12   Sketch of a characteristic curve AB
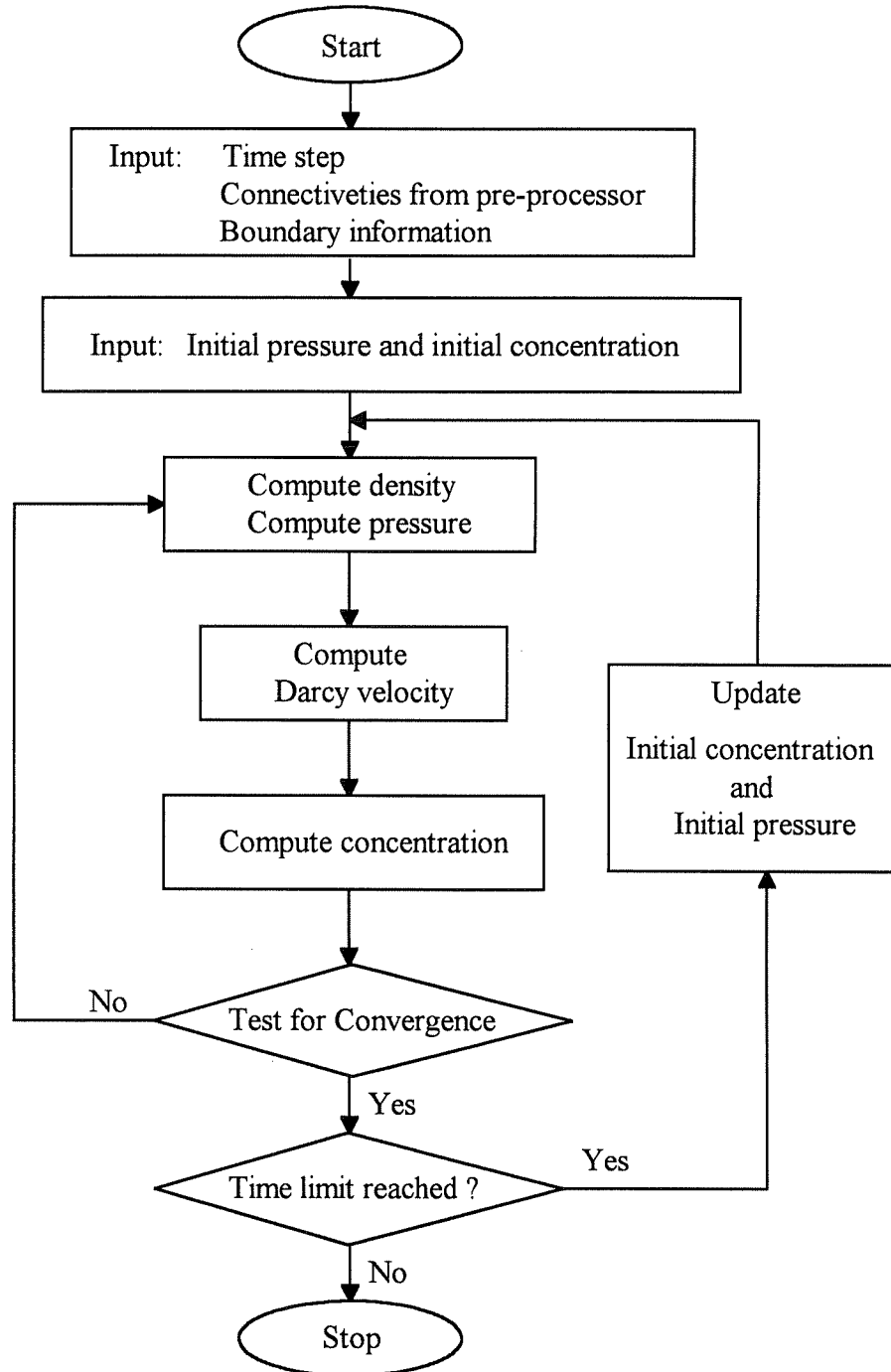
Figure 4.13   Flow chart of computation procedure

$$\Psi = \Psi_1 + (\Psi_1 - \Psi_2)\,\tilde{z}$$

$$\Psi = \Psi_2, \quad \frac{\partial \tilde{C}}{\partial \tilde{z}} = 0$$

D   C

$$\tilde{C} = 0$$

$$\frac{\partial \Psi}{\partial \tilde{x}} = 0$$

$$\frac{\partial \tilde{C}}{\partial \tilde{x}} = 0$$

E

$$\tilde{C} = 1$$

F

$$\tilde{C} = 0$$

A   B

$$\Psi = \Psi_1, \quad \frac{\partial \tilde{C}}{\partial \tilde{z}} = 0$$
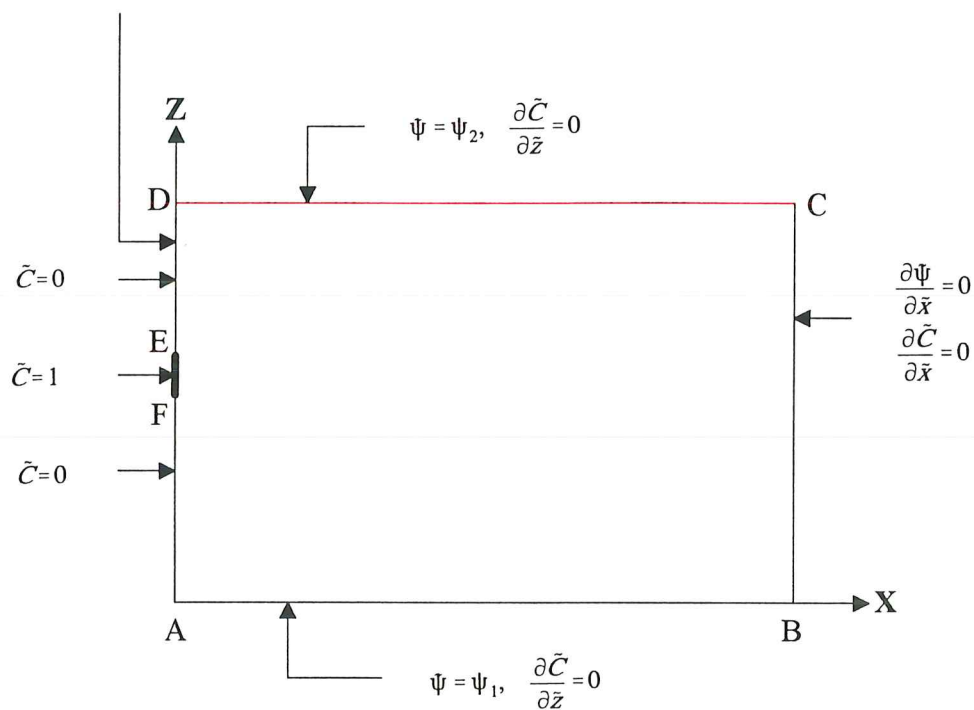
Figure 5.1 Calculation domain and boundary conditions

Concentration isolines (Min: 0.1, Max: 0.9)
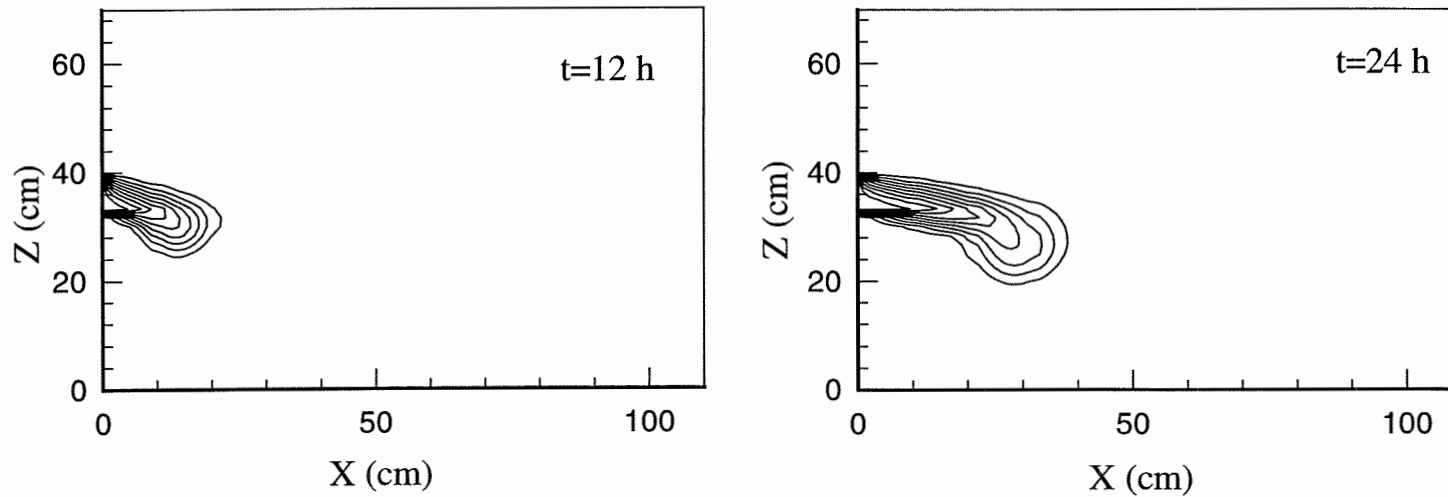
Figure 5.2 Instability development for a 2000-mg/L NaCl source in homogeneous media
at t=12,24,36,42,48,54,60,66,72,84,96,108 and 120 hours

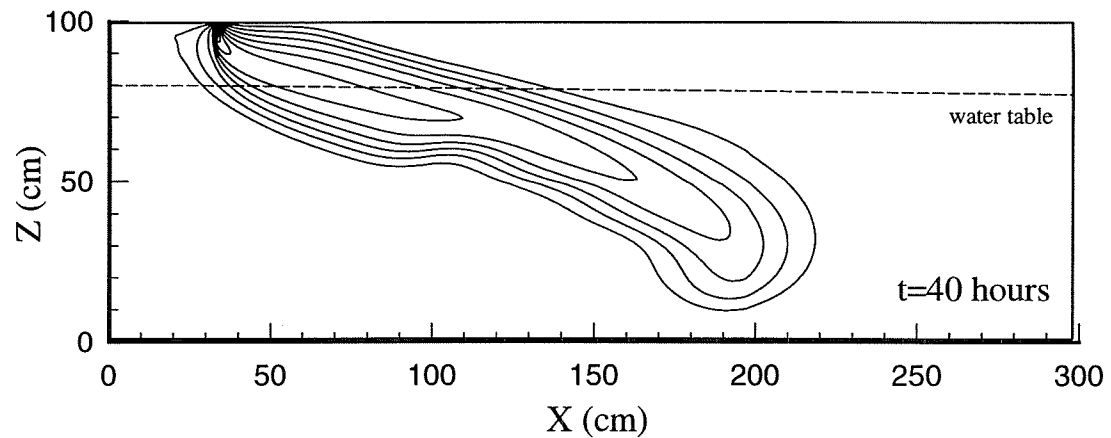Concentration isolines (Min: 0.1, Max: 0.9)
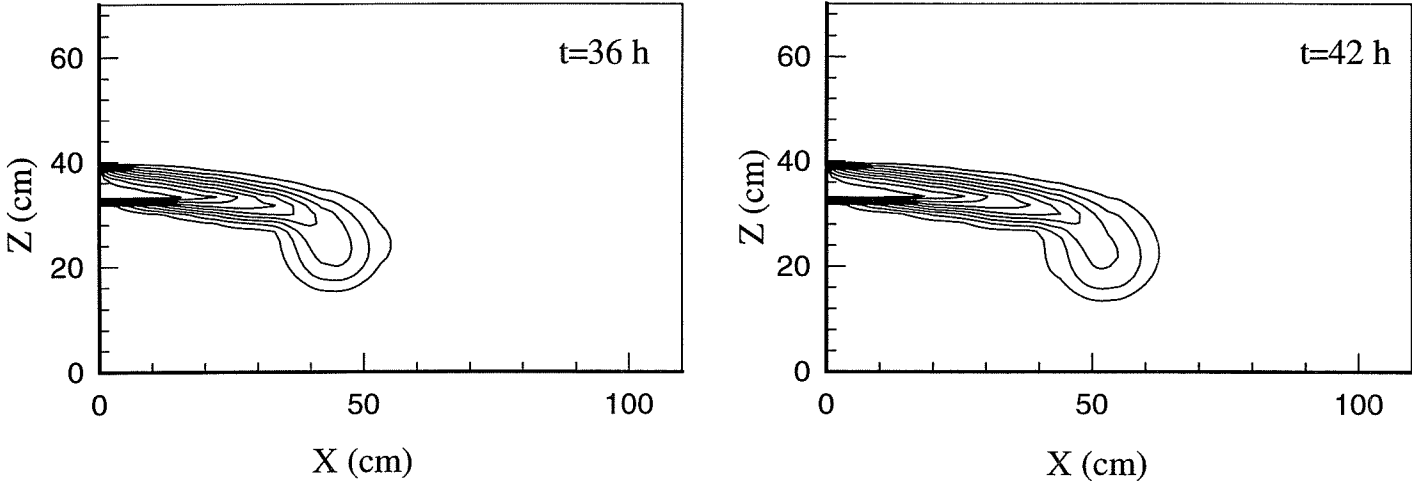
Figure 5.2   Continued

Concentration isolines (Min: 0.1, Max: 0.9)
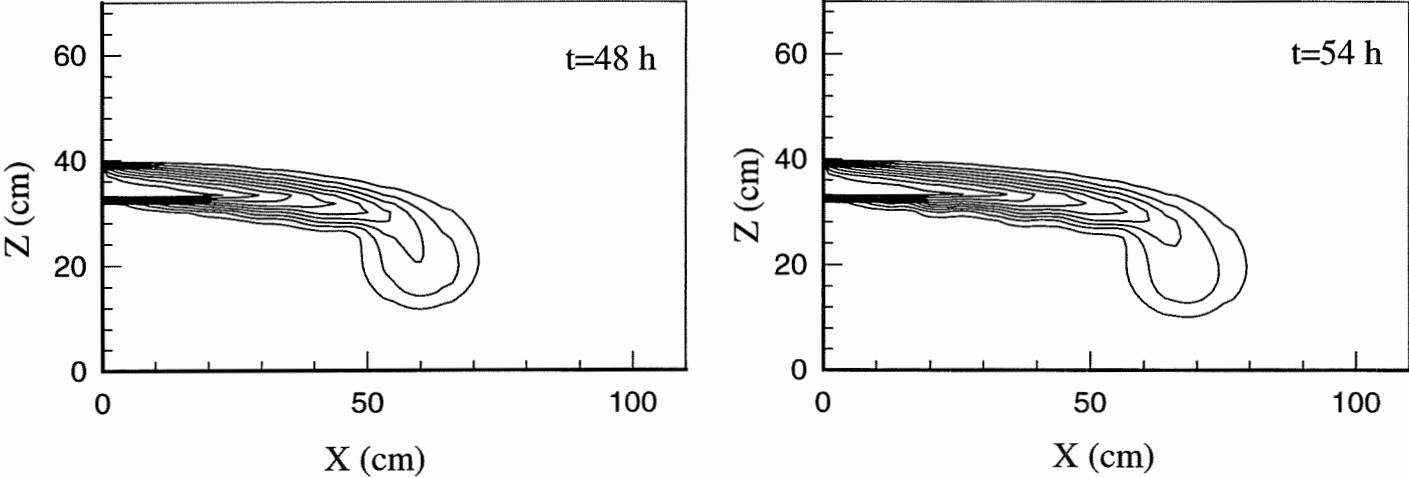
Figure 5.2   Continued
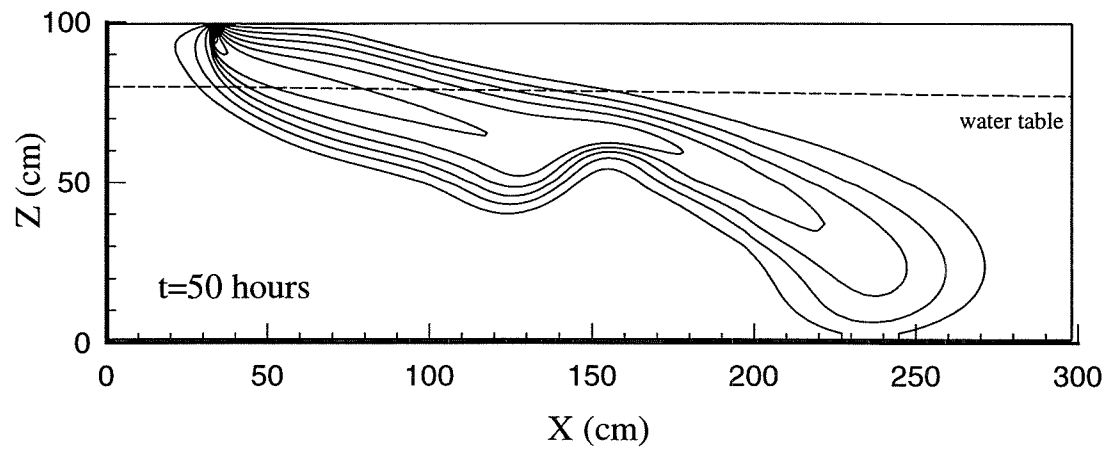
Concentration isolines (Min: 0.1, Max: 0.9)
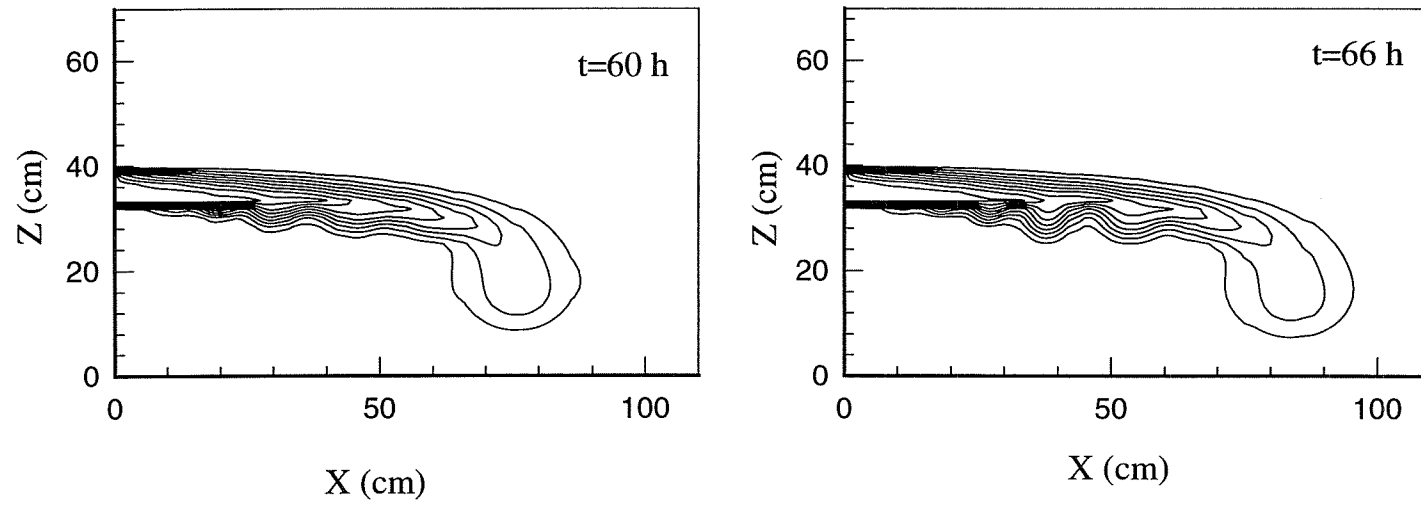
Figure 5.2   Continued

Concentration isolines (Min: 0.1, Max: 0.9)
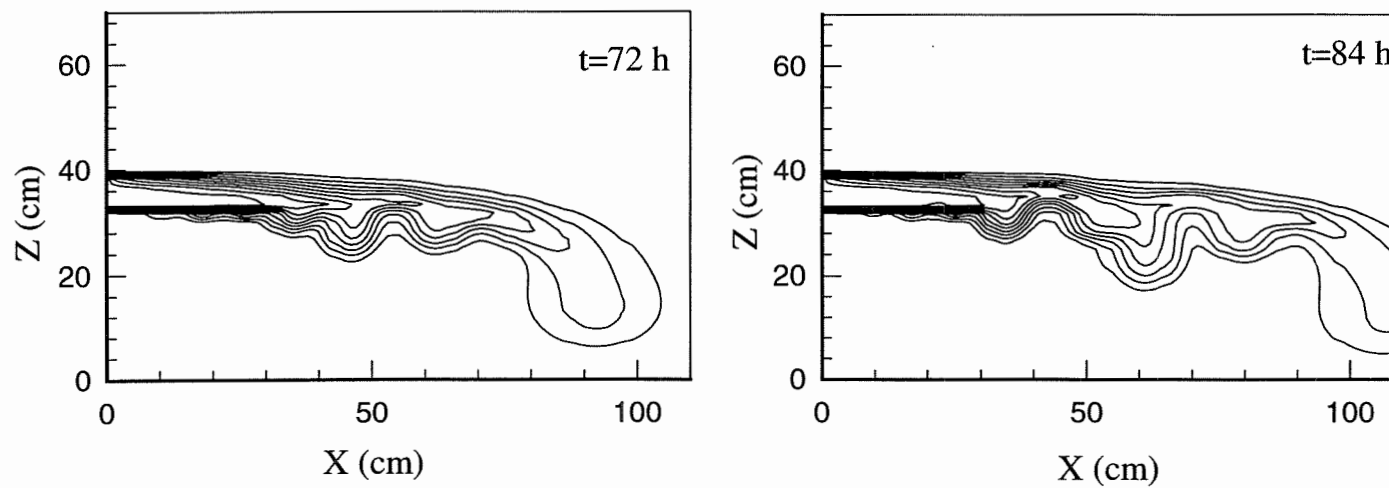
Figure 5.2   Continued

Concentration isolines (Min: 0.1, Max: 0.9)
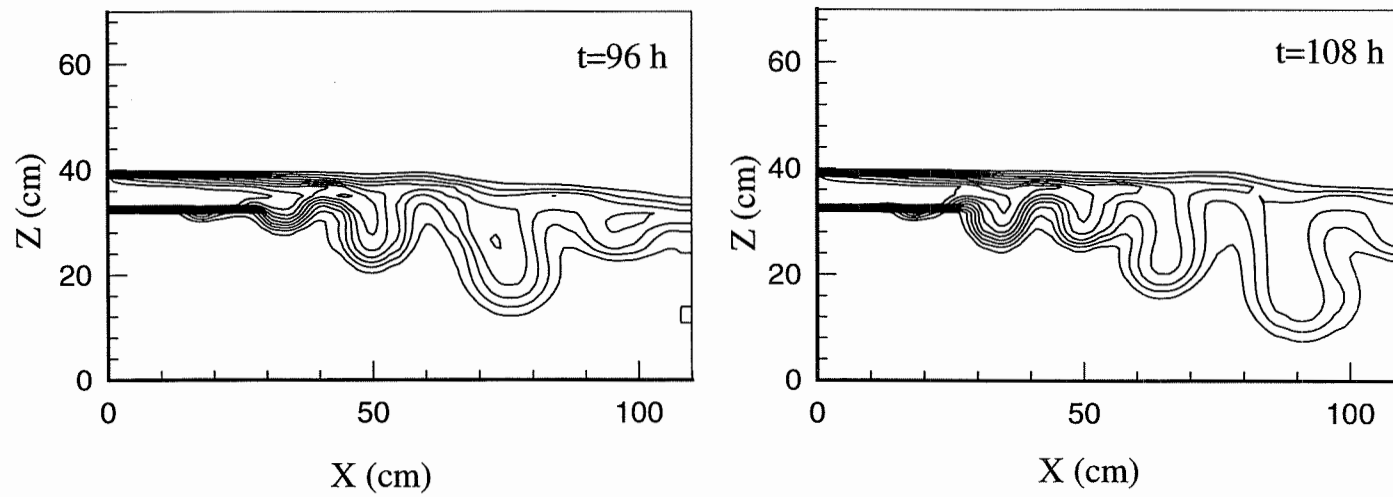
Figure 5.2   Continued

Concentration isolines (Min: 0.1, Max: 0.9)
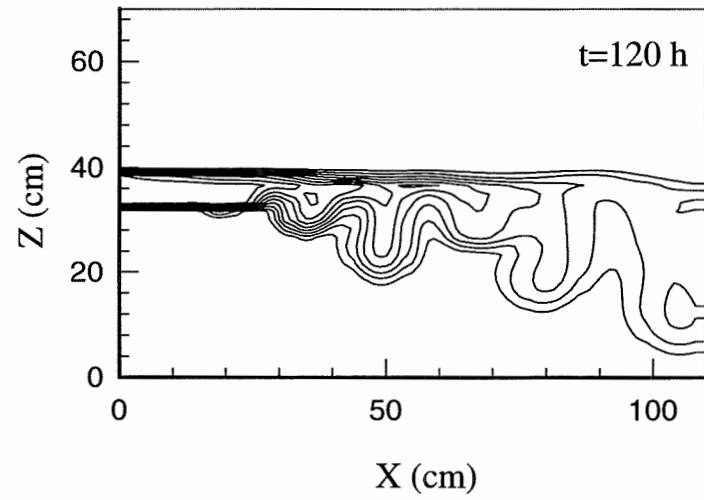
Figure 5.2   Continued

Concentration isolines (Min: 0.1, Max: 0.9)
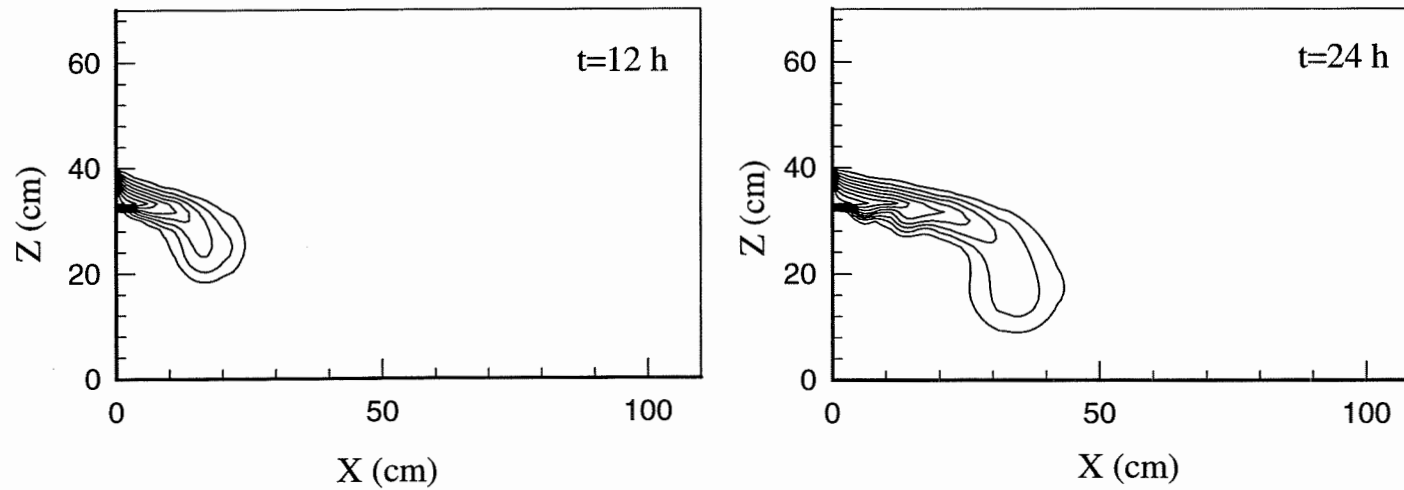
Figure 5.3 Instability development for a 5000-mg/L source in homogeneous media
at t=12,24,36,42,48,54,60,66 and 72 hours
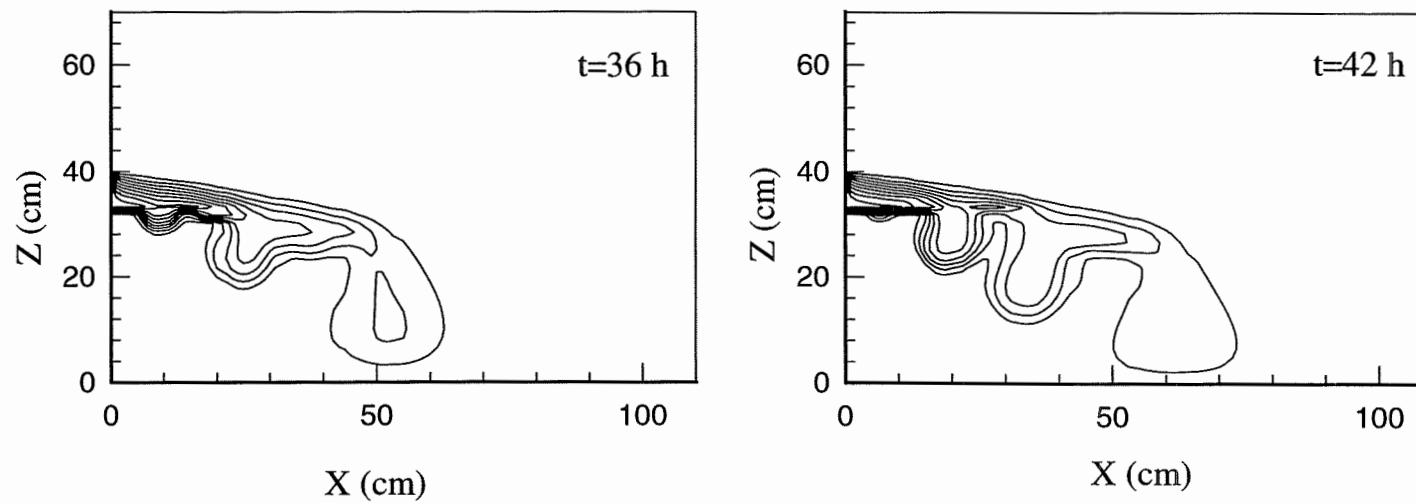
Concentration isolines (Min: 0.1, Max: 0.9)

Figure 5.3   Continued

Concentration isolines (Min: 0.1, Max: 0.9)
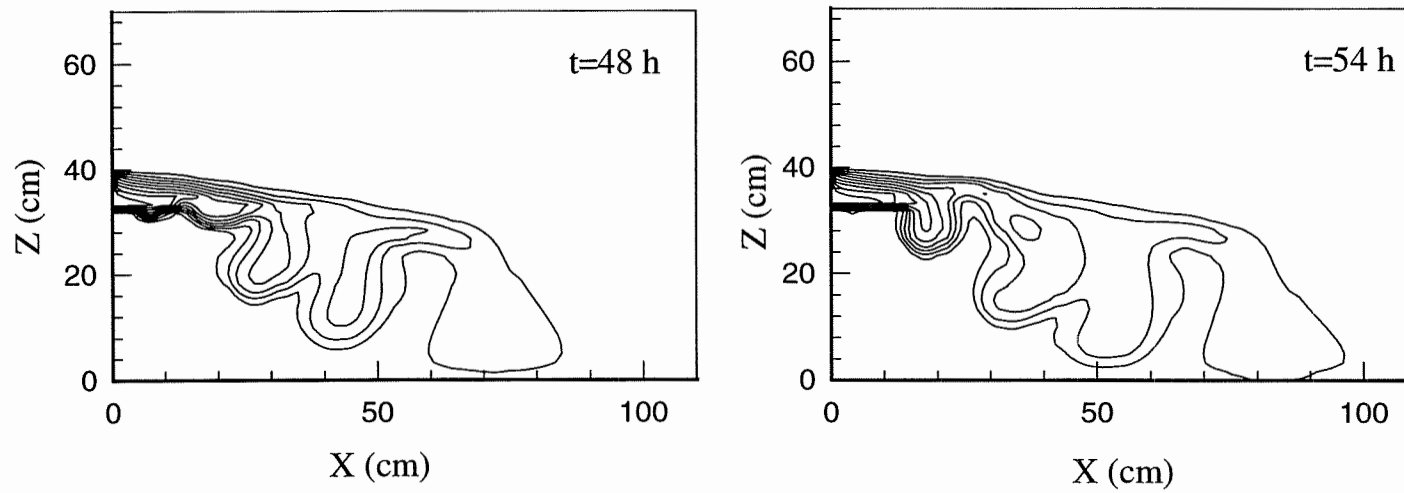
Figure 5.3   Continued

Concentration isolines (Min: 0.1, Max: 0.9)
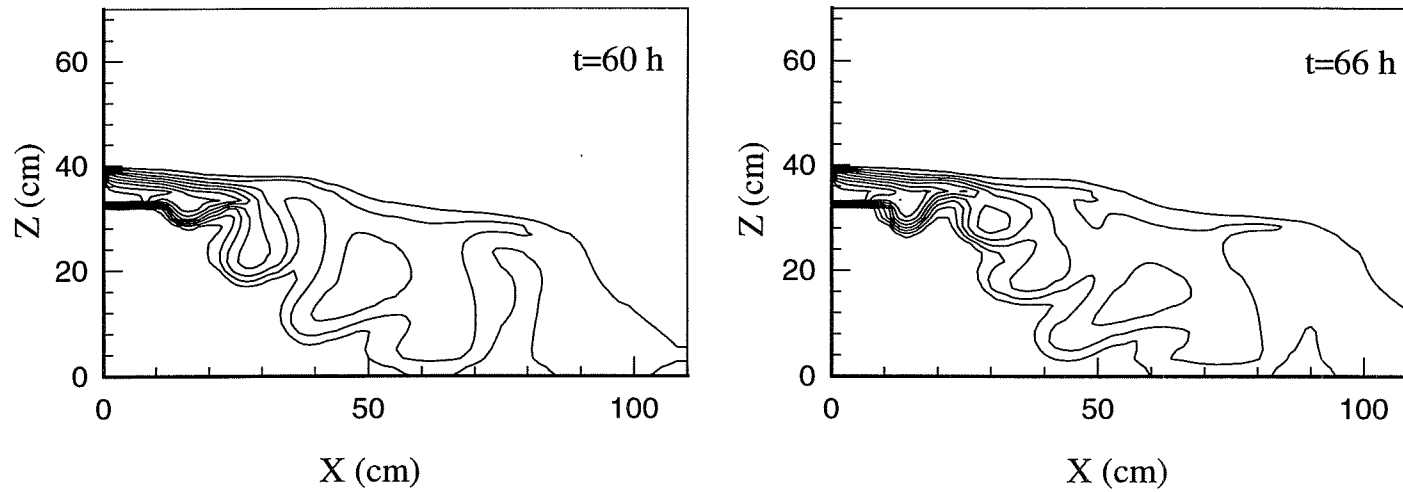
Figure 5.3 Continued

Concentration isolines (Min: 0.1, Max: 0.9)
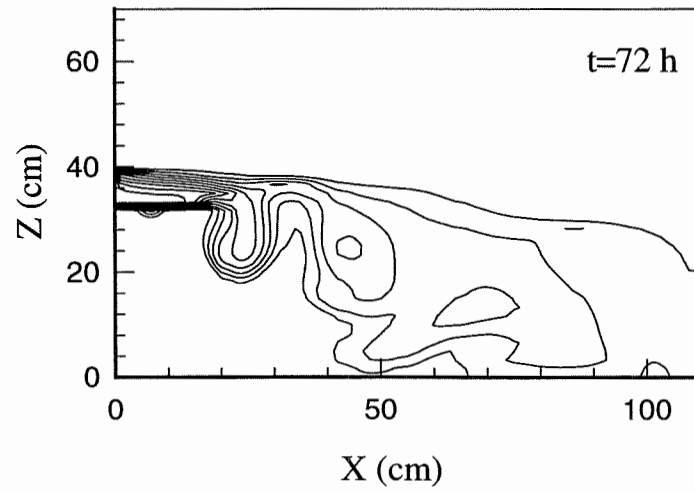
Figure 5.3   Continued

Concentration isolines (Min: 0.1, Max: 0.9)
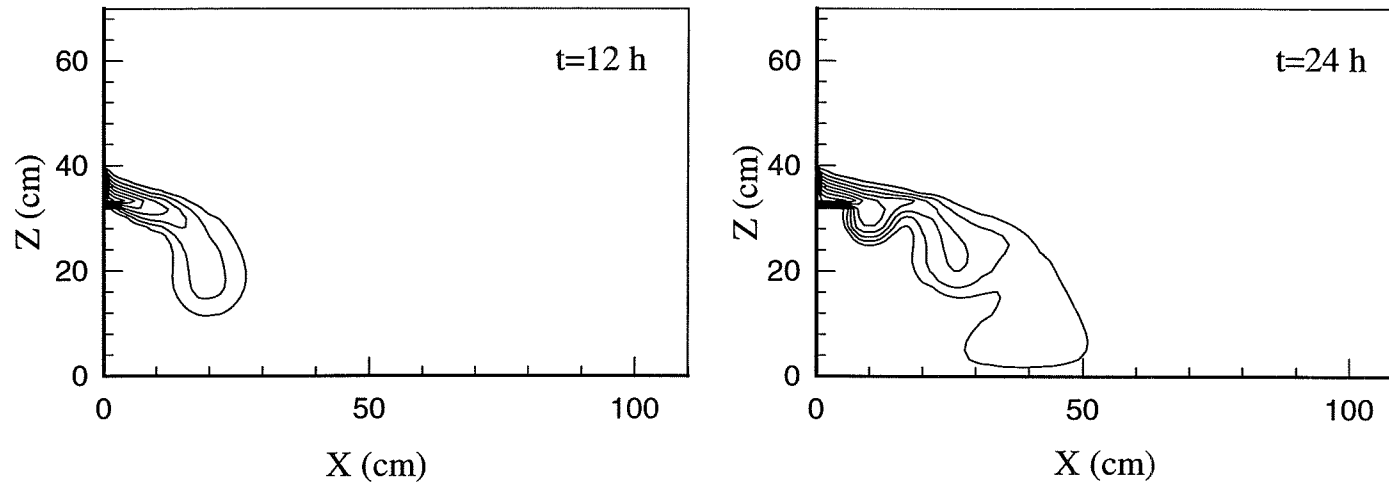
Figure 5.4 Instability development for a 10,000-mg/L NaCl source in homogeneous media at t=12,24,36,42,48 and 54 hours
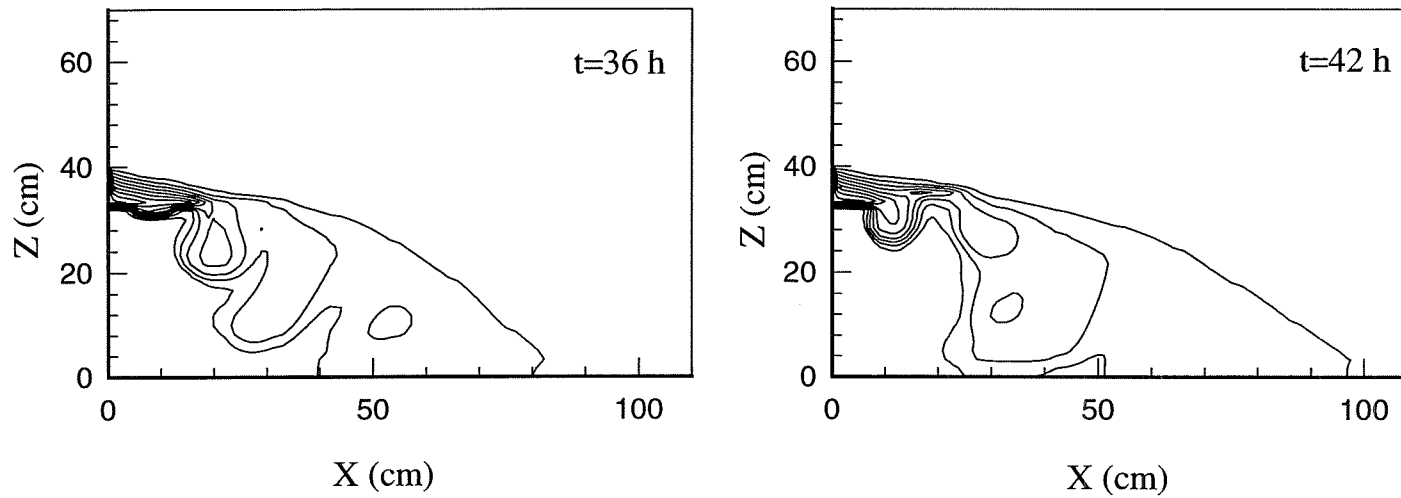
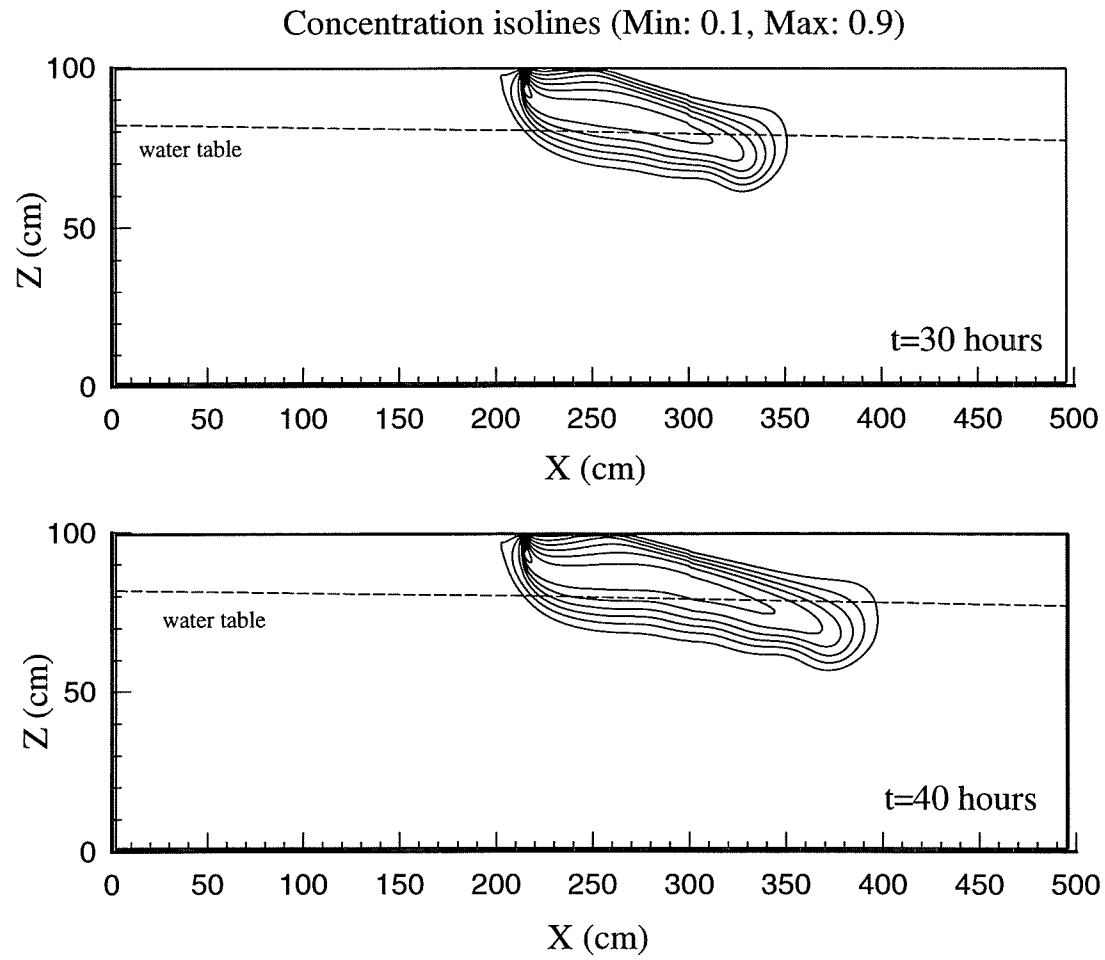Concentration isolines (Min: 0.1, Max: 0.9)

Figure 5.4   Continued

Concentration isolines (Min: 0.1, Max: 0.9)
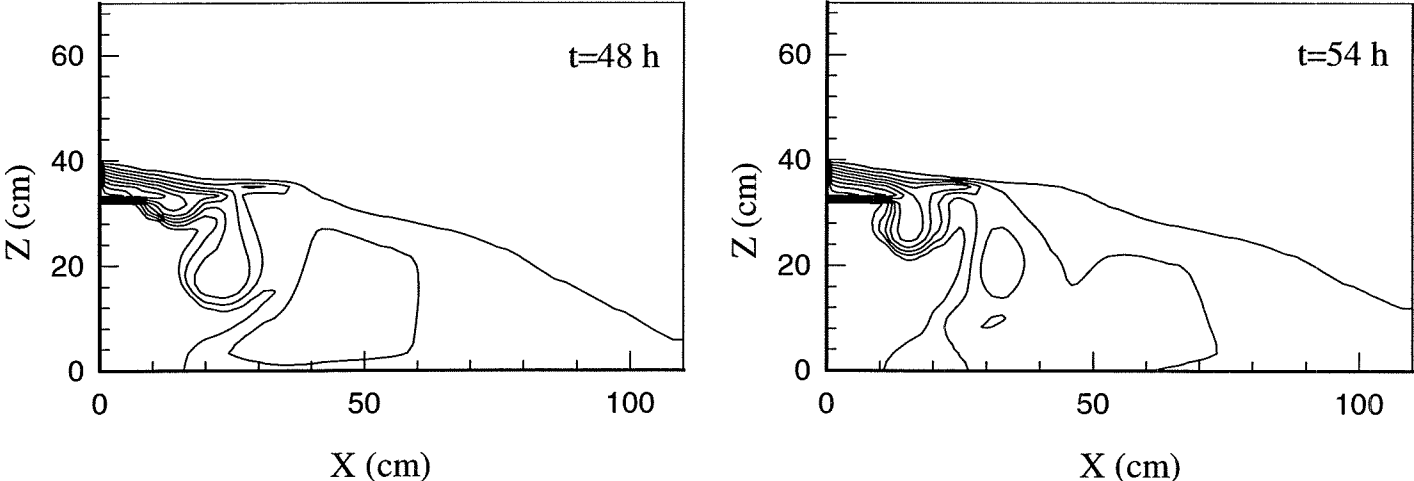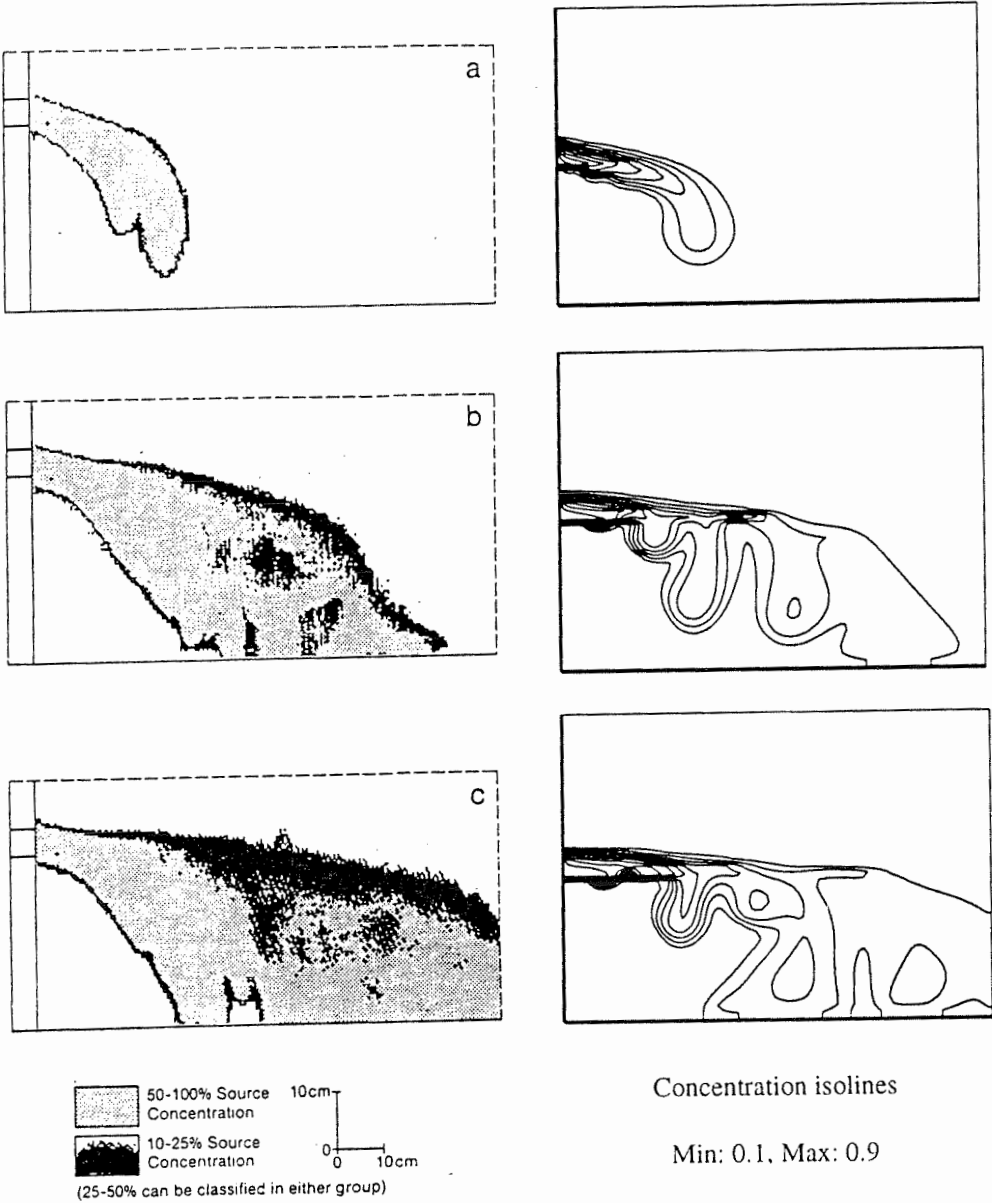
Figure 5.4 Continued

Figure 5.5 Instability development for a 5,000 mg/l NaCl source in homogeneous media at (a) t=12 hours, (b) t=54 hours, and (c) t=72 hours

Concentration isolines (Min: 0.1, Max: 0.9)
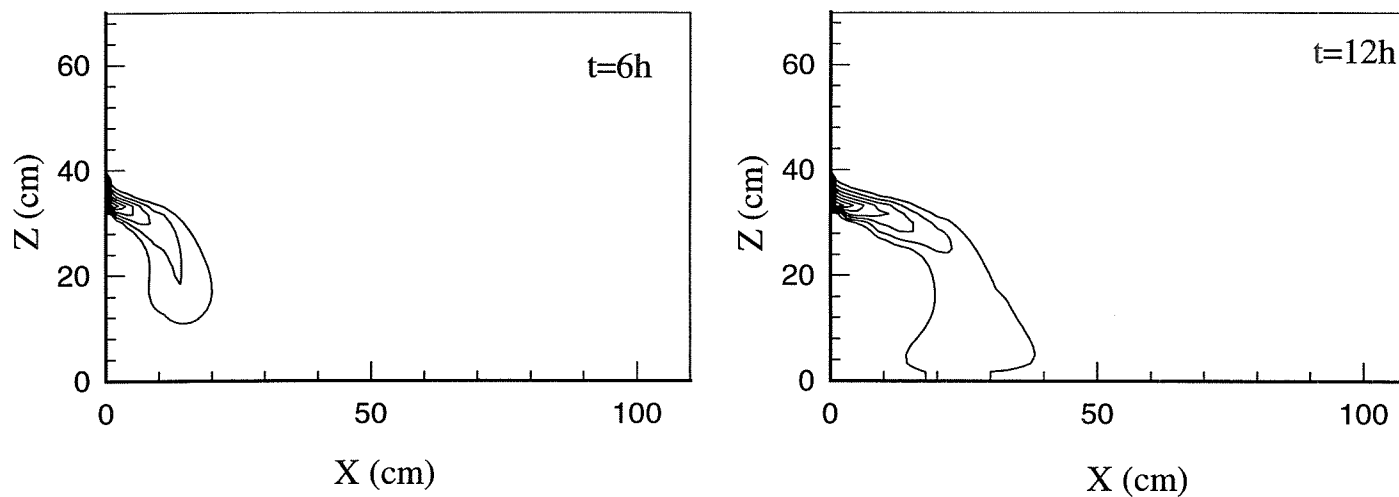
Figure 5.6 Instability development for a 25,000-mg/L source in homogeneous media at t=6, 12, 18, 24, 30, 36, 42, 48 and 54 hours
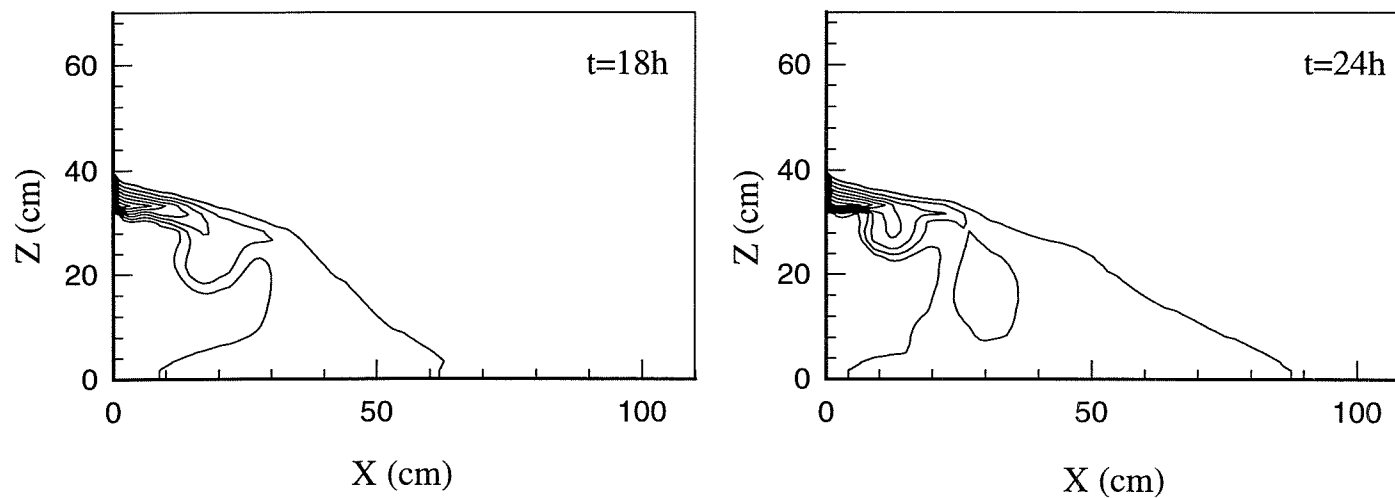
Concentration isolines (Min: 0.1, Max: 0.9)

Figure 5.6   Continued

Concentration isolines (Min: 0.1, Max: 0.9)
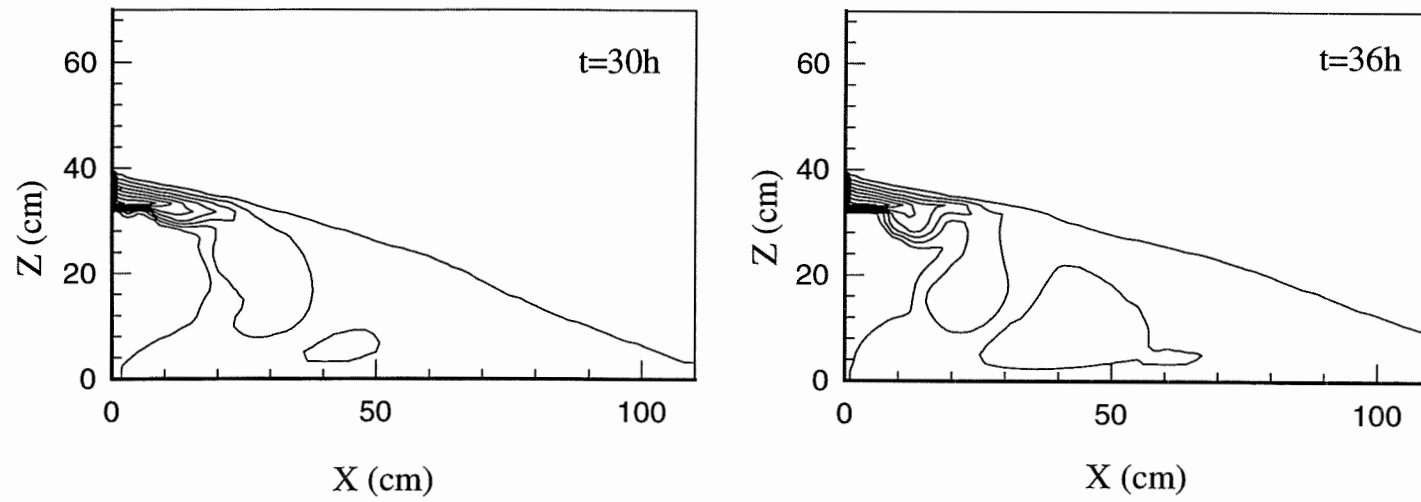
Figure 5.6   Continued

Concentration isoline (Min: 0.1, Max: 0.9)
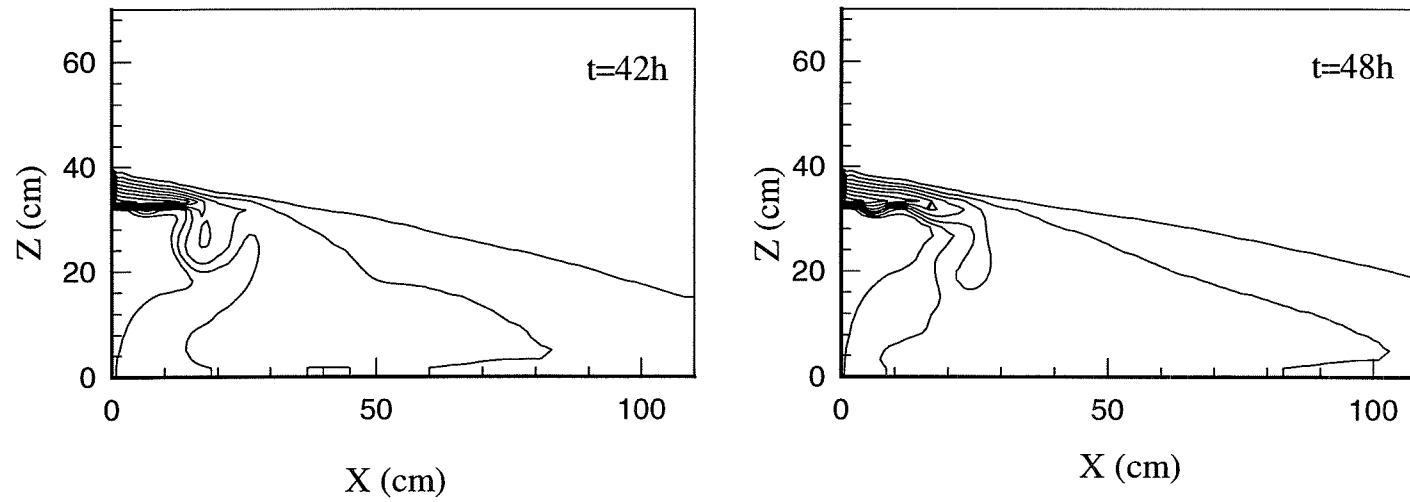
Figure 5.6   Continued

Concentration isolines (Min: 0.1, Max: 0.9)
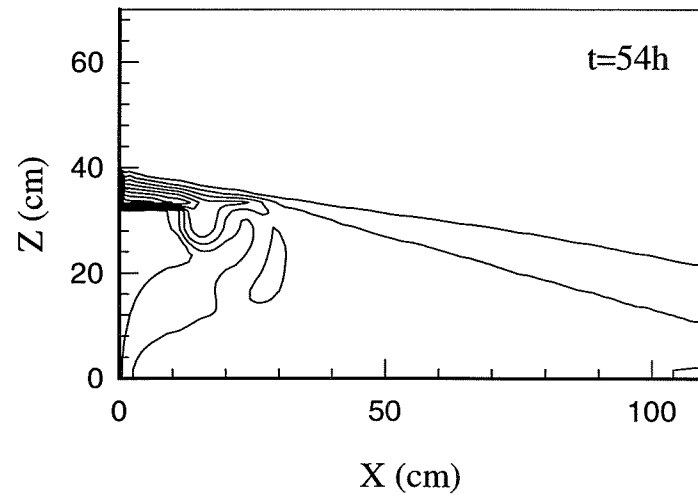
Figure 5.6   Continued

Concentration isolines (Min: 0.1, Max: 0.9)
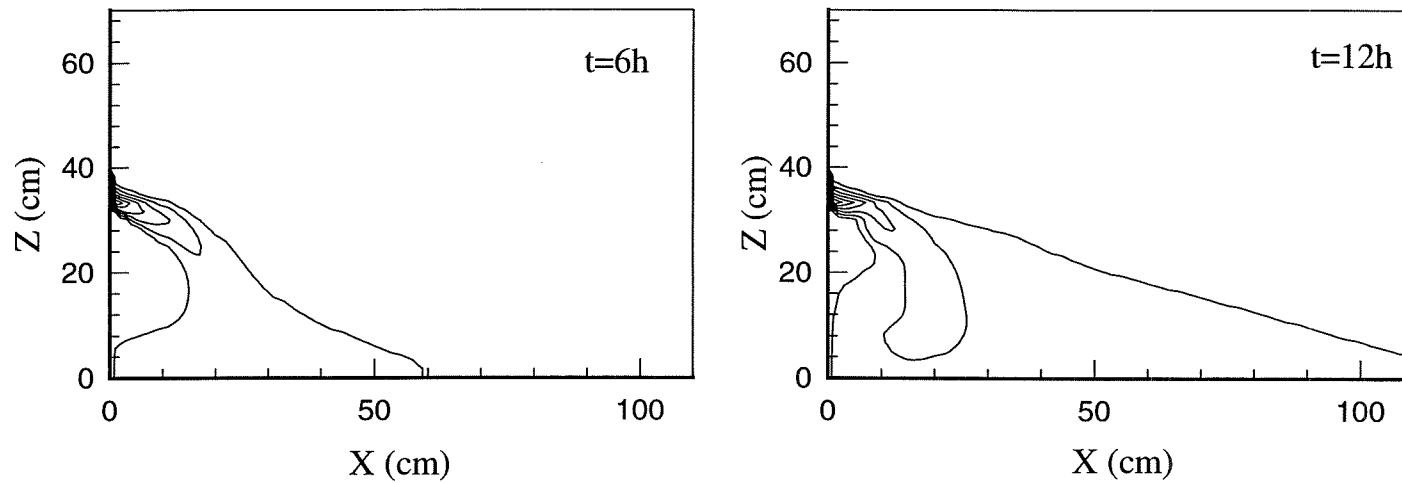
Figure 5.7 Instability development for a 100,000-mg/L source in homogeneous media
at t=6, 12 and 18 hours

Concentration isolines (Min: 0.1, Max: 0.9)
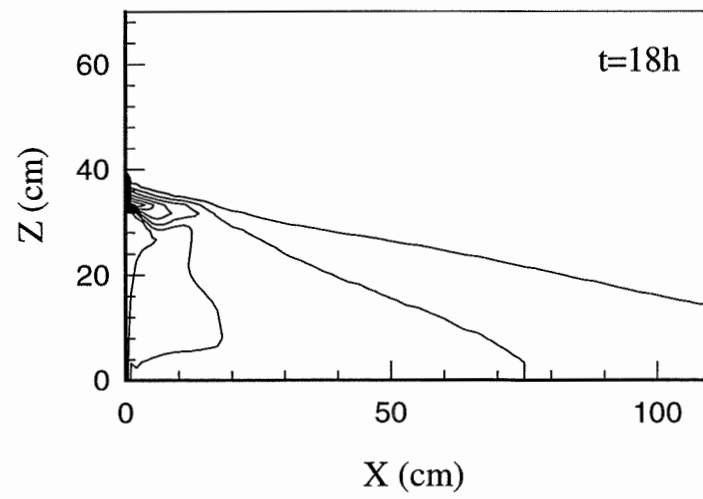
Figure 5.7 Continued

Concentration isolines (Min: 0.1, Max: 0.9)
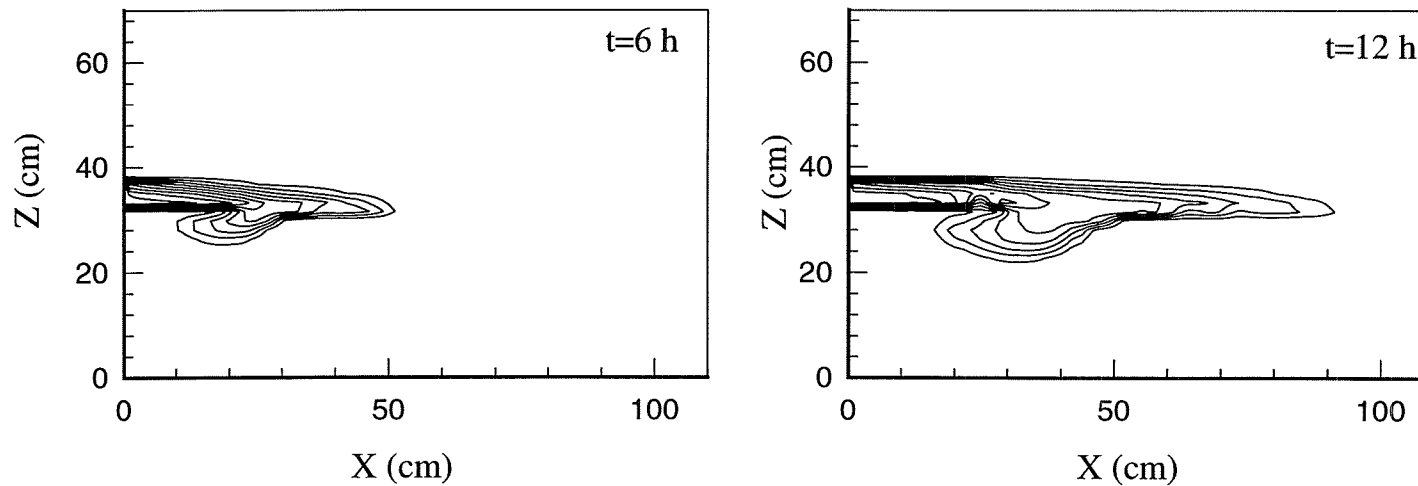
Figure 5.8 Instability development for a 5000-mg/L NaCl source in heterogeneous media
at t=6,12,18,24,30,36,42,48,54,60 and 66 hours

Concentration isolines (Min: 0.1, Max: 0.9)
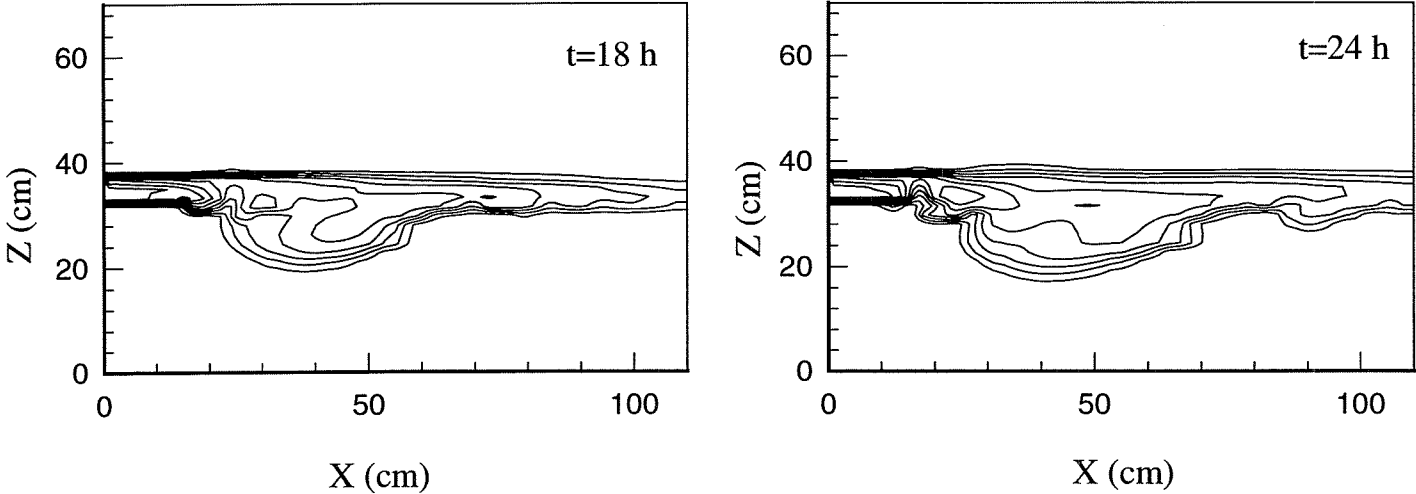
Figure 5.8 Continued

Concentration isolines (Min: 0.1, Max: 0.9)
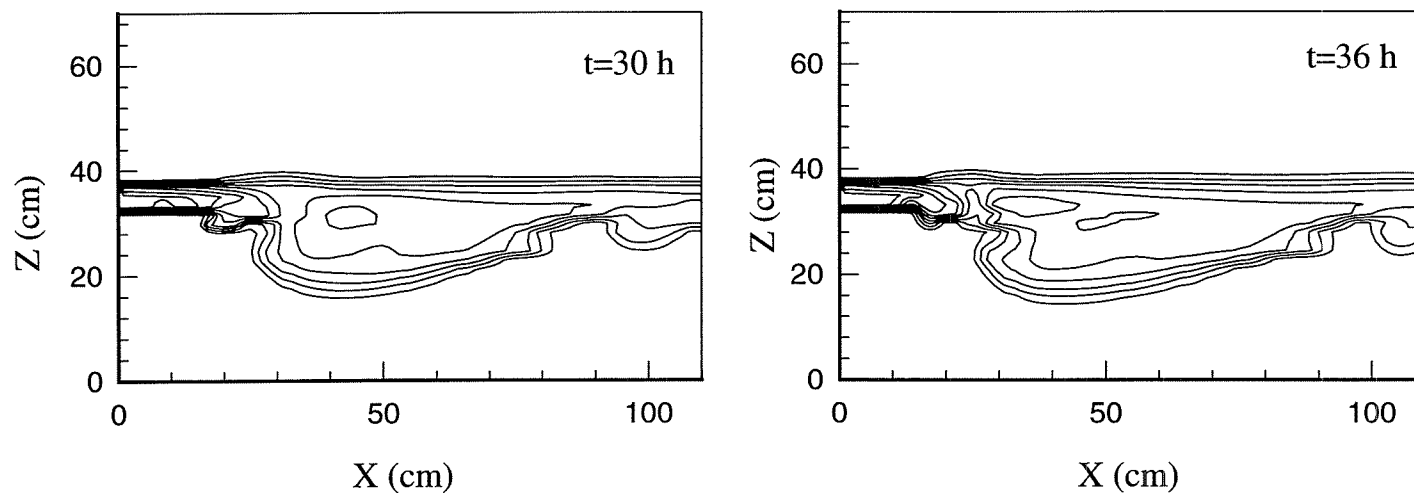
Figure 5.8   Continued

Concentration isolines (Min: 0.1, Max: 0.9)
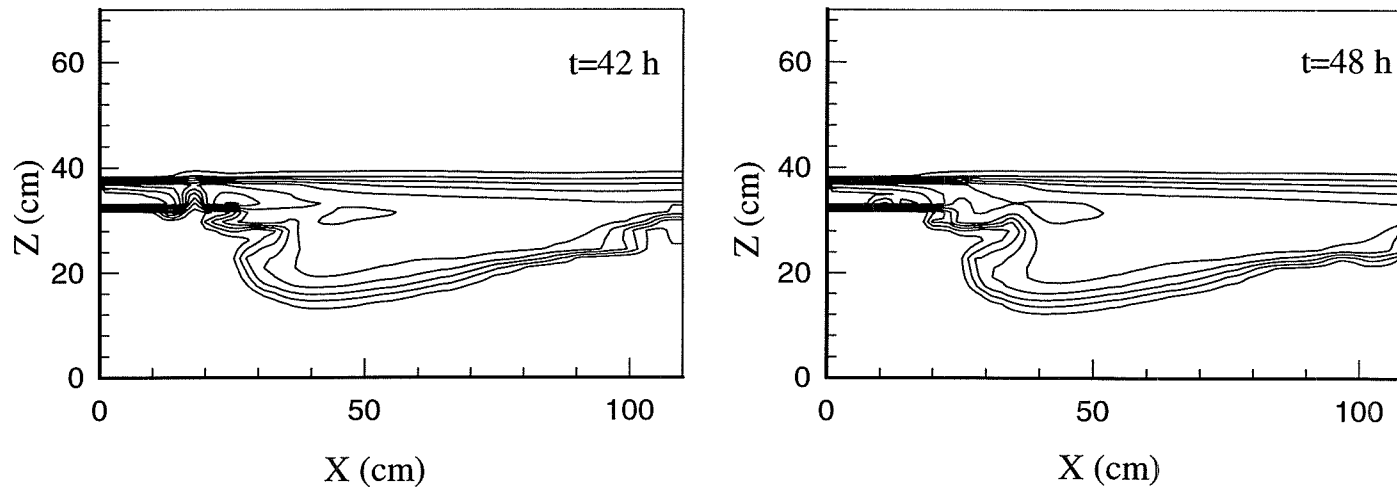
Figure 5.8   Continued

Concentration isolines (Min: 0.1, Nax: 0.9)
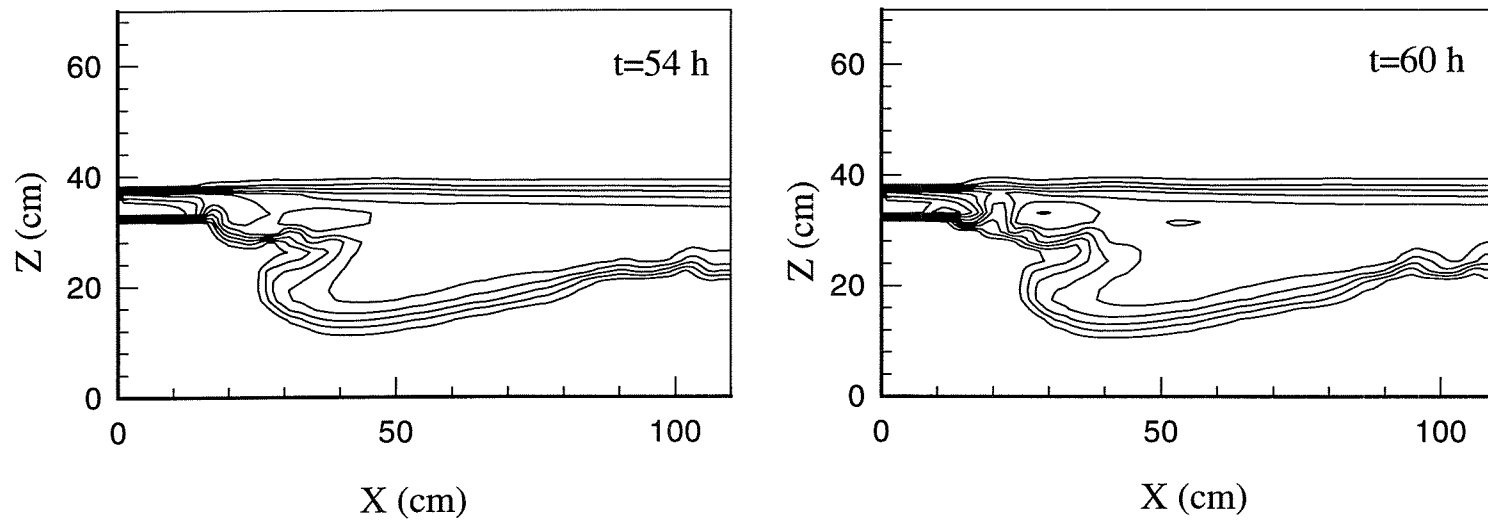
Figure 5.8   Continued

Concentration isolines (Min: 0.1, Max: 0.9)
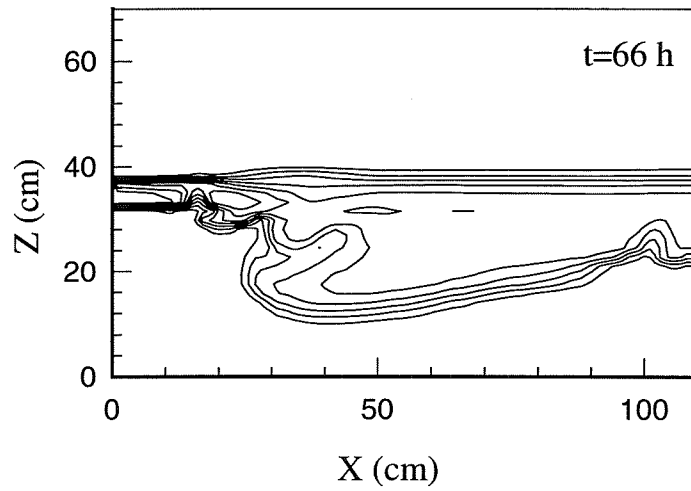
Figure 5.8 Continued

Concentration isolines (Min: 0.1, Max: 0.9)
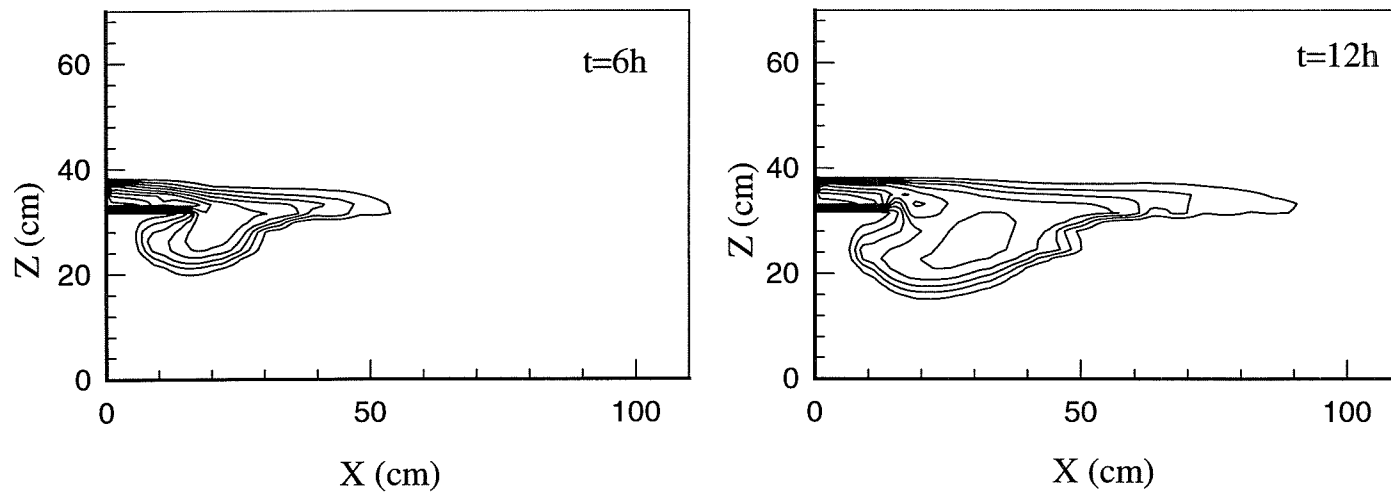
Figure 5.9 Instability development for a 10,000-mg/L NaCl source in heterogeneous media
at t=6, 12, 18, 36, 42, 48, 54, 60, 66 and 72 hours
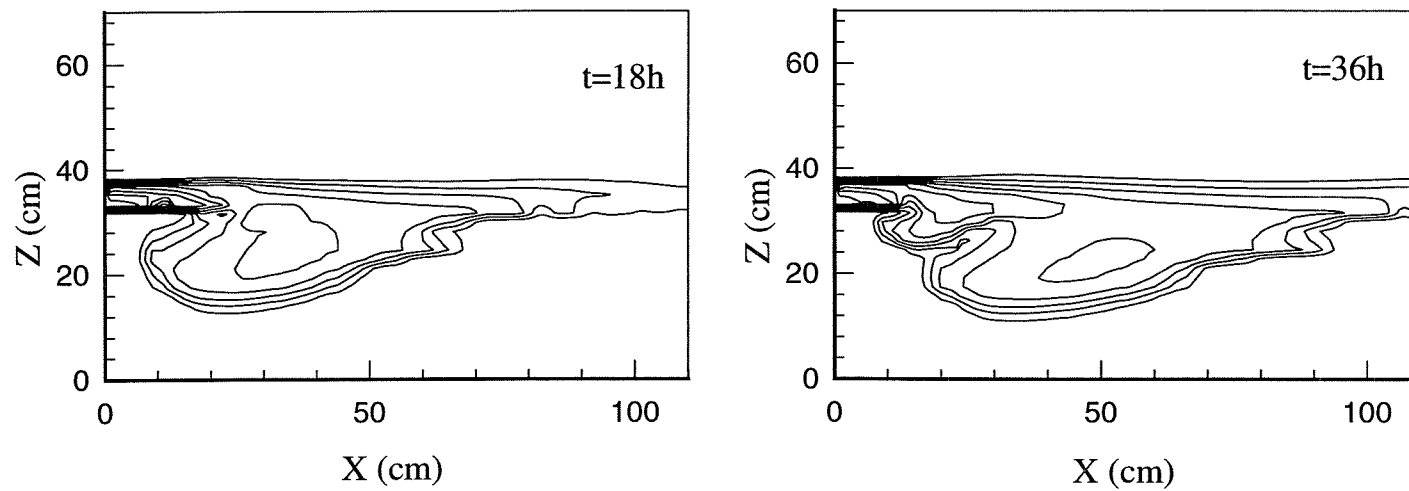
Concentration isolines (Min: 0.1, Max: 0.9)

Figure 5.9   Continued

Concentration isolines (Min: 0.1, Max: 0.9)

Figure 5.9   Continued

Concentration isolines (Min: 0.1, Max: 0.9)

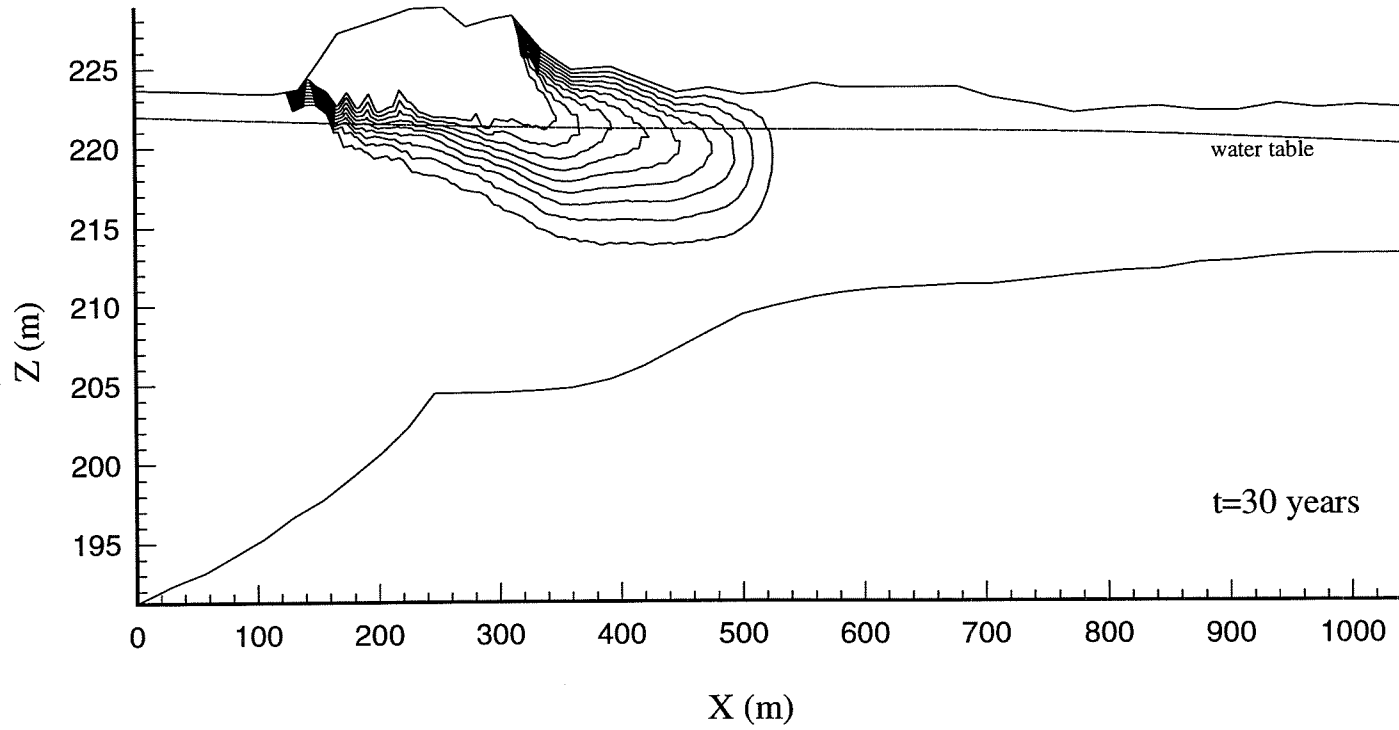

Figure 5.9   Continued

Concentration isolines (Min: 0.1, Max: 0.9)

Figure 5.9   Continued

50-100% Source Concentration

10-25% Source Concentration

(25-50% can be classified in either group)

10cm

0

0   10cm

Experimental Results
(Reproduced from Schincariol and Schwartz [1990])

Concentration isolines

Min: 0.1, Max: 0.9

Numerical Simulation

Figure 5.10   Instability development for a 5,000 mg/l NaCl source in heterogeneous
media at (a) t=12 hours, (b) t=24 hours, (c) t=54 hours, and (d) t=66 hours

50-100% Source
Concentration

10-25% Source
Concentration

(25-50% can be classified in either group)
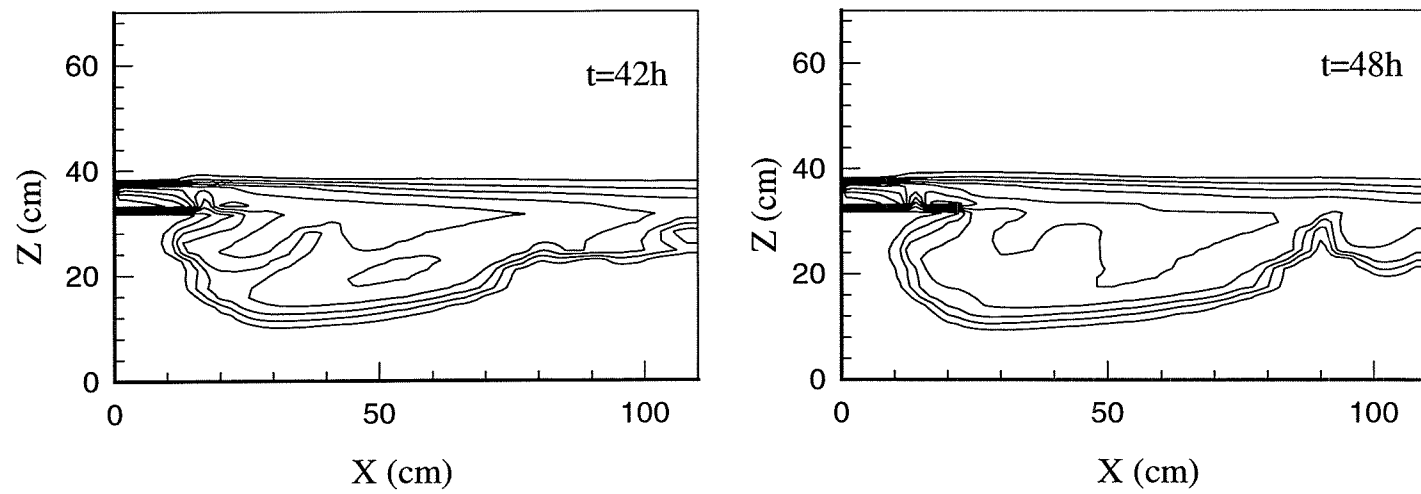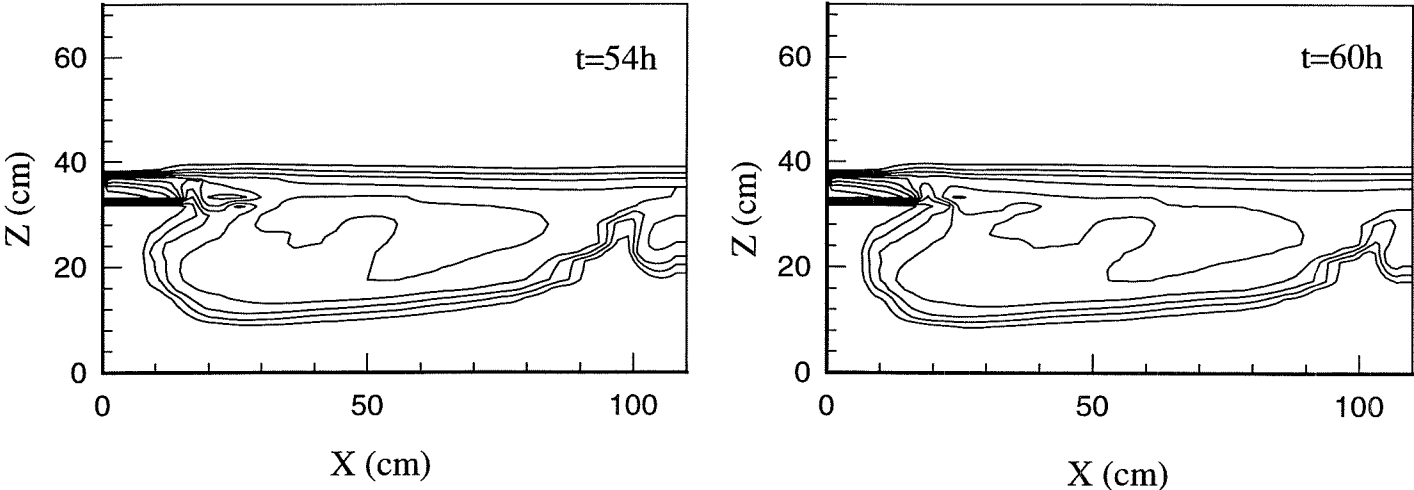
Concentration isolines

Min: 0.1, Max: 0.9
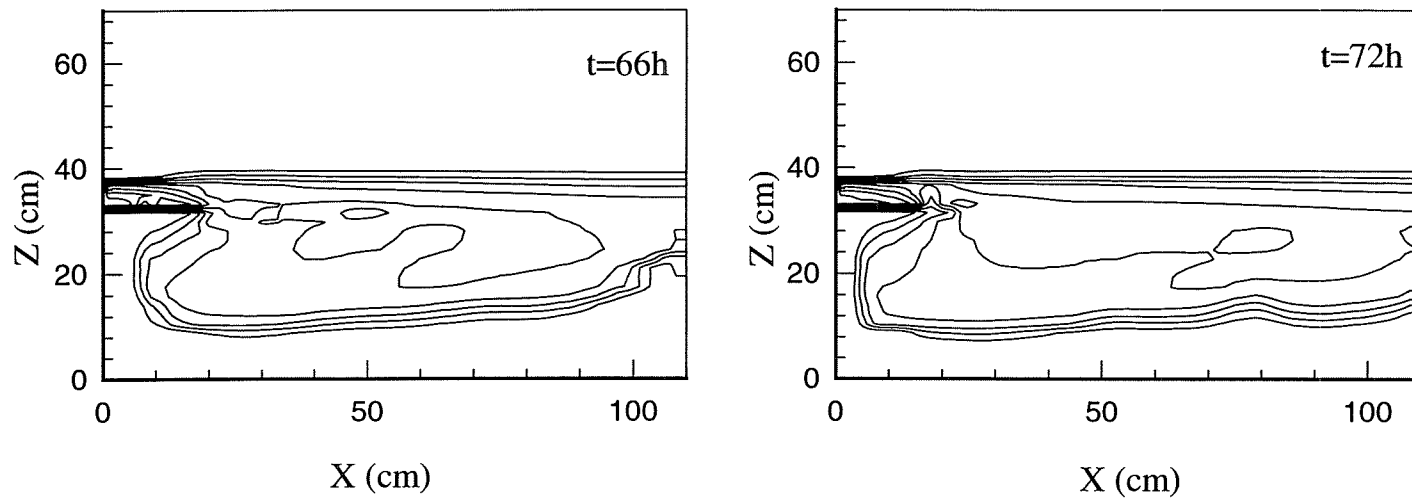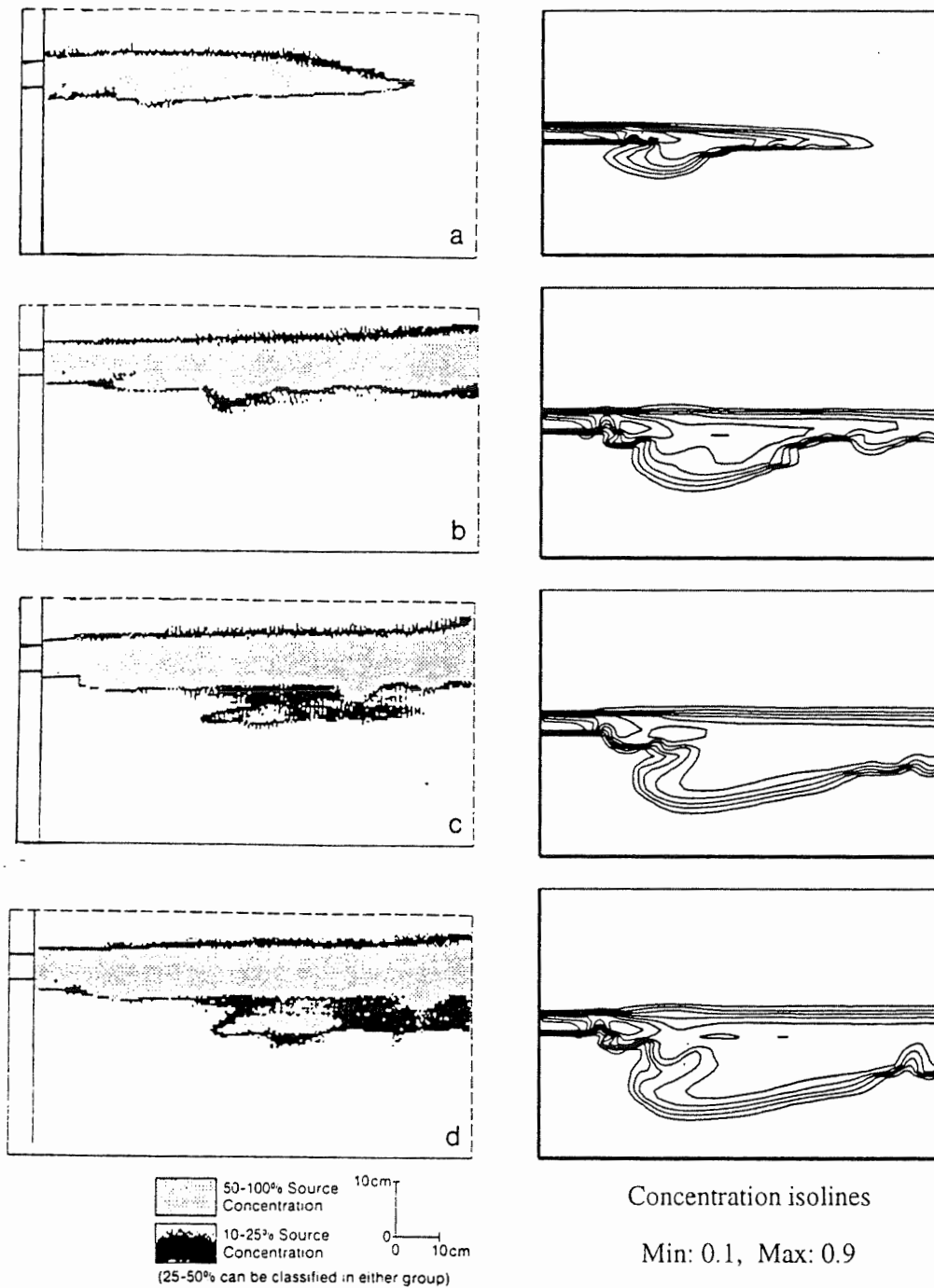
Experimental Results
(Reproduced from Schincariol and Schwartz [1990])

Numerical Simulation
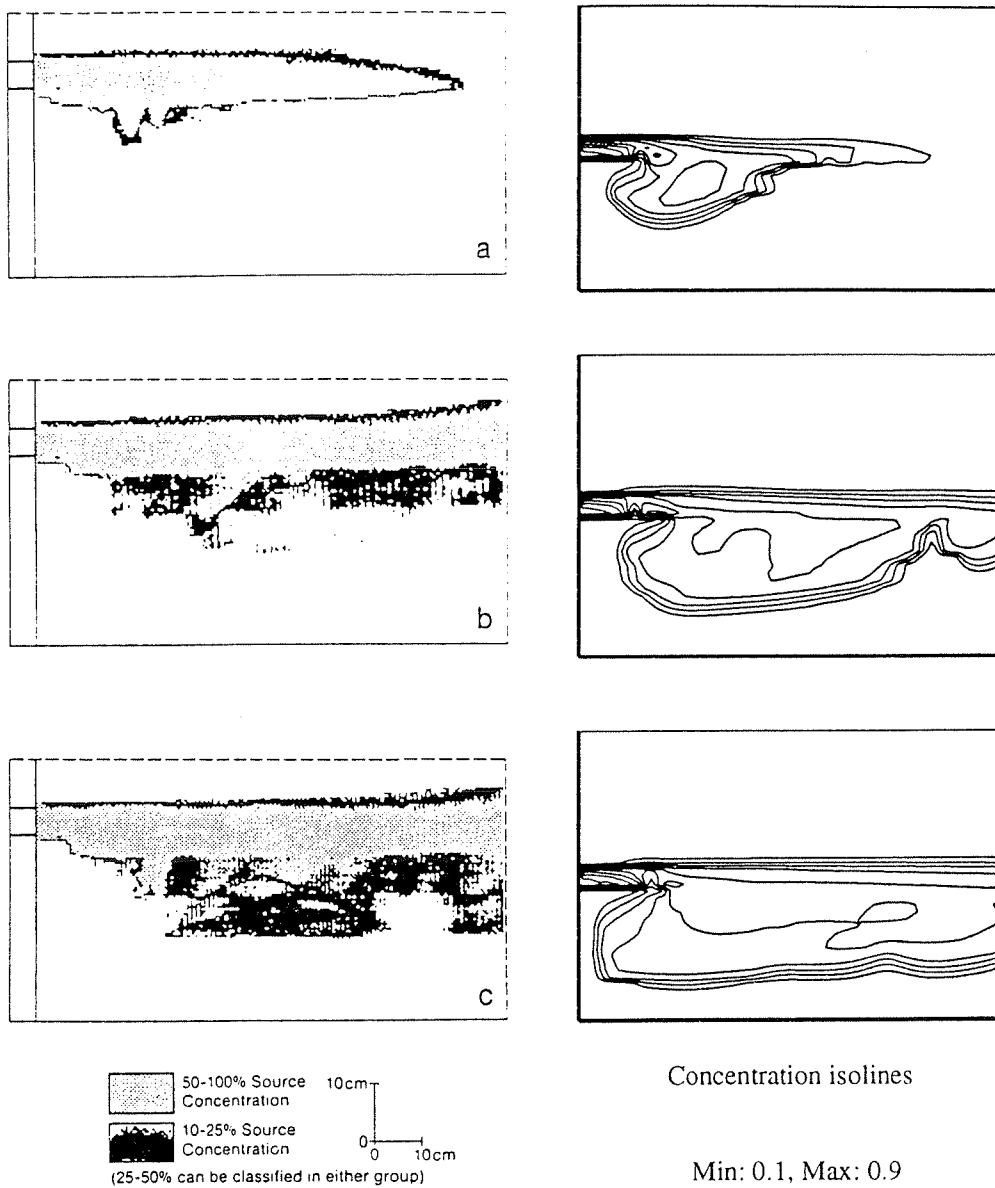
Figure 5.11   Instability development for a 10,000 mg/l NaCl source in heterogeneous
media at (a) t=12 hours, (b) t=48 hours, and (c) t=72 hours
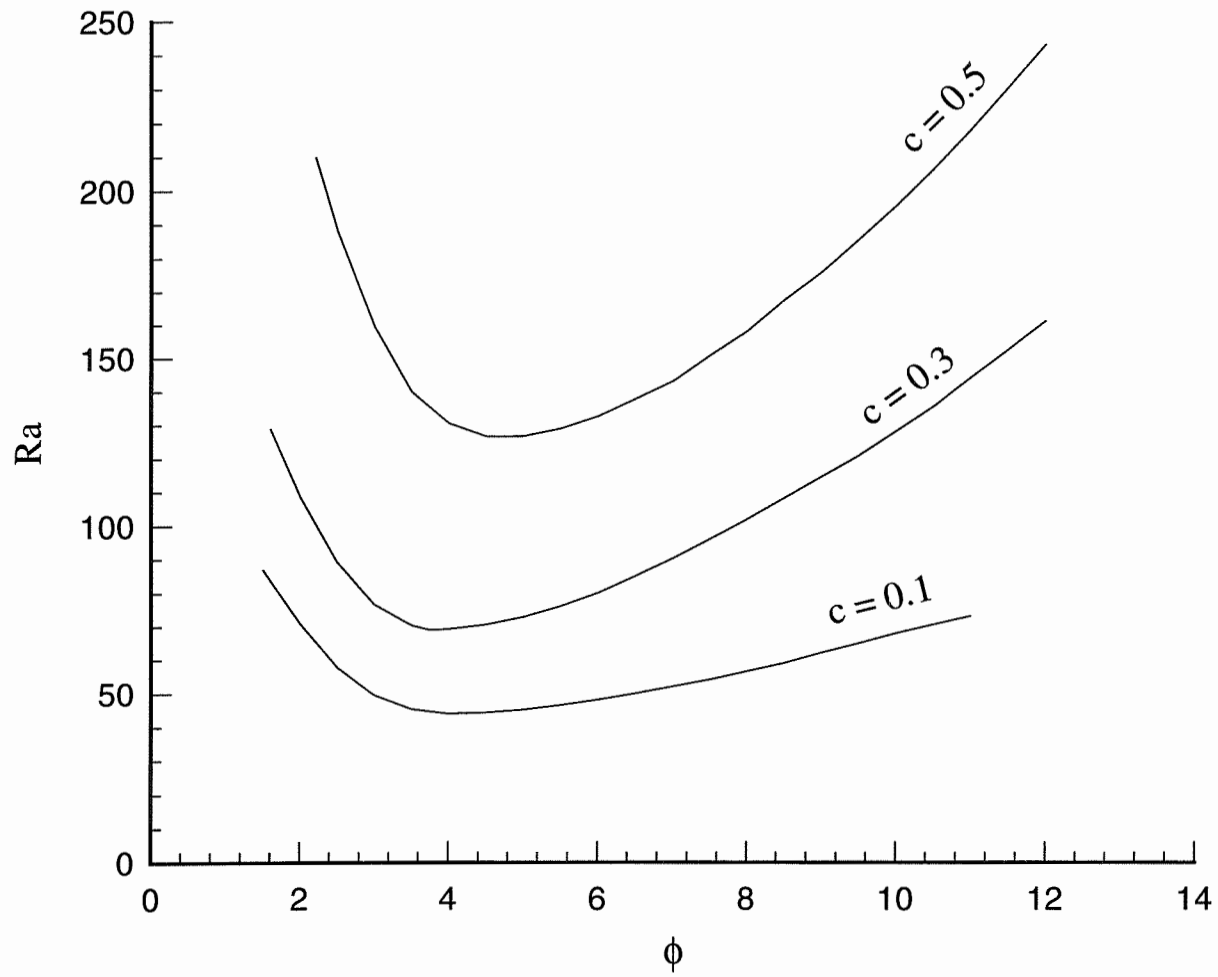
Figure 6.1   Neutral stability curve for c=0.1, 0.3 and 0.5
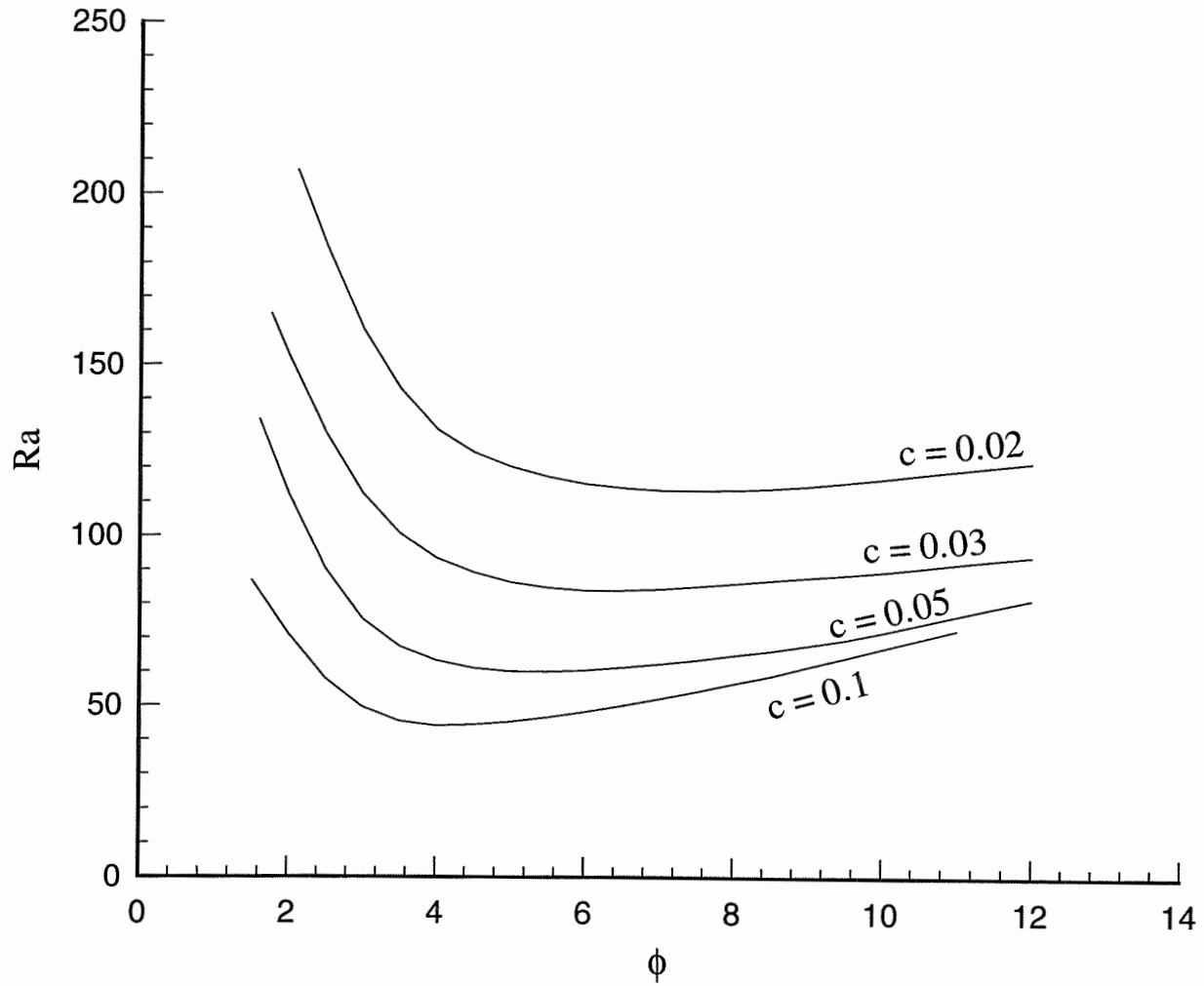
Figure 6.2   Neutral stability curve for c=0.1, 0.05, 0.03 and 0.02
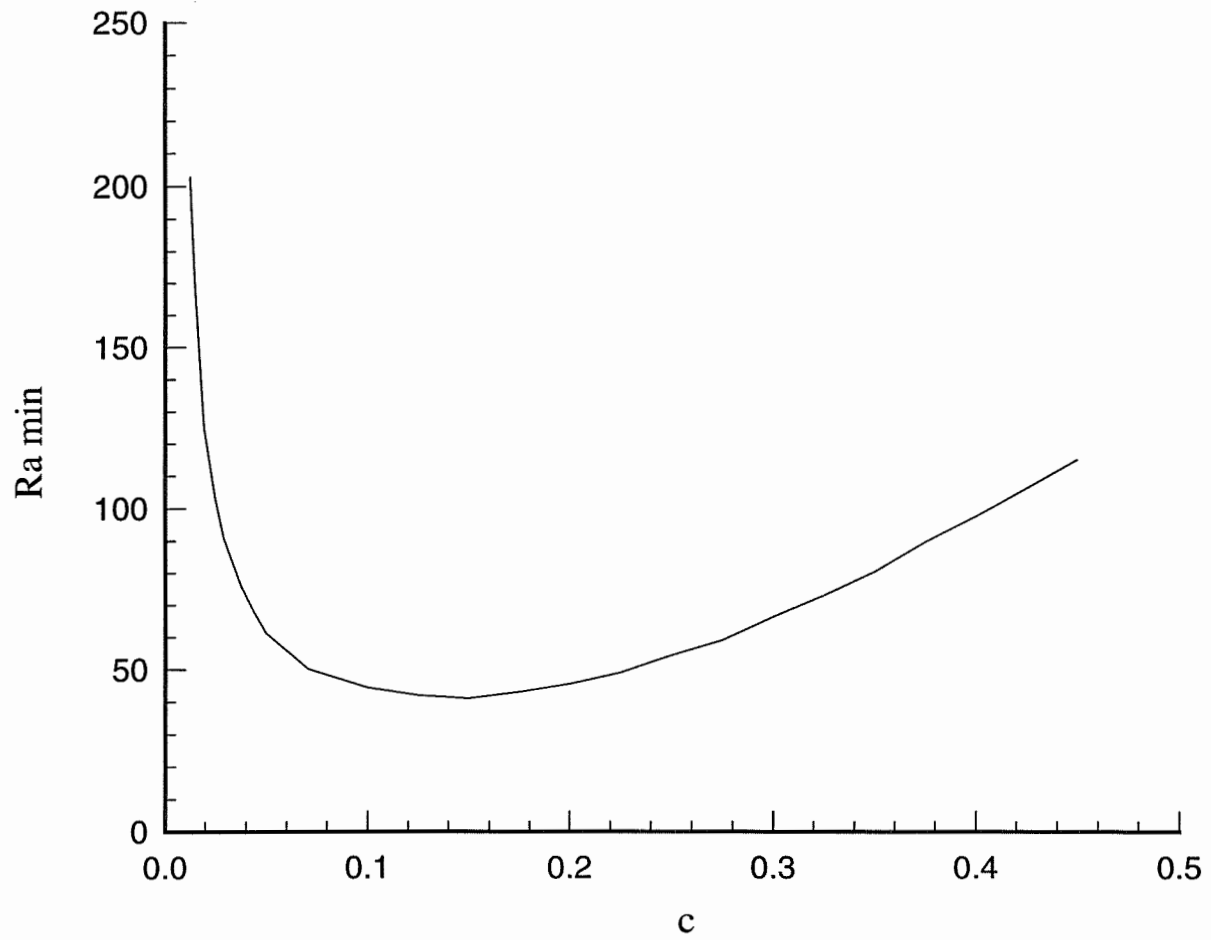
Figure 6.3   Critical Rayleigh number versus concentration length scale
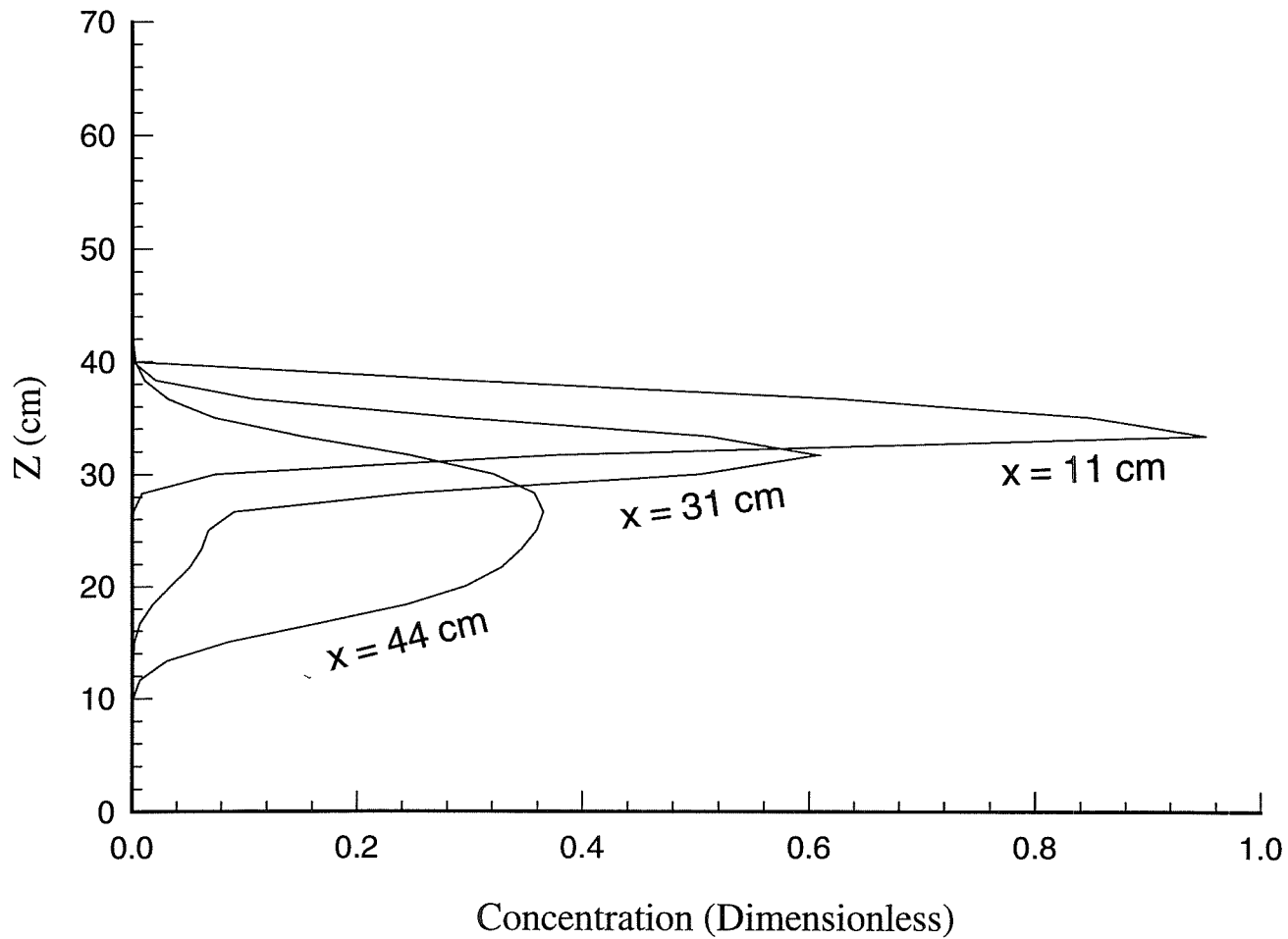
Figure 6.4   Concentration profile for a 2000-mg/L NaCl source at three cross sections, x = 11 cm, 31 cm and 44 cm at time t = 36 hours
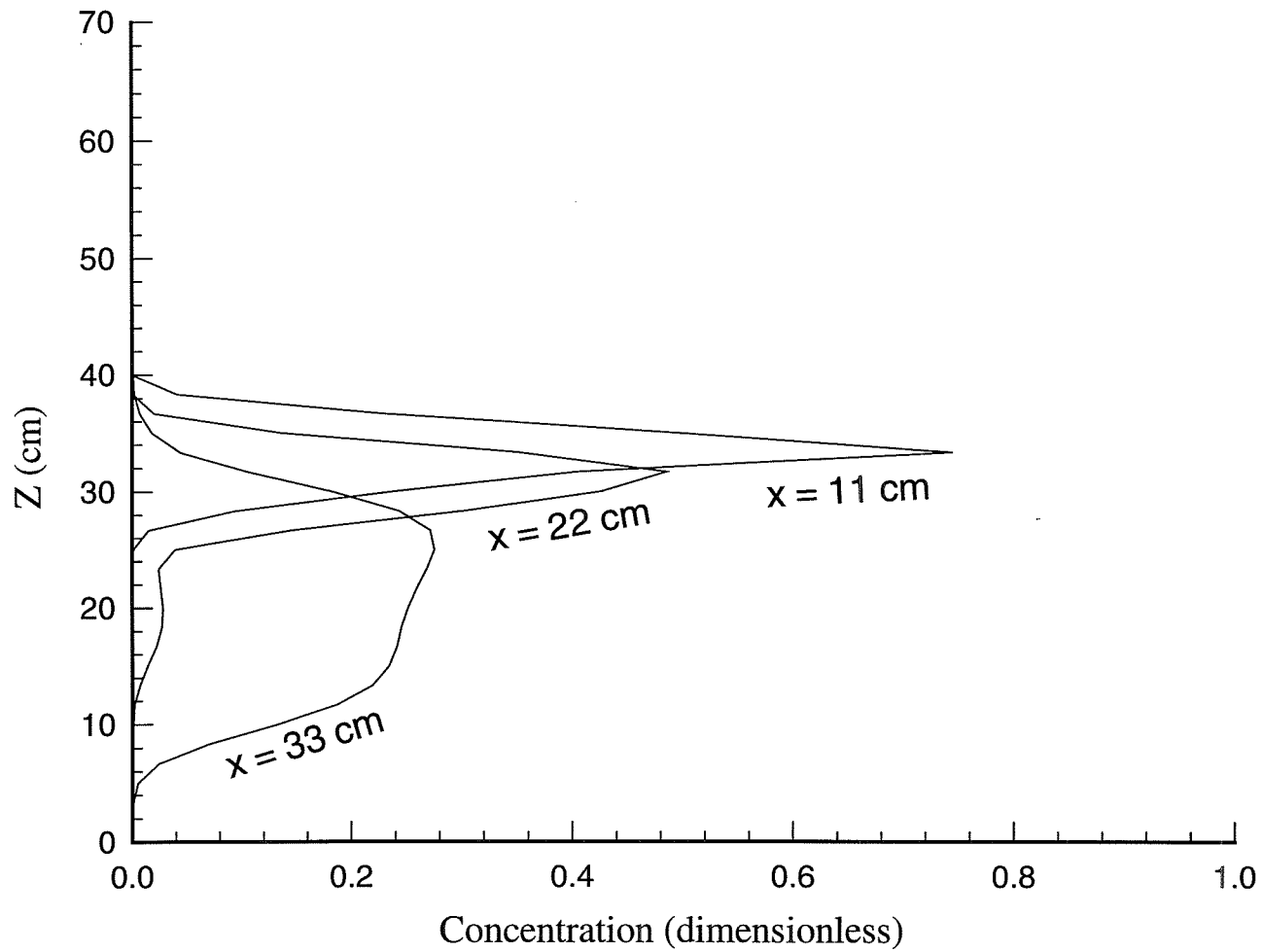
Figure 6.5 Concentration profile for a 5000-mg/L NaCl source at three cross sections, x = 11 cm, 22 cm and 33 cm at time t = 24 hours.

$$\rho\, K_{zz}\left(\frac{\partial p^*}{\partial z} + \frac{\rho}{\rho_0}\right) = 0$$
$$C = 0$$

$$q_L = \rho\, K_{zz}\left(\frac{\partial p^*}{\partial z} + \frac{\rho}{\rho_0}\right), \quad C = 1$$

$$\rho\, K_{zz}\left(\frac{\partial p^*}{\partial z} + \frac{\rho}{\rho_0}\right) = 0, \quad C = 0$$

Z

G F E   D

$$\rho\, K_{xx}\frac{\partial p^*}{\partial x} = 0$$
$$C = 0$$

$$\rho\, K_{xx}\frac{\partial p^*}{\partial x} = 0$$
$$\frac{\partial C}{\partial x} = 0$$

H   water table C

$$p^* = h_1 - z$$
$$C = 0$$

$$p^* = h_2 - z$$
$$\frac{\partial C}{\partial x} = 0$$

A   B **X**

$$\rho\, K_{zz}\left(\frac{\partial p^*}{\partial z} + \frac{\rho}{\rho_0}\right) = 0, \quad \frac{\partial C}{\partial z} = 0$$
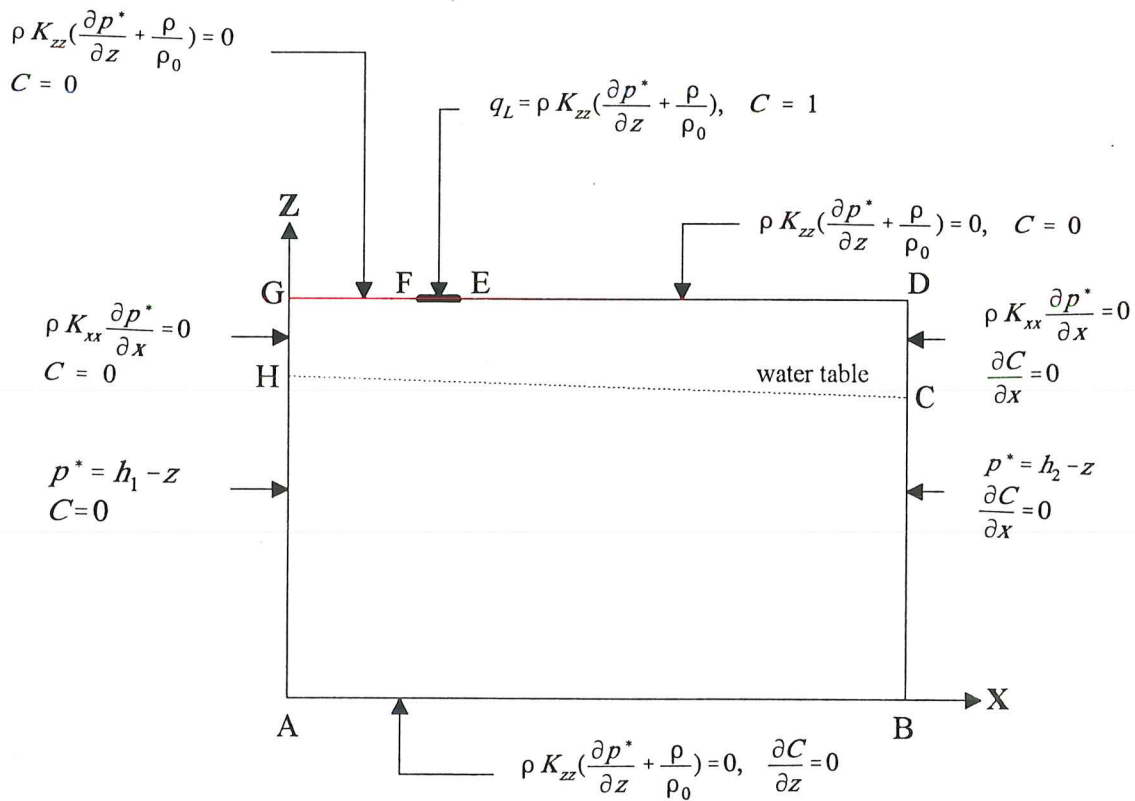
Figure 7.1 Calculation domain and boundary conditions

Concentration isolines (Min: 0.1, Max: 0.9)
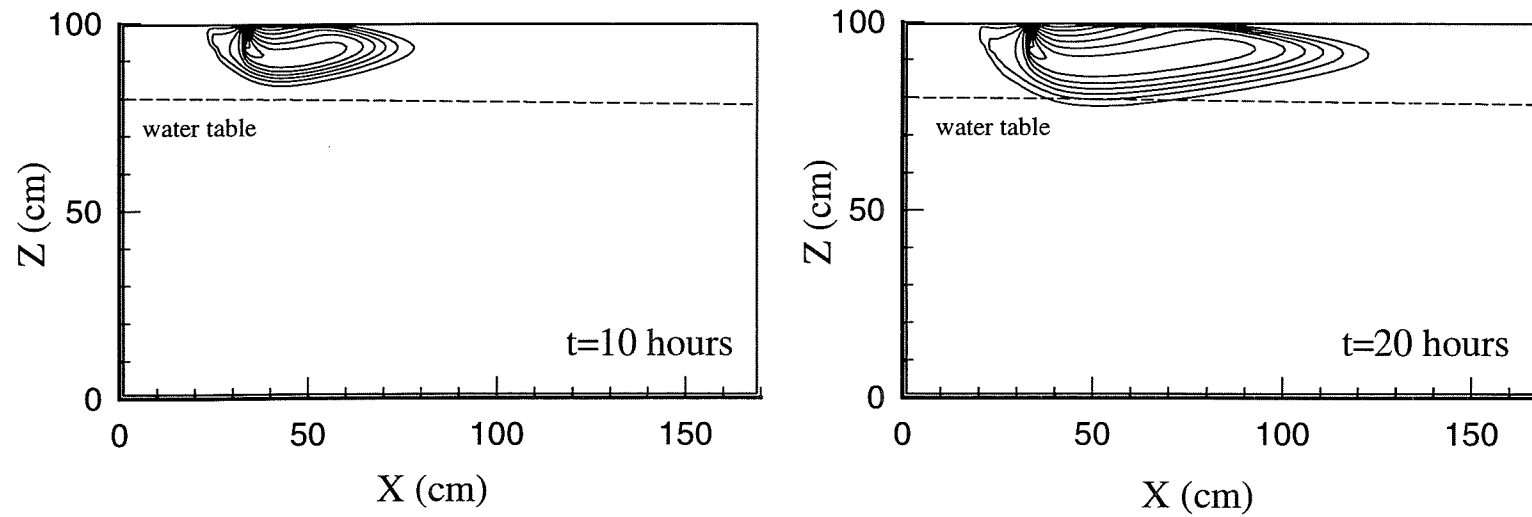
Figure 7.2   A neutral comtaminant plume at t= 10, 20, 30, 40 and 50 hours
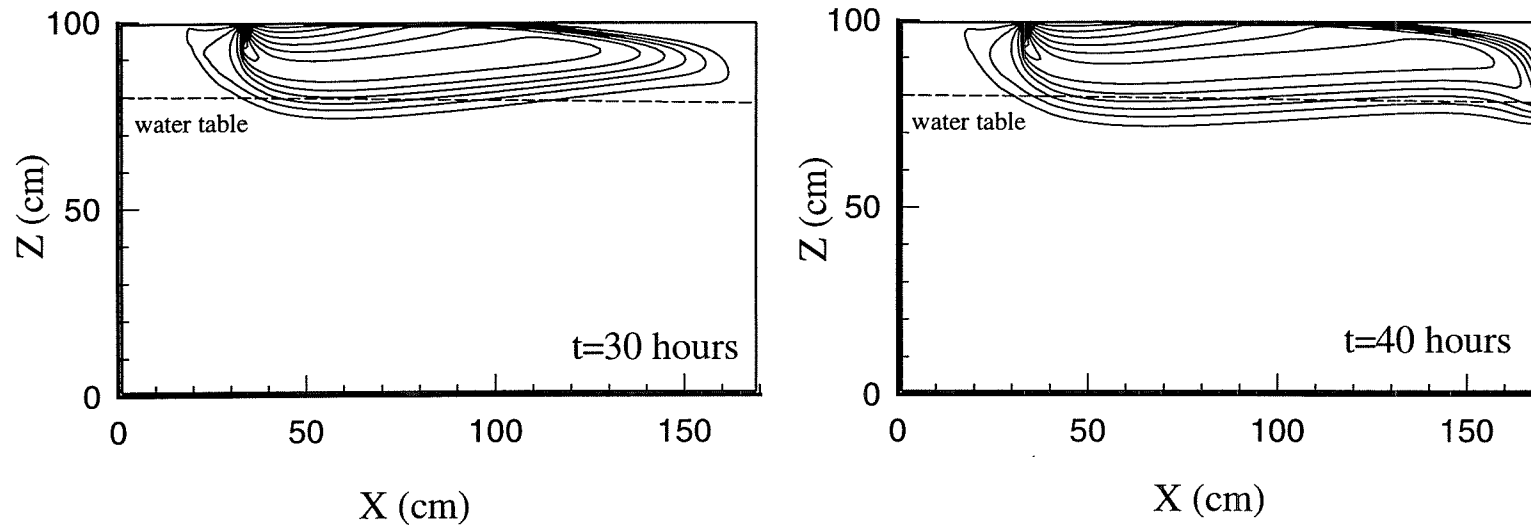
Concentration isolines (Min: 0.1, Max: 0.9)

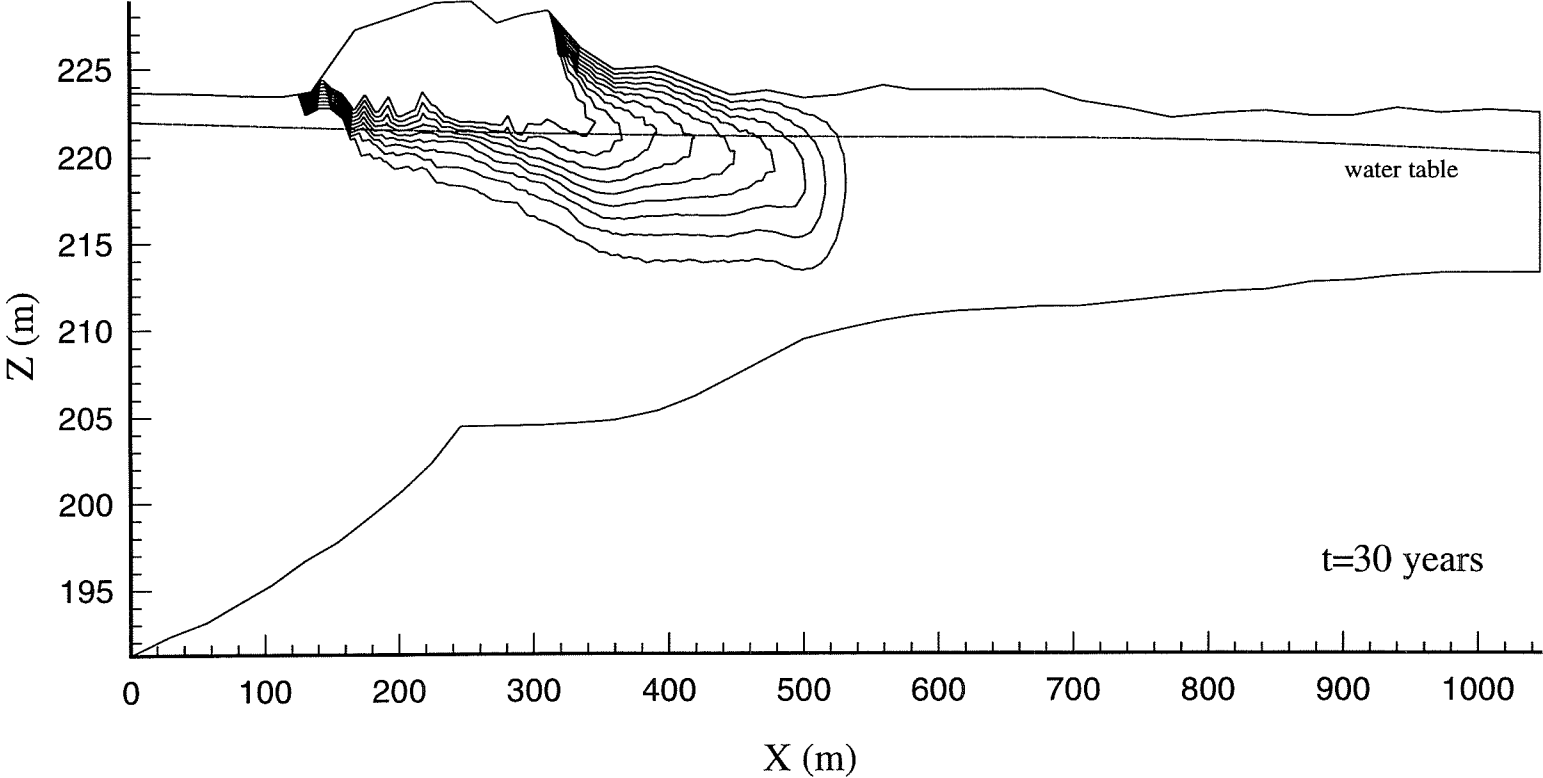Figure 7.2   Continued

Concentration isolines (Min: 0.1, Max: 0.9)
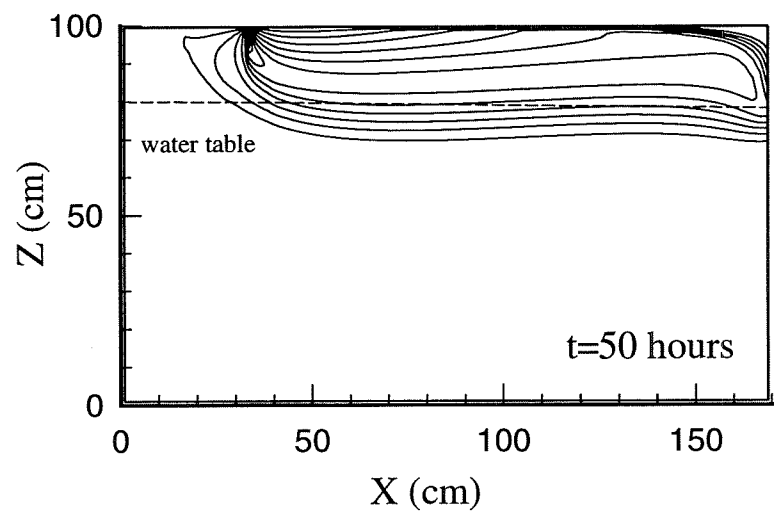
Figure 7.2 Continued

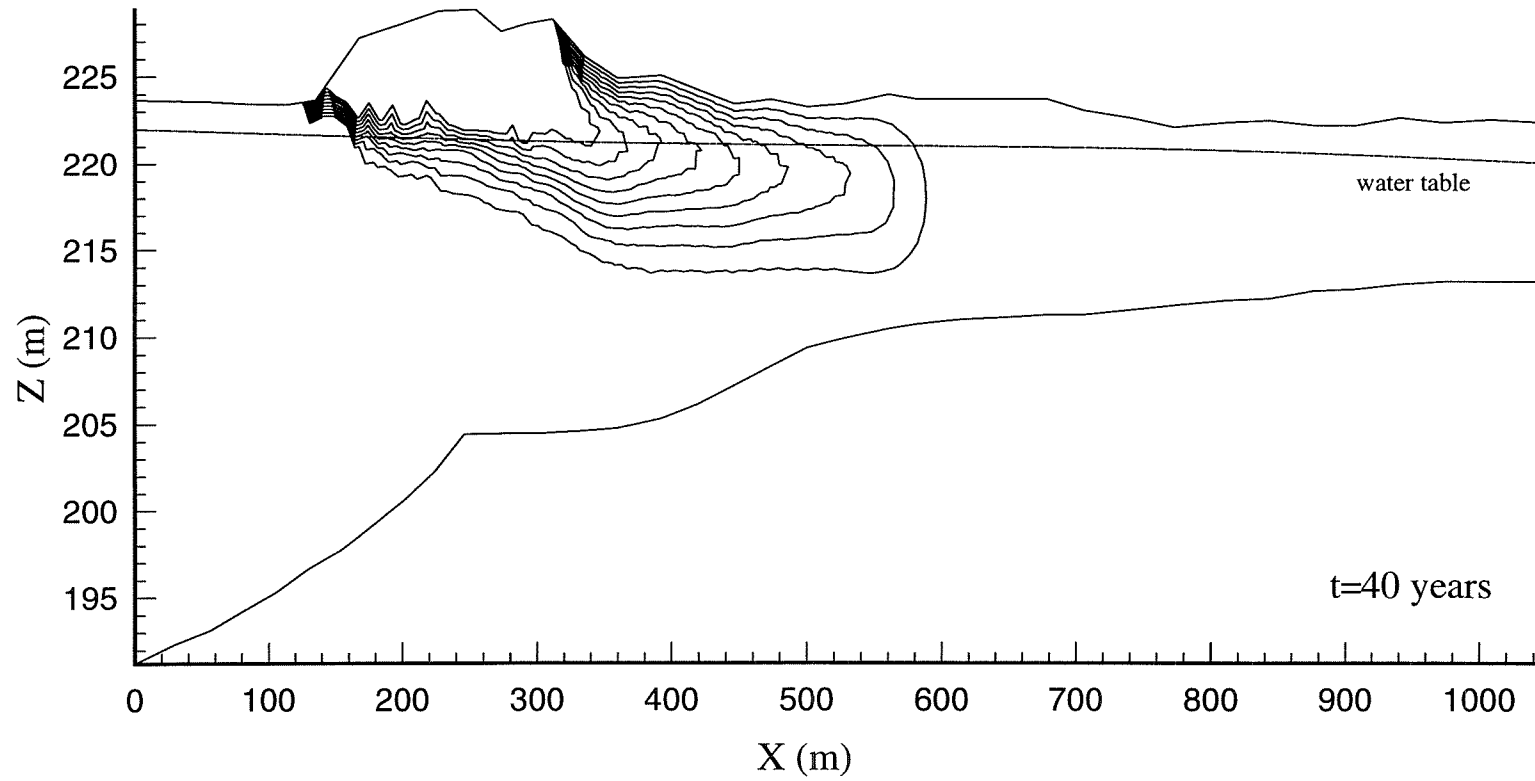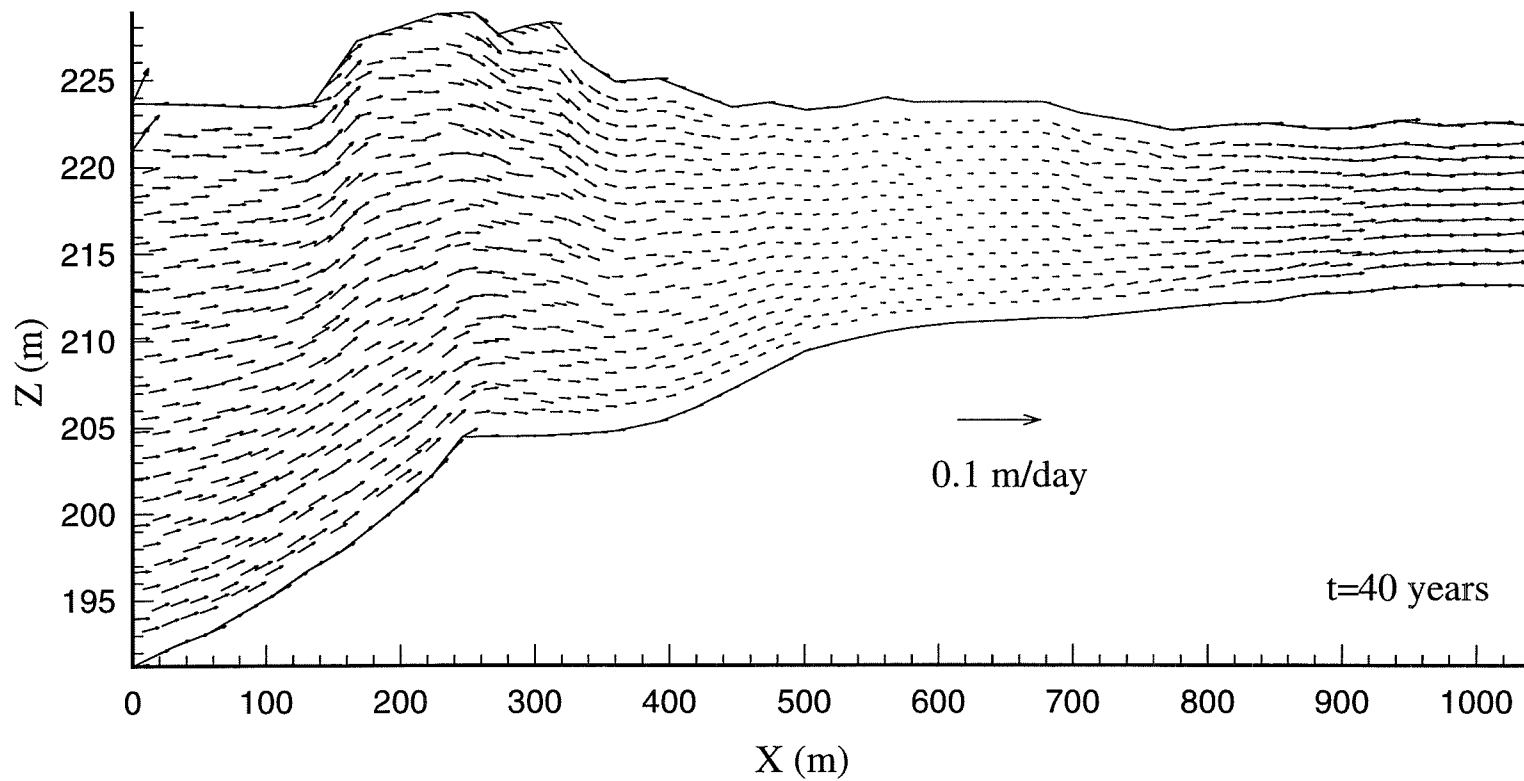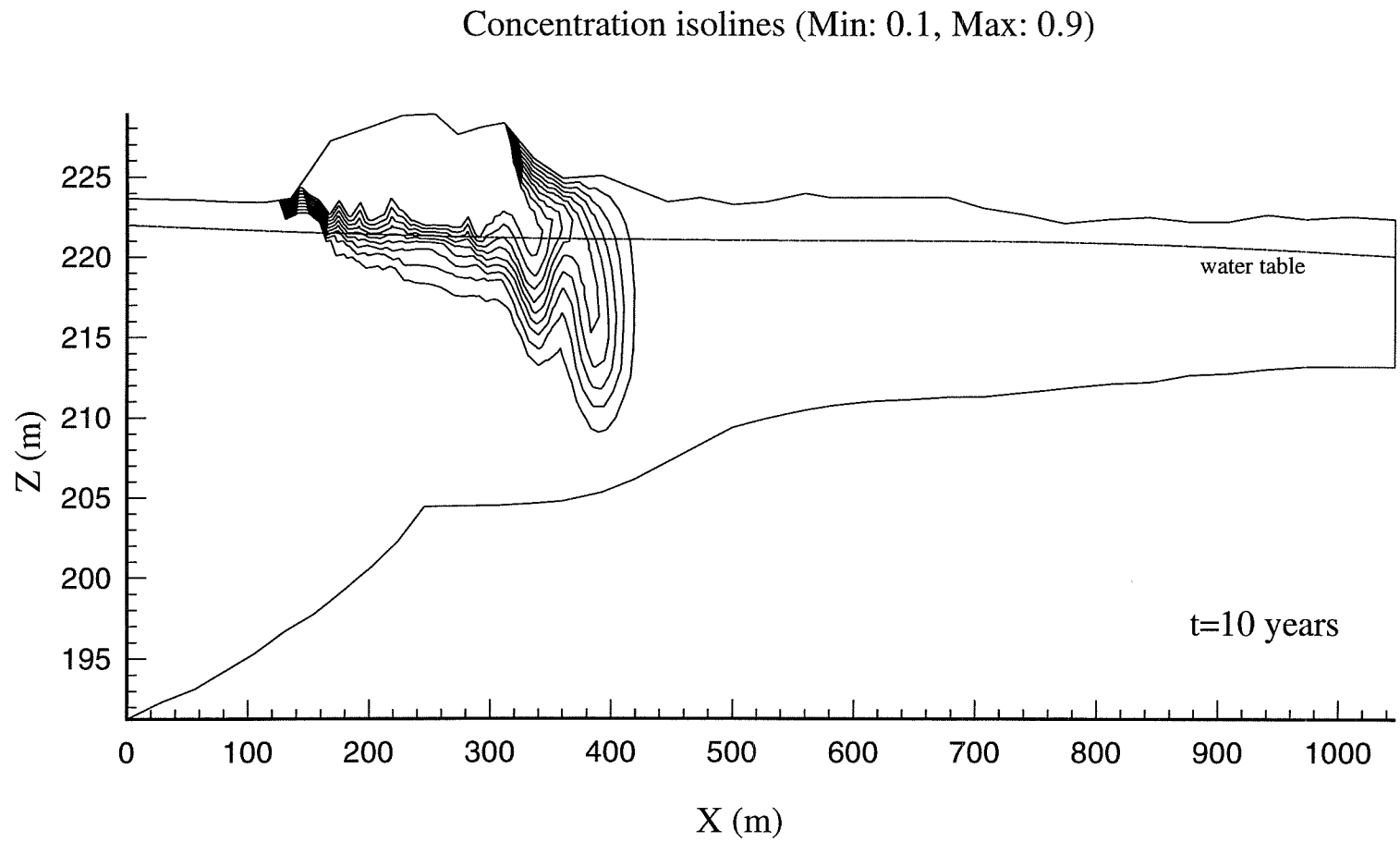Concentration isolines (Min: 0.1, Max: 0.9)
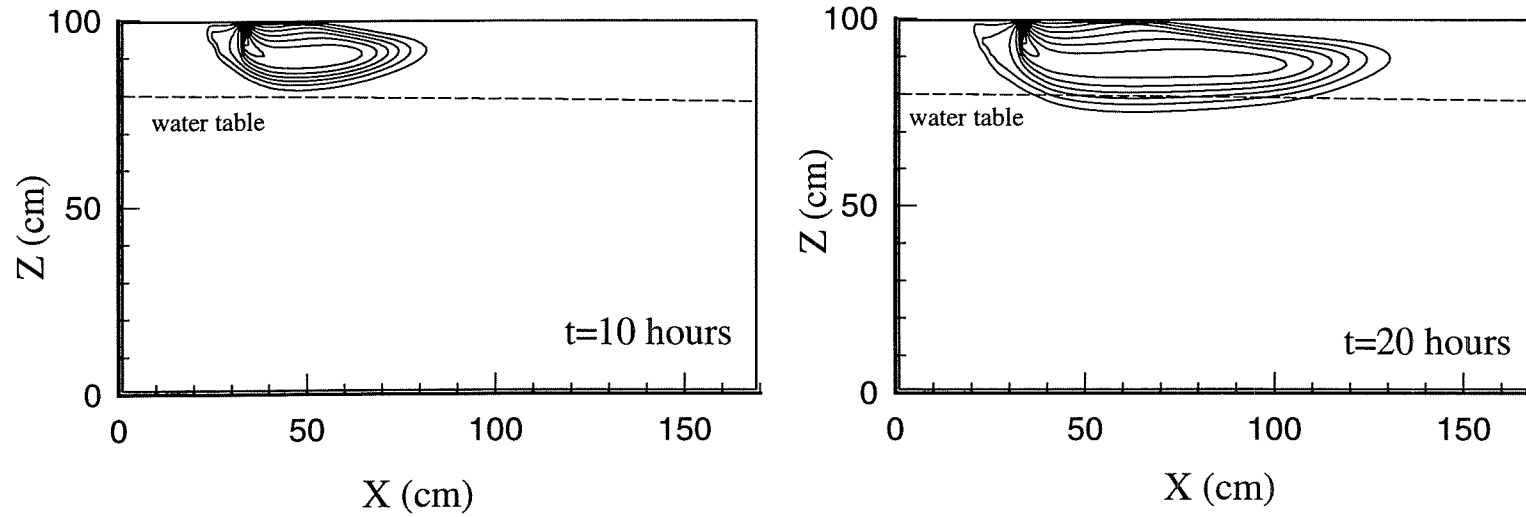
Figure 7.3   Instability development for a contaminant source (ε=0.0072)
at t= 10,20,30,40 and 50 hours
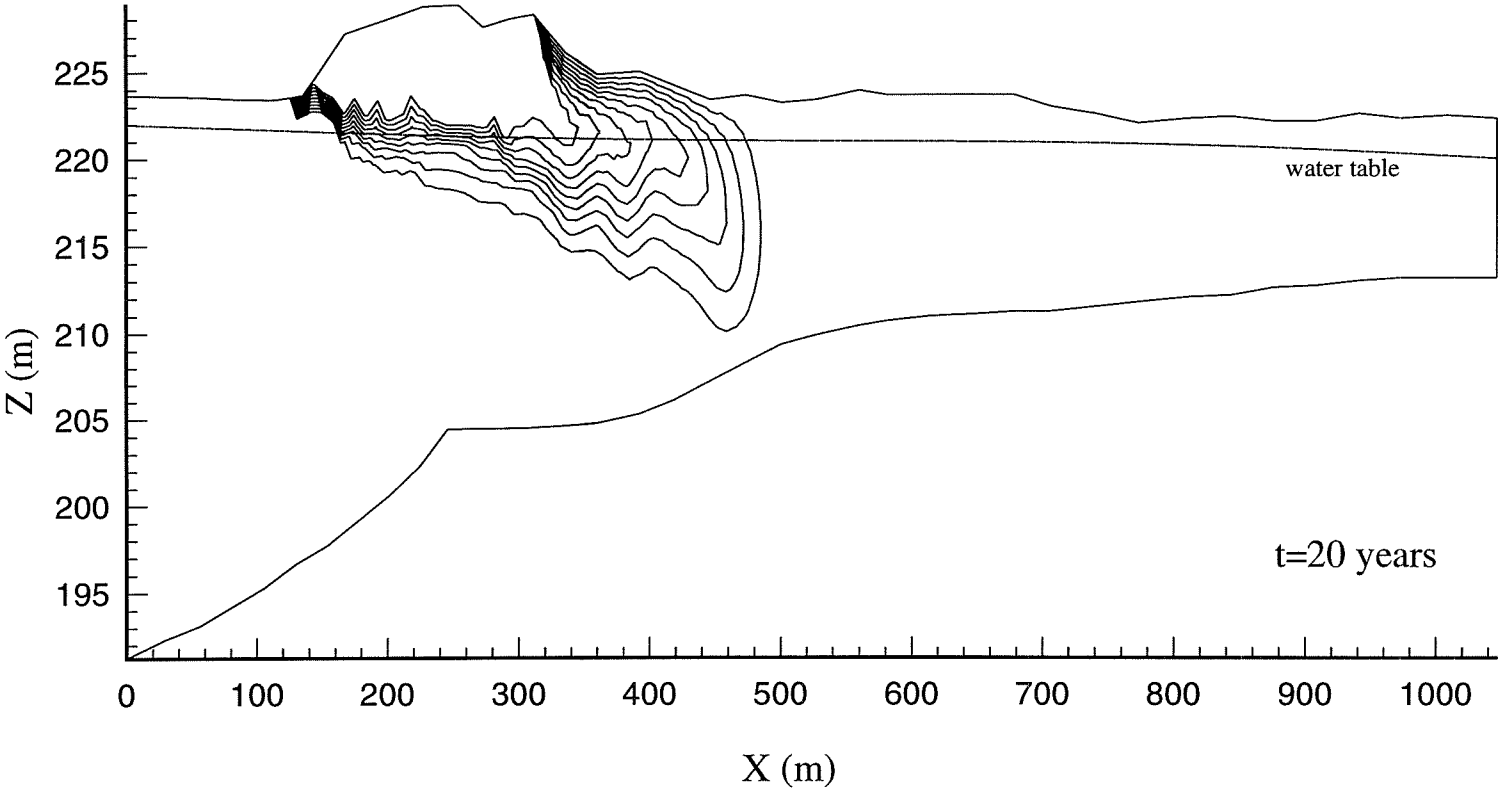
Concentration isolines (Min: 0.1, Max: 0.9)
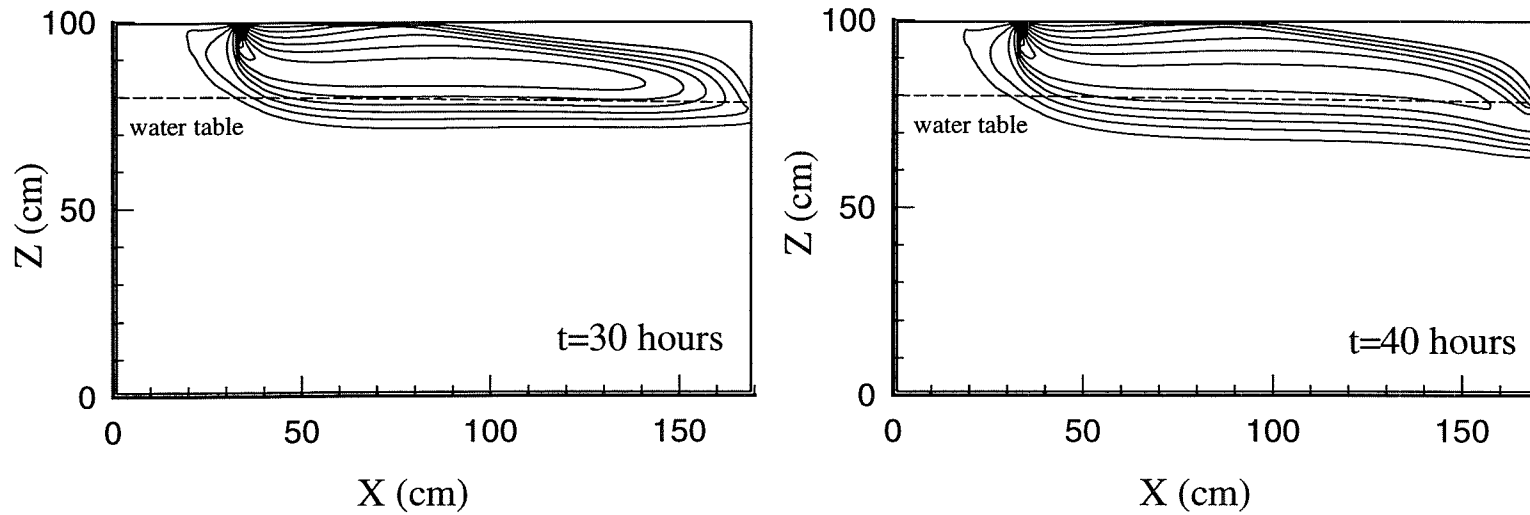
Figure 7.3   Continued

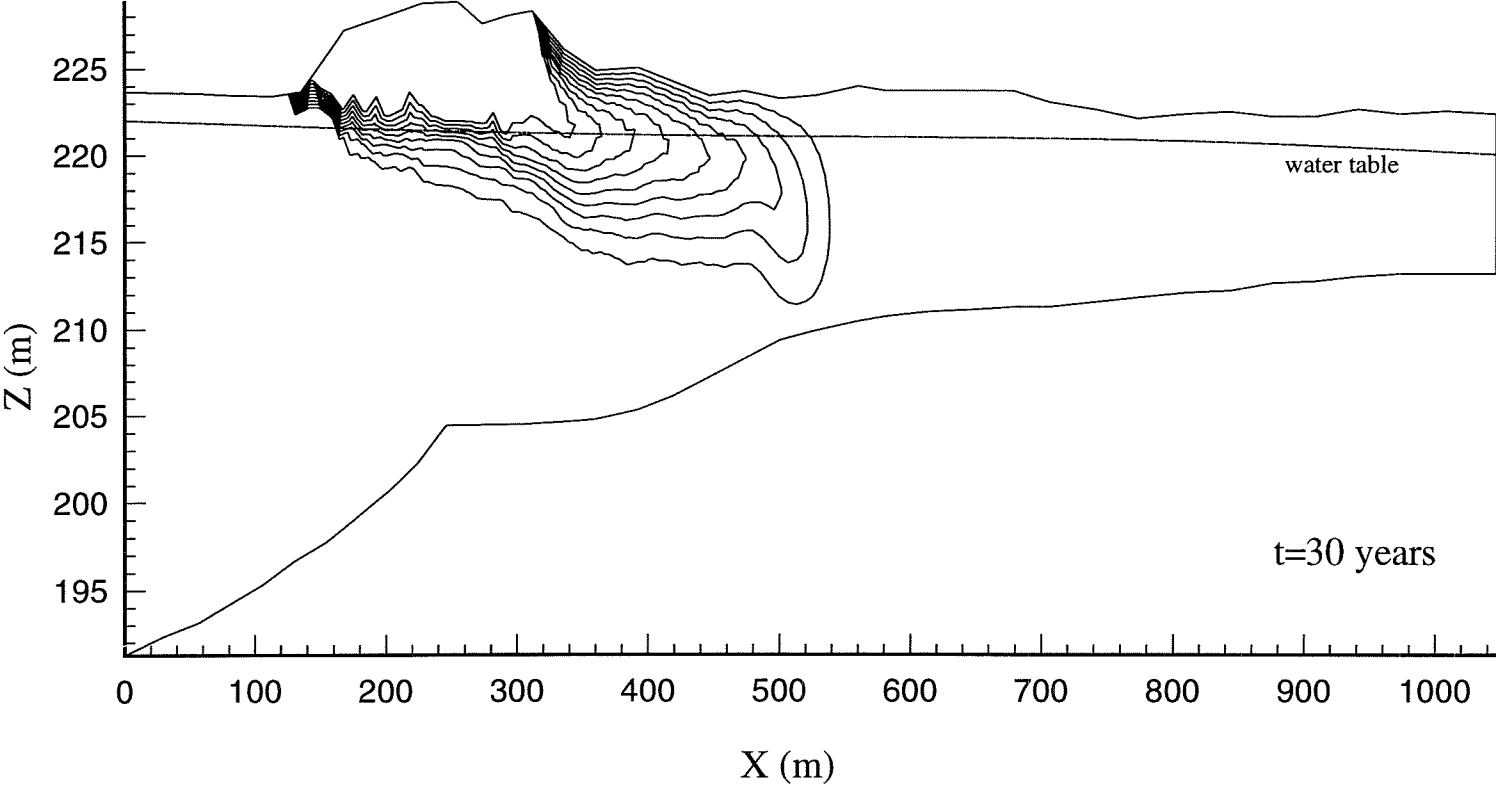Concentration isolines (min: 0.1, Max: 0.9)
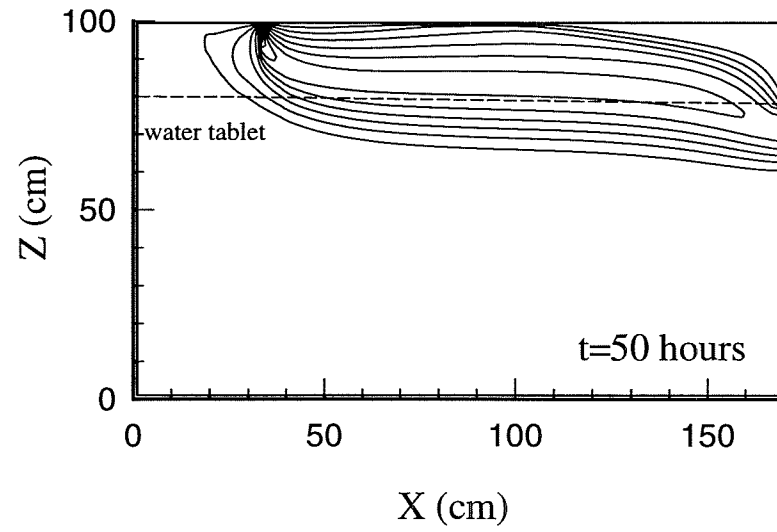
Figure 7.3   Continued

Concentration isolines (Min: 0.1, Max: 0.9)
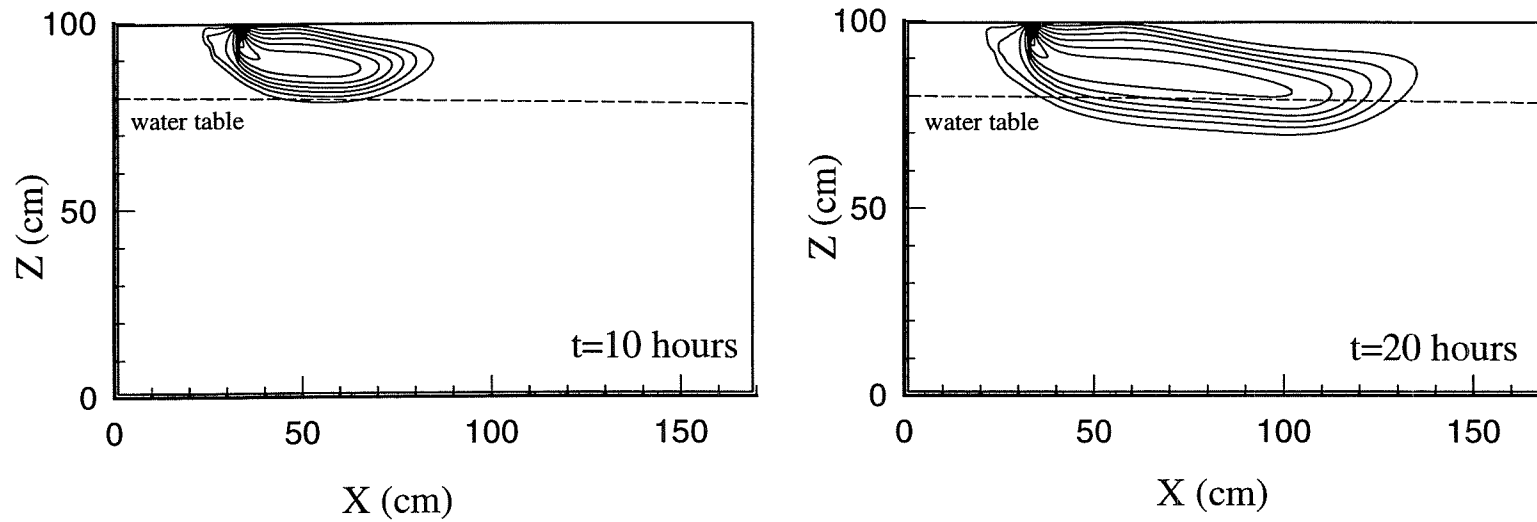
Figure 7.4   Instability development for a contaminant source   ($\varepsilon=0.014$)

at t= 10,20,30,40 and 50 hours
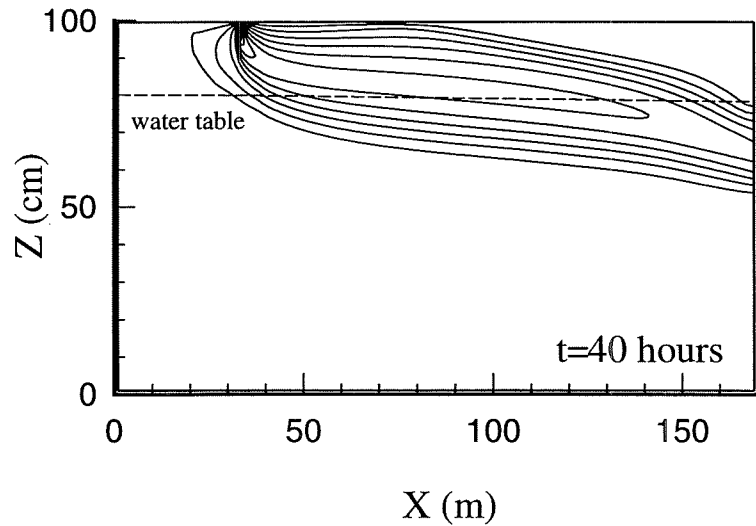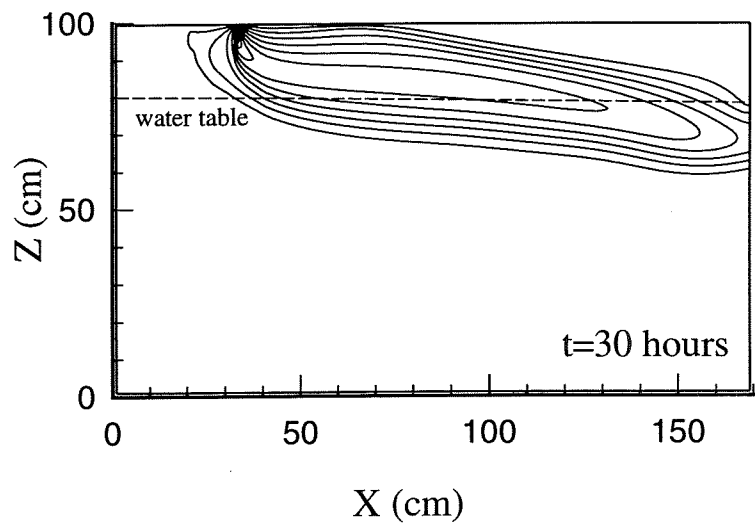
Concentration isolines (Min: 0.1, Max: 0.9)

Figure 7.4   Continued

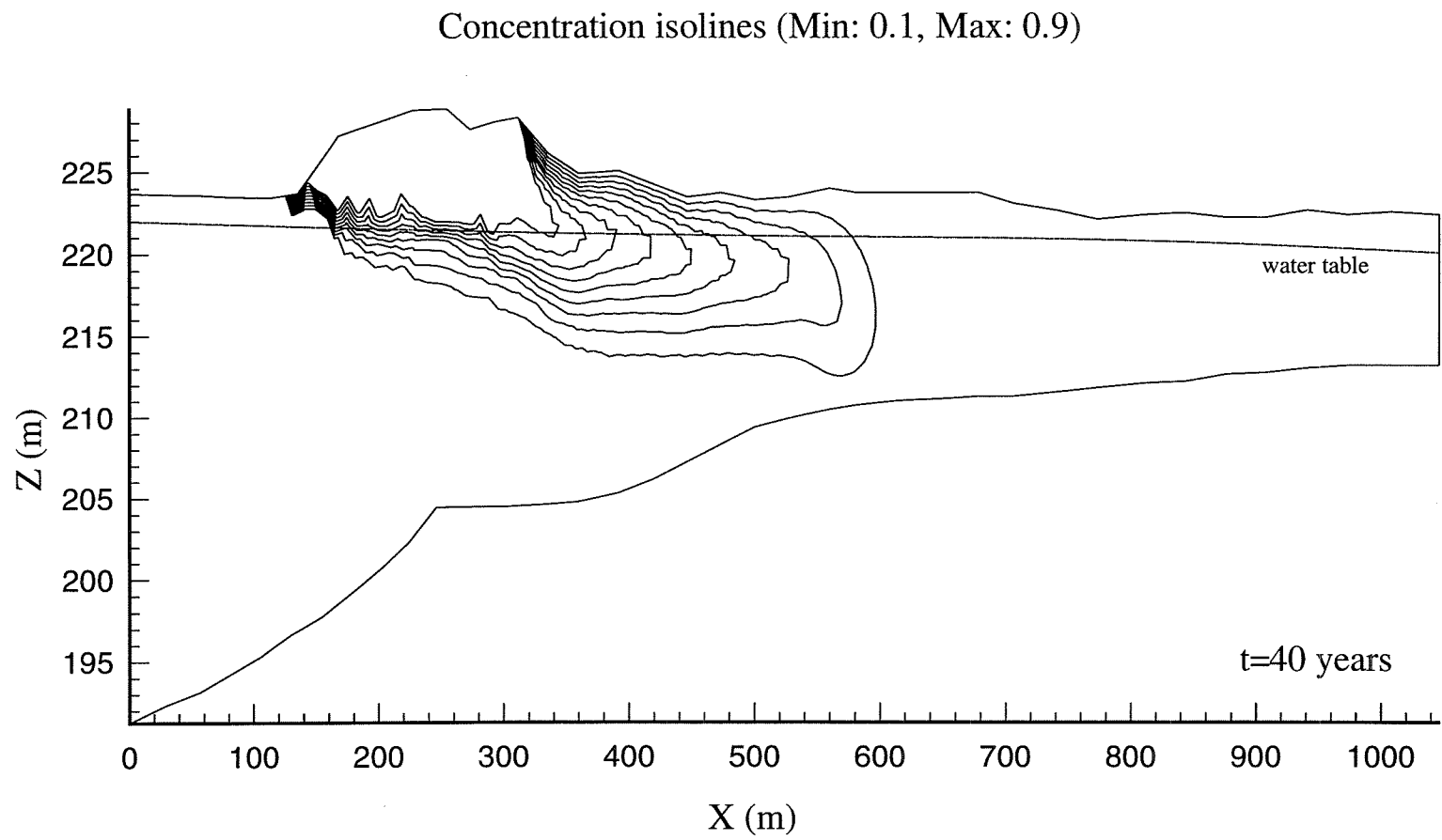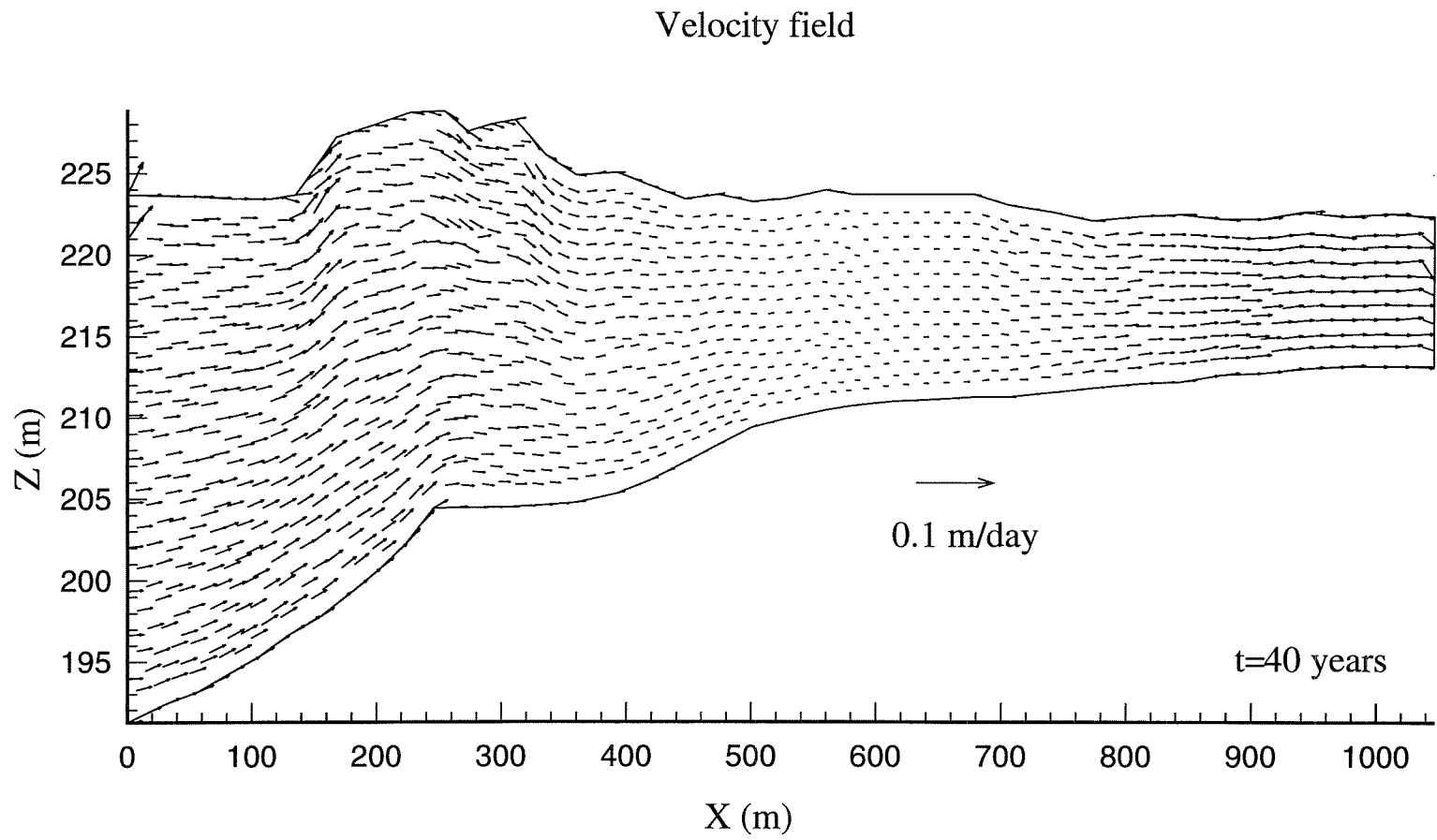Concentration isolines (Min: 0.1,Max: 0.9)
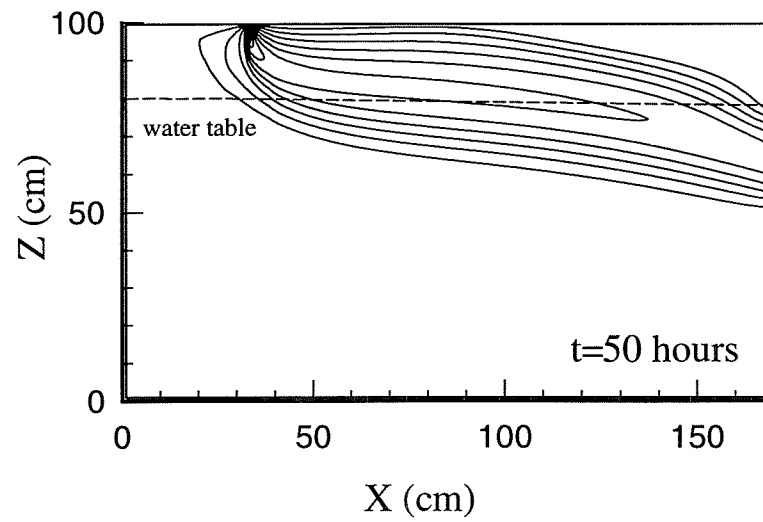
Figure 7.4   Continued

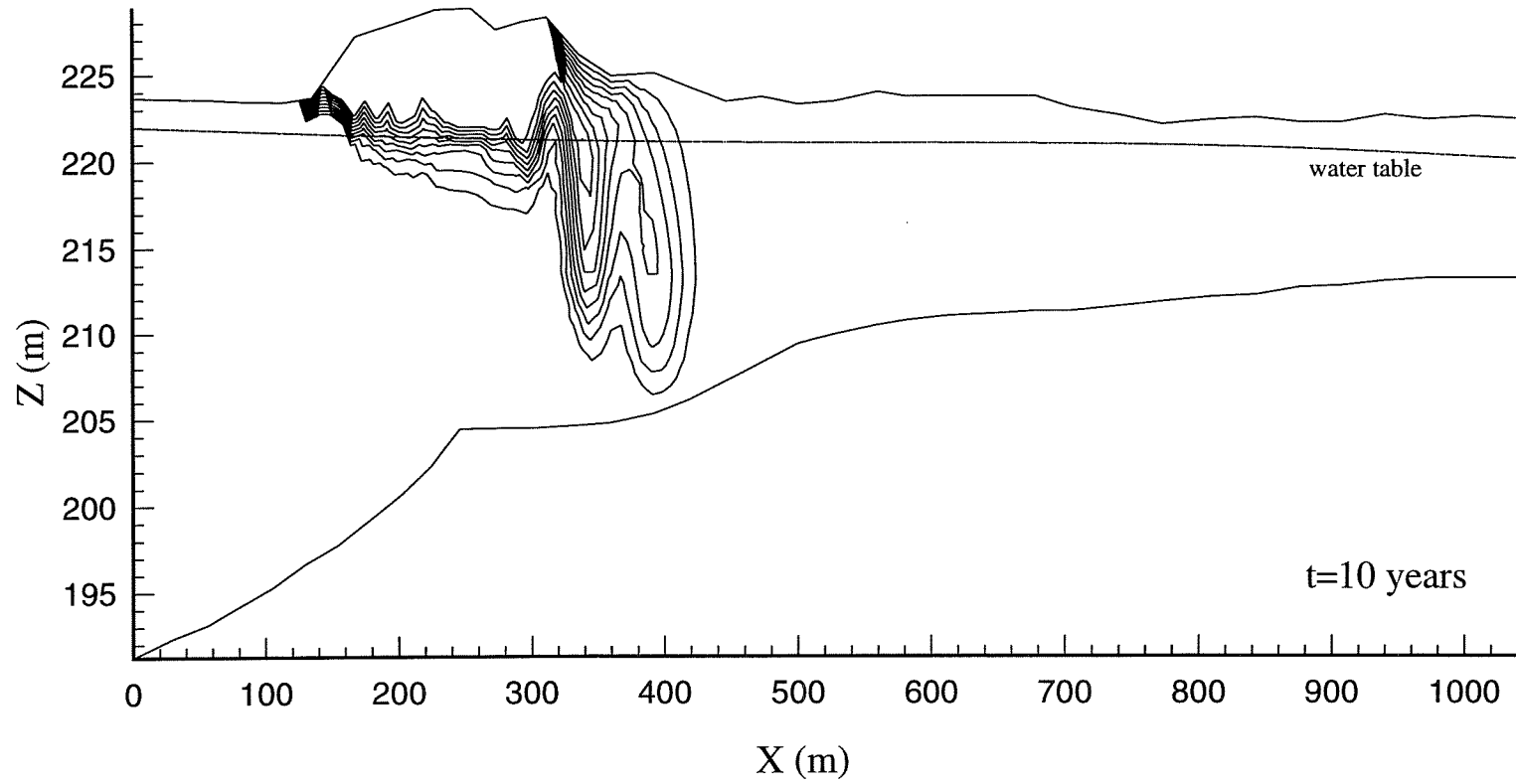Concentration isolines (Min: 0.1, Max: 0.9)
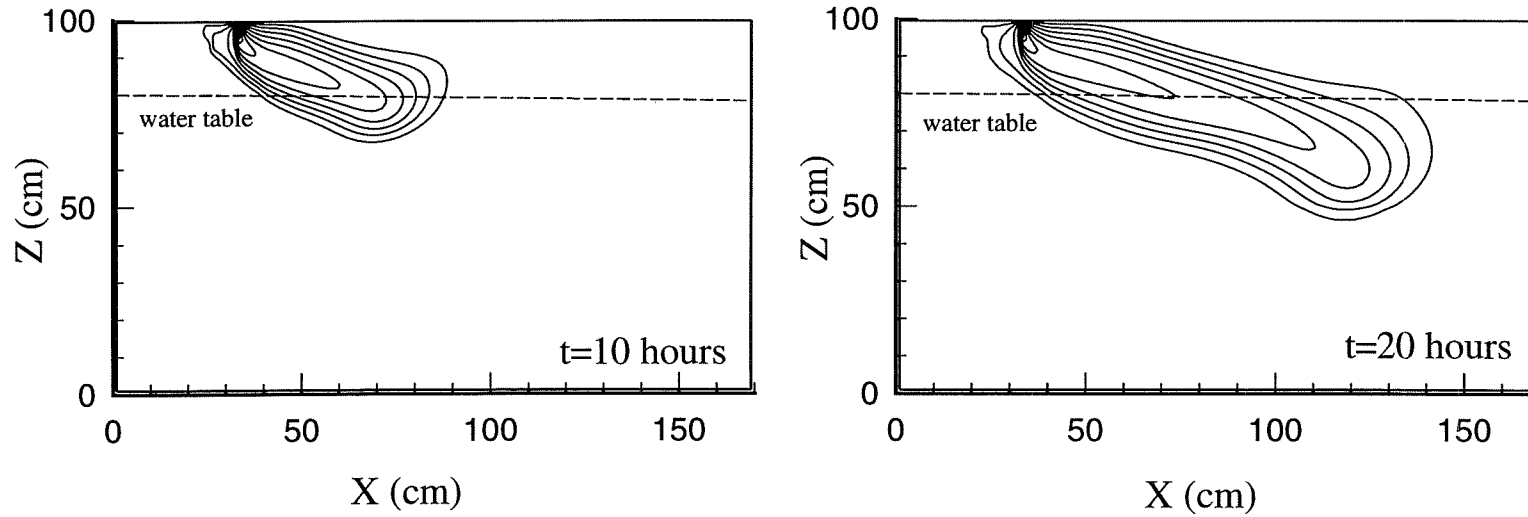
Figure 7.5   Instability development for a contaminant source (ε=0.028)
at t= 10,20,30,40 and 50 hours

Concentration isolines (Min: 0.1, Max: 0.9)
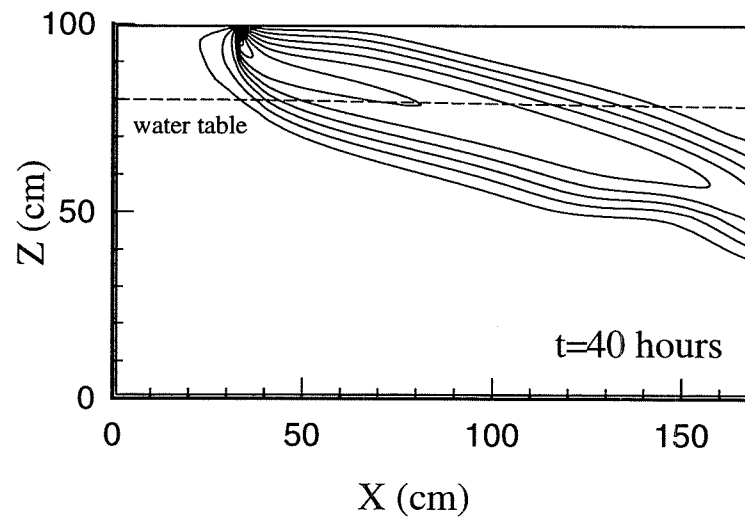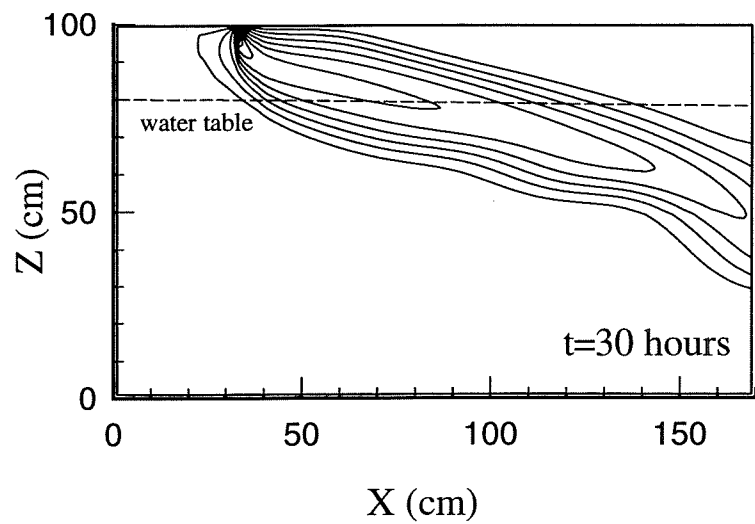
Figure 7.5   Continued

Concentration isolines (Min: 0.1, Max: 0.9)
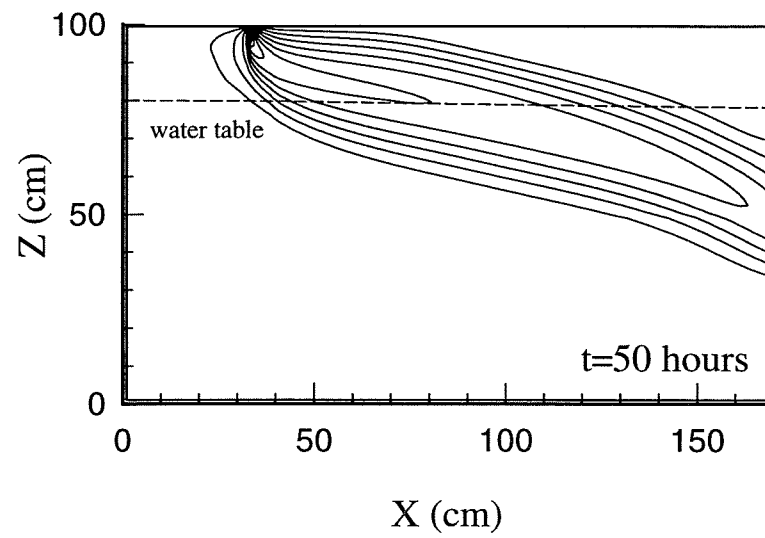
Figure 7.5   Continued
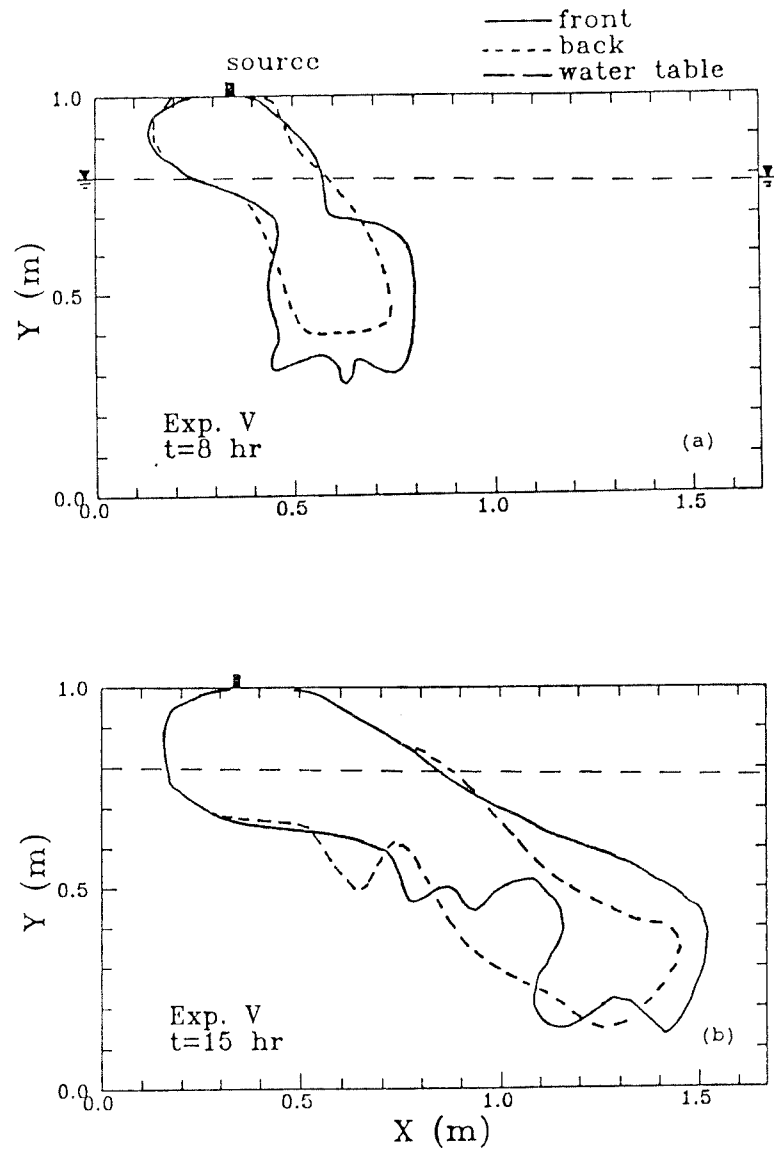
Figure 7.6 Plume outlines curves of an unstable dense plume of experiment C_V at (a) 8 hours, (b) 15 hours, (c) 32 hours, and (d) 52 hours ($\varepsilon = 0.014$) (Oostrom, 1992)

Figure 7.6   Continued
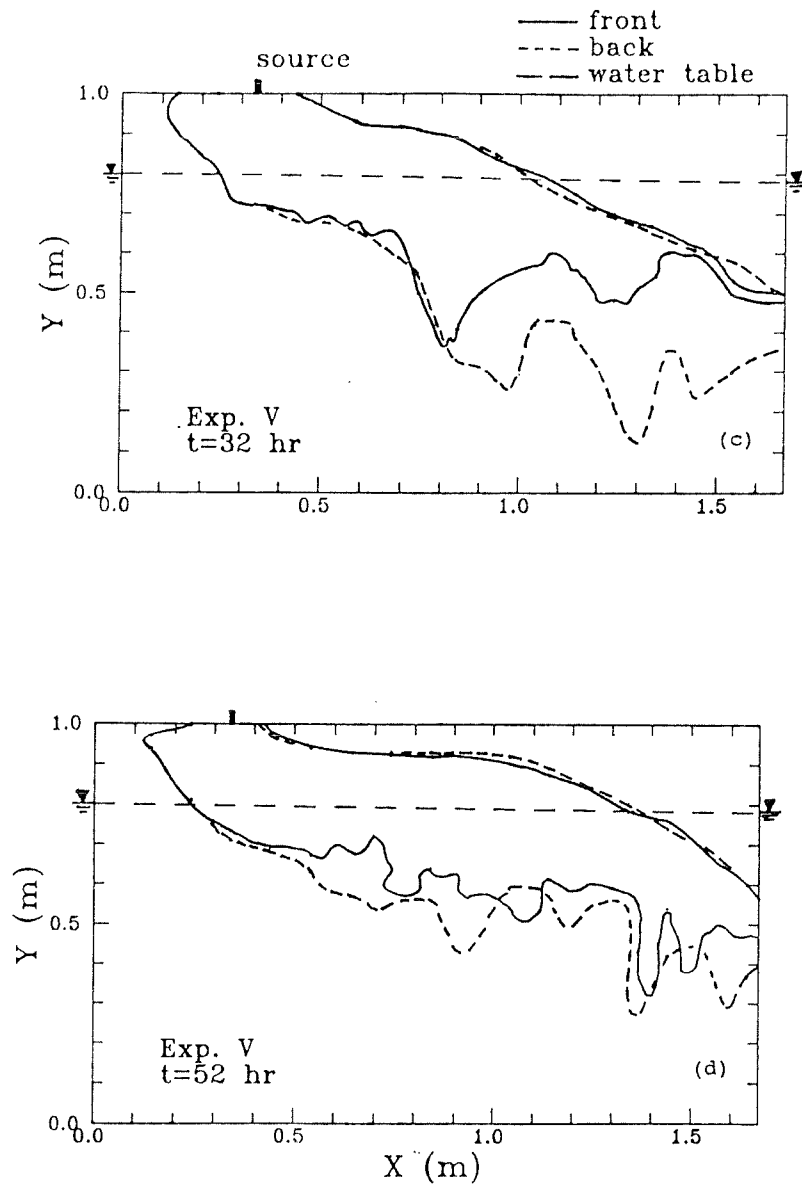
Concentration isolines (Min: 0.1, Max: 0.9)
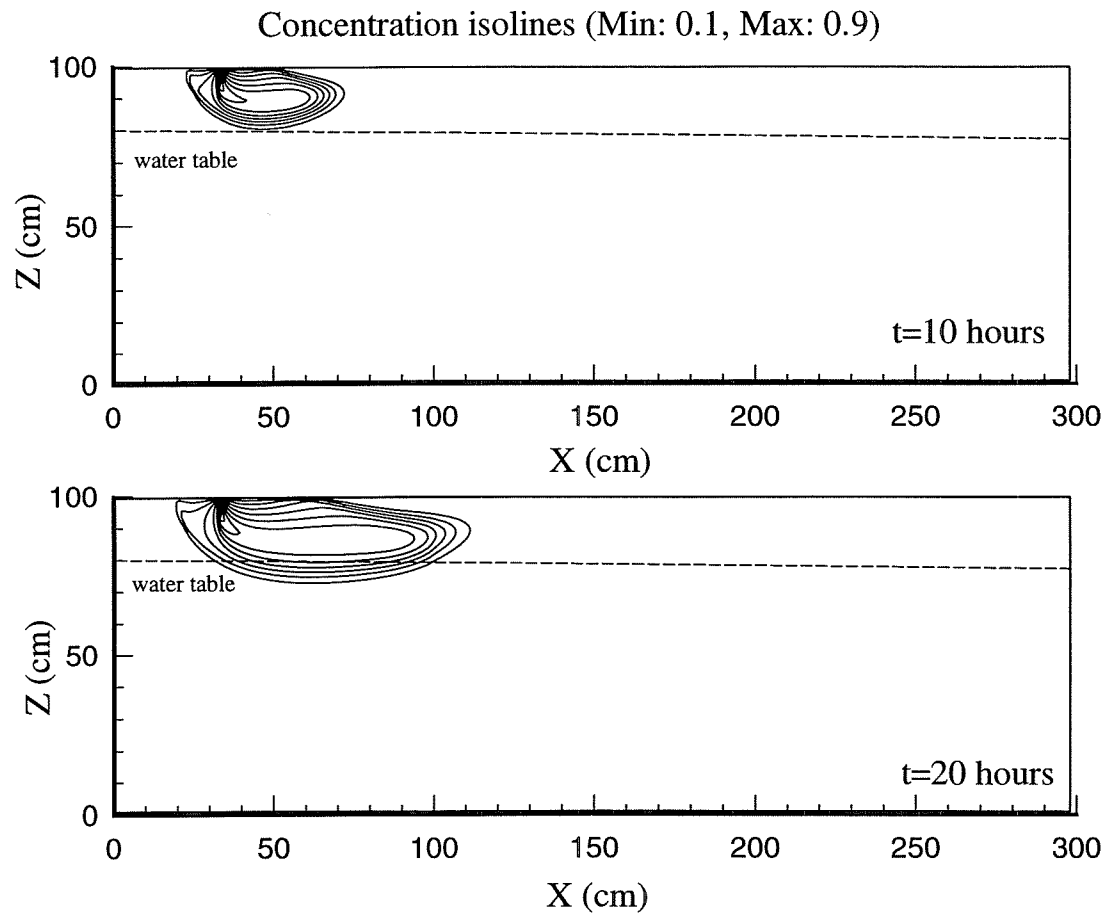
Figure 7.7 Instability development for a contaminant source
(ε=0.0072) at t= 10,20,30,40 and 50 hours
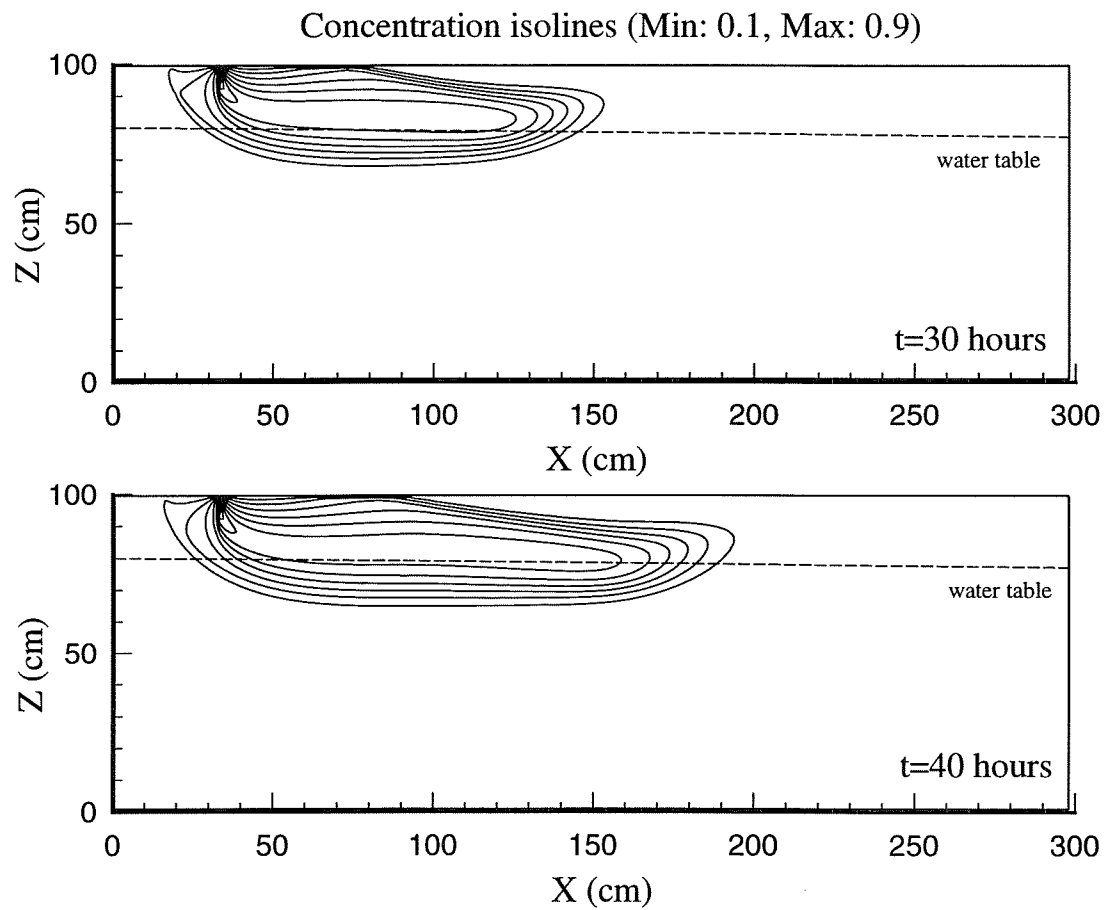
Concentration isolines (Min: 0.1, Max: 0.9)

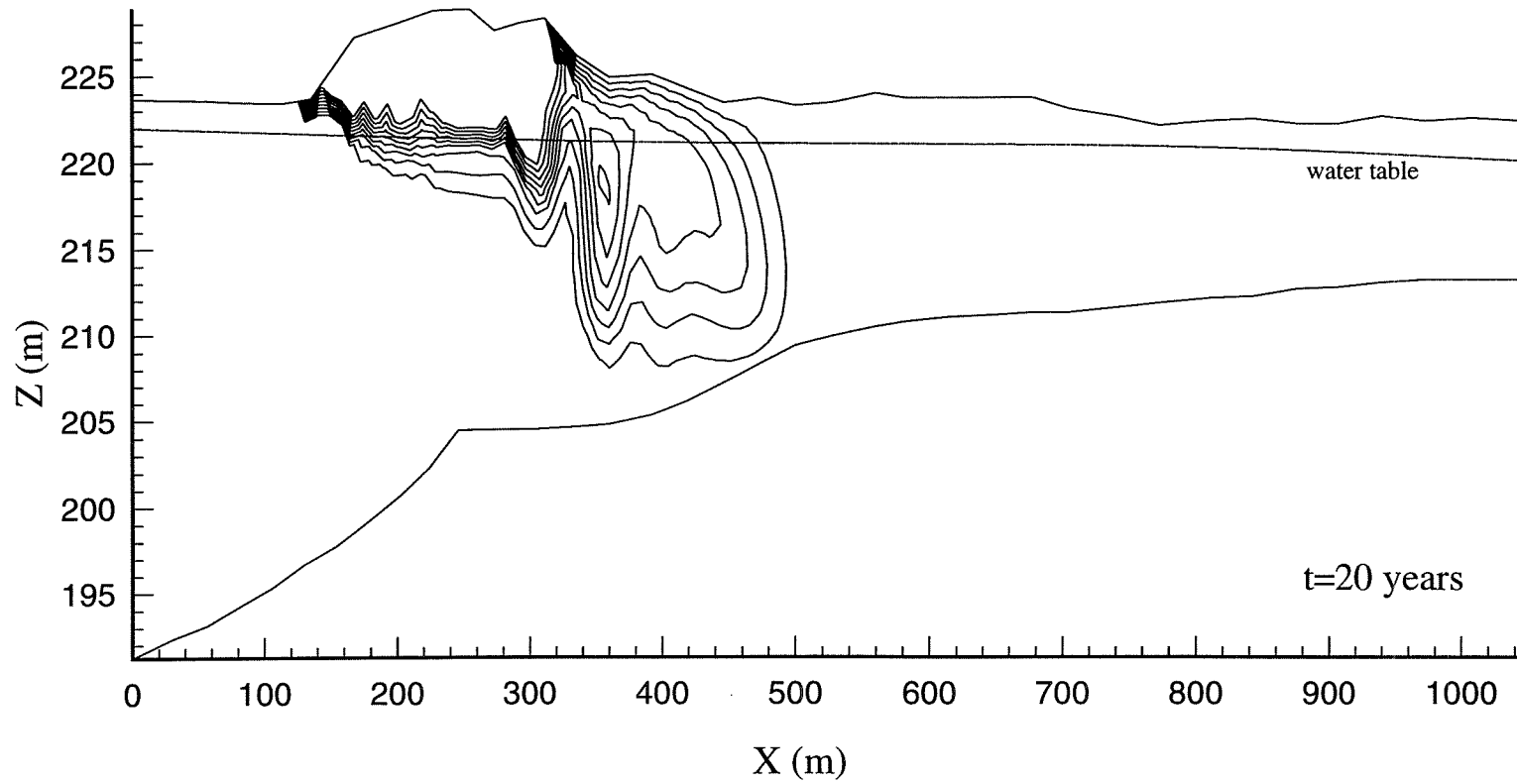

Figure 7.7   Continued

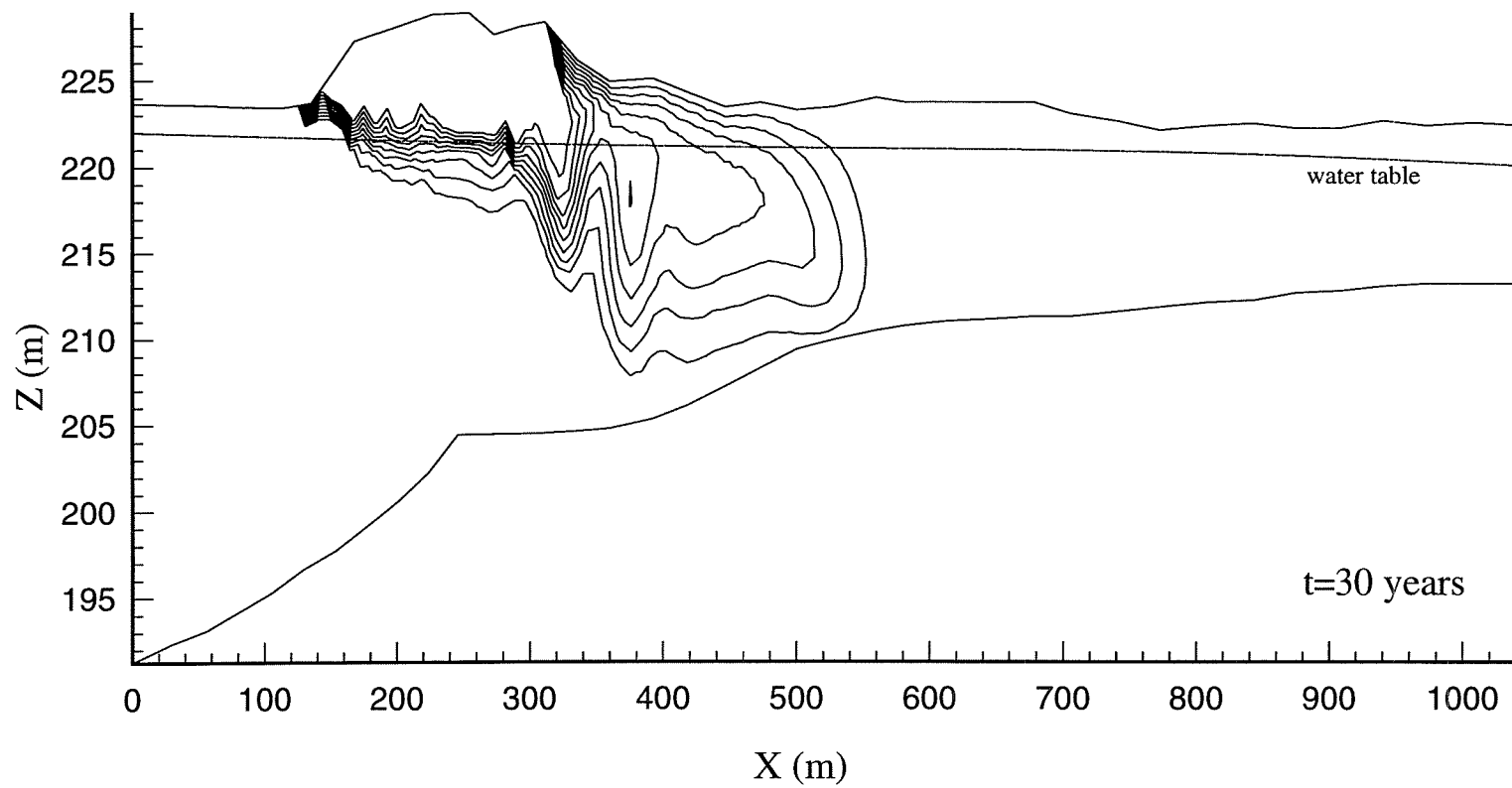Concentration isolines (Min: 0.1, Max: 0.9)

Figure 7.7   Continued
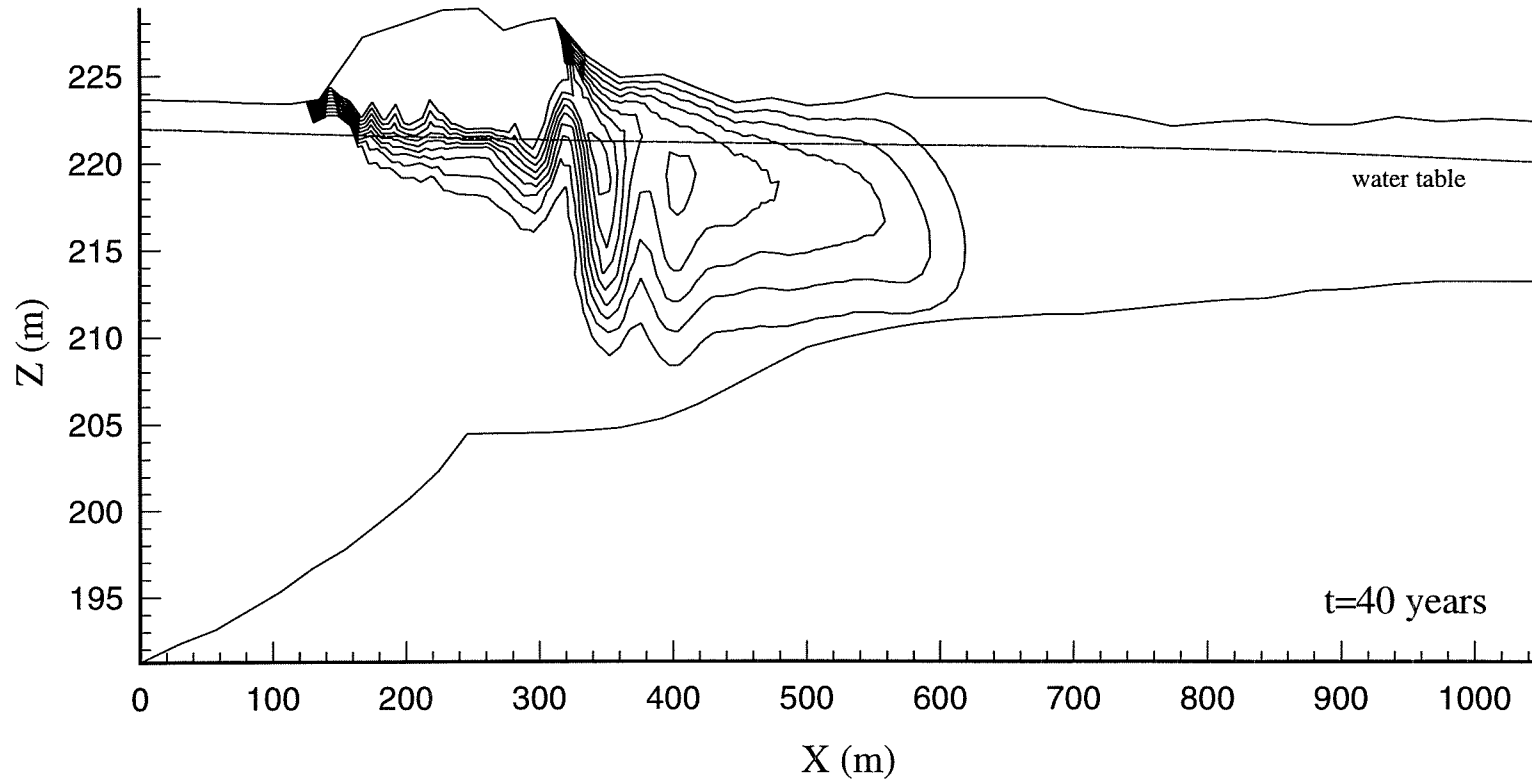
Concentration isolines (Min: 0.1, Max: 0.9)

Figure 7.8   Instability development for a contaminant source
(ε=0.014) at t= 10,20,30,40 and 50 hours

Figure 7.8   Continued

Concentration isolines (Min: 0.1, Max: 0.9)

Figure 7.8   Continued
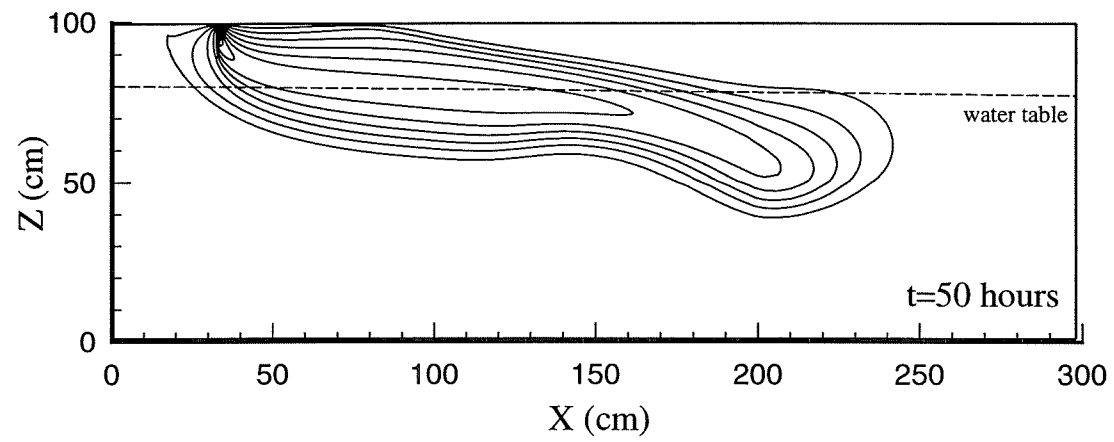
Concentration isolines (Min: 0.1, Max: 0.9)
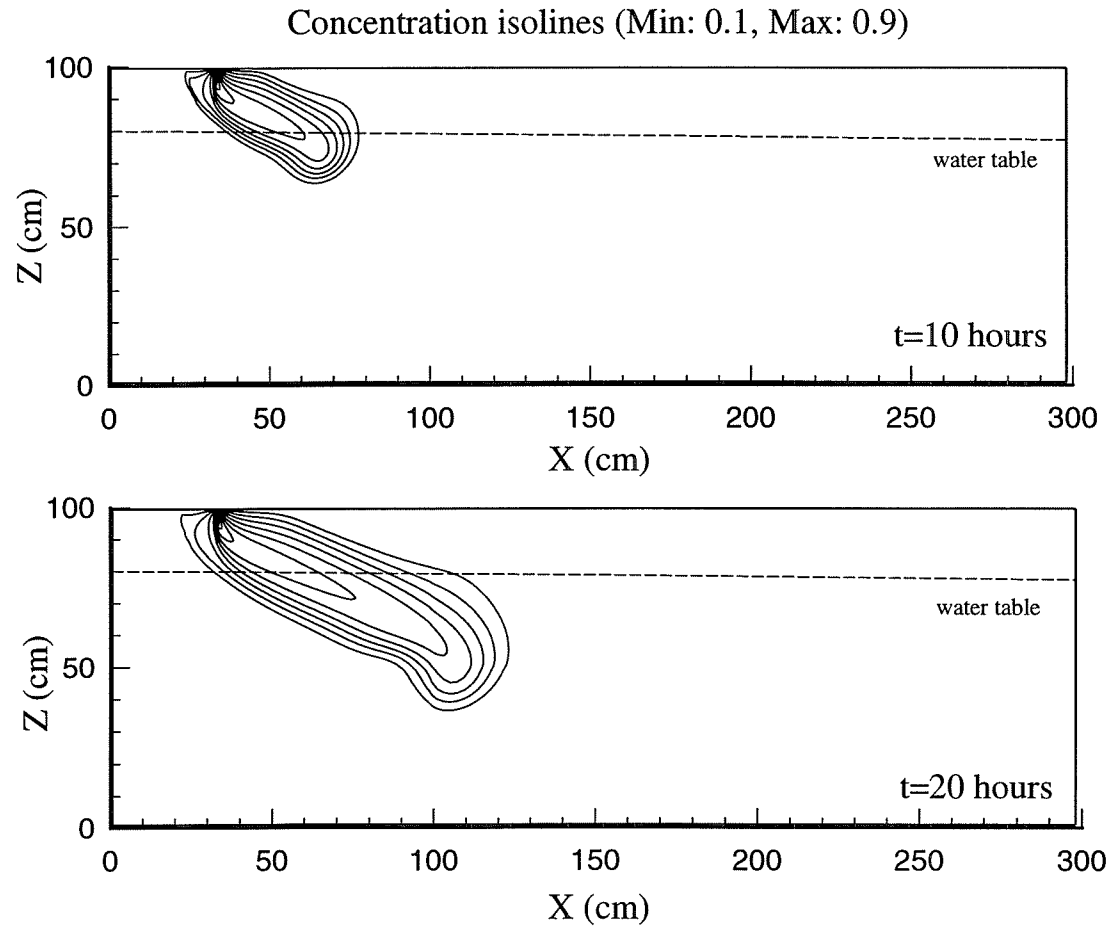
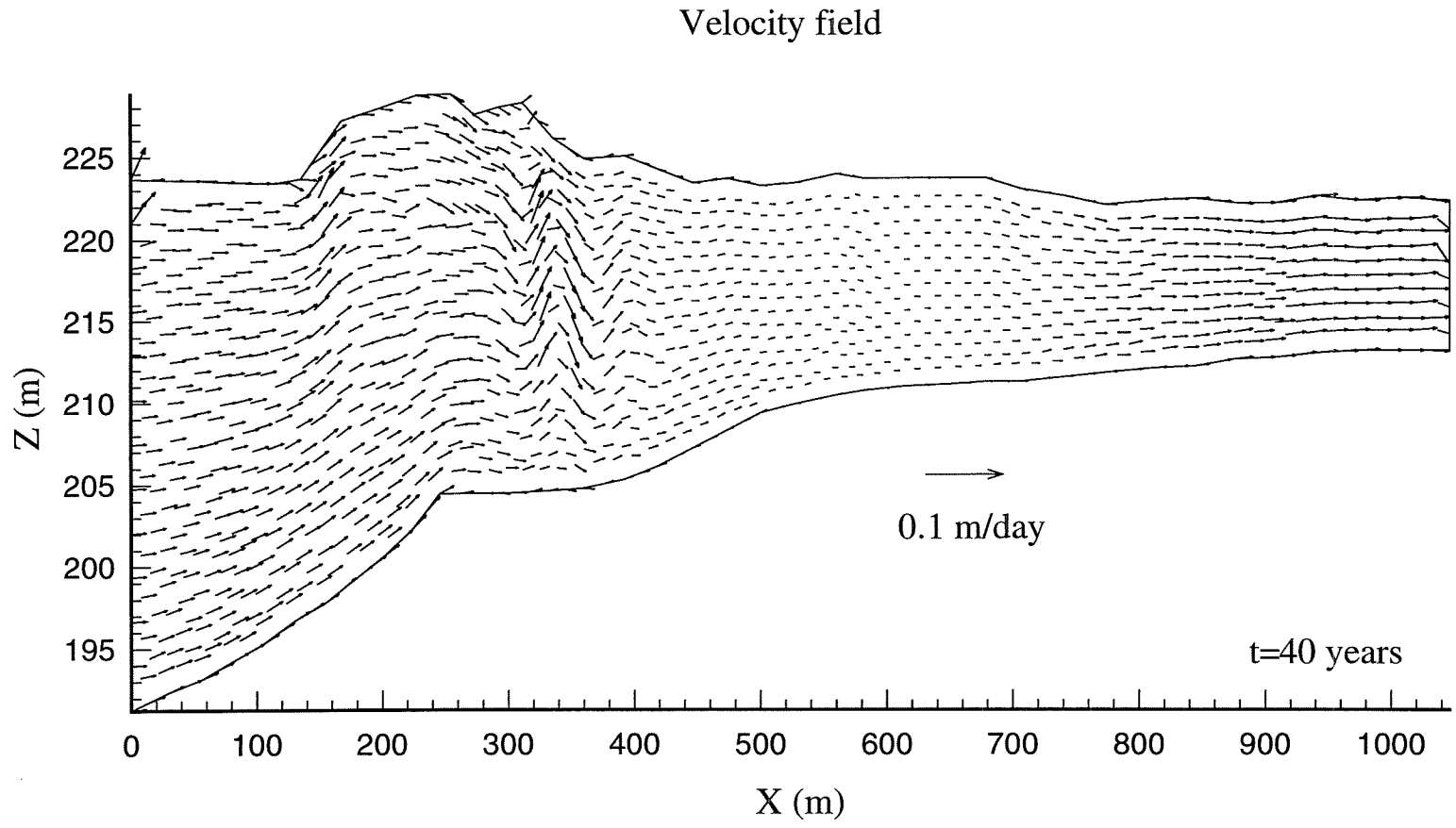Figure 7.9   Instability development for a contaminant souce
(ε=0.028) at t= 10,20,30,40 and 50 hours

Concentration isolines (Min: 0.1, Max: 0.9)

Figure 7.9   Continued
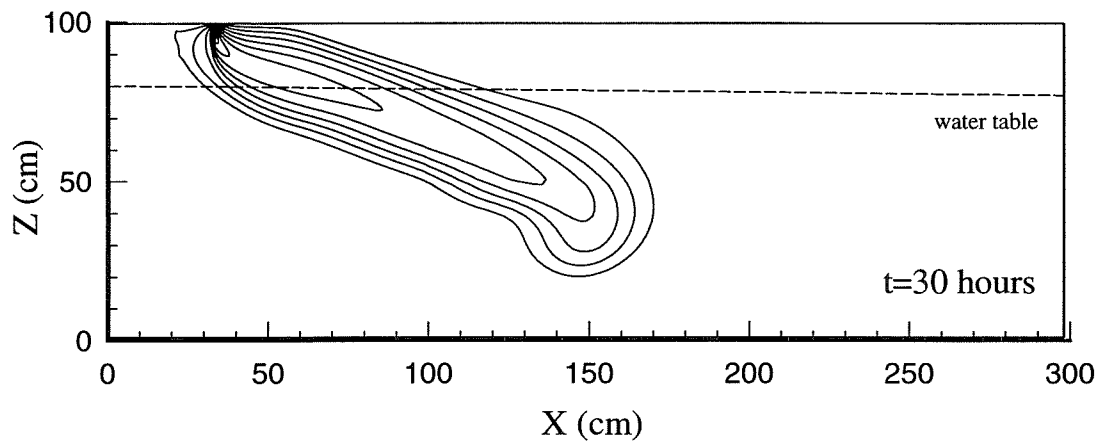
Concentration isolines (Min: 0.1, Max: 0.9)

Figure 7.9   Continued
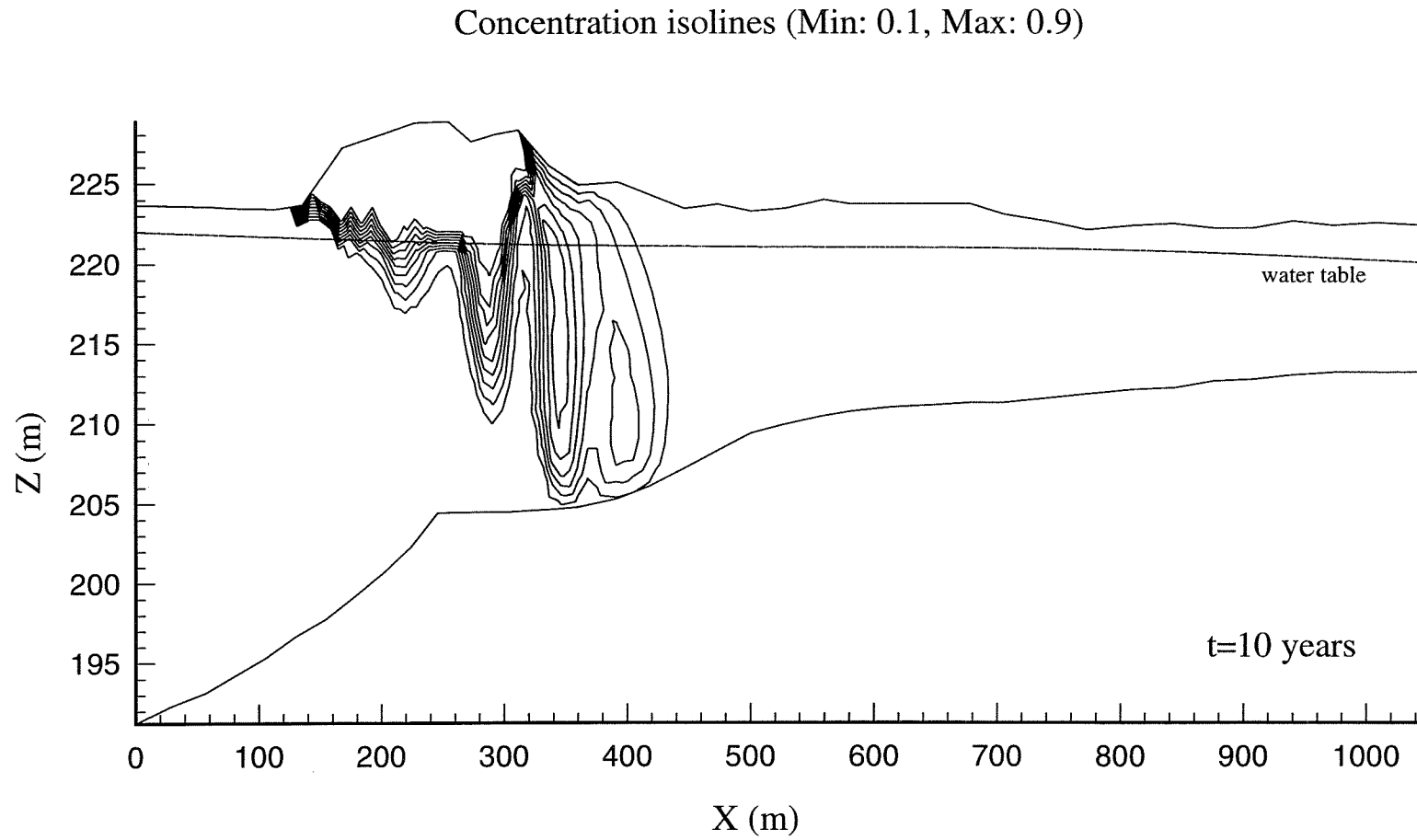
Concentration isolines (Min: 0.1, Max: 0.9)
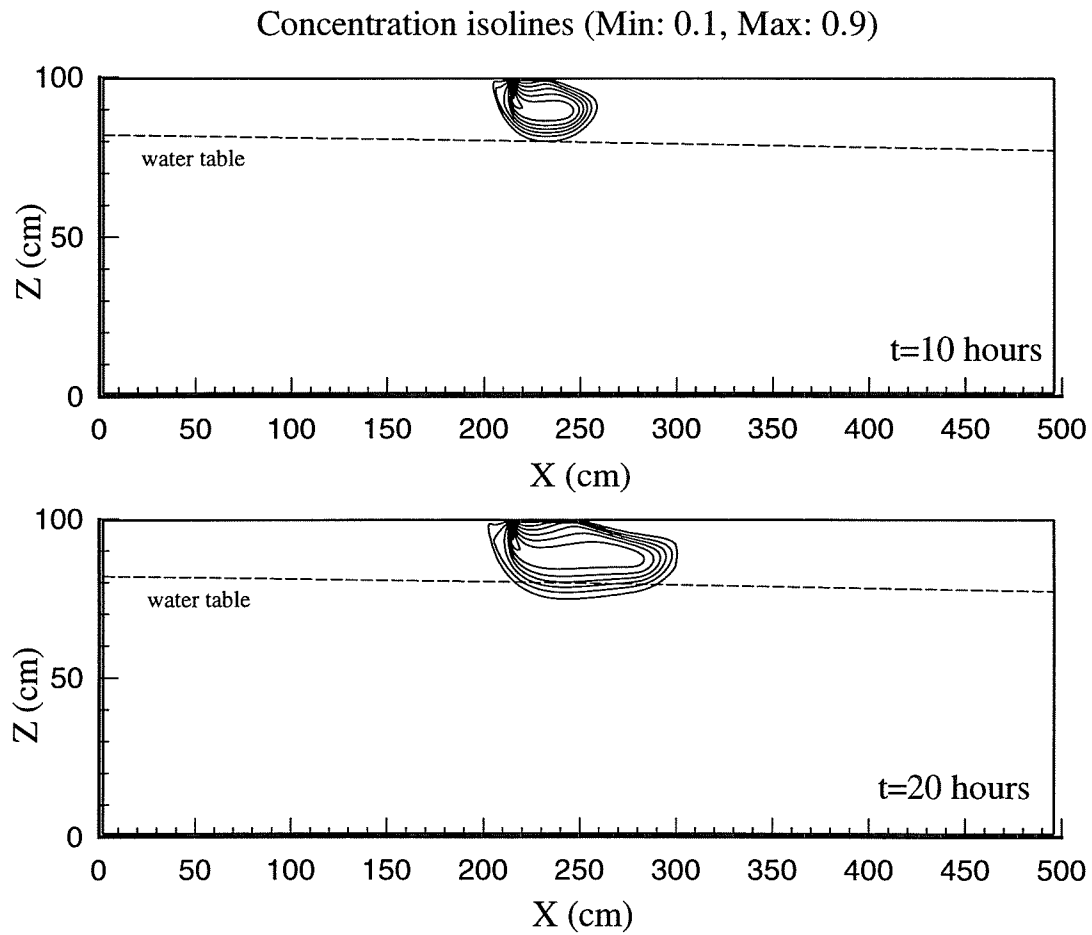
Figure 7.10   Instability development for a contaminant source
(ε=0.0072)   at t= 10,20,30,40 and 50 hours
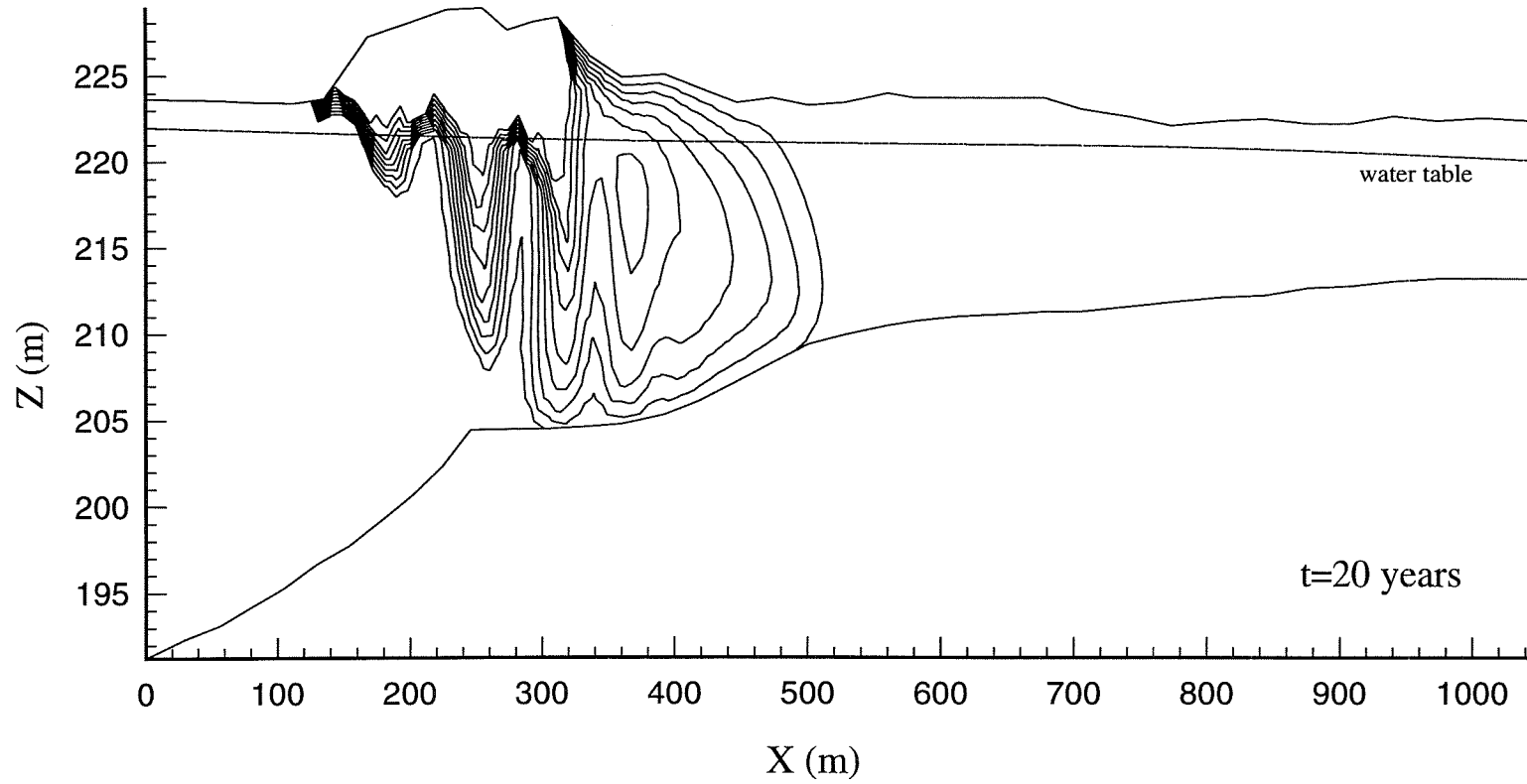
Concentration isolines (Min: 0.1, Max: 0.9)

Figure 7.10   Continued

Cocentration isolines (Min: 0.1, Max: 0.9)
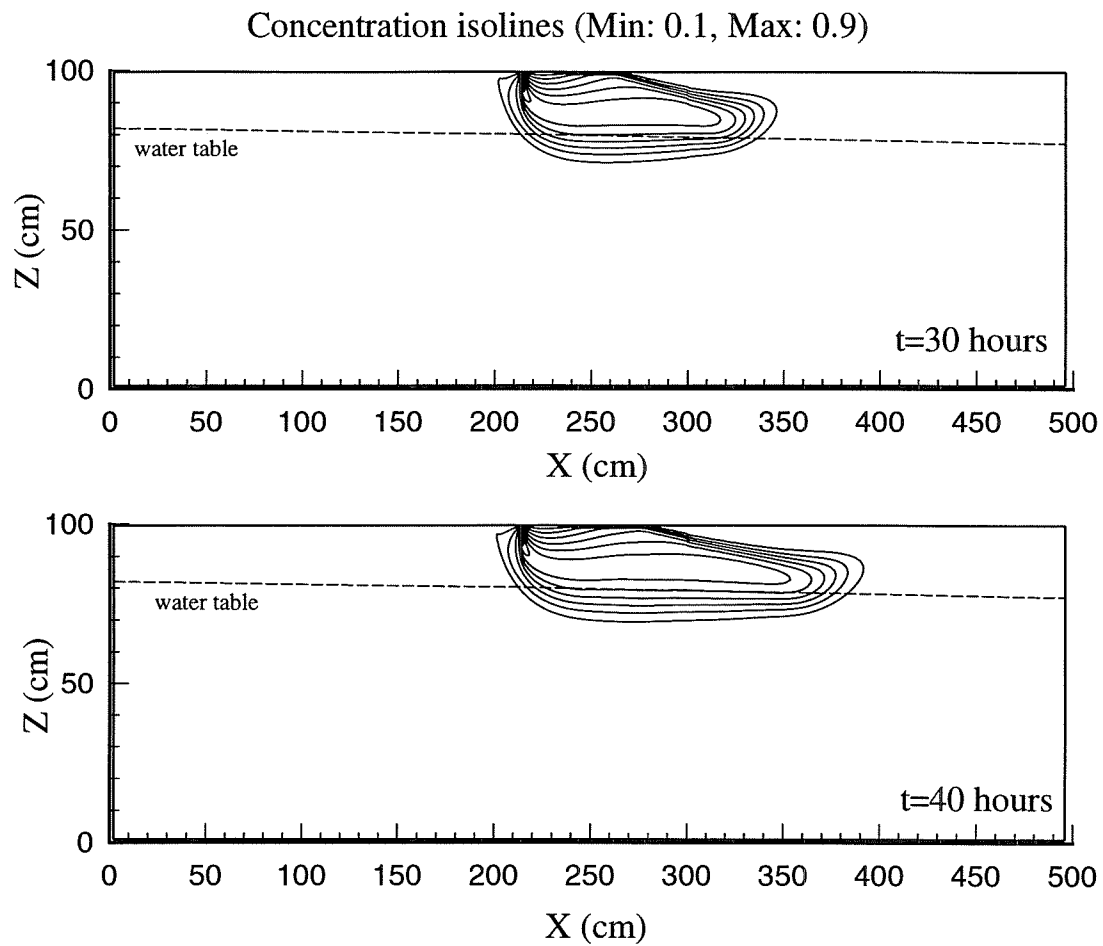
Figure 7.10   Continued

Concentration isolines (Min: 0.1, Max: 0.9)

Figure 7.11   Instability development for s contaminant source
(ε=0.014)   at t= 10, 20, 30, 40 and 50 hours

Concentration isolines (Min: 0.1, Max: 0.9)

Figure 7.11   Continued

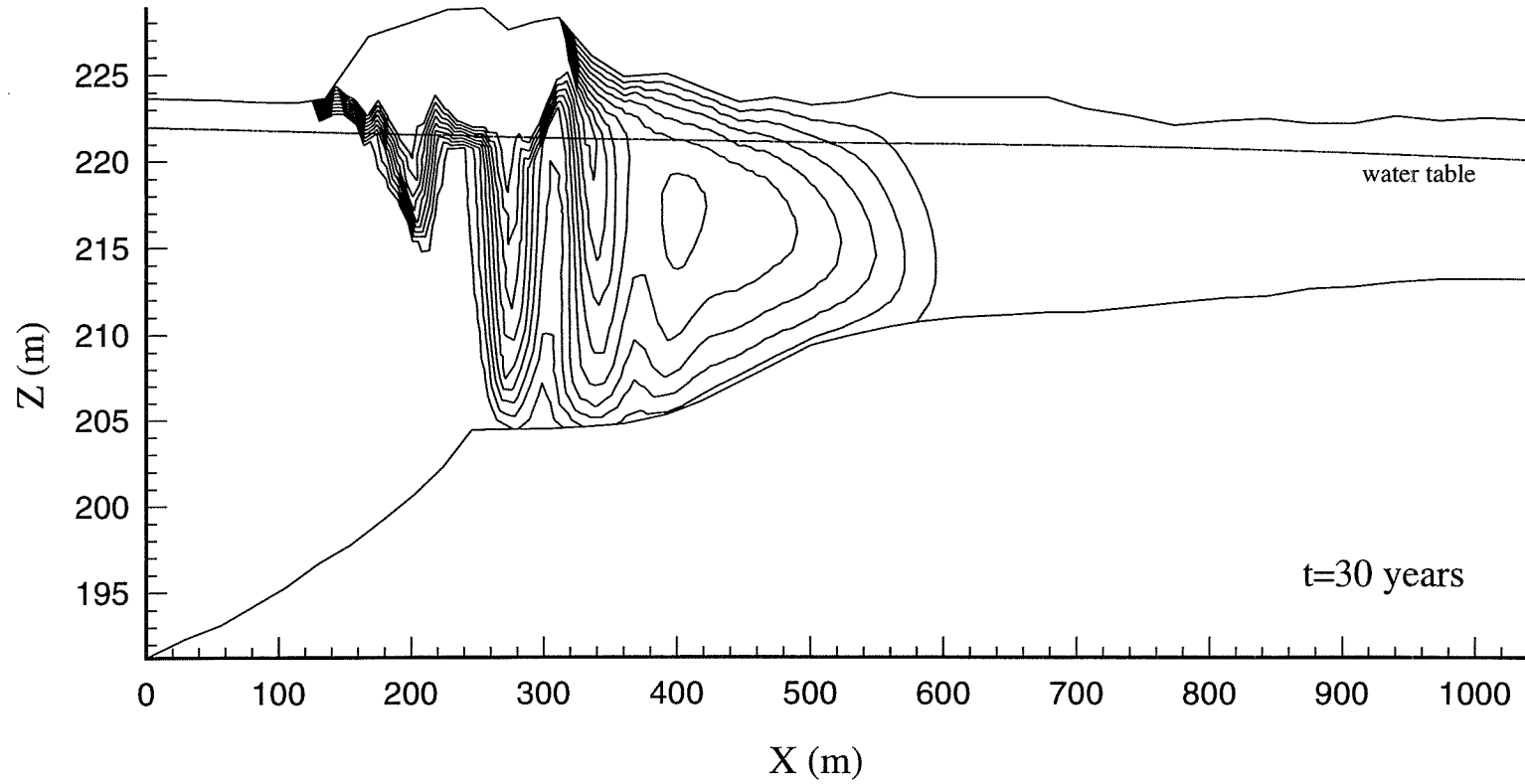Concentration isolines (Min: 0.1, Max: 0.9)

Figure 7.11   Continued
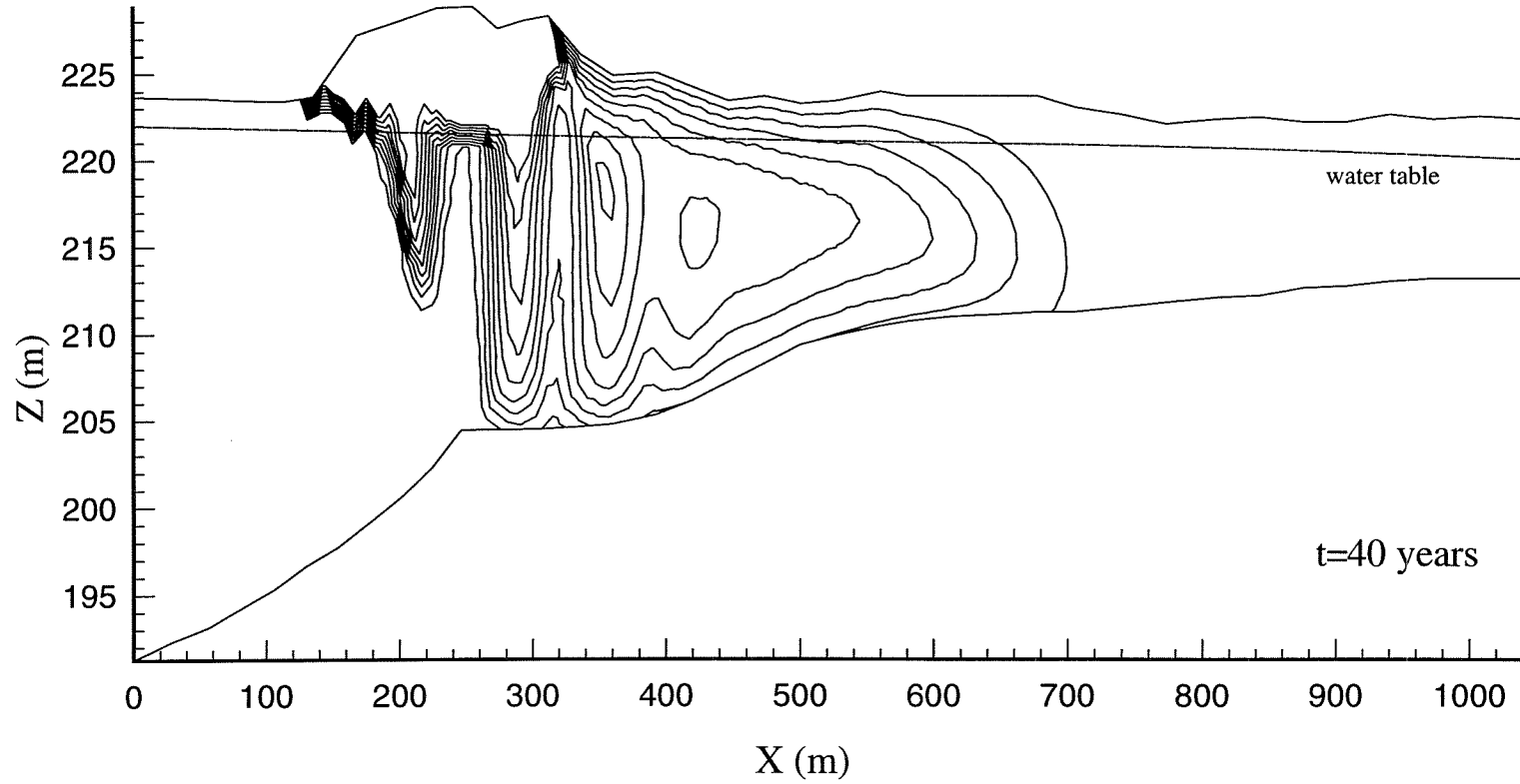
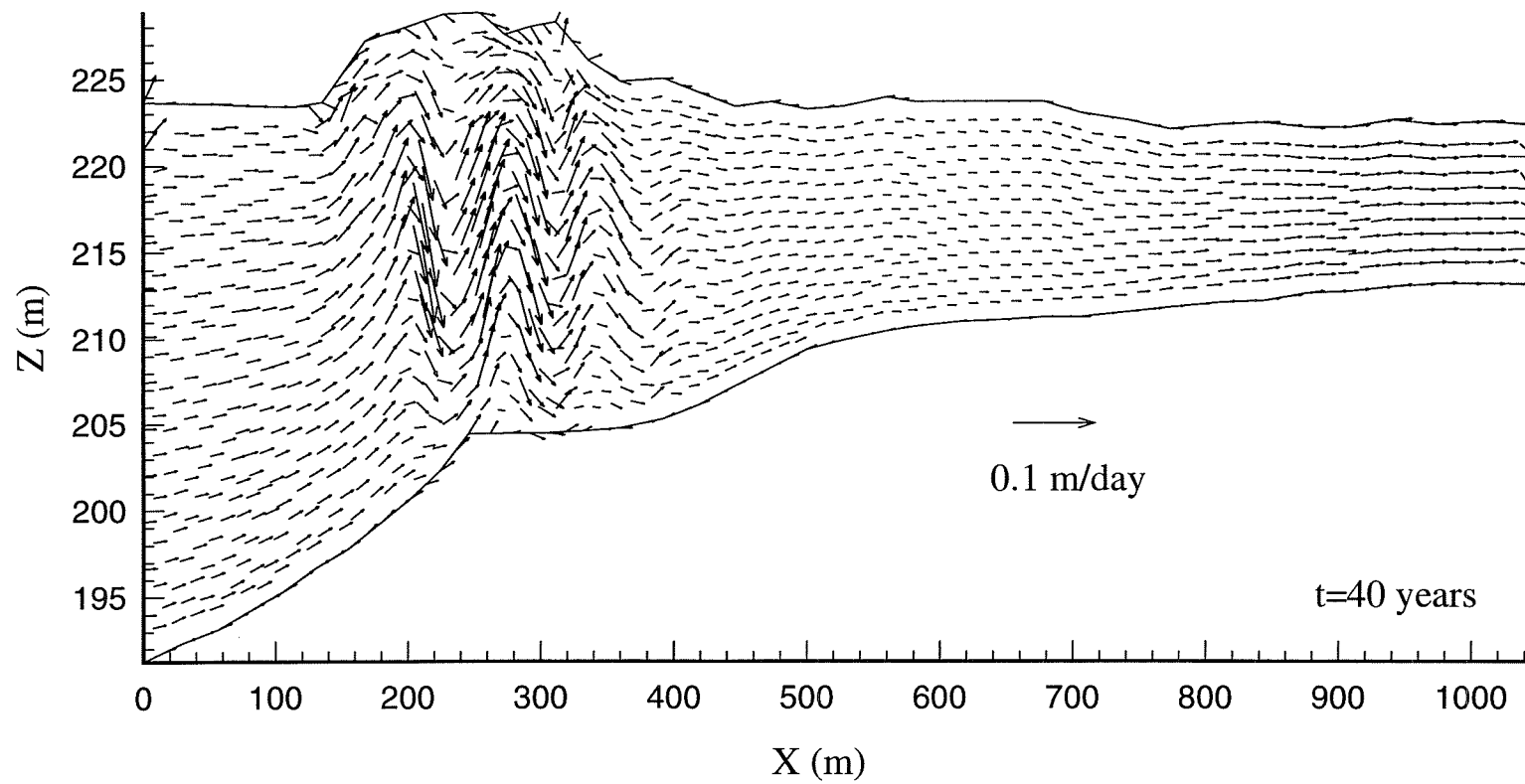Concentration isolines (Min: 0.1, Max: 0.9)

Figure 7.12   Instability development for a contaminant source
(ε=0.028)   at t= 10,20,30 and 40 hours

Concentration isolines (Min: 0.1, Max: 0.9)
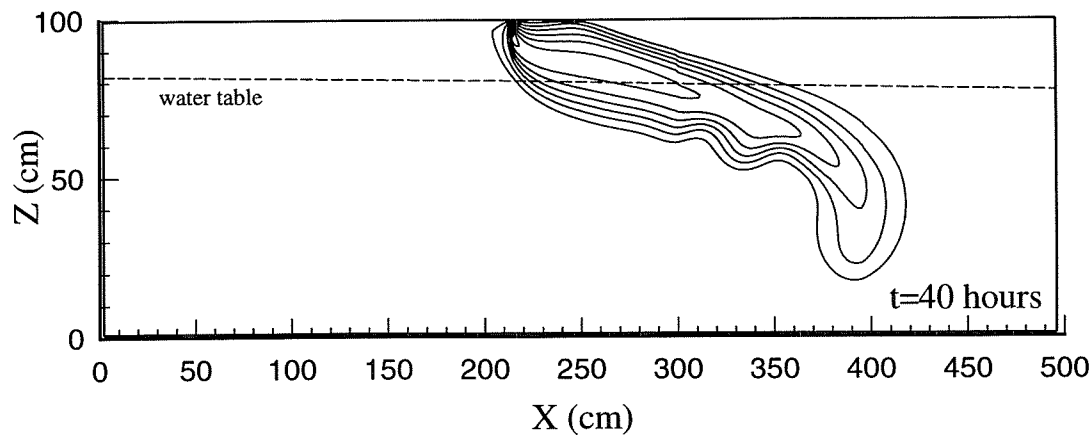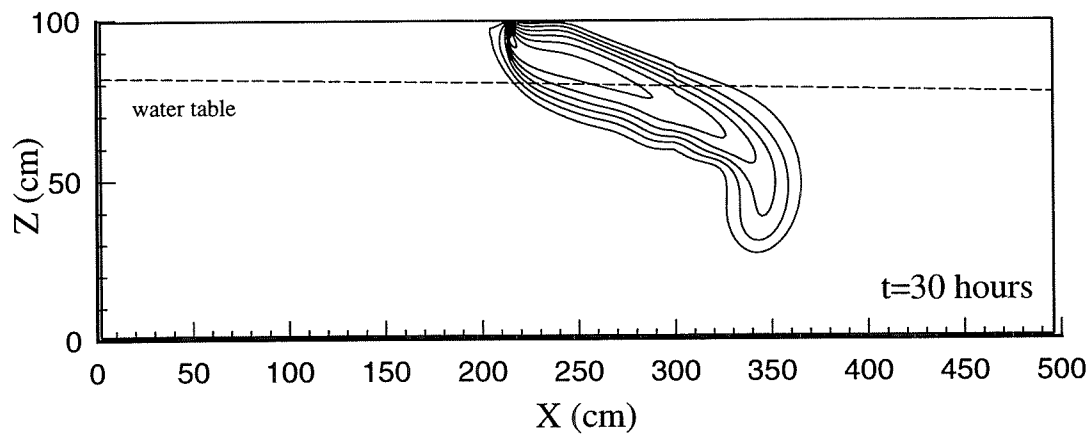
Figure 7.12   Continued
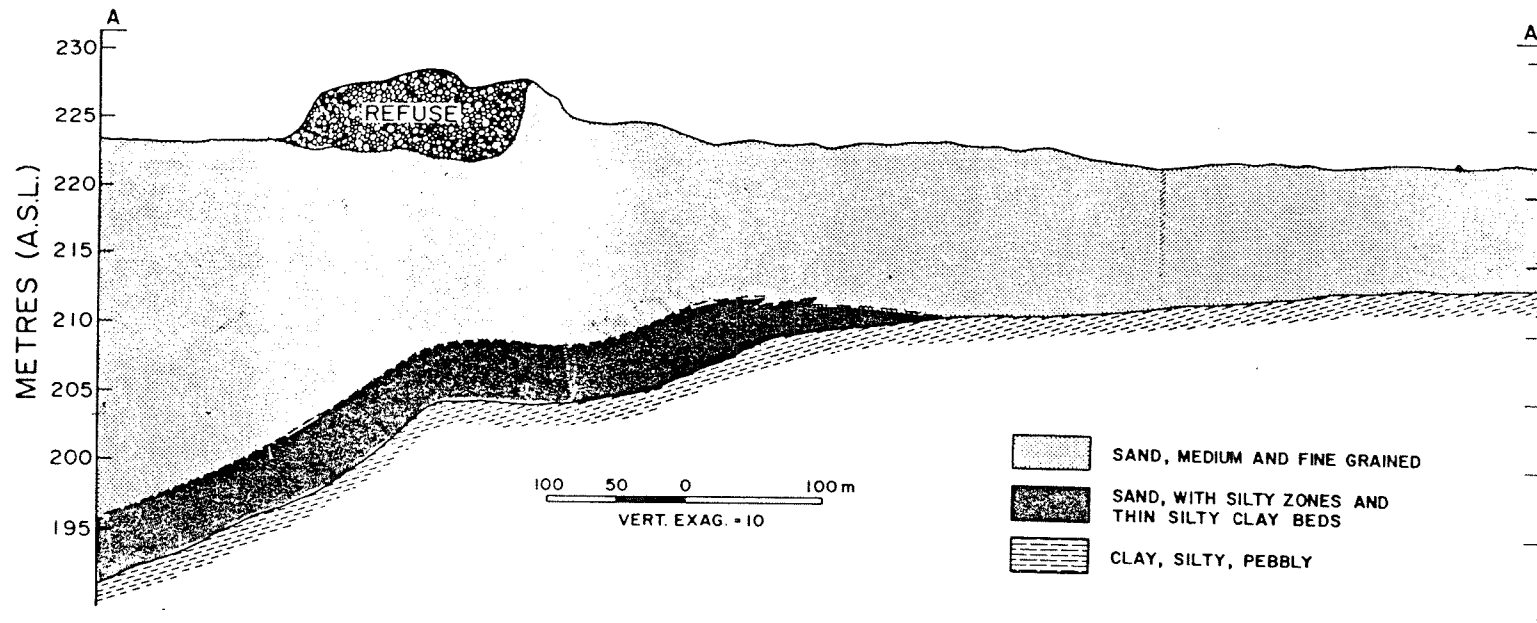
Figure 8.1   Longitudinal geological cross-section along the main direction of groundwater flow
(MacFarlane et al., 1983)
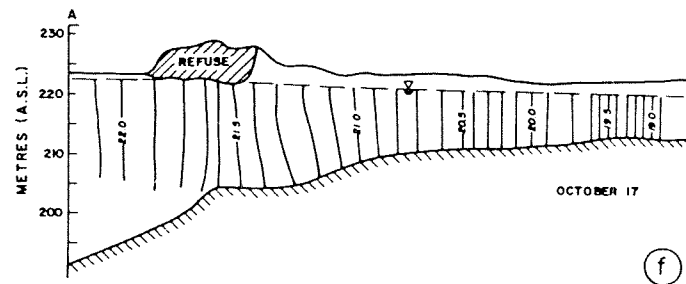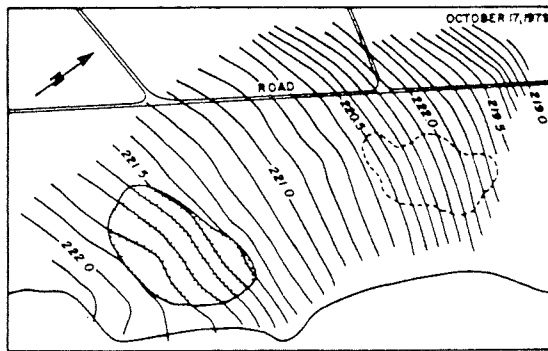
Figure 8.2   Water table map and hydraulic head along the longitudinal cross-section
(MacFarlane et al., 1983)
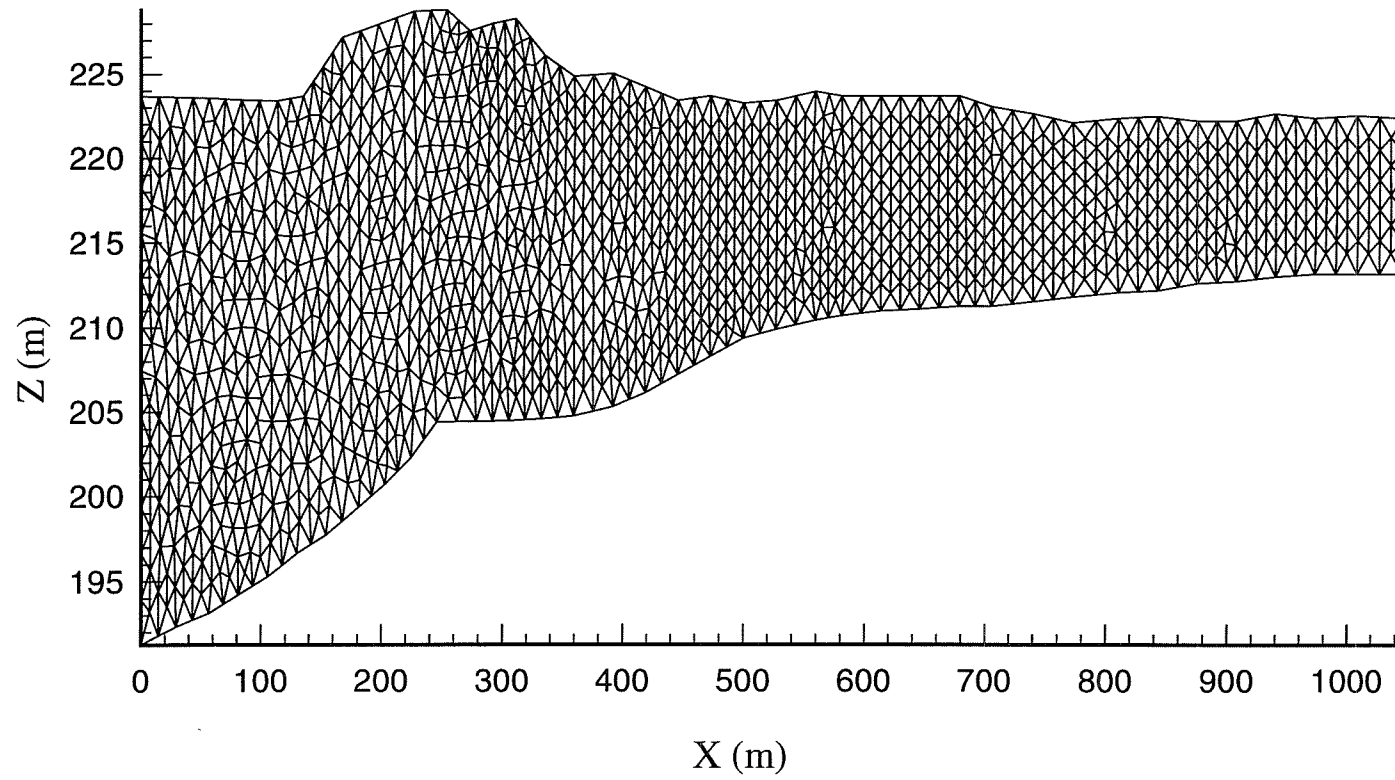
Figure 8.3   Computational domain and mesh

Concentration isolines (Min: 0.1, Max: 0.9)
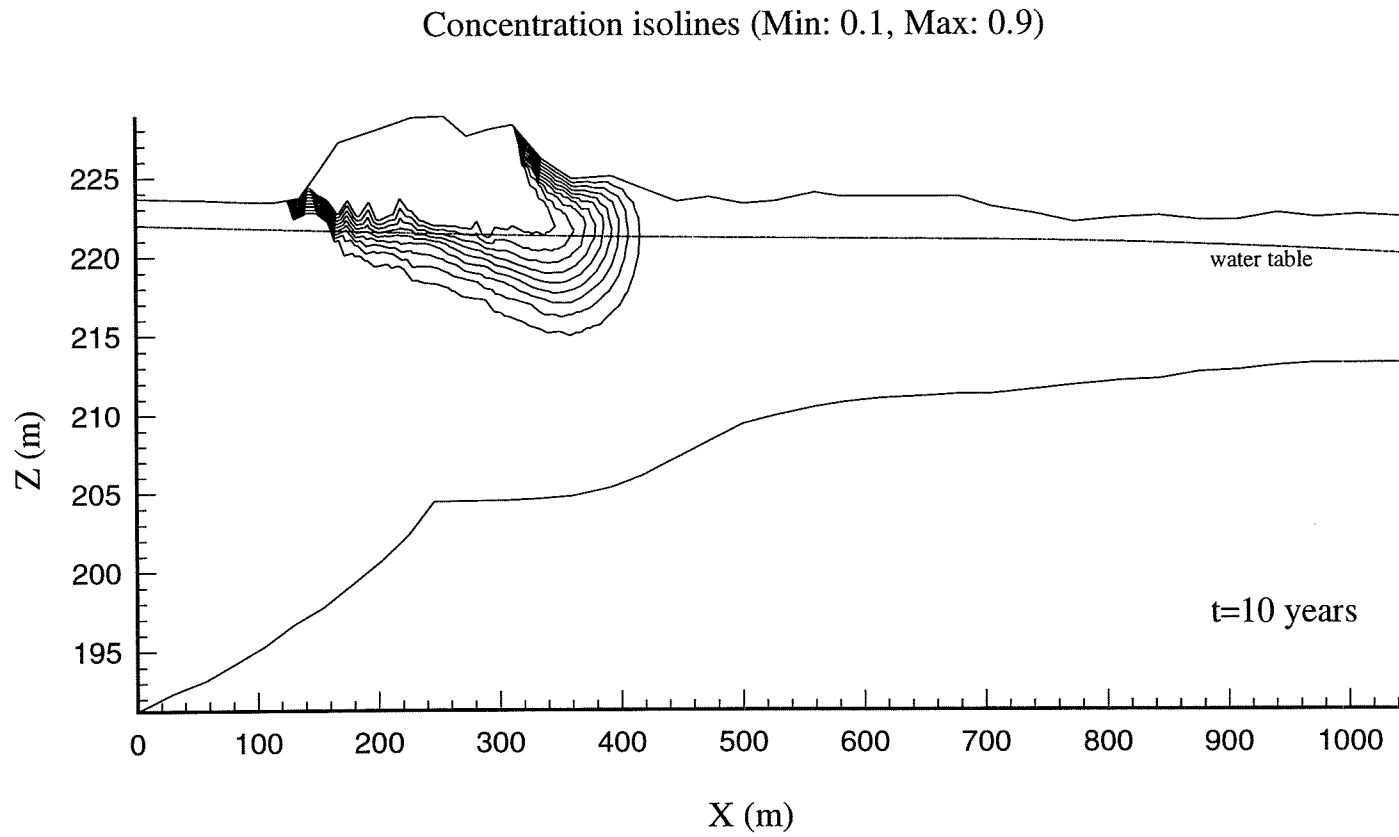
Figure 8.4   A neutral contaminant plumeat t=10, 20, 30 and 40 years

Concentration isolines (Min: 0.1, Max: 0.9)
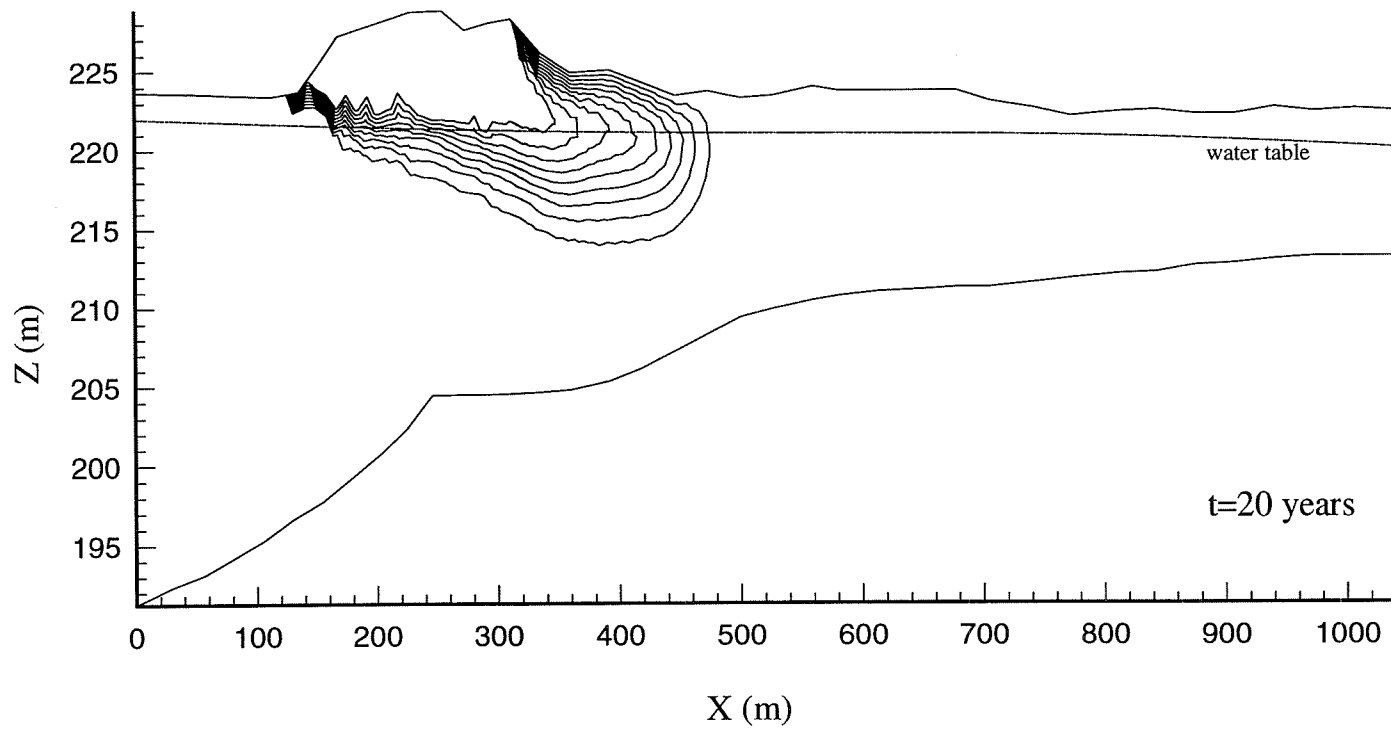
Figure 8.4   Continued

Concentration isolines (Min: 0.1, Max: 0.9)

Figure 8.4   Continued
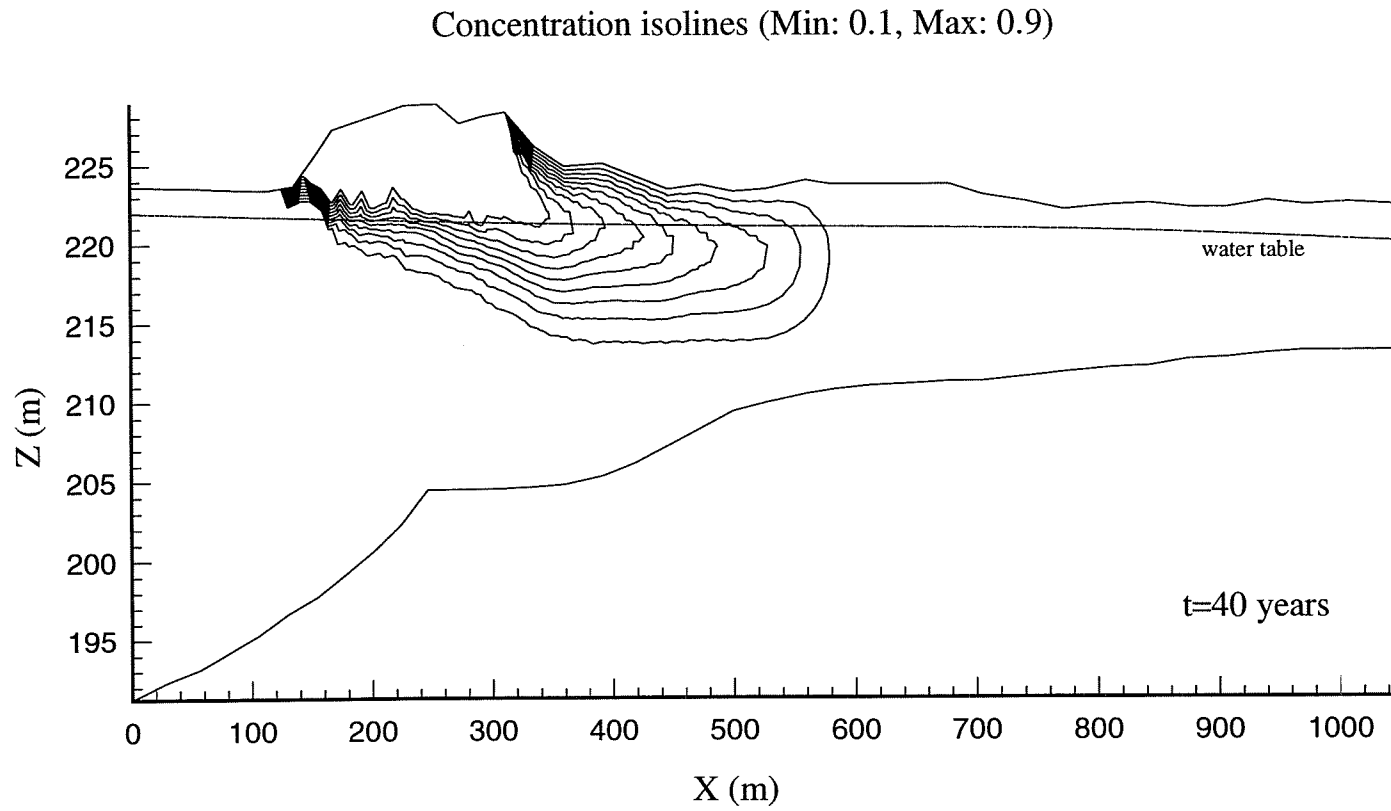
Figure 8.4   Continued

Velocity field

Figure 8.4   Continued
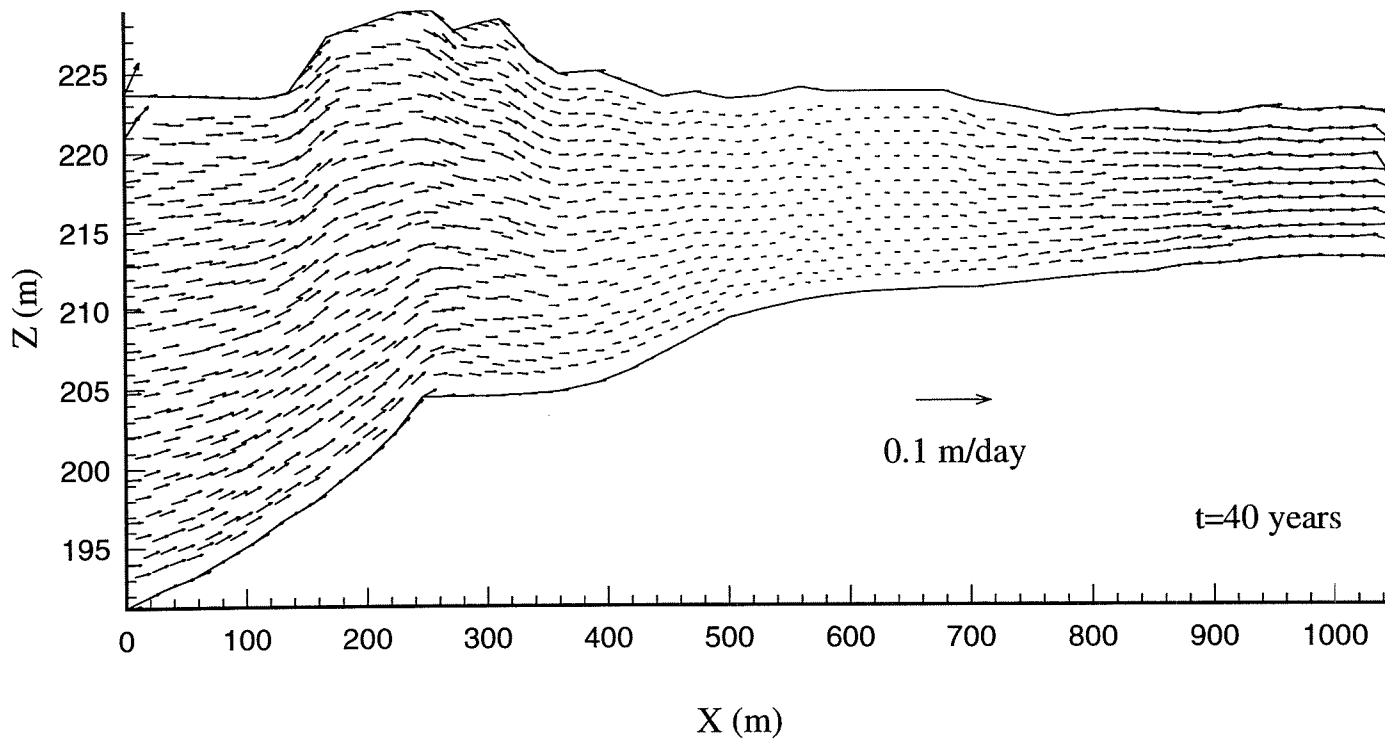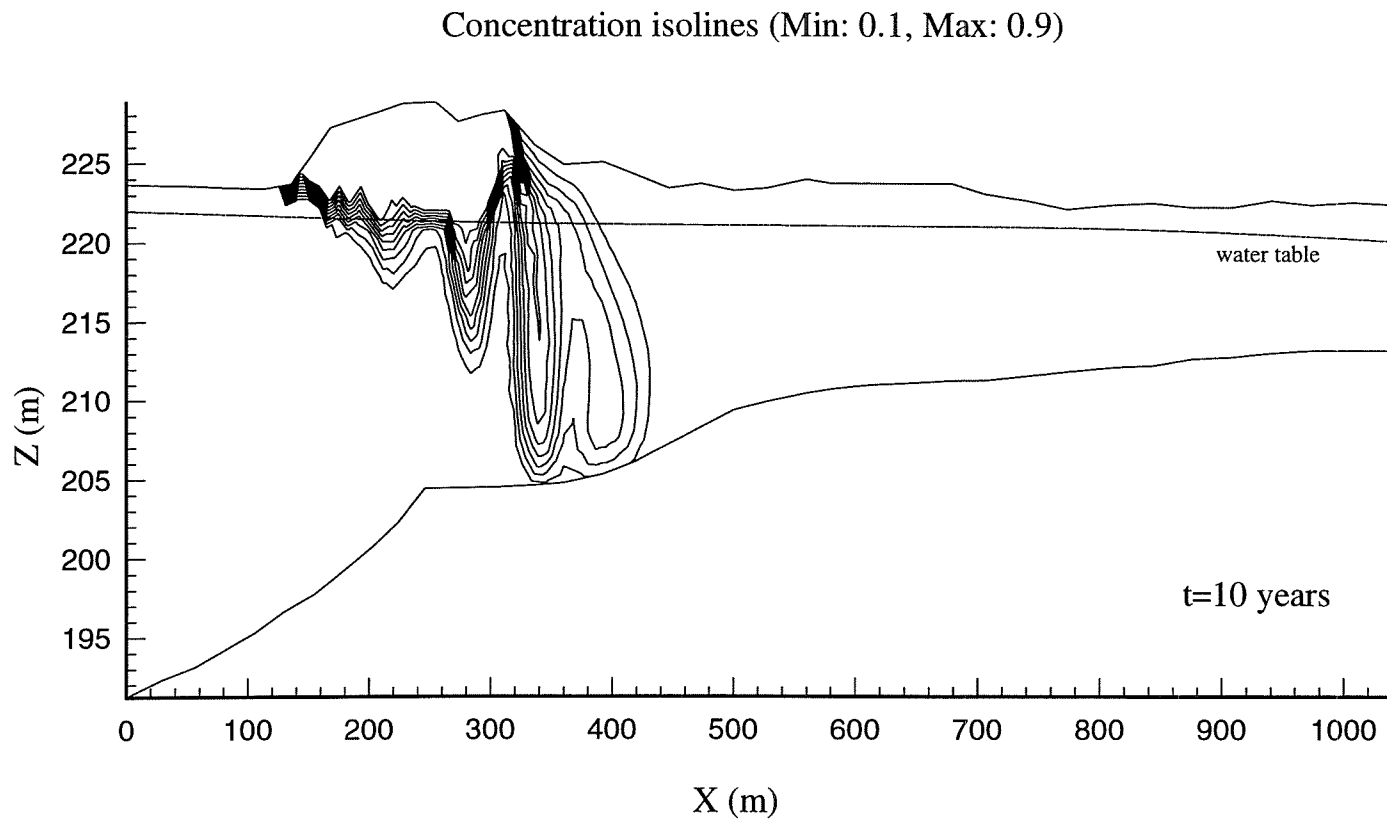
Concentration isolines (Min: 0.1, Max: 0.9)
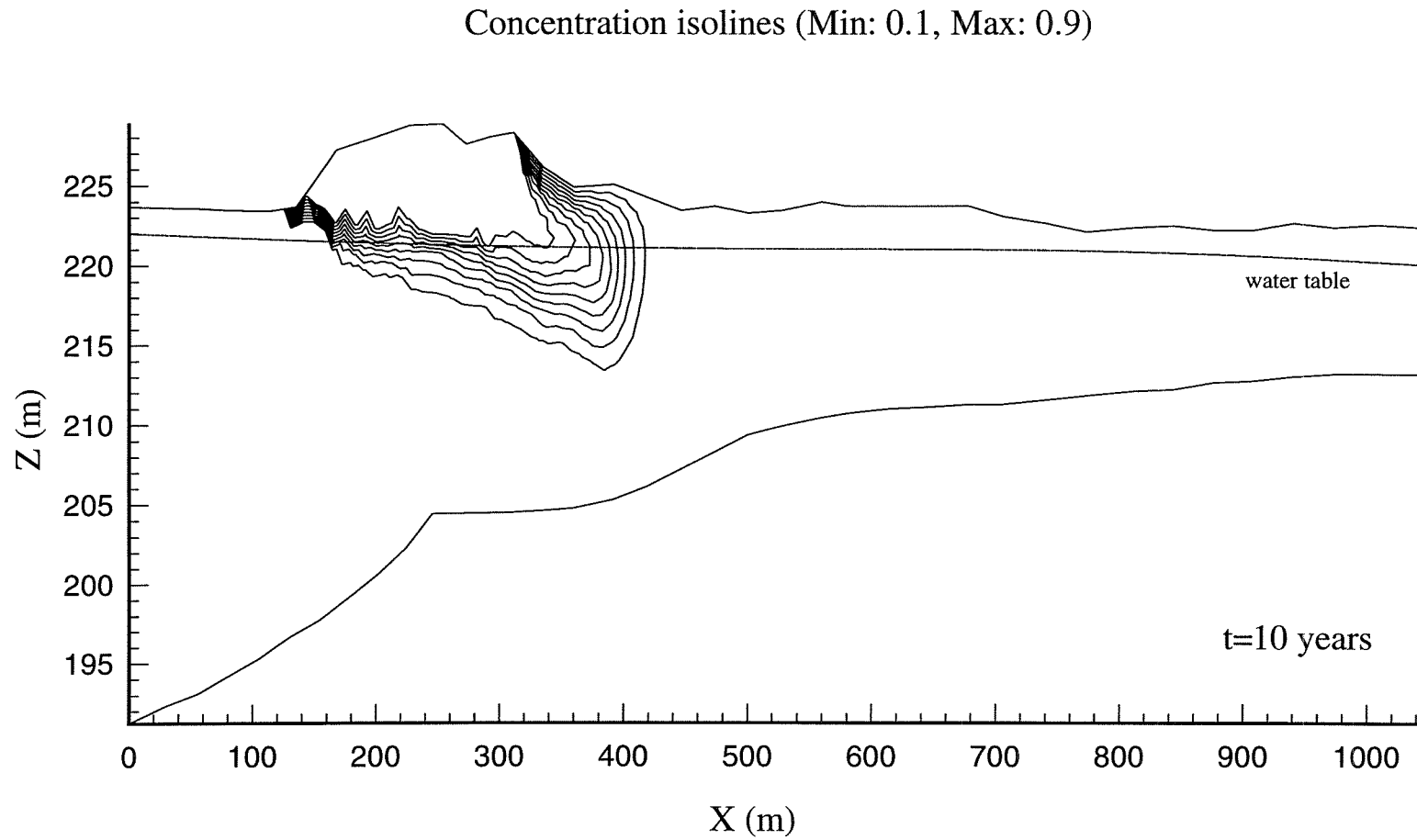
Figure 8.5   Instability development for a contaminant source ($\varepsilon=0.0014$)
at t=10, 20, 30 and 40 years
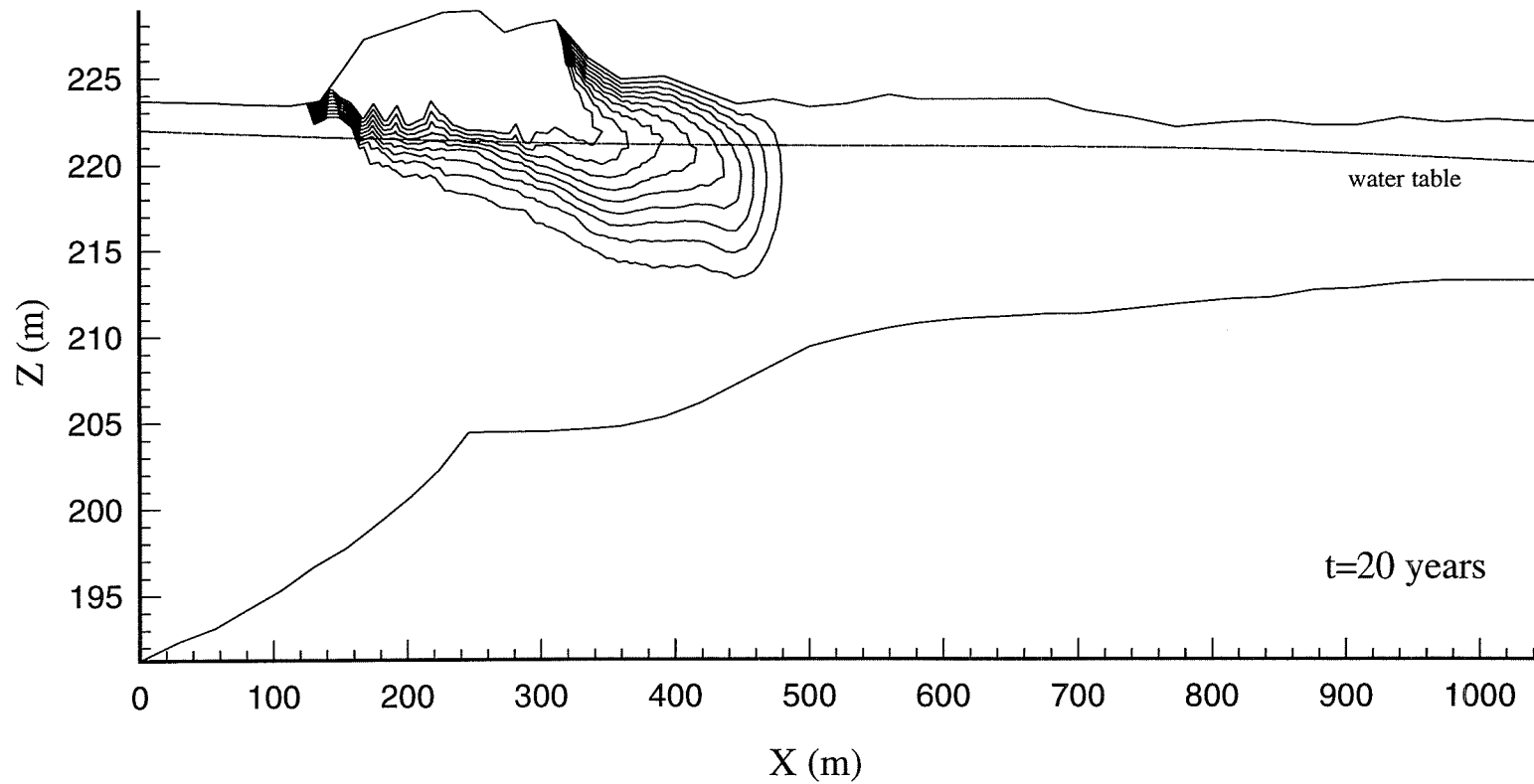
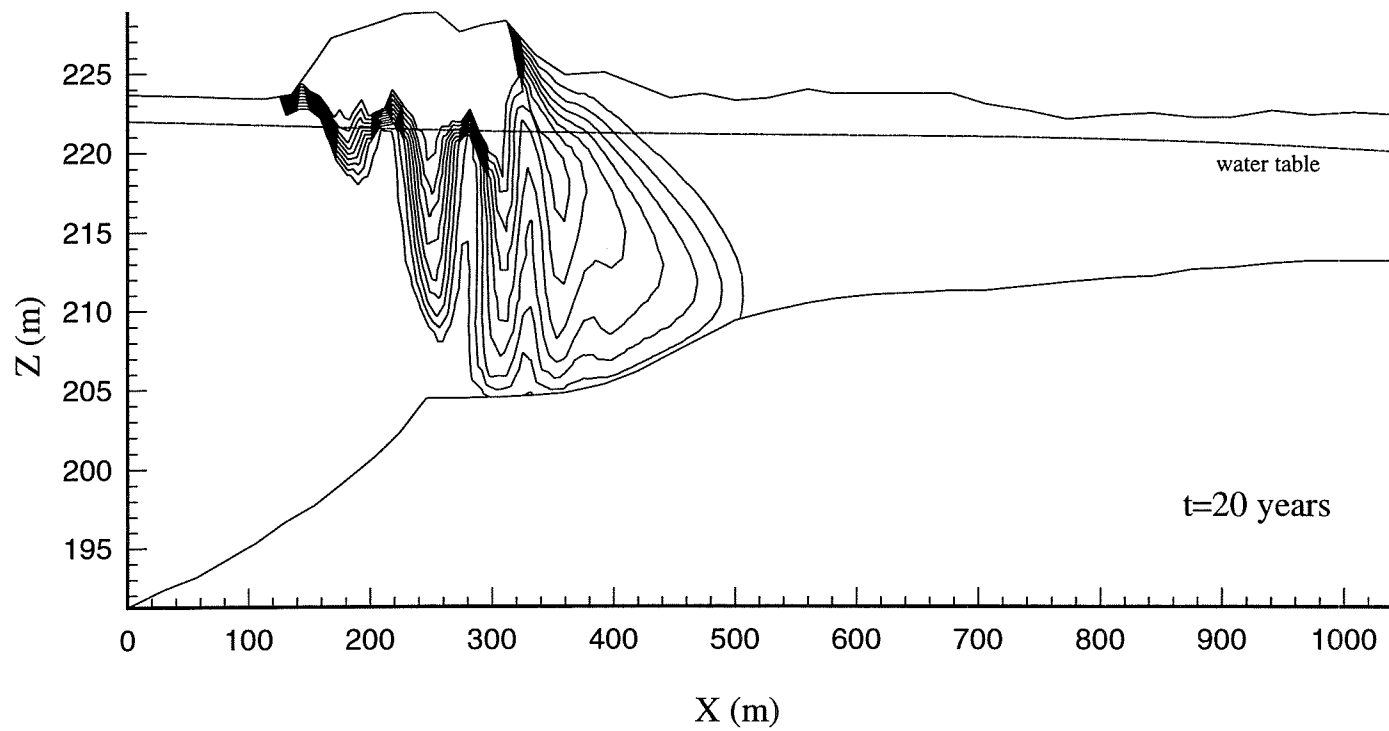Concentration isolines (Min: 0.1, Max: 0.9)

Figure 8.5   Continued

Concentration isolines (Min: 0.1, Max: 0.9)

Figure 8.5   Continued

Concentration isolines (Min: 0.1, Max: 0.9)

Figure 8.5   Continued

Velocity field

Figure 8.5   Continued

Concentration isolines (Min: 0.1, Max: 0.9)

Figure 8.6   Instability development for a contaminant source (ε=0.0025)
at t=10, 20, 30 and 40 years

Concentration isolines (Min: 0.1, Max: 0.9)

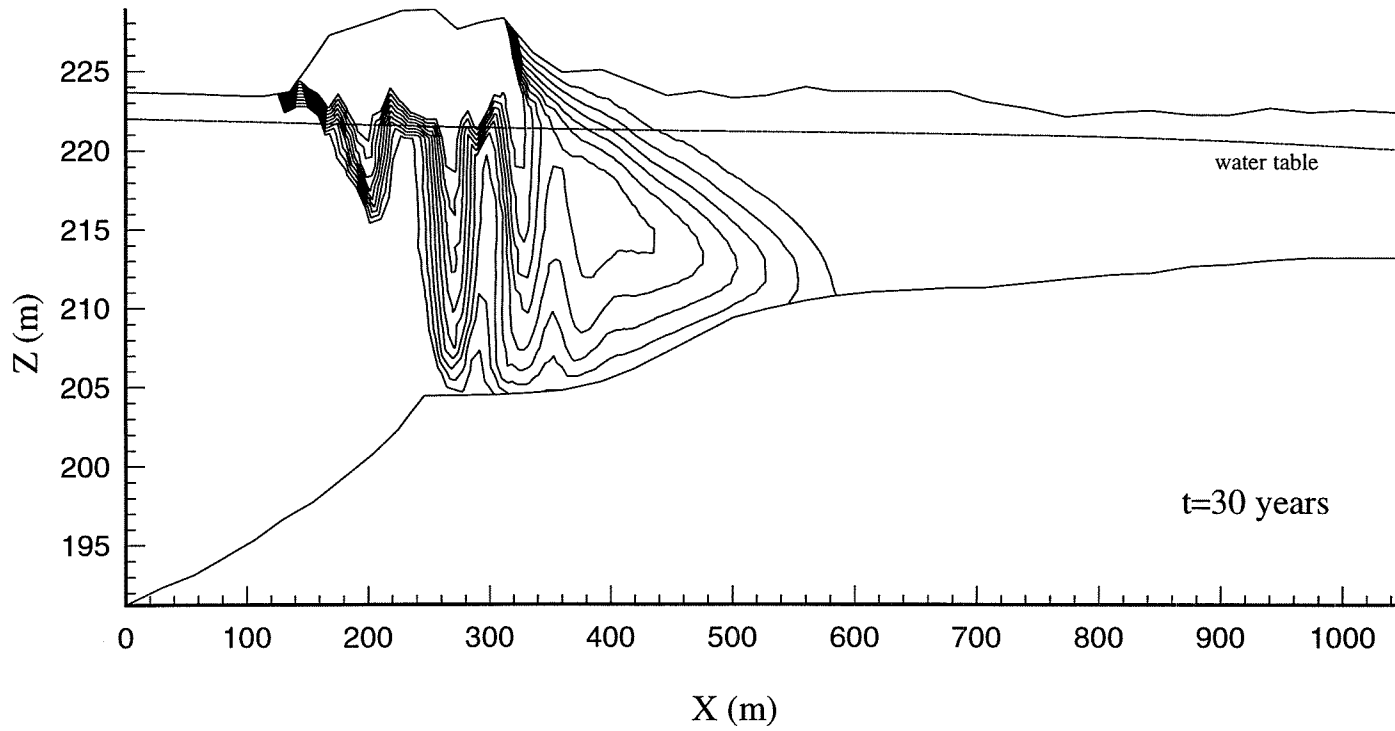Figure 8.6   Continued

Concentration isolines (Min: 0.1, Max: 0.9)

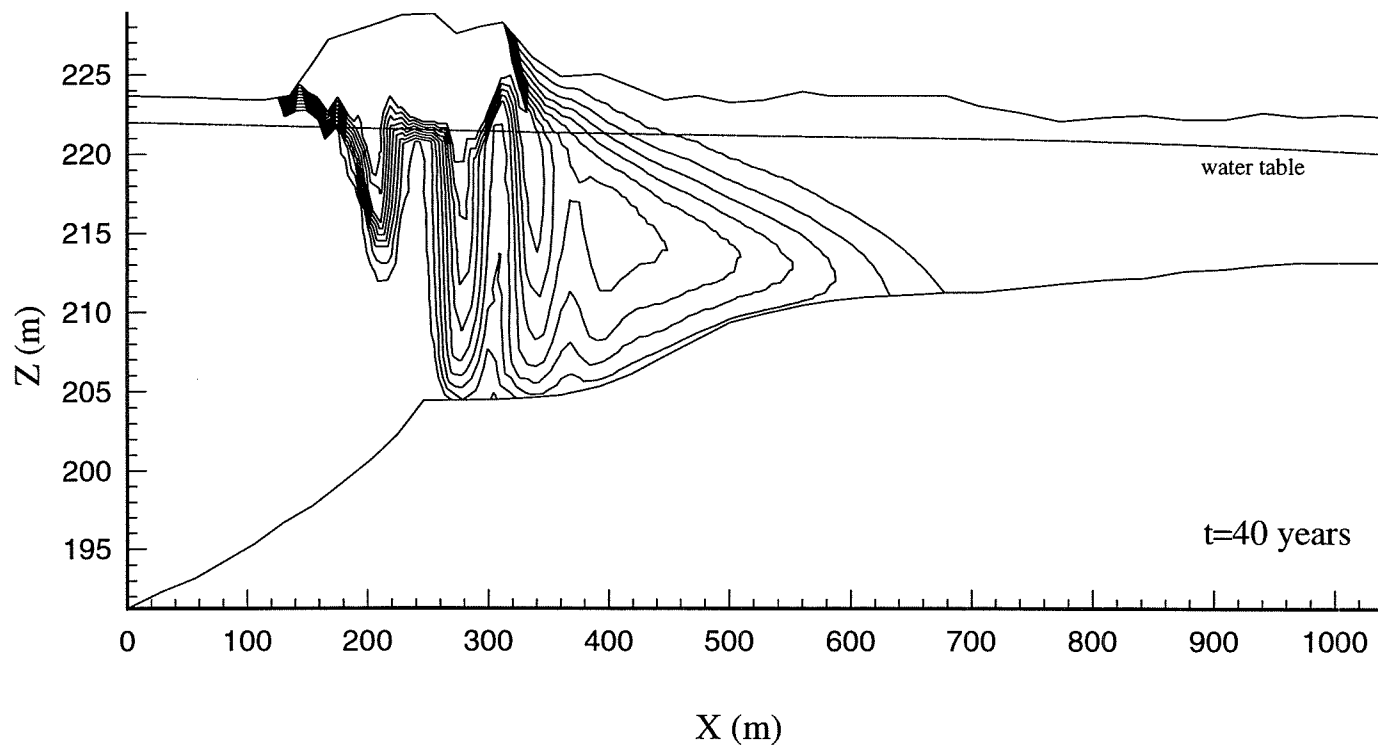Figure 8.6   Continued

Concentration isolines (Min: 0.1, Max: 0.9)

t=40 years

water table

X (m)

Z (m)

Figure 8.6   Continued

Figure 8.6   Continued

Concentration isolines (Min: 0.1, Max: 0.9)

Figure 8.7 Instability development for a contaminant source (ε=0.0036)
at t=10, 20, 30 and 40 years

Concentration isolines (Min: 0.1, Max: 0.9)

Figure 8.7   Continued

Concentration isolines (Min: 0.1, Max: 0.9)

Figure 8.7   Continued

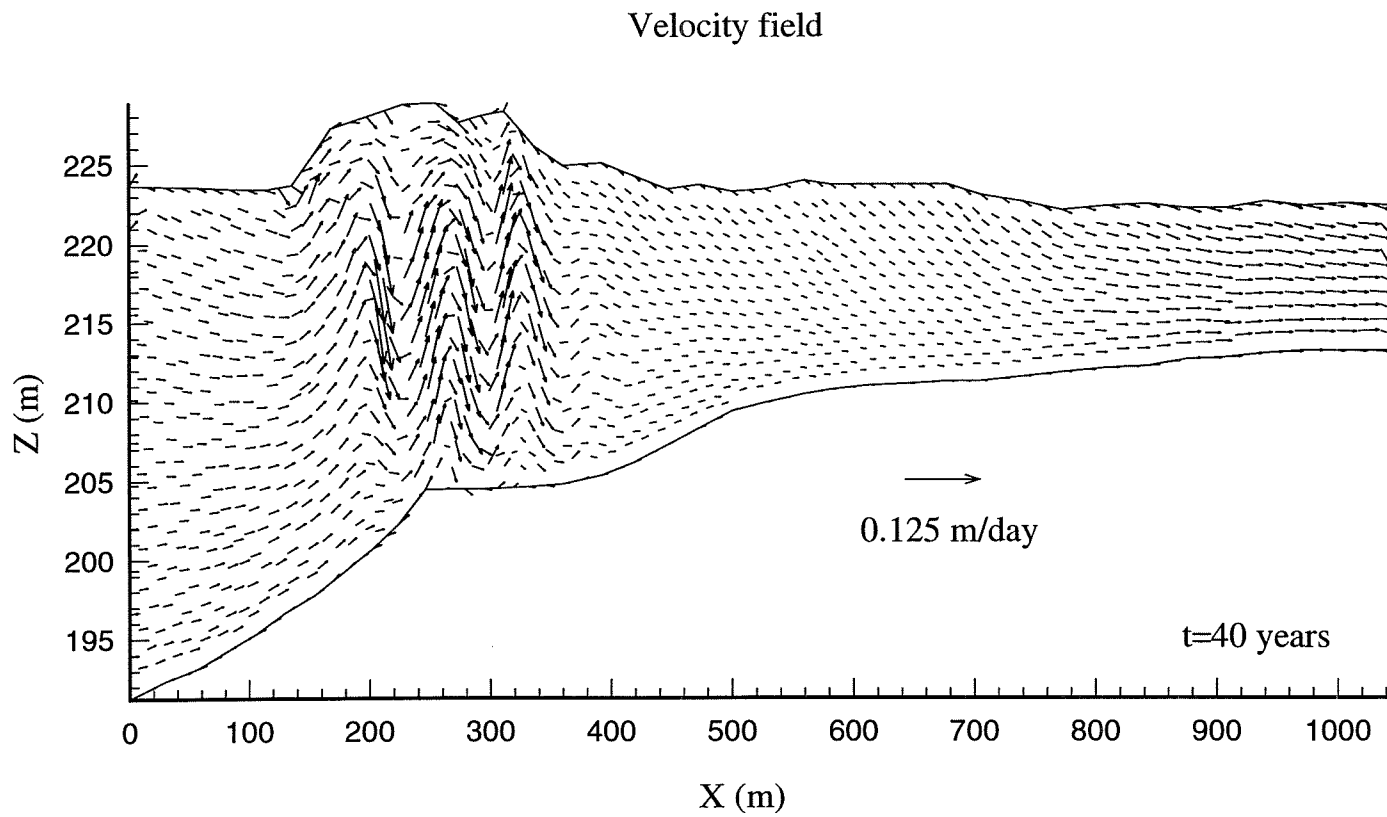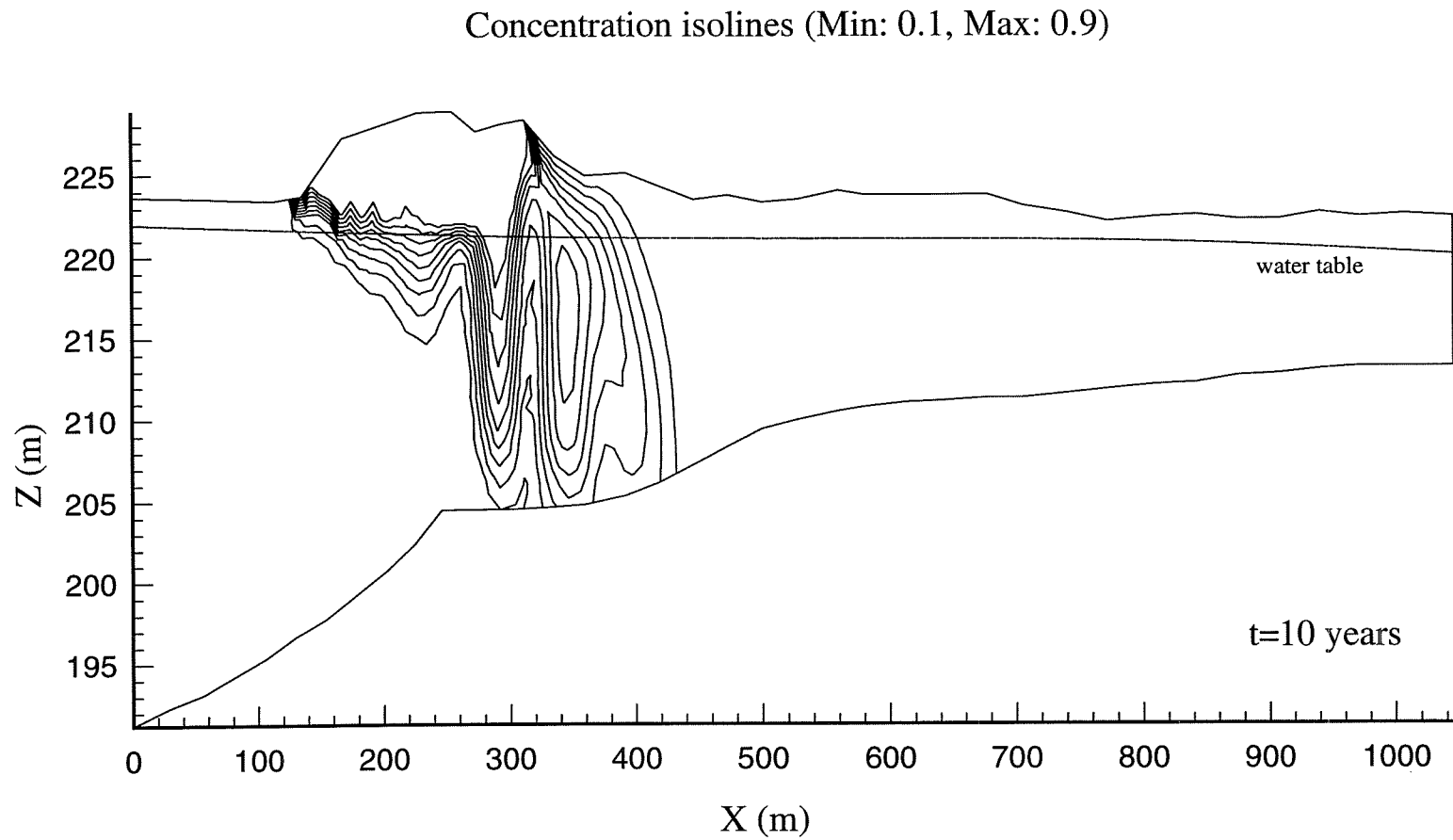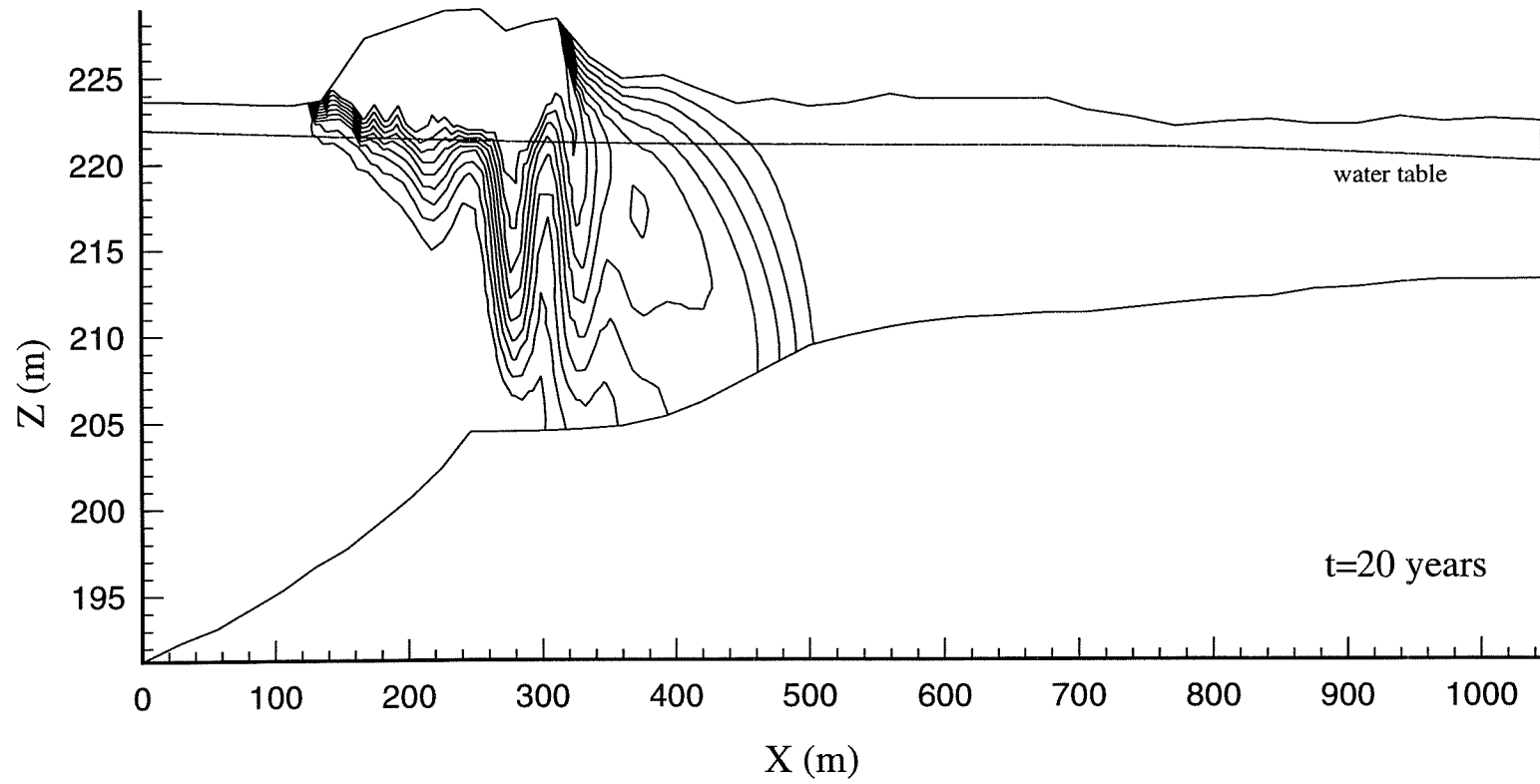Concentration isolines (Min: 0.1, Max: 0.9)

Figure 8.7   Continued

Velocity field

Figure 8.7   Continued

Concentration isolines (Min: 0.1, Max: 0.9)

Figure 8.8   Instability development for a contaminant source ($\varepsilon=0.0055$)
at t=10, 20, 30 and 40 years

Concentration isolines (Min: 0.1, Max: 0.9)

Figure 8.8   Continued

Concentration isolines (Min: 0.1, Max: 0.9)

water table

t=30 years

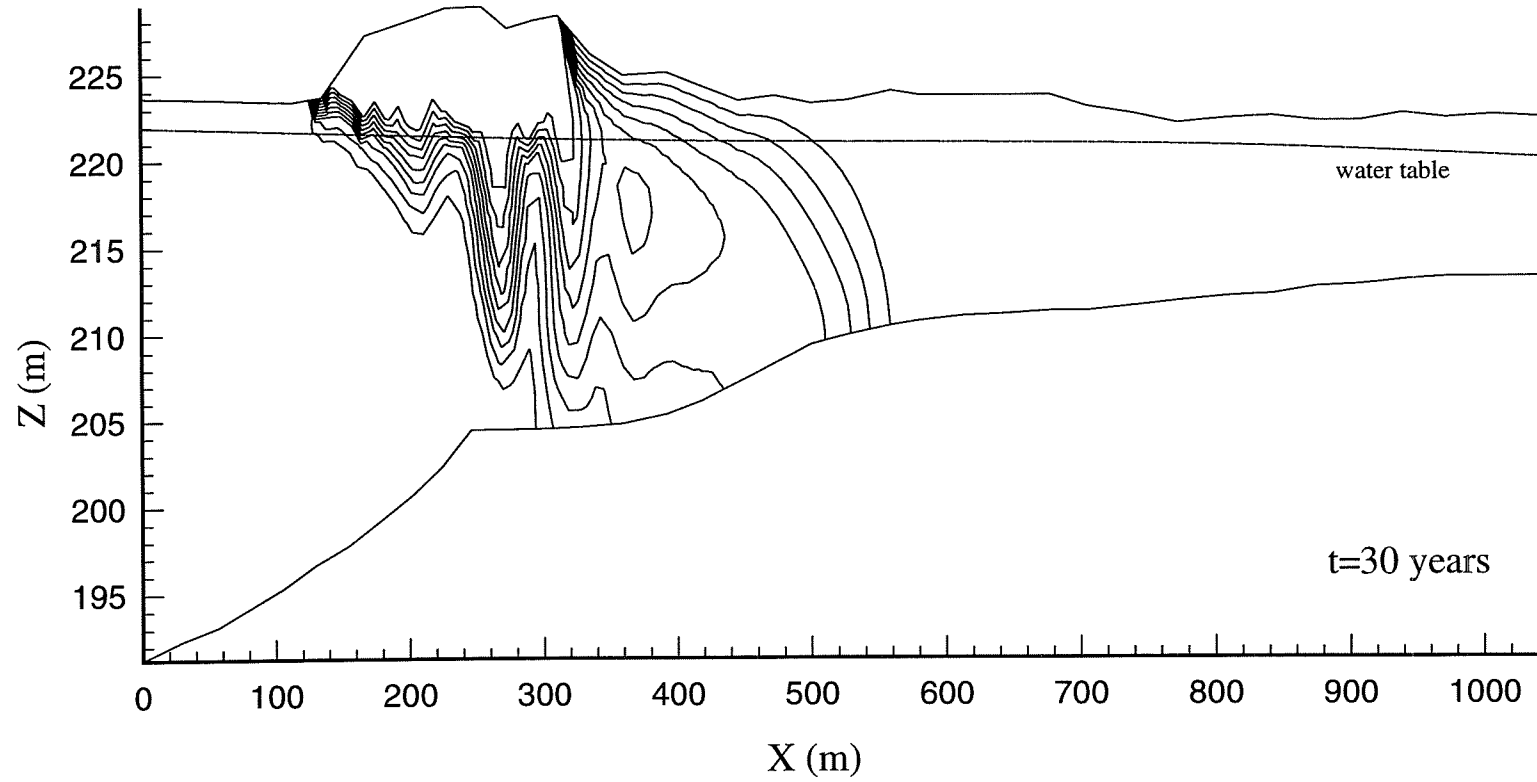Figure 8.8 Continued

Concentration isolines (Min: 0.1, Max: 0.9)

Figure 8.8   Continued

Velocity field

Figure 8.8   Continued

Figure 8.9 Isoline of chloride (mg/L) and sulfate (mg/L) along the longitudinal cross-section (MacFarlane et al., 1983)

Concentration isolines (Min: 0.1, Max: 0.9)

water table

t=10 years

Figure 8.10 Instability development for a contaminant source (ε=0.0055)

at t=10, 20, 30 and 40 years

Concentration isolines (Min: 0.1, Max: 0.9)

Figure 8.10 Continued

Concentration isolines (Min: 0.1, Max: 0.9)

Figure 8.10 Continued

Concentration isolines (Min: 0.1, Max: 0.9)

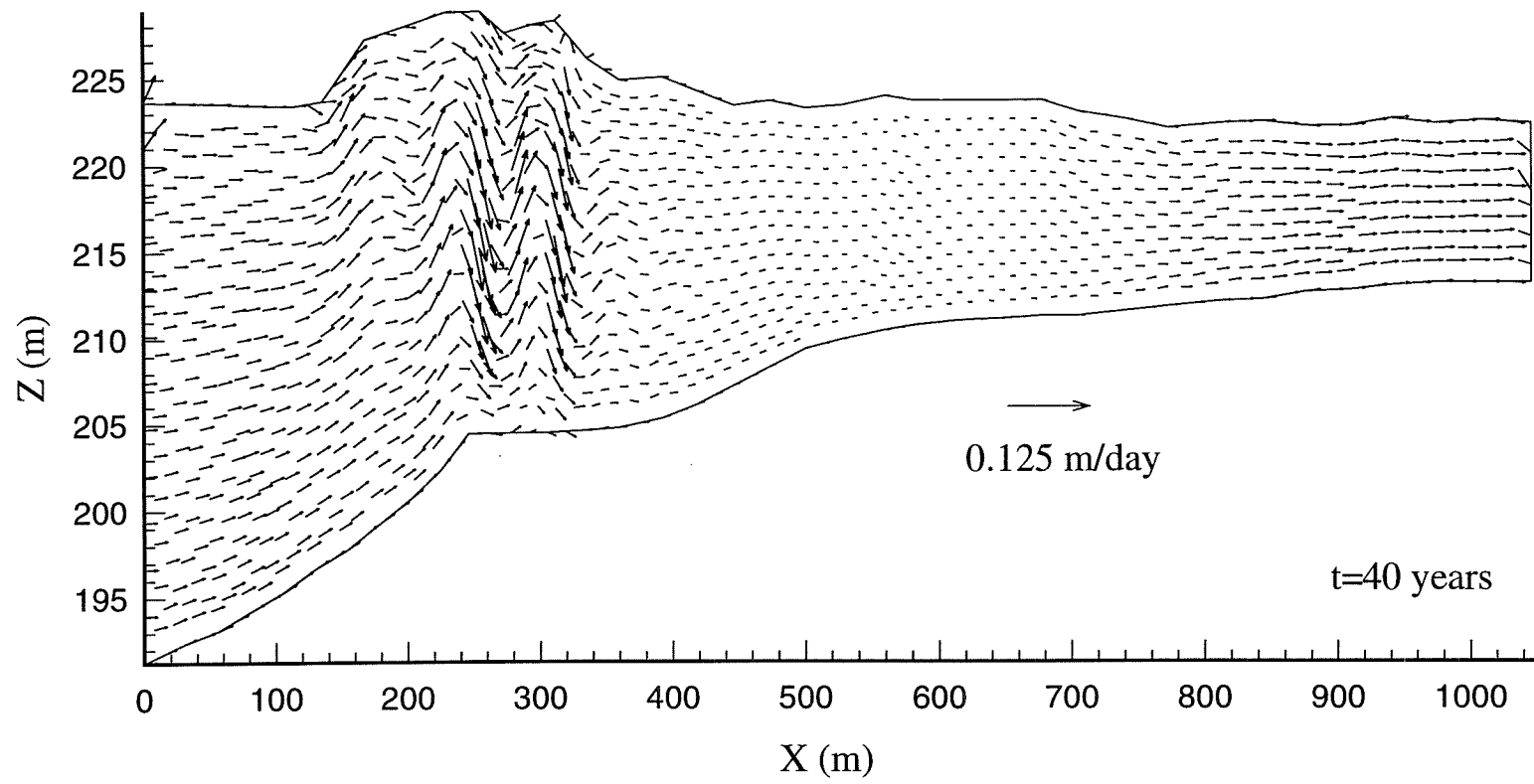Figure 8.10 Continued

Velocity field

Figure 8.8 Continued

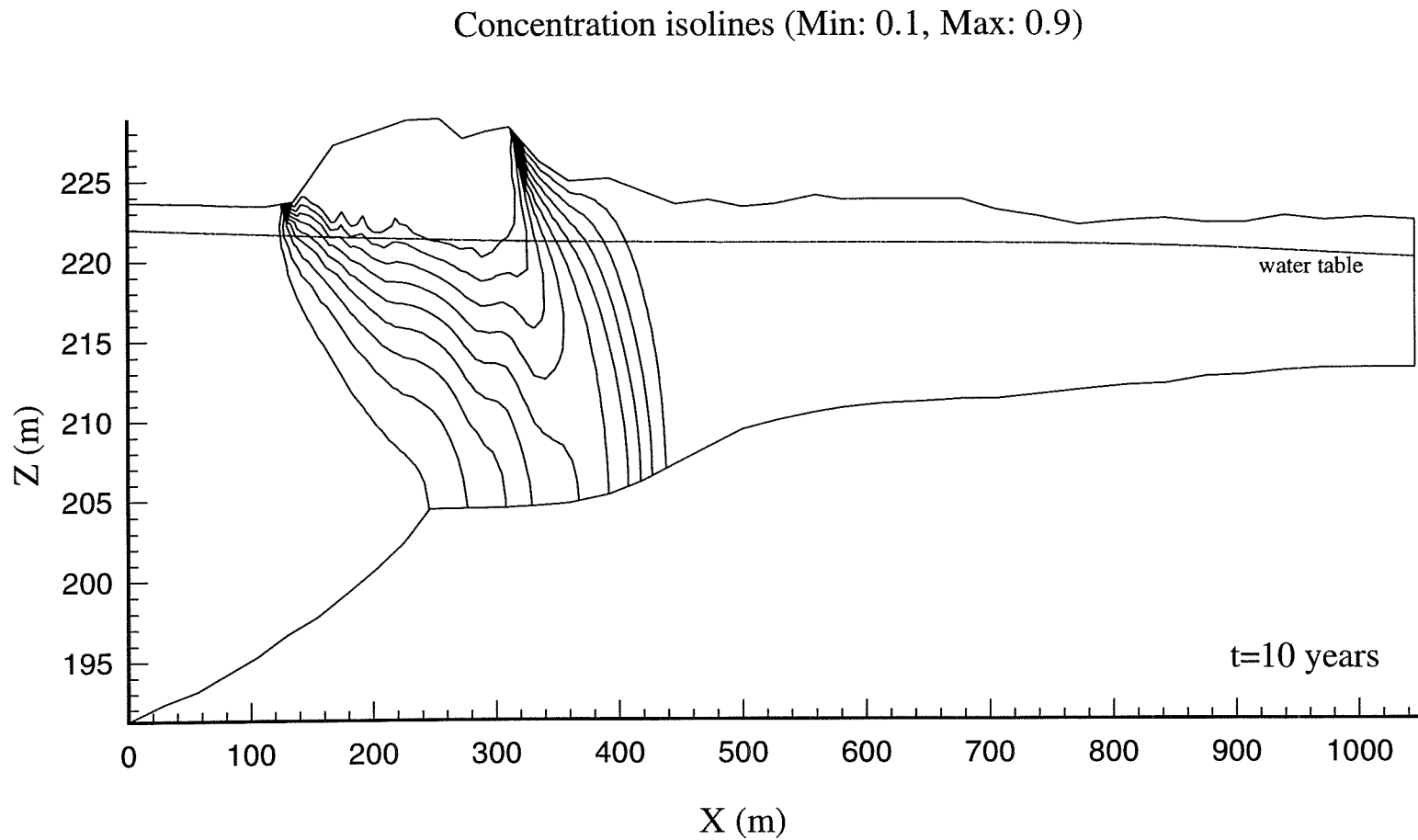Concentration isolines (Min: 0.1, Max: 0.9)

Figure 8.11   Insatbility development for a contaminant source ($\varepsilon=0.0055$, $a_T =0.1$ m) at t=10, 20 30 and 40 years

Concentration isolines (Min: 0.1, Max: 0.9)
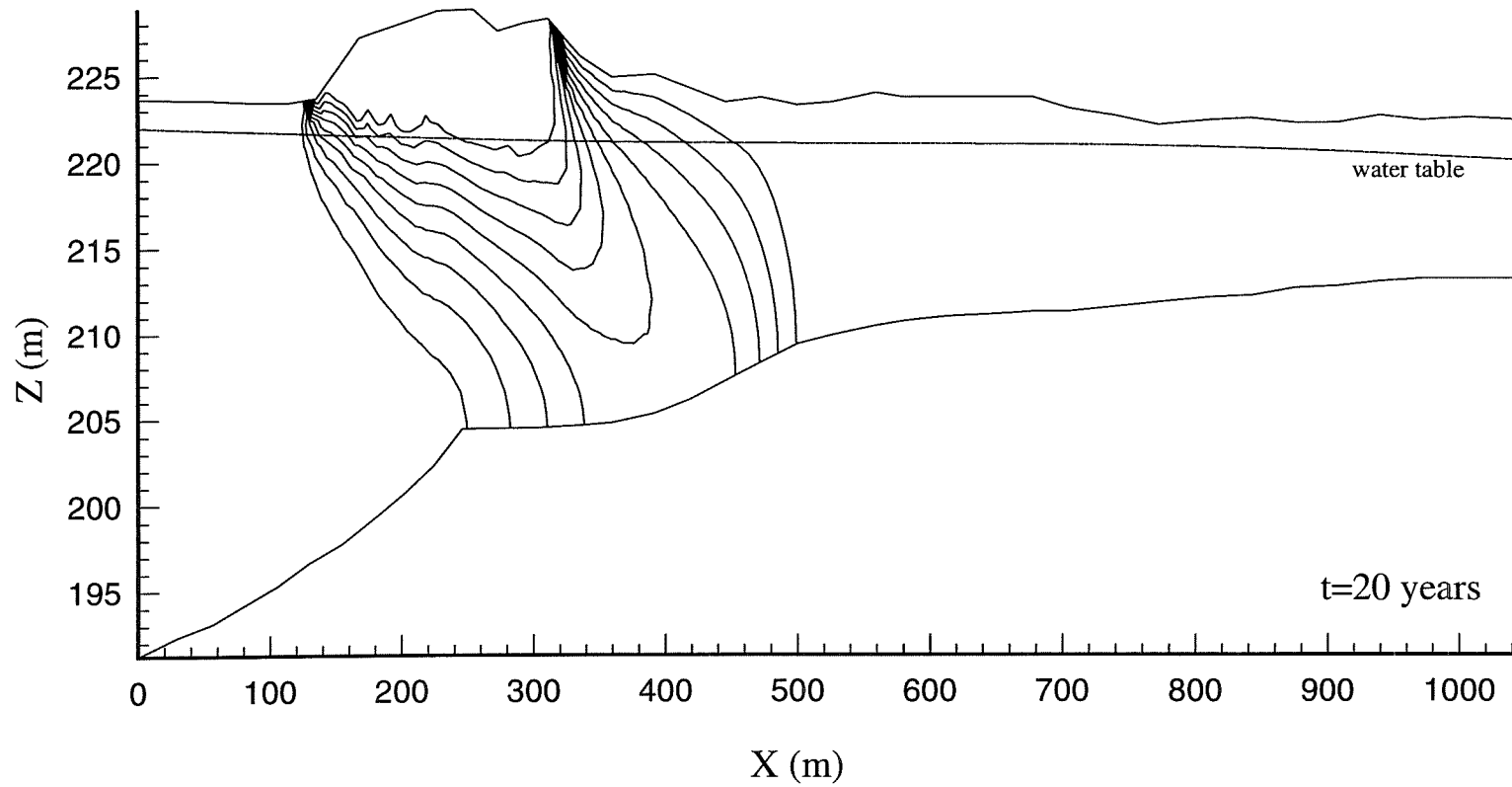

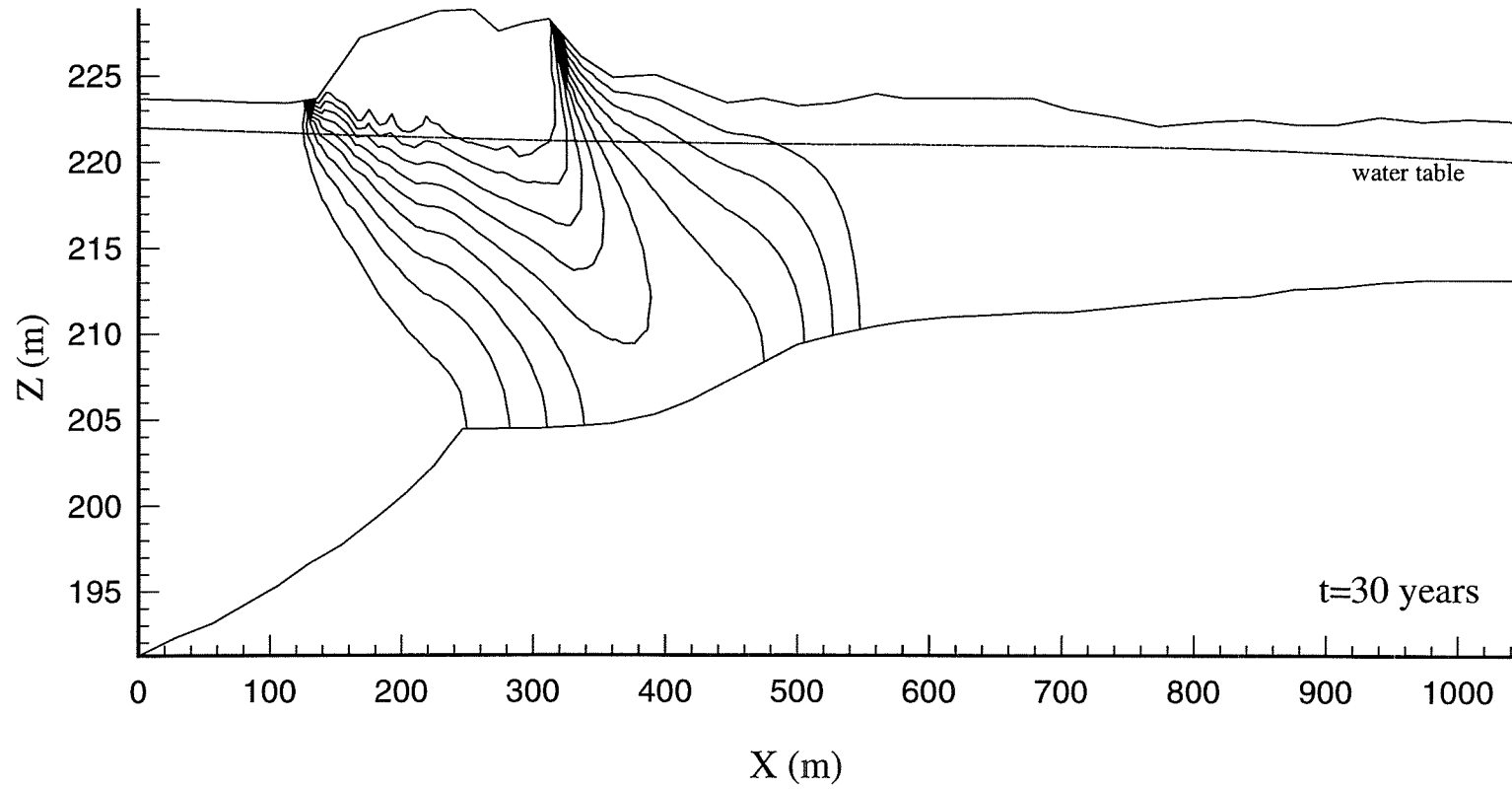Figure 8.11   Continued

Concentration isolines (Min: 0.1, Max: 0.9)

Figure 8.11   Continued

Concentration siolines (Min: 0.1, Max: 0.9)
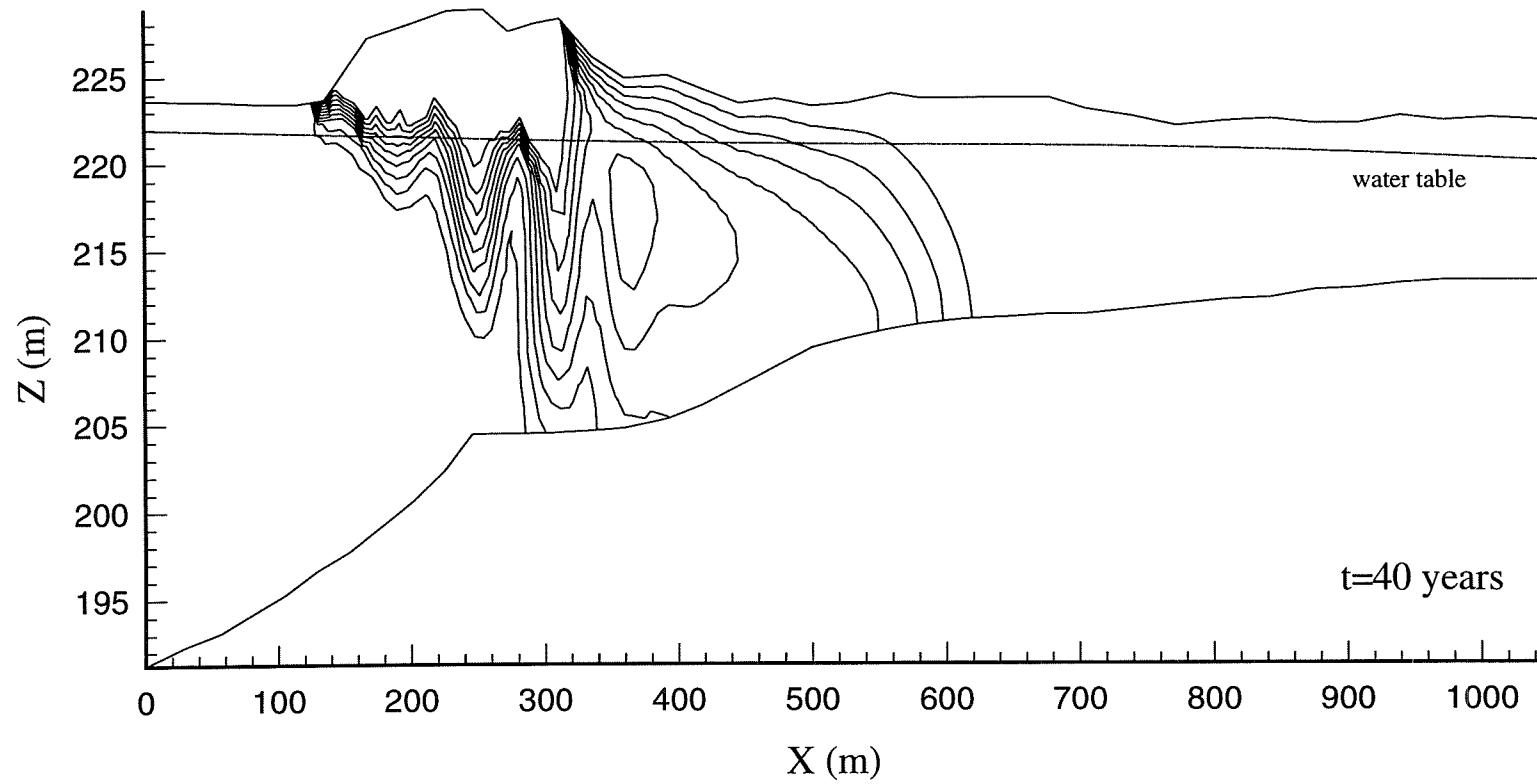
Figure 8.11   Continued

Velocity field

0.125 m/day

t=40 years

Figure 8.10   Continued

Concentration isolines (Min: 0.1, Max: 0.9)

Figure 8.12   Instability development for a contaminant source (ε=0.0055, a_T=0.5 m)
at t=10, 20, 30 and 40 years

Concentration isolines (Min: 0.1, Max: 0.9)

Figure 8.12   Continued

Concentration isolines (Min: 0.1, Max: 0.9)

water table

t=30 years

Z (m)

X (m)

Figure 8.12   Continued

Concentration isolines (Min: 0.1, Max: 0.9)

t=40 years
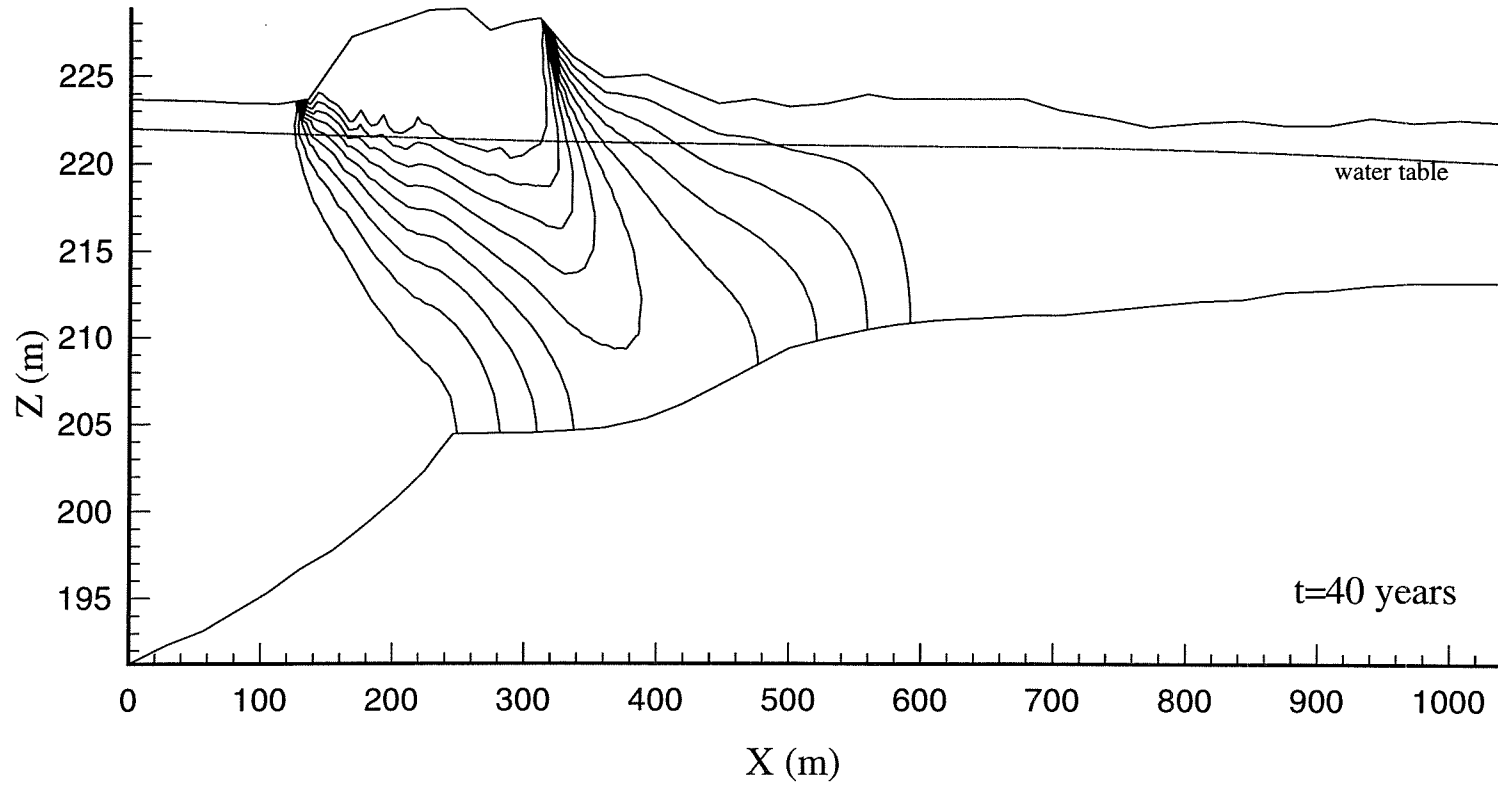
Figure 8.12   Continued

Velocity field

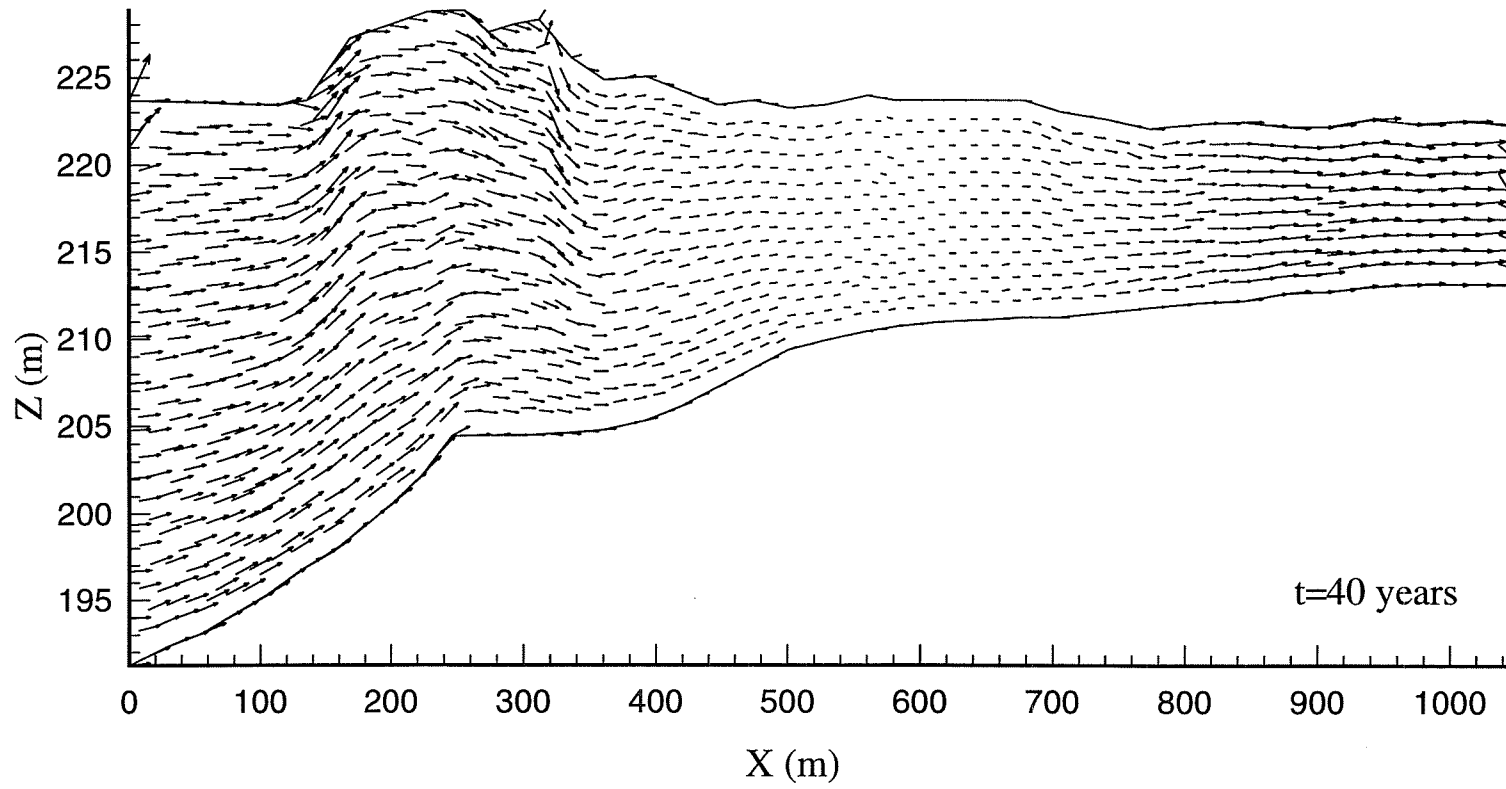Figure 8.12   Continued